Nanoscale characterization of biodegradable, lean magnesium alloys: a detailed study of their microstructure–property correlations

Martina Cihova

Department of Materials
ETH Zurich

2019

ETH *zürich*

Diss. ETH No. 26283

Nanoscale characterization of biodegradable, lean magnesium alloys: a detailed study of their microstructure–property correlations

A thesis submitted to attain the degree of

DOCTOR OF SCIENCES of ETH ZURICH

(Dr. sc. ETH ZURICH)

presented by

MARTINA CIHOVA

Dipl.-Ing. Bioengineering, Karlsruhe Institute of Technology

born on July 9th, 1987

citizen of Germany

accepted on the recommendation of

Prof. Dr. Jörg F. Löffler, examiner
Prof. Dr. Cécile Hébert, co-examiner
Prof. Dr. Daniela Zander, co-examiner

2019

Acknowledgements

This work is the result of a time full of inspiration, doubts, excitement, frustration, curiosity and motivation – a time I will gratefully remember. It would have not been possible without the precious support of numerous people.

First and foremost, I would like to express my sincere gratitude to my thesis advisor *Prof. Jörg F. Löffler* for supervision and guidance. I am thankful for the opportunity to conduct research in your group and for having provided an outstanding infrastructure. I am grateful for the trust you had in me and my sometimes off-track research interests, allowing to get into the research field I felt so fascinated about. Thank you for consistent encouragement, for your confidence in me and for the freedom provided.

Thanks go also to *Prof. Cécile Hebert* from Ecole Polytechnique Fédérale de Lausanne (EPFL) and *Prof. Daniela Zander* from Rheinisch-Westfälische Technische Hochschule (RWTH) Aachen for co-refereeing this work.

Sincere acknowledgements go to *Dr. Robin E. Schäublin*, who joined my PhD project at a later stage but with all the more scientific support and enthusiasm. Thank you for your interest in the project, for endless and very vivid discussions, for your great patience, for training me on the TEM and teaching me about metallurgy, crystallography and the "D's". Sharing fascination and joy, appreciation for the beauty of microscopy, but also puzzlement and doubts, made this collaboration a truly enriching one. Thank you for challenging me, for giving room for outside-the-box thinking and for allowing me to challenge you back.

Heartfelt thanks go also to *Prof. Peter J. Uggowitzer*, who despite his partial retirement had always an open ear for scientific questions and personal advice. I greatly appreciate you took me on this exciting journey to the world of magnesium. Thank you for many inspirational scientific insights and enriching discussions, for sharing your invaluable experiences, for many laughs, anecdotes about science and life and for sharing your enthusiasm.

Next, I want to present my deep acknowledgements to *Dr. Patrik Schmutz* from Swiss Federal Laboratories for Materials Science and Technology (EMPA) Dübendorf, who generously opened the doors to laboratory equipment and to the world of corrosion science. I truly appreciate the time you took for establishing experimental setups and for the intense and invaluable scientific discussions. You and your team at EMPA made each visit a very joyful and enriching one. I want to thank especially *Dr. Claudia Cancellieri,* who supported greatly in the experiments.

in the political questions of our department and beyond. I am proud of what SAM achieved in the last years. Keep it up! Enjoy! Speak up! Have fun!

I want to thank my family and friends for their caring support, for encouraging words, for their understanding of my frequent absence, and for all the joyful times and laughs.

Finally and wholeheartedly, I thank my beloved husband *Jürgen* for his unconditioned support and patience throughout this PhD journey. Thank you for your unlimited trust in me, for your consistent encouragement and support, for your understanding. But most importantly, thank you for reminding me of the truly important things and simply for making me smile every single day.

To our family, with endless gratitude and love

Summary

Micro- and nanoscale intermetallic phases play a critical role for the properties of magnesium (Mg) alloys because they may initiate and control the local corrosion processes via microgalvanic coupling and govern the mechanical properties via precipitation hardening or their active role in grain refinement.

This thesis aims at establishing a thorough mechanistic understanding of the role of the micro- and nanostructure, specifically that of intermetallic phases, for the properties of Mg-based lean alloys with an alloying-element content below 1 at.% of two alloying systems: the Mg–Zn–Ca (ZX) system, with a strong focus on the correlations of the alloys' microstructure and their corrosion susceptibility, and the Mg–Al–Ca–Mn (AXM) system for its correlations of microstructure and mechanical performance. In both cases analytical transmission electron microscopy (TEM), which allows simultaneous access to morphological, chemical and structural information, was utilized to characterize the chemical distribution of the alloying elements and the type of intermetallic phases, which provides the basis for their correlation with the alloys' properties.

Biodegradable ZX-lean alloys have the potential to change as temporary implants the way how cardiovascular and muscoskeletal conditions are treated. Their general suitability for biomedical applications has been demonstrated, but so far the material characterization mainly focused on the macroscopic length scale with little insights into the microstructure-induced corrosion mechanisms at play. However, their in-depth understanding is crucial for a tight control over the degradation behavior in physiological environment and thus critical to a successful clinical outcome.

A quasi-*in situ* TEM method was developed, which allows for the local investigation of the same area before and after corrosion attack at its very early stages. It was combined with *ex situ* cross-sectional TEM analysis of the corrosion products that formed as a well-developed surface layer after prolonged immersion in simulated body fluid. Both methods applied in concert allowed accessing the alloy dissolution on the nanoscale from seconds to hours. Nanometric intermetallic particles (IMPs) composed of Mg_2Ca were found to dissolve preferentially and rapidly after a few seconds of immersion. In contrast, those composed of a ternary IM1-phase were observed to act as local cathodes, which facilitated the hydrogen-reduction reaction on their surface and accelerated Mg-matrix dissolution in their vicinity. High-resolution TEM analysis of the IM1-phase IMPs revealed that electrochemically active Ca and Mg dissolve preferentially, whereas Zn is cathodically protected and gradually enriches, leading to dealloying of the IMPs and their gradual ennoblement. This

mechanism of *cathodically polarized dealloying* was documented for the first time to occur in Mg alloys and is believed to apply for other intermetallic phases and other active alloying systems.

The role of nanometric IMPs in the *macroscopic* degradation behavior of ZX-lean alloys (at a scale relevant to implants, i.e. surface areas of the order of mm² to cm²) was investigated *in vitro* by means of electrochemical methods and complemented by TEM analysis. To this end, two model alloys were used that differed solely in their IMP type, hosting exclusively either Mg_2Ca- or IM1-type IMPs. A significant shift of the corrosion potential E_{corr} towards higher values and an increase of the cathodic reaction rates upon polarization marked the impact of cathodically active IM1-type IMPs on the macroscopic electrochemical response. Despite the nanometric size of the IMPs, their phase type was found to govern the rate of degradation on a macroscopic scale, determined from hydrogen evolution, and charge and current transients. The degradation rate was higher when the IMPs were composed of the IM1 phase compared to the Mg_2Ca phase. The *in vitro* observations were confirmed by *in vivo* investigations upon implantation of the two ZX-model alloys with tailored IMP types into femoral shafts of rats. Micro-computed tomography and histological analysis showed that both alloys are well tolerated by the surrounding tissue with early implant–bone contact and no signs of excessive hydrogen-gas release or inflammation, and are thus rated suitable for their use as temporary bone-implant materials.

Irrespective of the IMP type, both ZX alloys showed a dynamically increasing cathodic activity with progressing dissolution. High-resolution analytical TEM analysis revealed nanometric Zn clusters, which likely formed via noble-element redeposition at the interface of the Mg metal and the corrosion-product-layer. These facilitate as additional nano-cathodes the gradual increase of the alloys' cathodic activity.

In light of the mechanical properties of ZX-lean alloys, the IMPs were found to play a crucial role as effective obstacles to grain-boundary motion in ensuring a fine-grained microstructure. In fact, grain-boundary strengthening was identified to be the far dominating hardening mechanism in ZX-lean alloys, with a *Hall–Petch* constant determined at 255 MPa $\mu m^{1/2}$. In contrast, the contribution of IMPs to the alloys' strength by precipitation hardening is negligibly small, 3 MPa at maximum, owing to their insufficient number density.

Motivated by a lack of hardenability in ZX-lean alloys, an alternative alloy was developed based on the AXM system, also lean in composition, for an intended application in the transportation sector, which imposes a high demand on easy processability and low costs. The alloy-design concept was assisted by thermodynamic calculations and directed towards a microstructure that contains an Al–Mn-pinning phase and an Al–Ca-hardening phase for grain-growth control and age-hardenability,

respectively. The optimized alloy Mg–Al0.6–Ca0.28–Mn0.25 (in wt.%) (AXM100) shows a remarkable age-hardening response of 100 MPa in the *T6* peak-aged condition, corresponding to an increase of ~62%, thus generating a tensile yield strength of 253 MPa. A multiscale microstructural analysis combining light microscopy, TEM, and atom probe tomography, related the superior hardening to the precipitation of nanometric and monolayered *Guinier–Preston* zones composed of Al and Ca. Grain growth during high-temperature treatments was successfully retarded by thermally stable Al–Mn dispersoids, the composition of which was determined to be β-Mn. However, the grain size still needs to be reduced overall to make AXM100 a competitive Mg alloy for commercial deployment.

In sum, the identification of the microstructural contributors to the macroscopic alloy properties in ZX- and AXM-lean alloys presented in this thesis has generated a detailed understanding of the corresponding microstructure–property correlations in these alloys. This sets the premises for tailoring and further optimizing their degradation behavior and mechanical performance.

Zusammenfassung

Mikro- und nanoskalige intermetallische Ausscheidungen spielen eine entscheidende Rolle für die Eigenschaften von Magnesiumlegierungen indem sie sowohl über mikrogalvanische Kopplung die lokalen Korrosionsprozesse initiieren und massgeblich kontrollieren können, als auch durch Ausscheidungshärtung oder durch ihre aktive Rolle in der Feinkornhärtung zu den resultierenden mechanischen Eigenschaften beitragen.

Das Ziel dieser Arbeit ist die Erarbeitung eines umfassenden mechanistischen Verständnisses und die Beschreibung des Einflusses der Mikro- und Nanostruktur, insbesondere der intermetallischen Ausscheidungen, auf die Eigenschaften von sogenannten 'mageren' Mg-basierten Legierungen. Als magere Legierungen werden solche angesehen, die einen Gesamtlegierungselementanteil von maximal 1 at.% aufweisen, also mikrolegiert sind. Zwei Legierungssysteme werden betrachtet: das Mg–Zn–Ca (ZX) System, mit Fokus auf die Korrelation von Mikrostruktur und Korrosionseigenschaften, und das Mg–Al–Ca–Mn (AXM) System, mit Fokus auf die Korrelation von Mikrostruktur und mechanischen Eigenschaften. Für die Untersuchungen beider Systeme wurde analytische Transmissionenelektronenmikroskopie (TEM) intensiv eingesetzt, welche gleichzeitig Aufschluss über morphologische, chemische und strukturelle Informationen einer Probe gewährt. Anhand detaillierter TEM-Analysen war es möglich, die chemische Verteilung der Legierungselemente sowie die vorherrschenden intermetallischen Phasen zu charakterisieren. Die Kenntnis über diese mikrostrukturellen Aspekte bildet die Grundvoraussetzung, um Korrelationen zu den Legierungseigenschaften aufstellen zu können.

Biodegradierbare magere ZX-Legierungen haben das Potenzial durch ihren Einsatz als temporäre Implantate die Behandlungsmethoden von kardiovaskulären und muskuloskelettalen Indikationen grundlegend zu revolutionieren. Die grundsätzliche Eignung dieser Legierungen für den biomedizinischen Einsatz konnte bereits aufgezeigt werden. Allerdings beschränkte sich die materialseitige Charakterisierung bislang weitestgehend auf die makroskopische Grössenordnung, welche nur bedingt Zugang zu den sich abspielenden lokalen Korrosionsmechanismen bietet. Ein tiefgehendes Verständnis dieser Mechanismen und insbesondere des Einflusses der Mikro- und

Nanostruktur ist entscheidend für ein kontrolliertes Degradationsverhalten in physiologischer Umgebung und damit für den klinischen Erfolg.

Ein quasi-*in situ* TEM Protokoll wurde entwickelt, welches einen direkten Vergleich eines identischen Probenbereichs vor und nach Korrosionsangriff erlaubt. Die hohe laterale Auflösung gewährt Einblicke in die lokalen, nanoskaligen Korrosionsereignisse für die initialen Stadien des Korrosionsangriffs. Diese Methode wurde kombiniert mit *ex situ* TEM-Querschnittsanalysen von ausgereiften Korrosionsprodukten, d.h. solchen, die nach einem ausgedehnten Korrosionsangriff einen deckenden Oberflächenfilm gebildet haben. Beide Protokolle wurden hinsichtlich eines Korrosionsangriffs in simulierter Körperflüssigkeit optimiert. In Kombination ermöglichten diese beiden Protokolle den Zugang zur Beobachtung der wirksamen lokalen Korrosionsprozesse, die innert weniger Sekunden bis mehrerer Stunden in der Immersionsflüssigkeit stattfinden. Es wurde beobachtet, dass sich nanoskalige intermetallische Partikel (IMPs) aus Mg_2Ca bevorzugt und sehr rasch – bereits nach wenigen Sekunden Immersion – vollständig auflösen. Demgegenüber steht eine ternäre sogenannte IM1-Phase, welche als lokale Kathode identifiziert wurde. Als solche fungiert diese Phase nicht nur als Ort für die Wasserstoffreduktion, sondern bewirkt auch eine drastische Beschleunigung der anodischen Matrixauflösung in der unmittelbaren Umgebung. Hochaufgelöste TEM-Analysen der IM1-IMPs zeigen, dass sich die elektrochemisch aktiven Elemente Ca und Mg selektiv aus der IM1 Phase herauslösen, wohingegen Zn kathodisch geschützt vorliegt und sich folglich zunehmend anreichert. Diese entgegengesetzten Auflösungseigenschaften der Elemente in der IM1-Phase führen zu einem 'Dealloying', welches eine fortlaufende Veredelung dieser Phase zur Folge hat. Die Beobachtung dieses sogenannten kathodisch-polarisierten Dealloyings wurde für Mg-Legierungen hier zum ersten Mal beschrieben und seine Wirkung auch in anderen intermetallischen Phasen und anderen Legierungssystemen postuliert.

Der Einfluss dieser nanoskaligen IMPs auf die makroskopischen Abbaueigenschaften von mageren ZX-Legierungen (in der für Implantate relevanten Grössenordnung, d.h. im Bereich mm^2 bis cm^2) wurde zunächst für *in vitro* Bedingungen anhand von elektrochemischen Methoden und komplementären TEM Analysen getestet. Zu diesem Zweck wurden zwei Modelllegierungen herangezogen, die sich lediglich in dem Phasentyp der IMPs unterscheiden, d.h. IMPs vorweisen, die entweder ausschliesslich aus der Mg_2Ca oder der IM1 Phase bestehen. Eine signifikante Verschiebung des Korrosionspotentials E_{corr} zu höheren Werten sowie eine Steigerung der kathodischen

Reaktionsraten bei Polarisation kennzeichnete den Einfluss der kathodisch aktiven IM1-IMPs auf die makroskopische elektrochemische Antwort. Trotz ihrer nanoskaligen Grösse sind die IMPs in der Lage, einen markanten Unterschied in der makroskopischen Korrosionsrate zu erzielen, was in einer veränderten Wasserstoffentwicklung sowie veränderten Strom- und Ladungstransienten messbar war. Dabei erhöhte sich die Korrosionsrate, wenn die IMPs aus den IM1-Phasen bestanden. Diese Erkenntnisse, die durch *in vitro* Untersuchungen erzielt wurden, konnten in einer anschliessenden *in vivo* Studie in einem Rattenmodell bestätigt werden. Hochauflösende Computertomographie und histologische Untersuchungen zeigten eine grundsätzlich positive Gewebereaktion auf beide Materialien mit früher Osseointegration und ohne sichtbare Anzeichen von exzessiver Wasserstoffentwicklung oder Entzündungsreaktionen. Die Ergebnisse dieser präklinischen Untersuchungen bewerten beide Materialien als grundsätzlich geeignet für ihren Einsatz als Implantatmaterialien für Osteosyntheseanwendungen.

Unabhängig vom IMP-Typ zeigten beide ZX-Legierungen einen dynamischen Anstieg der kathodischen Reaktionskinetik mit fortschreitender Materialauflösung. Dieses Verhalten kann vermutlich auf Zinkcluster zurückgeführt werden, welche durch hochaufgelöste analytische TEM Analysen in der Korrosionsschicht nachgewiesen werden konnten und wahrscheinlich durch elektrochemische Abscheidung an der metallischen Grenzfläche zur Korrosionsschicht entstanden sind. Solche metallischen Cluster agieren als zusätzliche 'Nano-Kathoden', welche eine fortschreitende Erhöhung der kathodischen Aktivität in ZX-Legierungen ermöglichen.

Bezüglich der mechanischen Eigenschaften von ZX-Legierungen konnte aufgezeigt werden, dass die IMPs eine wesentliche Rolle für die Feinkornhärtung spielen, indem Sie die Korngrenzenaktivität effektiv hemmen und somit ein feinkörniges Gefüge gewährleisten. Die erhobenen Daten zeigen eindeutig, dass Feinkornhärtung den weitaus bedeutendsten Härtungsmechanismus für magere ZX-Legierungen darstellt, mit einer *Hall-Petch* Konstante, die zu 255 MPa $\mu m^{1/2}$ bestimmt wurde. Demgegenüber stellt die Ausscheidungshärtung, die durch die IMPs erzielt werden kann, mit maximal lediglich etwa 3 MPa eine vernachlässigbar geringe Härtewirkung dar.

Ausgehend von der Erkenntnis, dass mit mageren ZX-Legierungen keine zufriedenstellende Warmaushärtung erzielt werden kann, wurde ein alternatives Legierungsdesign erarbeitet. Mit dem Ziel einer aushärtbaren Legierung stützte sich dieser Projektteil auf das AXM Legierungssystem

(ebenfalls beschränkt auf eine mikrolegierte Zusammensetzung), mit dem beabsichtigen Einsatz in der Transportindustrie. In dieser liegt, anders als in der Medizintechnologiebranche, ein hoher Wettbewerbsdruck bezüglich Kosten vor und damit verbunden die Anforderung einer einfachen und energieeffizienten Verarbeitbarkeit. Das Legierungsdesign wurde durch thermodynamische Simulationen unterstützt und zielte auf eine Mikrostruktur ab, die einerseits eine thermisch stabile Al–Mn-reiche Phase zur Limitierung von Kornwachstum auch bei erhöhten Temperaturen («particle pinning») beinhaltet, und andererseits eine Al–Ca-reiche Phase zur Warmaushärtung nach der Warmumformung. Die optimierte Legierung mit der Zusammensetzung Mg–Al0.6–Ca0.28–Mn0.25 (in wt.%) (AXM100) zeigt ein bemerkenswertes *T6*-Warmaushärtungspotential von etwa 100 MPa, welches einer Steigerung der Zugfestigkeit um ~62% auf 253 MPa entspricht. Multiskalige Einblicke in die Mikro- und Nanostruktur anhand von Lichtmikroskopie, TEM und Atomsondentomographie zeigen, dass die Ausscheidung von geordneten und monolagigen *Guinier–Preston* Zonen als Vorläufer der Gleichgewichtsphase Al_2Ca für die bemerkenswerte Warmaushärtung verantwortlich ist. Darüber hinaus konnte ein Kornwachstum bei höheren Temperaturen erfolgreich durch Al–Mn Dispersoide verhindert werden, die als β-Mn Phase identifiziert wurden. Trotz dieser Kontrolle über die Korngrösse ist eine weitere Kornfeinerung für AXM100 anzustreben, um die Feinkornhärtung auszuschöpfen und somit die Legierung konkurrenzfähig zu kommerziellen Mg-Legierungen zu machen.

Zusammengefasst wurden im Rahmen dieser Arbeit die mikrostrukturellen Merkmale identifiziert, welche für die makroskopischen Eigenschaften von mageren ZX- und AXM-Legierungen verantwortlich sind und damit ein umfassendes Verständnis ihrer fundamentalen Mikrostruktur–Eigenschaftskorrelationen ermöglicht. Dieses Verständnis liefert die Voraussetzungen für eine weitere Materialoptimierung hinsichtlich des Degradationsverhaltens und der mechanischen Eigenschaften.

Content

Glossary

	Unit	Description
α	-	Obstacle strength
β	°	Tilt angle (stereo microscopy)
δ	m	Thickness of TEM foil
μ	GPa	matrix shear modulus
σ_o	MPa	Friction stress for dislocation movement

	Unit	Description
A_f	(%)	Elongation to fracture
$CRSS$	-	Critical resolved shear stress
b	Å	Amplitude of Burgers vector
d	m	diameter
D	m	Grain size
D_{max}	m	Max. possible grain size according to *Hall–Petch* estimation
E_{OCP}	V	Open circuit potential
E_{corr}	V	Corrosion potential
f	m^{-3}	Volume fraction
H_V	-	Vicker's hardness
i_o	$A\,cm^{-2}$	Exchange current density
i_{corr}	$A\,cm^{-2}$	Corrosion current density
k_y	$MPa\,\mu m^{1/2}$	*Hall–Petch* constant
l	m	Interparticle spacing
M	-	Taylor factor
n	-	Number count
N	m^{-3}	Number density
p	m	Paralla
T	°C, K	Temperature
t	s	Time
TYS	MPa	Tensile yield strength
UTS	MPa	Ultimate tensile strength
Z	-	Atomic number

APT	Atom probe tomography
BF	Bright field
BSE	Backscattered electron
ED	Electron diffraction
EDS	Energy-dispersive X-ray spectroscopy
G.P.	Guinier Preston
FOLZ	First-order Laue zone
HAADF	High angle annular dark field
HR	High resolution
if	Interface
IMP	Intermetallic particle
p.o.	*post operationem*
REE	Rare-earth element
ROI	Region of interest
SABACO	Same Area Before and After COrrosion
SBF	Simulated body fluid
SEM	Scanning electron microscopy
SE	Secondary electron
sht	Solution-heat treated
SSSS	Super-saturated solid solution
STEM	Scanning transmission electron microscopy
T5	Temper: As extruded + artificially aged
T6	Temper: sht + artificially aged
TEM	Transmission electron microscopy
XHP	Ultrahigh purity
xSEM	Cross-sectional SEM
xTEM	Cross-sectional TEM

Materials

	wt.%	at.%
XHP	Mg99.999	
ZX10	Mg–Zn1.0–Ca0.3	$MgZn_{0.37}Ca_{0.18}$
ZX20	Mg–Zn1.5–Ca0.25	$MgZn_{0.56}Ca_{0.15}$
AXM100	Mg–Al0.6–Ca0.28–Mn0.25	$MgAl_{0.54}Ca_{0.17}Mn_{0.11}$

1 Introduction

1.1 General introduction

1.1.1   Magnesium – a unique metal

Magnesium (Mg) was discovered and first isolated in 1808 by the British chemist Sir Humphry Davy [1] and became available in larger quantities from the 1830s following the findings of French scientist Antoine A. B. Bussy, who managed to isolate metallic Mg by fusing magnesium chloride with metallic potassium [2].

Ever since Mg gained importance as powder in pyrotechnics and as the lightest structural metal in a number of industrial applications, especially for those in the transportation and biomedical sectors [3, 4]. In these sectors, with a density of 1.74 g cm^{-3} at 20 ºC, corresponding to only about 65% of that of aluminum (2.7 g cm^{-3}) and even only about 38% of the density of titanium (4.5 g cm^{-3}), Mg presents an attractive alternative to both established lightweight metals. Compared to polymers, while Mg's density is slightly higher than that of typical fiber-reinforced plastics (typically on the order of 1.2 – 2.0 g cm^{-3}, depending on the choice of resin and fiber and their respective percentage), it offers greater compressive strength and stability at higher operating temperatures. Because weight reduction goes along with a reduction of CO_2 emission and fuel consumption, it is indeed the superior strength-to-weight ratio of Mg alloys that is usually the prime reason for their consideration in engineering design. However, balancing its strength with other properties such as corrosion resistance, creep or its limited ductility is still focus of intense research.

Mg is the eighth-most abundant element in the earth crust, where it occurs mainly in the form of insoluble carbonates, sulfates and silicates, and is a plentiful element in sea water, where it occurs in ionic form or as carbonates [3]. Owing to its large stock and relative ease of extraction, Mg is available at modest costs. The economic advantage is extended by Mg's recyclability [5] and the relatively low temperatures required for its processing (T_m = 650 ºC, typical processing temperatures for hot forming 250 – 450 ºC). Furthermore, Mg provides castability and machinability, which are both prerequisites for its industrial applicability, and weldability, and offers excellent damping properties and high thermal conductivity [3].

Mg occurs not only naturally in the earth crust but is also abundantly present in living species including humans, where it plays a vital role for many cellular and enzymatic functions [6], such as in the synthesis of proteins and nucleic acids, DNA and RNA, and in green plants [7], where it is among other functions considered the 'powerhouse' behind photosynthesis for its central role in chlorophyll's efficient use of light.

Besides this wealth of its attractive characteristics as an engineering material and its vital role in organic processes, Mg is an exceptionally challenging material in terms of handling: it is highly reactive in aqueous solutions and air, which entails a considerable corrosion susceptibility, and its flammability presents a potential safety hazard, requiring particular precautions.

1.1.2   The use of magnesium as a biomaterial

Physiological role and distribution of Mg

Mg is the fourth-most abundant mineral in the human body with a mass of about 21 –28 g in an average adult [6] and the second-most common intracellular cation [8]. Mg belongs to the essential elements, i.e. elements that are vital for normal physiological function and cannot be synthesized by the body but require dietary intake at a recommended daily dose of 280 – 350 mg for adults [9]. Approximately 99% of the total Mg in the body is found intracellularly in bone (50 – 60%), muscles (25 – 30%) and non-muscular soft tissue (20 – 25%), and only about 1% resides as extracellular Mg in serum and red blood cells (Figure 1.1) [8]. The magnesium balance is maintained by the intestine, the bones and the kidneys, and excess can be harmlessly excreted through the urinary tract [6].
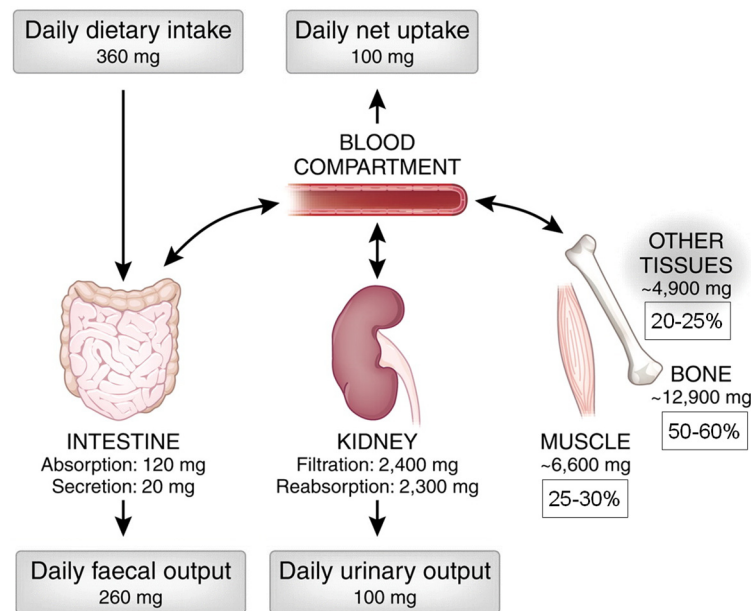
Figure 1.1: Magnesium balance and distribution in the human body. Adjusted from [8].

As a cofactor in > 300 enzymatic reactions, Mg fulfills numerous intracellular physiological functions, including ionic transport, energy metabolism, synthesis of proteins and nucleic acids, and cell proliferation [6]. Furthermore, it plays an essential role in bone formation, neuromuscular stability and muscle contraction [6]. In fact, accumulating evidence supports that Mg has

osteoconductive properties [10, 11], i.e. it stimulates bone growth on a surface, and osteoinductive properties [12, 13], i.e. it induces bone formation. In contrast, its deficiency affects the expression of pro-inflammatory cytokines, which activates bone resorption and thus presents a risk factor for osteoporosis [14].

Mg as a biomaterial: a historical view

With the important role Mg plays in the human body, it is not surprising that soon after its discovery in the 19th century its potential applicability as a biomaterial was explored. In fact, the use of Mg as a biomaterial dates back to 1878 when the physician Edward C. Huse reported the use of Mg wires as a ligature to stop bleeding vessels in humans and observed the dissolution of Mg over time [15]. Further studies followed, with pioneering work conducted by the physician Erwin Payr, who tested Mg for its use as intravascular tubes to treat cardiovascular conditions and also, among others, as fixator pins, nails and wires to treat musculoskeletal indications [16-18]. Payr described the observation of gas formation as a degradation product and postulated that the *in vivo* corrosion of Mg was owing to a combined effect of dissolved salts, tissue oxygen, water content, carbon dioxide and chemical cellular processes [16, 17]. The pre-clinical and clinical studies on Mg-based biomaterials proceeded into the 1920s, but the interest in them vanished almost completely after owing to their inappropriate performance – mainly the too rapid degradation. The latter was likely due to the low material purity available at that time, and concomitant excessive formation of subcutaneous gas cavities, and due to a lack of engineering solutions to overcome these limiting properties.

It was not until the 1990s that Mg as a biomaterial gained again increasing attention. This was stimulated by improvements in metal purification technology and alloy development, which both paved the way to essential improvements in corrosion resistance. Since then immense efforts were devoted to basic and translational research in order to understand the biodegradation behavior of Mg and its alloys in physiological environment [10, 19] and their impact on the biological response [10, 12, 13, 20], to develop materials with improved properties [21, 22] and to demonstrate their clinical potential [4, 11, 23]. A comprehensive historical review on Mg implants is provided by Witte in Ref. [24].

Mg as a new temporary implant material

Mg as a *biodegradable* biomaterial contrasts the traditional *bioinert* metallic biomaterials, i.e. mainly titanium and its alloys, surgical stainless steel and cobalt–chromium alloys, which have been designed towards optimized corrosion and wear resistance [25]. In orthopedics, despite the generally successful use and many years' proven functionality of these bioinert alloys, their permanent use

4

poses a risk due to possible complications, in particular peri-implant infections or aseptic implant loosening [26], but also implant fracture, implant dislocations, or allergic reactions or hypersensitivity to the material [27]. In such cases or prophylactically, the implant is removed in a second surgery. In pediatrics, implant removal is even a standard procedure as to prevent the implant from impairing the patient's growth. This secondary surgery entails besides an immense economic burden, a health risk and discomfort for the patient.

Polymeric biodegradable implants, usually based on polyesters composed of homopolymers or copolymers of glycolide and lactide, have been designed to overcome these limitations and entered the clinics initially in the 1960s as biodegradable sutures [28] and later, in the 1980s, as biodegradable implants for orthopedics [29, 30]. However, their intrinsic mechanical properties with a significantly reduced strength compared to metallic biomaterials (Table 1.1) limit their use for load-bearing applications. Furthermore, their degradation, which proceeds via hydrolysis and entails a drop of the tissue pH, is associated with inflammatory tissue response and necrosis [30, 31].

Table 1.1: Mechanical parameters of bone tissue and common biomaterials used for osteosynthesis and musculoskeletal treatments. Data were compiled from Refs. [32-34].

Tissue/material	Density (g cm^{-3})	*TYS* (MPa)	*UTS* (MPa)	Young's modulus (GPa)
Cortical bone	1.8 – 2.0	105 – 114	35 – 283	5 – 23
Cancellous bone	1.0 – 1.4	NA	1.5 – 38	0.01 – 1.6
Ti–Al6–V4	4.43	760 – 880	830 – 1025	110
Stainless Steel	8.0	200 – 300	450 – 650	190 – 205
Synthetic HA	3.1	NA	40 – 200	70 – 120
PLA/PGA/PLLA	1.2 – 1.7	15 – 75	29 – 100	0.4 – 7
Mg cast	1.74	20	65	41 – 45
Mg wrought	1.74	100	180	41
Mg–Zn–Ca-lean alloy (ZX10) extruded	1.79	140 – 247	240 – 268	NA

NA: not available; HA: hydroxyapatite; PLA: Polylactide; PGA: Polyglocolide; PLLA: Poly-L-lactide

Mg-based biomaterials combine the ability to biodegrade, thus rendering a second surgery for implant removal unnecessary, with the advantage of superior mechanical properties of metallic materials (Table 1.1). In fact, for those applications that are load-bearing, Mg holds the advantage not only over biodegradable polymers but also over the traditional bioinert metals for its Young's modulus (41 – 45 GPa), which is close to that of human bone (5 – 23 GPa) (Table 1.1). The close match of the elastic properties improves bone regeneration by circumventing stress shielding, a

phenomenon resulting from inhomogeneous stress transfer on the bone, which limits the bone-healing process, may lead to implant loosening, and is observed in patients treated with bioinert metals that impose a much larger Young's modulus (≥ 110 GPa) [35]. In contrast, owing to Mg's characteristics of being osteoconductive or -inductive, Mg-based implants or Mg-depleting permanent implants [36] are associated with enhanced, *actively stimulated* osseointegration, i.e. integration of the implant into the bone tissue [37]. For that reason its application in the treatment of musculoskeletal conditions [4, 23] received particular attention. Besides, temporary implants based on Mg have been extensively explored for the treatment of cardiovascular conditions [38, 39], for its applicability in tissue engineering [40], and for absorbable sutures [41], wound-closing devices [42] and degradable drug-carriers for local and controlled drug elution [43].

Crucial for a successful clinical outcome is a degradation behavior that is tailored to the intended application. In this context, the application's characteristics are to be considered such as the specific implantation site with the prevalent tissue type, degree of blood perfusion, or mechanical load condition, which all may influence the material degradation. Figure 1.2 presents the optimal time course for the gradual resorption of an Mg implant and the mutual tissue-healing process for the example of fractured bone. Mechanical integrity of the implant is required until bone healing is sufficiently advanced for the tissue to progressively take over part of the load. From this point, the mechanical strength of the implant, concomitant with its volume, should gradually decline at a rate that matches the new-bone formation of the surrounding healing tissue.
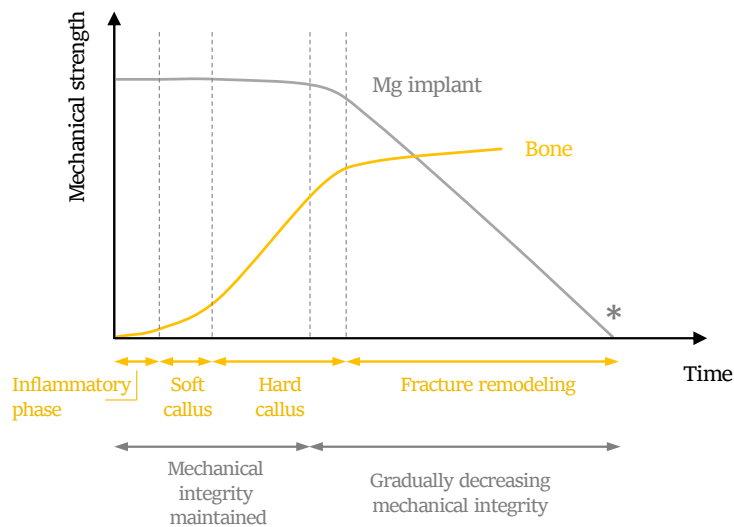

Figure 1.2: Ideal degradation behavior of an Mg-based implant and concurrently occurring biological processes involved in bone-fracture healing. The asterisk marks the point in time of completed implant degradation. Modified from [4].

Following intensive pre-clinical and clinical studies in the last two decades, first Mg-based products recently arrived in the clinics. While this thesis can only give a brief insight into the *status quo* of the clinical translation of Mg-based implants, a comprehensive overview on this subject is provided in recent review articles by Zhao et al. [4] and Han et al. [39].

In the field of orthopedic implants, an Mg-alloy compression screw is available from the company Syntellix AG (MAGNEZIX®, Syntellix AG, Germany). While their first product was launched in 2013 for the treatment of Hallux valgus [44], a forefoot deformation, the product portfolio is now expanded by screws and pins of different sizes. In the pivotal trial, a comparable clinical outcome to the treatment with permanent Ti implants was reported along with no signs of foreign-body reactions, osteolysis or systemic inflammatory reactions [44]. Gas formation remained uncommented in this study.

Later studies showed positive clinical outcomes in the majority of the patients, comprising reduced pain and improved mobility compared to permanent Ti implants cases [45-47]. Although left uncommented in the report of the pivotal trial [44], radiographs of the following studies frequently revealed a radiolucent area around the implants, which was associated with the formation of gas cavities [46, 47]. It was concluded from these observations that although the implant property of being osteoconductive may be questioned, the fracture healing was not impaired [47]. Despite the generally positive results, clinical complications were also observed: for instance, signs of osteolysis and early implant disintegration after only 6 weeks of implantation were reported [46]. No explanation for the increased implant-degradation rate in these patients was provided.

From a material's perspective, these commercial osteosynthesis implants are made from an Mg–Y–RE–Zr alloy [48], similar to the commercial WE43 alloy with a nominal composition of 3.7 – 4.3 wt.% yttrium, 2.0 – 2.5 wt.% neodymium, 0.4 – 1.0 wt.% zirconium, and a maximum of 1.9 wt.% of other rare-earth elements (REEs) [49]. The mechanical properties (*TYS* of 260 MPa, *UTS* of 290 MPa and elongation to failure, $A_f > 8\%$) are the result of their production route, namely powder extrusion [48]. It should also be noted that the REEs contained, such as Y, Nd and Gd, may entail questionable biosafety [50-53] (see section 1.1.3. '*Design considerations for the development of biodegradable implant materials*').

In contrast, a biologically safe composition is provided by the commercial products from Korean U&I Corporation (Resomet®, Mg–5 wt.%Ca–1 wt.%Zn alloy, approval in Korea cleared in 2015) for the osteofixation of hand fractures [23]. Gas accumulation could be observed in the radiographs around the implants, comparable to those implants made from the Mg–Y–REE–Zr alloy, though the normal fracture-healing rate was not affected by the Mg-based implant [23].

Additional commercial products can be expected soon from Chinese Dongguan Eontec Co., Ltd. (99.99 wt.% Mg) for the fixation of vascularized bone graft [54], and from the Austrian BRI.Tech company (BRI.Tech GmbH, Austria, Mg–0.45 wt.%Zn–0.45wt.%Ca alloy, ZX00, which was developed at ETH Zurich in collaboration with Medical University Graz). In both cases, Mg-based osteosynthesis implants are currently tested in first-in-man studies with encouraging results ([54, 55]).

In the field of cardiovascular intervention, *Biotronik* launched the first Mg-based drug-eluting stent (Magmaris®, Biotronik AG, Germany) for the treatment of coronary-artery diseases in 2016 [56]. The product is made from the same Mg–Y–REE–Zr alloying system as mentioned above, ergo entailing the same potential concerns regarding biological safety. The Mg-based stent demonstrated in preceding pre-clinical [57] and first-in-man trials [58, 59] considerably lower thrombogenicity (i.e. induction or promotion of thrombus formation) than a commercial biodegradable polymeric stent [57] and – in combination with a drug-eluting coating releasing an antiproliferative agent – much reduced restenosis rate (i.e. reclosure of the blood-vessel lumen) compared to a permanent control stent made of stainless steel [58]. Moreover, the number of incidents of target lesion failure (i.e. cardiac mortality, target-vessel myocardial infarction or target-vessel revascularization) was reduced in patients up to 12 months following treatment with an Mg-based stent compared to polymeric stents [59]. The long-term results are just as convincing, with no cases of thrombosis and no signs of restenosis reported up to 36 months *post operationem* [38].

At the time this thesis was written, newest reports summarizing the clinical outcome of about 2000 patients treated with the Magmaris® stent report a good or very good clinical outcome in 96% of the cases [60]. However, cases reporting severe clinical complications related to the Mg-based stent need to be also mentioned. Significant early-stent restenosis and early loss of radial force were observed [61, 62], potentially related to overly rapid degradation in an infant patient [61], or potentially related to the medical history comprising diabetes of an adult patient [62]. While the causes of these occasional failures remain speculations to date, the patient-to-patient variations – potentially related to age or medical conditions – underline the necessity for a more detailed understanding of the fundamental processes with which the Mg-based implants corrode in complex physiological environment. A deeper understanding of the impact of Mg and its corrosion products on the biological processes, comprising enzymatic, cellular and genetic reactions, is also urgently required. Only a comprehensive understanding of the biomaterial–biological interactions will allow to predict and with that eventually control the implant's degradation and thus ensure patient safety.

1.1.3   Design considerations for the development of biodegradable implant materials

Materials for biomedical applications pose a particular challenge to materials science as they must meet both, engineering and physiological requirements. The Mg-based alloys that are commercially available today, including Mg–Al–Zn-based (AZ series) and Mg–Y–REE-based (WE series) alloys, were originally not designed for the biomedical use but for lightweight structural applications [63]. Nevertheless, candidates of these alloy series were intensively tested *in vitro* and *in vivo* and even passed standard cytotoxicity assays [12, 22, 64]. Even more, a representative of the WE series, the alloy WE43, which was originally designed for aircraft and high-performance vehicles applications, has been used in first commercially available Mg-based implants (see section 1.1.2. '*The use of magnesium as a biomaterial*'). However, the awareness regarding biosafety concerns related to Al and REEs used in these alloys increases steadily, stimulated by reports that showed a potential association of Al with Alzheimer's disease [65], and the accumulation of REEs in bone [66, 67] and several organs [52, 67, 68], so far with unknown consequences. Thus, new materials are required that are designed specifically for their biomedical use.

The optimal material is simultaneously sufficiently **strong** *and* **ductile**. Mg has a large specific strength and the similarities to the mechanical properties of human bone (Table 1.1) provide, as mentioned, an advantage over bioinert metals as to prevent stress shielding. However, its hexagonal lattice structure exhibits an insufficient number of independent deformation systems, and thus renders Mg intrinsically brittle at room temperature. That and the low mechanical strength impair its applicability in load-bearing applications. For this reason, pure Mg has almost no industrial relevance. Much effort has therefore been devoted to increase the material strength and ductility. Additional slip systems can be activated by the addition of alloying elements [69, 70]. Generally, an appropriate choice of the alloying element (Table 1.2) can strengthen the material by solid-solution strengthening, by acting as grain refiner and/or by precipitation hardening. For instance, alloying with REEs has been shown to significantly improve room-temperature ductility [69, 71].

Alternatively or additionally, texture and grain-size engineering by thermomechanical processing are efficient strategies to improve the mechanical properties [33, 72-76] by activating additional slip systems [77, 78]. Manipulation of the texture and grain size, while maintaining reasonable ductility, can be obtained by hot forming such as extrusion [33, 73, 79], rolling [74], or severe plastic deformation [75, 76], which all aim at a refined grain size. As a result, wrought fine-grained Mg alloys have large industrial relevance.

Table 1.2: Effect of common alloying elements in Mg on mechanical properties and corrosion resistance. Data compiled from [21, 69, 80, 81].

Alloying element	Max. solubility/ wt.%	Effect of alloying element on			
		Grain refinement	Strength	Ductility	Corrosion resistance
Al	12.7	+	+	+	+
Ca	1.35	+	+	-	-
Gd	23.49	+	+		-
Li	5.5		-	++	
Mn	2.2	+	+	-	+
Y	11.4	+	+	+	+
Zn	6.2		+	+	-
Zr	0.58	++	+	+	-

*The optimal material **degradation** is **homogeneous** and sufficiently **slow**.* Magnesium's resorbability, while presenting the fundamental property in the context of its application as a temporary biomaterial, at the same time remains the major challenge in the development of suitable Mg alloys. A controlled, slow and homogeneous degradation is essential to match the rate of degradation with the rate of the healing progress of the surrounding healing tissue (Figure 1.2), to ensure mechanical integrity of the implant, and to avoid tissue irritation and degradation-product accumulation which would impair the healing process [12, 82].

Alloying is the main strategy to tune the degradation characteristics [21]. Ideally, alloying elements are chosen that have a high solubility in Mg and possess greater nobility than Mg (Table 1.2), thereby enhancing the electrochemical potential of the Mg matrix. In this light, (coarse) precipitation is to be avoided because secondary phases may not only function as cathodic spots, thus accelerating the corrosion rate, but also lead with a corrosion rate that typically differs from that of Mg to an inhomogeneous corrosion front [83, 84]. Following this thought of line, amorphous Mg alloys, i.e. metallic glasses, appear attractive [81, 85]. The rapid cooling at which these materials are produced allows for an exceptional high alloying content without precipitation. Corrosion resistance and homogeneity are thus often associated with Mg-based metallic glasses that are superior to their crystalline counterparts [86]. Nevertheless, Mg-based metallic glasses have thus far not gained practical relevance in the biodegradable implant field, because they cannot satisfy its demands of sufficient plastic strain and reveal embrittlement due to structural relaxation at body temperature [87, 88].

Owing to the difficulties to control degradation, much effort has been devoted to surface modifications and coatings, which are meant to lower Mg's reactivity and prevent an initial burst release of corrosion products [89]. The treatments tested range from inorganic calcium–phosphate-

containing conversion layers [90] over biodegradable polymer coatings [91] to high-purity Mg deposition layers [92]. While many were shown to indeed generate the desired reduction of corrosion rate, surface coatings bear additional risks such as delamination or cracking [91, 93] or accelerated long-term degradation [94], and present an additional hurdle in the certification process of biomedical products, which should not be underestimated. Thus, whenever possible, alloys are preferred that do not rely on surface coatings.

*The optimal material has a **low impurity level***. Owing to Mg's high electrochemical activity it possesses a low tolerance for impurities, which are commonly of more noble nature compared to Mg. Noble impurities thus deteriorate the corrosion resistance, especially above a certain threshold concentration set by the element's solubility limit [95]. The most critical ones are Fe, Cu and Ni, with tolerance limits in the ppm range [95]. A vacuum-distillation process to obtain ultrahigh-purity Mg (XHP Mg, 99.999% [96]) was thus developed at ETH Zurich, resulting in a Fe level of < 2 ppm and a total impurity concentration of < 7 ppm [97]. The corrosion rate of XHP Mg was shown to be significantly reduced compared to commercially pure Mg in *in vitro* and *in vivo* testing conditions [97].

Details concerning Mg's corrosion behavior are addressed in the following section 1.1.6. '*Magnesium corrosion*'.

*The material composition is **biologically safe***. The addition of alloying elements to Mg as a measure to improve both, mechanical and corrosion properties, has to be carefully considered if the material's intended use is the implantation into the human body. In fact, many alloying elements commonly used in Mg alloys bear a potential health risk, such as Al and REEs as mentioned above, and should thus be avoided. An overview of alloying elements in Mg, and their physiological role and pathophysiological impact at an excessive concentration is given in literature, e.g. in Refs. [22, 32, 80, 81, 98], and summarized in Table 1.3. From this compiled data it is obvious that many of the elements that are biomedically questionable are congruent to those that provide an efficient improvement to either strength or degradation rate or both, including Al, REEs and Li. With that it literally becomes a battle of strength and slow degradation versus toxicity.

In this context, it is important to highlight that a 'biocompatible composition' is not determined by the choice of alloying elements alone but also depends on the dose with which these alloying elements and other degradation products are released (see Table 1.3 for daily allowances of common alloying elements). For that reason, the material composition must be chosen in light of the alloy's degradation rate.

Table 1.3: Biological appearance, role and pathophysiology of Mg and common alloying elements used in Mg alloys. Data compiled from [8, 32, 52, 66-68, 80].

Element	Blood-serum level	Biological role	Pathophysiology/ Toxicology	Daily allowance
Mg	$18 - 26$ mg L^{-1}	Important in bone structure; co-regulator of energy metabolism, cell proliferation, and protein synthesis; regulator of more than 350 proteins; stabilizer of DNA and RNA	No evidence for toxicity	0.7 g
Al	Total $2.1 - 4.8$ µg	–	Neurotoxicity and accumulation in bone; risk factor in generation of Alzheimer's disease; decreases osteoclast viability; mild foreign-body reaction was observed in Mg alloys *in vivo*	Total amount in human < 300 mg
Ca	$88 - 104$ mg L^{-1}	Most abundant mineral in the human body; structure of bone/ teeth; essential element	Metabolic disorder; kidney stones	0.8 g
Gd	< 0.1 mg L^{-1}	–	Accumulation in bone and various organs	–
Li	$2 - 4$ ng L^{-1}	–	Over-dosage causes kidney and lung dysfunctions and nervous system disorders	$0.2 - 0.6$ mg
Mn	< 0.8 µg L^{-1}	Essential trace element; important role in metabolic cycle of e.g. lipids, amino acids and carbohydrates; influences the function of the immune system, bone growth, blood clotting, and cellular energy regulation and neurotransmitter	Neurotoxic; toxic dosage 10 µM	4 mg
Y	< 0.1 mg L^{-1}	–	Accumulation in bone and various organs	–
Zn	$0.81 - 1.14$ mg L^{-1}	Essential trace element; essential for the immune system; co-factor for specific enzymes in bone and cartilage	Neurotoxic at higher concentrations	15 mg
Zr	Total ≤ 250 mg	–	Accumulation in liver, spleen and gall bladder	3.5 mg

1.1.4   Design considerations for the development of Mg alloys outside the biomedical field

For a material's intended application outside the biomedical field, the biological safety is largely irrelevant and, hence, a considerably wider spectrum of alloying elements is available for the material design. In fact, a different set of requirements is defined for the material design in lightweight structural applications, e.g. for those in the transportation sector.

The optimal material must be produced at **low cost** *and via an* **easy process**. For lightweight structural applications for the transportation sector economic factors are significantly more important than in the biomedical field. This puts a high demand on the costs, which affects the choice of alloying elements and demands an easy, low-energy and low-scrap processability.

The optimal material has a **high corrosion resistance**. The requirements regarding the material's corrosion properties also differ from those set for the biomedical context. In fact, the material is designed towards high corrosion resistance because the material's use does not intend its degradation. Alloying with elements that have a high solid solubility in Mg to elevate its electrochemical potential and at the same time render the surface oxides more stable is thus the main strategy, and is among others provided by Al and Y [21, 99]. This is often combined with the strategic alloying of elements that can 'trap' impurities, thus inactivating them and making the material less susceptible for impurity-driven corrosion acceleration. Mn is a candidate commonly used for this task, because its precipitates have a high solubility for Fe [21, 100]. However, the corrosion resistance is generally only of secondary relevance because of the standard use of protective paint, and greater efforts are devoted to improving the material's mechanical performance.

The optimal material has **high strength** *and appropriate* **ductility**. High strength, appropriate ductility, and improved fatigue resistance are generally the most crucial properties for the commercial use of a material. The strategies achieving this property combination were presented above, with the difference, however, that outside the biomedical field a larger pool of possible alloying elements is available.

In light of the required high strength and the simultaneous constraint of low cost and low-energy processability, the ability to harden the material post-processing or post-shaping is especially attractive. This **hardenability** of a material can be achieved by precipitation hardening [79, 101, 102], referred to as age-hardening, provided that an appropriate alloying composition and appropriate thermomechanical processing conditions are found. A suitable composition offers (i) high solubility of the hardening phase at elevated temperature – the solution-treatment temperature, which ideally equals the processing temperature to shape the material – and (ii) considerably reduced solubility at low temperature – the artificial-aging temperature [101]. For a high hardening potential the

precipitation needs to occur homogeneously at a high number density and generate strong obstacles to dislocation movement. The design of age-hardenable alloys thus comprises optimizing of (i) the alloying composition and (ii) the thermomechanical processing conditions.

Figure 1.3 summarizes schematically the main properties to be considered in the material design of Mg-based (a) implant materials and (b) materials for light-weight structural applications.
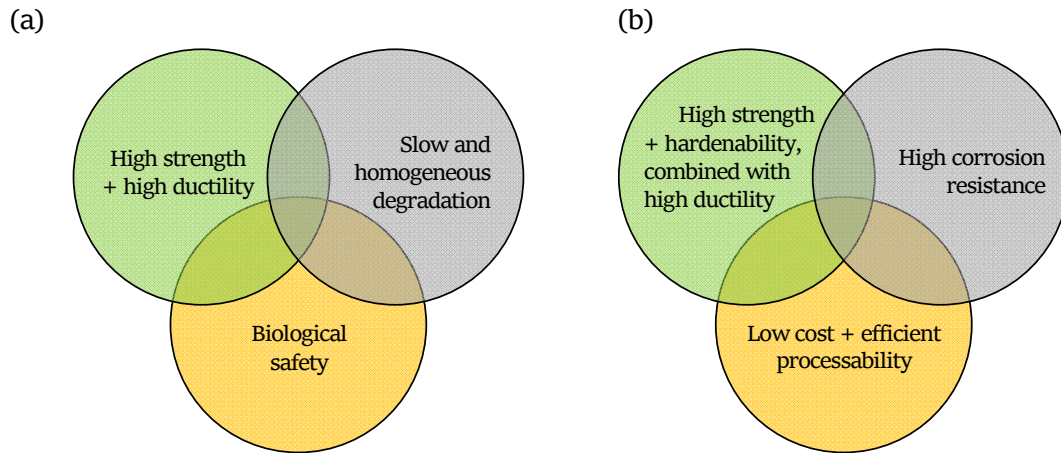
Figure 1.3: Aspects guiding the design of magnesium alloys for (a) biomedical applications and (b) lightweight structural applications.

In addition to the mentioned requirements, further comparably minor ones must be considered, including but not limited to **castability, affordability, availability, machinability, formability, and recyclability**. Lastly, while specific threshold values must be achieved and there cannot be any negotiation regarding the biological safety, it should be kept in mind that material design remains an exercise in the "art of compromise".

1.1.5   Mg–Zn–Ca System

The design principles and requirements regarding mechanical performance, corrosion behavior and biological safety presented in the previous chapter coalesce in alloys made from magnesium, zinc (Zn) and calcium (Ca), denominated ZX alloys as per ASTM declaration [49]. ZX alloys are extensively studied in this thesis for their microstructure–property correlations and are thus presented here in detail.

ZX alloys are especially attractive for their compositional choice in light of biological safety. In fact, just like Mg, Zn and Ca are also physiologically essential minerals to the human body, which thus possesses the required metabolic pathways to safely 'digest' them [68]. In fact, implants made from Mg–Zn–Ca alloys show good biocompatibility and increased bone deposition around them *in*

vivo in pre-clinical [23, 103-105] and clinical trials [23]. However, unlike Mg and Ca, which are both mass elements, Zn is a trace element in the human body (Table 1.3). At elevated concentration, Zn can affect the vascular system, deteriorate the heart function and impair cell growth [53, 106]. Its release from the implant thus needs to be more closely controlled than that of Mg or Ca, setting requirements to a controlled, sufficiently slow implant degradation rate.

In these alloys, Zn had been chosen as the main alloying element for its benefits to improve castability and formability [107], and to provide reasonable grain-growth restriction [108, 109], and a moderate age-hardening potential [110]. Furthermore, with a relatively high solubility in Mg, at 6.2 wt.% at 340 °C, it possesses a relatively high solid-solution-strengthening potential [111]. In terms of the corrosion performance, Zn was reported to lower the corrosion rate of Mg when added in small quantities [112], supposedly because it can increase the tolerance of Mg to impurities [113, 114], but is considered to accelerate the same when added in a concentration greater than a certain threshold value [112, 114, 115]. The value that is often referred to is 2.5 wt.% Zn, reported by Hanawalt in 1942 [114]. However, a significantly increased corrosion rate with the Zn content was already observed at lower levels [115-117]. The threshold depends greatly on the presence or absence of Mg_xZn_y intermetallic phases, which accelerate the corrosion due to micro-galvanic coupling [116], and thus on the composition and the thermomechanical history of the sample.

Ca, on the other hand, is added to Mg for its benefits of significantly reducing the melt flammability [118], weakening the texture [73, 119] and thereby lowering the tension-compression asymmetry [119], increasing the strength due to grain refinement [120], and improving the creep resistance [121]. Furthermore, Ca's minute solubility at low temperatures (max. solubility of 0.82 at.% (1.35 w.t%) at 516 °C and practically no solubility at temperatures below 250 °C [122]) favors its precipitation at those temperatures that are typical for aging treatments. While the aging response of binary Mg–Ca is only moderate, Ca addition to age-hardenable alloys, among others also Mg–Zn, influences the precipitation behavior of the respective hardening phase, which can result in a significant improvement of the aging response [110, 123]. In terms of corrosion performance, Ca addition drastically reduces Mg's already poor corrosion resistance, leading to exceptionally fast corrosion rates [124, 125]. This is especially the case for Ca concentrations exceeding the solubility limit and owed to the formation of the anodic and highly reactive Mg_2Ca intermetallic phase [124, 125]. An effective threshold of 1 wt.% is often reported for the Ca concentration above which the corrosion resistance of Mg–Ca binary alloys drastically declines [22, 124]. It should, however, be noted that the threshold critically depends on the thermomechanical history of the alloy [125].

In order to fully benefit from the potential of both, Zn and Ca, their amount and ratio need to be optimized and balanced. In fact, an excessive content of either Zn or Ca is known to result in overly

coarse precipitates and with that in a declined age-hardening potential [126, 127], and reduced ductility [120, 128]. Furthermore, with an increasing Zn content hot tearing is favored [129] and the alloy's solidus temperature lowered, which narrows the possible processing-temperature range [130]. In terms of the corrosion performance, moderate addition of Zn to the Mg–Ca system effectively lowers the degradation rate [103, 131], while an excessive addition drastically accelerates the same [115, 131].

Early efforts at the Laboratory of Metal Physics and Technology at ETH Zurich were first directed towards optimizing the mechanical properties of Mg–Zn–Ca alloys following a micro-alloying concept [130, 132]. To this end, Hänzi et al. [130] used systematic thermodynamic simulations (using Pandat software package with the database PanMg8 [133]) combined with electron-microscopy-based microstructural analysis to balance the Zn and Ca content and to obtain a microstructure that contains intermetallic particles (IMPs) with their characteristics optimized for grain-boundary pinning according to *Zener* [134]. For an efficient pinning the volume fraction of the pinning phase, which was predicted to be the ternary $Mg_6Zn_3Ca_2$ phase ([130, 133] and Figure 1.4), needs to be sufficiently high, but yet low enough to avoid its coarse precipitation, which would result in a declined ductility. Furthermore, their approach aimed at simultaneously maximizing the Zn content for the sake of benefitting from solid-solution strengthening, while also maintaining the possibility for aging via the MgZn hardening phase [133, 135]. On the one hand, a minimum addition of Ca of 0.2 wt.% was deemed necessary to stabilize a sufficiently high fraction of $Mg_6Zn_3Ca_2$ phase. On the other hand, a maximum concentration for Ca was identified at 0.6 wt.%, above which the continuous increase of the $Mg_6Zn_3Ca_2$ phase with Ca addition at the expense of the MgZn phase would reduce the volume fraction of the latter too severely [130].
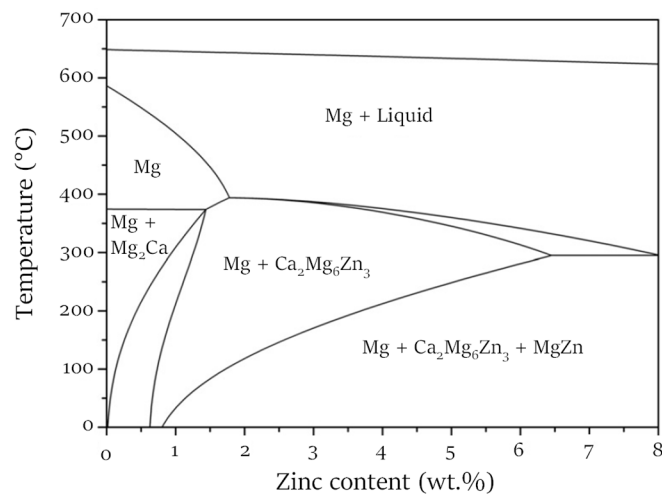

Figure 1.4: Isopleth for 0.25 wt.% Ca in the Mg–Zn–Ca system [130].

As for Zn, a minimum content of 3 wt.% was found necessary to form the MgZn hardening phase at a typical artificial-aging temperature of 160 °C (Figure 1.4 for Ca = 0.25 wt.%). The effective minimum Zn content, however, is somewhat higher because Zn is consumed to form $Mg_6Zn_3Ca_2$, increasingly so with a higher Ca content, and was thus suggested to be 4 wt.% [130]. To maximize the Zn content in solid solution for solution strengthening, an even higher Zn content was suggested. An upper limit of 6 wt.% was proposed and originates from the solubility limit of Zn (~6.4 wt.% for Mg containing 0.25 wt.% Ca [130]).

To summarize, the diligent efforts by Hänzi et al. [130] resulted in the proposed compositional window of 0.2 – 0.4 wt.% Ca and 5 – 6 wt.% Zn. The optimized alloy with Mg–Zn5.0–Ca0.25, denominated ZX50, in its extruded state exhibited favorable mechanical properties with a *TYS* and *UTS* of 210 MPa and 295 MPa, respectively, an A_f of 26% [67, 130], and an artificial-aging potential of about 45 MPa [130].

In a next step, the suitability of the optimized alloy ZX50 as a biomaterial was tested by implanting it in the femurs of a small-animal model [10, 82, 136]. The implant degradation progressed astonishingly fast and already 12 weeks *post operationem* complete implant resorption occurred [10, 136]. This rapid degradation rate along with the concomitant hydrogen-gas release was undoubtedly non-acceptable for a temporary implant material. Hofstetter et al. [136] analyzed the material explanted after two weeks of implantation and revealed that the implant was surrounded by Zn-rich accumulations. The authors concluded from these observations, that the Zn-rich intermetallic phases, which were according to their computational data the so-called IM1 ($Mg_6Zn_3Ca_2$) and IM3 ($Mg_5Zn_{13}Ca_2$) phases, must have been responsible for the rapid dissolution and inferred that these phases were to be avoided when a slow and homogeneous degradation was desired [136]. The detailed corrosion mechanisms of the Zn-rich phases and their impact on the overall alloy degradation were, however, not addressed thus far and are thus subject to investigation in the thesis presented. In this context, it should be noted that in general not only the phase type but also its volume fraction and distribution control the corrosion rate. With this in mind, a reduction of the phases' volume fraction may suffice to reduce the alloy's degradation rate to a level suitable for the biomedical application intended, while still allowing to benefit from a potential advantage of the Zn-rich intermetallic phases for the mechanical performance. The validity of this hypothesis is also a subject of investigation in the presented thesis.

Design concept and processing of Mg–Zn–Ca-lean alloys

The design concept and processing of lean Mg–Zn–Ca alloys used in this thesis are described in the following and are based on the earlier work of Hofstetter et al. [33, 82, 137].

The before-mentioned drastic degradation speed of the ZX50 alloy gave rise to attempts of minimizing the Zn content to a level at which the formation of the presumably cathodically active ternary IM1 and IM3 phases can be safely avoided [136]. Such a radical reduction of alloying content, however, presents a major challenge to maintain the mechanical strength and ductility required and optimized in the ZX50 alloy as presented above.

A successful solution was found in the so-called high-strength low-alloyed (HSLA) approach, which is commonly applied to increase the strength of steels by generating a fine dispersion of carbides, which, in turn, generate a refined grain size [138]. Building on this concept, Hofstetter et al. [33] refined the overall alloying content by setting the Zn content to 1 wt.%, balanced the Zn-to-Ca ratio accordingly, and worked out a thermomechanical processing sequence (details are described below and in Figure 1.6). All these measures combined aimed at a fine dispersion of IMPs, which are intended to refine the microstructure by controlling dynamic recrystallization and acting as grain-boundary pinning points during hot forming. Furthermore, the goal was for the IMPs to be composed of the Mg_2Ca phase to control a slow and homogeneous degradation (details on electrochemical aspects of ZX alloys will be presented below in section 1.1.6. '*Magnesium corrosion*'). As in the study of Hänzi et al. [130], the alloying design of Hofstetter et al. [33, 82] was assisted by thermodynamic calculations (using MatCalc simulation software and database mc_mg_v1.006 [139]), which can provide guidance as to which phases are expected as a function of temperature (Figure 1.5).

The optimized alloy had an alloying content of 1 wt.% Zn and 0.3 wt.% Ca and is referred to as ZX10 [33, 82]. Figure 1.5 shows the calculated phase diagram for this composition. Note that the calculations assume thermodynamic equilibrium. It reveals that for this alloy and in the temperature regime of interest for processing, i.e. ~200 – 450 °C, two intermetallic equilibrium phases are expected: up to 280 °C a **ternary IM1 phase**, which is then gradually replaced by the **binary Mg_2Ca phase** with increasing temperature and fully replaced from 330 °C. The solvus temperature of the Mg_2Ca phase was predicted to be at ~410 °C, which leaves a processing window for a solution-heat treatment (*sht*) of about 90 °C (with T_{liquid} = 500 °C). As for the ternary IM1 phase, it should be noted that the calculations account for a distinct composition of **$Mg_6Zn_3Ca_2$** whereas the authors suggest that it may indeed be subject to compositional variations in the range of **$Ca_3Mg_xZn_{15-x}$ (4.6 ≤ x ≤ 12, in at.%)** as previously reported by Zhang et al. [140]. In fact, the precise composition and structure of the ternary phase in the Mg–Zn–Ca system is highly debated in literature. A summary of the literature available and a detailed experimental analysis of the ternary-phase IMPs in ZX-lean alloys will be presented in Chapter 2.
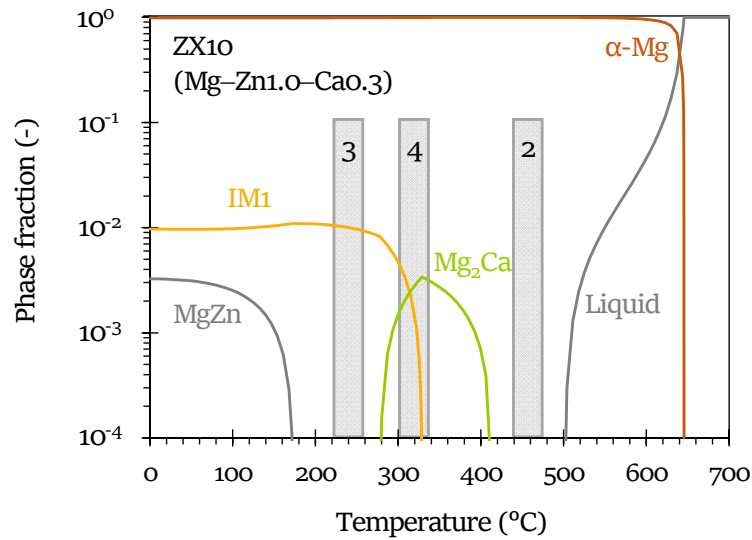
Figure 1.5: Simulated phase diagram of the ZX10 alloy. The processing sequence developed is marked with (2): solid-solution heat treatment, (3) artificial aging, and (4) hot forming. Processing step (1) refers to casting and alloying and is not included in the diagram. Phase diagram modified from [33].

To achieve the desired precipitation of the pinning phase in a fine and homogeneous dispersion, the alloying design comprised the simultaneous optimization of the thermomechanical processing conditions for extrusion, as the chosen hot-forming process, and pre-extrusion heat treatments [33]. The elaborated processing sequence for the fabrication of ZX-lean alloys used in that study [33] is presented in Figure 1.6 and includes the following steps:
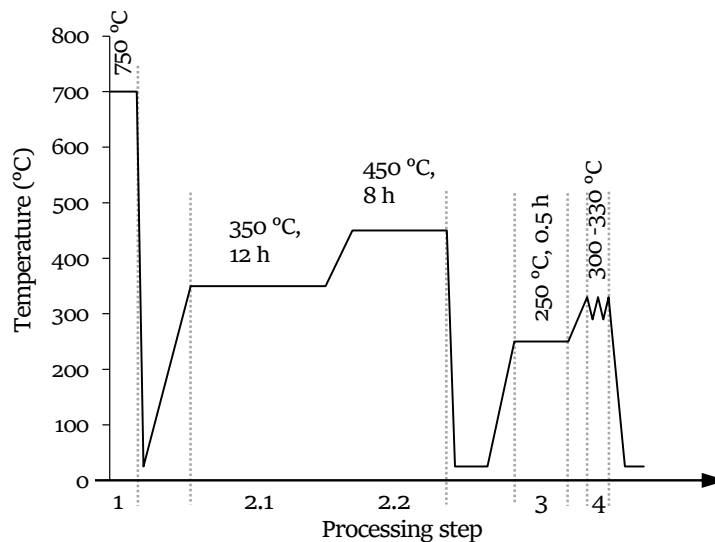
Figure 1.6: Processing sequence of ZX-lean alloys used in this study. 1: casting, 2: homogenization, 3: artificial aging, 4: extrusion.

(1) Mg is cast and alloyed with Zn and Ca at 750 °C, followed by directional cooling to avoid shrinkage cavities,

(2) two-step homogenization treatment (2.1: 350 °C for 12 h, 2.2: 450 °C for 8 h) with the second step simultaneously presenting a solution-heat treatment, followed by fast cooling to achieve a super-saturated solid solution,

(3) artificial aging treatment at 250 °C for 30 min to precipitate intermetallic phases, which are assumed to function as obstacles during

(4) hot extrusion (indirect) at 300 – 330 °C.

Following this protocol a ZX10 alloy is produced which demonstrates a fine-grained and almost fully recrystallized microstructure and exhibits favorable mechanical properties with a *TYS* of ~240 MPa, an *UTS* of ~265 MPa, an A_f of 30%, and a low mechanical anisotropy of ~1.15 [33]. These specifications show that despite the reduction of Zn content, good mechanical properties could be successfully achieved by means of the HSLA concept. The reduction in the alloying content also brought the essential reduction in degradation rate compared to ZX50, and the ZX10 alloy showed a slow and homogeneous dissolution *in vitro* and *in vivo* [82, 136].
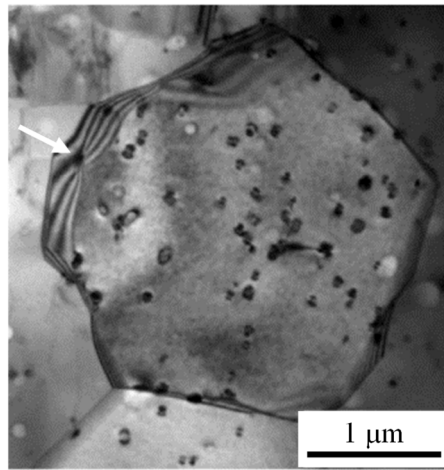
Figure 1.7: BF-TEM image of ZX10 after extrusion. Nanometric intermetallic particles (IMPs) are visible in dark contrast, and are contained within the grains and at the grain boundaries. The white arrow points at a precipitate that interacts with the grain boundary, causing its bowing [33].

TEM imaging confirmed that the elaborated protocol for the ZX10 alloy indeed generates a microstructure that contains IMPs in a fine and homogeneous distribution within the Mg-matrix grains and at the grain boundaries (Figure 1.7). The important role of the IMPs contained for the resulting microstructure was demonstrated by means of comparing the alloy with a ZX00 alloy of composition Mg–0.5Zn–0.15Ca (in wt.%). The microstructure of ZX00 was characterized by an absence of any secondary phase when the same thermomechanical process parameters as for ZX10

were applied, and resulted in a ~50% larger grain size compared to ZX10. This comparison could thereby demonstrate the effective grain-refining capabilities of IMPs in ZX10 and thus provide a rational for the superior mechanical performance compared to coarser-grained specimens of the same composition [33].

This important role of IMPs in the mechanical performance of ZX-lean alloys stimulates the interest in a deeper understanding of the IMPs' characteristics. Thus far, no chemical information of the nanometric IMPs was available. Hofstetter et al. [33] assumed them to be composed of the Mg_2Ca phase based on the computational data available (Figure 1.5) and taking into account a potential temperature increase during the extrusion process. However, it should be noted that the extrusion temperature chosen is in fact close to the temperature region in which the ternary IM1 phase is prospectively stable (see Figure 1.5), and the general validity of these calculated phase diagrams in both terms, the type of predicted phases and their temperature-dependent stability regions, has thus far not been demonstrated. Furthermore, it should be reminded that the extrusion process may not provide sufficient time to reach the thermodynamic equilibrium on which these calculations are based. A detailed investigation of the phases forming thus remains to be done and will be addressed in this thesis.

1.1.6   Magnesium corrosion

General Mg corrosion

Magnesium is an *active* material and significantly less noble than other engineering materials such as aluminum or steels. While its high corrosion susceptibility demonstrates a limitation for many engineering applications, its degradability in physiological conditions is a fundamental prerequisite for its use as a temporary implant material.

The corrosion reactions for Mg are demonstrated here to provide a basis for the description of Mg-alloy corrosion mechanisms derived in this thesis.

Magnesium dissolves in aqueous solution according to the following equations:

Anodic reaction (oxidation):	$Mg \rightarrow Mg^{2+} + 2\,e^-$	Eq. 1.1
Cathodic reaction (reduction):	$2\,H_2O + 2\,e^- \rightarrow 2\,OH^- + H_2$	Eq. 1.2
Overall reaction:	$Mg + 2\,H_2O \rightarrow Mg^{2+} + 2\,OH^- + H_2$	Eq. 1.3
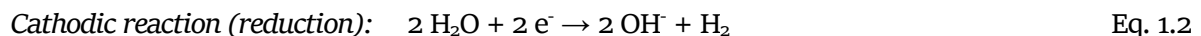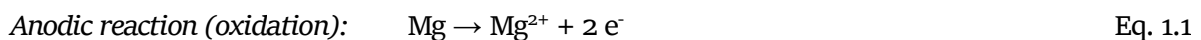
From these electrochemical reactions it is obvious that for each mol of Mg one mol of hydrogen gas (H_2) is formed. In other terms, for each gram of dissolving Mg metal ~1000 ml H_2 is generated (920 ml g^{-1} at 0°C, 1045 ml g^{-1} at 37 °C).

Besides H_2, also hydroxide ions (OH^-) are formed, which increase the near-surface pH value. At a sufficiently high pH value, the formation of magnesium hydroxide ($Mg(OH)_2$) is thermodynamically favored (see Pourbaix diagram, also E–pH diagram, in Figure 1.8) according to the following equation:

Product formation: $Mg^{2+} + 2\,OH^- \rightarrow Mg(OH)_2$ Eq. 1.4
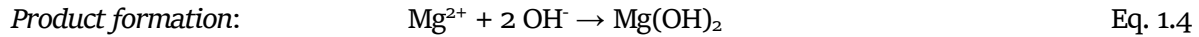
The critical pH value from which $Mg(OH)_2$ is stable is easily reached at the near-surface of the corroding Mg substrate [141, 142], especially for those placed in physiological solutions with a pH of 7.4, so that $Mg(OH)_2$ presents the main corrosion product in neutral and physiological conditions [114, 143, 144]. Some studies report besides $Mg(OH)_2$ the co-existence of MgO in the surface layer of corroding Mg substrates, with an inner MgO layer and an outer $Mg(OH)_2$ [144, 145] or mixed $MgO/Mg(OH)_2$ layer [146, 147]. However, the stability of MgO in aqueous solutions is debated [148, 149] and it is usually not found in Pourbaix diagrams reported for Mg (Figure 1.5) [148].
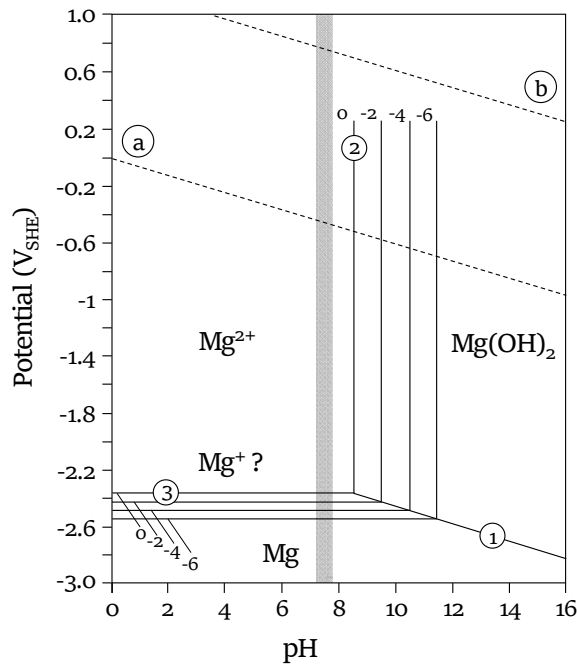
Figure 1.8: Pourbaix diagram for the magnesium–water system at 25°C. Replotted from [148]. *The different regions* are separated by the following reactions: (1) $Mg + 2H_2O \rightarrow Mg(OH)_2 + H_2$; (2) $Mg^{2+} + 2H_2O \rightarrow Mg(OH)_2 + H_2$; (3) $Mg + 2H_2O \rightarrow Mg^{2+} + 2OH^- + H_2$. Between line (a) and (b) water is stable. Below line (a) decomposition of H_2O into hydrogen and concomitant alkalization is favored. Above line (b) oxygen is evolved. The numbers adjacent to the vertical and horizontal lines indicate the logarithm of the Mg-ion concentration in solution. The grey bar marks the physiological pH value.

$Mg(OH)_2$ is porous and thus not a suitable protective layer [149, 150]. Consequently, the corrosion attack is, although slowed-down by the presence of $Mg(OH)_2$, not prevented. $Mg(OH)_2$'s stability is especially impaired in the presence of chloride ions (Cl^-) in solution [150, 151], which is inevitable the case in physiological fluids. Cl^- reacts with $Mg(OH)_2$ to form highly soluble magnesium chloride ($MgCl_2$) and OH^- (Eq. 1.5). $MgCl_2$ can also form directly from the reaction with Mg ions (Eq. 1.6)

$$Mg(OH)_2 + 2\,Cl^- \rightarrow MgCl_2 + 2\,OH^- \qquad\qquad \text{Eq. 1.5}$$

$$Mg^{2+} + 2\,Cl^- \rightarrow MgCl_2 \qquad\qquad \text{Eq. 1.6}$$

$MgCl_2$ is not stable in water and will dissolve to Mg^{2+} and $2Cl^-$ while leaving OH^- as one of the byproducts, which, in turn, again increases the solution pH value.

Besides chloride and various other species, also calcium and phosphorous (P) ions are present in physiological fluids. At the alkaline pH value generated by the Mg-corrosion reactions, the Ca and P ions from solution are consumed to form stable calcium phosphates or magnesium-substituted phosphates [152, 153], (Eq. 1.7). The underlying reaction can be described by:

$$10\,Ca^{2+} + 6\,PO_4^{3-} + 2\,OH^- \rightarrow Ca_{10}(PO_4)_6(OH)_2 \qquad\qquad \text{Eq. 1.7}$$
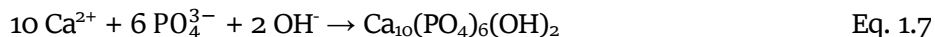
Interesting for Mg's application as a biomaterial is that these phosphates are chemically equal or similar to hydroxyapatite (HA) and therewith similar to bone. It is generally assumed that the Ca–P-precipitation-film offers some protection to Mg corrosion and thus slows down the progressing Mg-corrosion attack [12].

However, the precise chemistry, structure (amorphous to crystalline) and morphology of the precipitation products as well as those of the conversion products, such as $Mg(OH)_2$, and of the chloride-containing byproducts forming *in vitro* and *in vivo*, and their role in respectively the corrosion mechanisms and corrosion protection are still not sufficiently understood. Revealing them is thus still subject of intensive research. This task is complexified by the presence of alloying elements in Mg, which are known to modify the properties of the surface films forming on Mg substrates [114, 150, 154, 155]. Novel methods [156] that offer higher resolution [145, 157-159] and especially emerging *in situ* methods, which circumvent the necessity of drying [160, 161], overcome the previous technical limitations associated with these studies [156].

Mixed potential theory

The partial reactions of the single-electrode system Mg in water were expressed as half-cell reactions in Eq. 1.1, oxidation, and Eq. 1.2, reduction. Each has its own half-cell electrode potential

23

(also referred to as reversible potential E_{rev}, $E_{Mg/Mg2+}$ and $E_{H2/H+}$, Figure 1.9) and exchange current density (i_0). They cannot coexist separately on the same metal surface, and the total rate of oxidation has to be equal to the total rate of reduction (principle of charge conservation). Consequently, each electrode must polarize, i.e. shift in potential in either anodic or cathodic direction, to a common intermediate potential, which is a *mixed potential* [162] and referred to as corrosion potential (E_{corr}). This mixed-electrode state is experimentally accessible by potentiodynamic polarization experiments, as depicted as the green curve in Figure 1.9 (the basics of polarization experiments are described below in section '*Methods to study Mg corrosion*'). In this figure, the schematically pictured lines correspond to the reaction kinetics of both corrosion reactions, i.e. the metal deposition and dissolution, the latter merging into the anodic branch of the experimental curve, and the hydrogen evolution and oxidation, the former merging into the cathodic branch of the experimental curve. The intersection of anodic and cathodic branch provides the corrosion current density (i_{corr}).
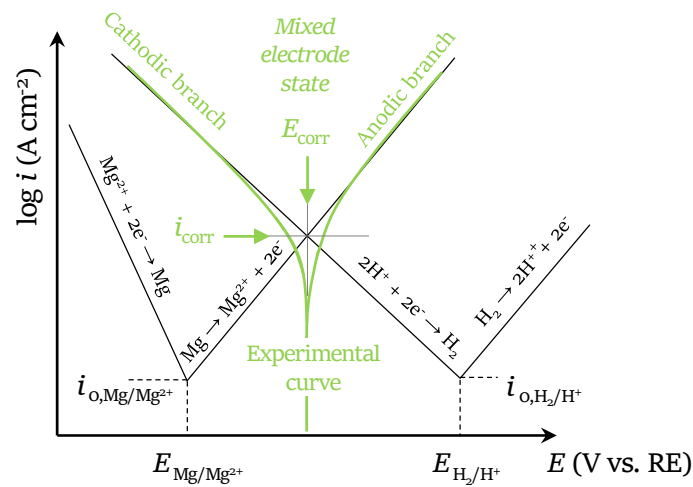
Figure 1.9: Schematic presentation of the mixed-potential plot for an Mg electrode in water, based on the mixed-potential theory. The corresponding experimental polarization curve is shown in green; RE refers to reference electrode.

Galvanic corrosion

Owing to Mg's low electrochemical potential and non-polarizable nature, it can reach very high rates of anodic dissolution already at low overpotentials. This makes Mg highly susceptible to galvanic corrosion when coupled to other, more noble, metals. The concept of galvanic corrosion is described in the following. Complete overviews of the corrosion modes – general, galvanic, pitting, crevice, intergranular and stress corrosion, corrosion fatigue – which are generally all of relevance to Mg, but not all in the direct context of this thesis, are described in literature, e.g. Refs. [95, 149, 163].

Galvanic corrosion occurs when two dissimilar metals are in electrical contact while immersed in a conductive electrolyte (Figure 1.10a). It is therefore also referred to as *bimetallic corrosion*. The difference in electrochemical potential between the two metals is the driving force for the preferential dissolution of the less noble one, the anode. The rate with which the oxidation of the anode occurs is thereby higher than it would be in its electrically uncoupled state. The more noble metal, presenting the cathode, experiences reduced corrosion rates compared to its uncoupled state and, in some cases, may not corrode at all (cathodic protection).
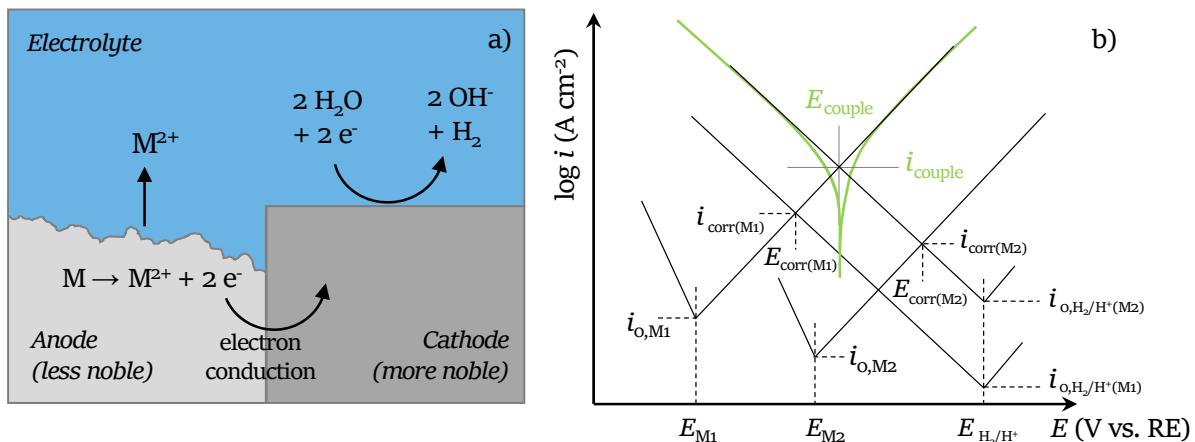
Figure 1.10: (a) Schematic presentation of galvanic coupling. (b) Schematics of the experimentally obtainable electrochemical polarization response (green curve) for a galvanic couple of metal 1 (M1) and metal 2 (M2), and the individual polarization curves for M1 as anode and M2 as cathode at the basis of the experimental curve; RE refers to reference electrode.

The polarization response of a galvanic couple is in accordance with the mixed-potential theory as described above and is schematically depicted in Figure 1.10b. The coupled potential (E_{couple}) establishes at a common intermediate value between the nominal corrosion potentials E_{corr} of the contributors. With that it is obvious that both electrodes may get considerably polarized from their nominal E_{corr} values. The extent of polarization is a function of the extent of cathodic reaction that can be sustained at the metal presenting the cathode.

The main factors influencing galvanic-corrosion rates are the

- potential difference between anode and cathode,
- electrolyte conductivity,
- cathode efficiency, and
- area ratio of anode and cathode.

To prevent galvanic corrosion, special care is required in the design of parts when Mg is used in conjunction with other materials and the parts' intended use involve their exposure to liquid or moisture. Besides these macroscopic scenarios under which galvanic corrosion can occur, it can also be provoked within the same metal by metallurgical heterogeneities that form *micro-galvanic cells*, such as intermetallic phases [21, 103, 116, 164], metallic impurity-derived [97, 113, 114] or oxide inclusions [165], or segregations [166, 167], and materials engineering approaches such as reinforcements [168, 169]. This usually highly localized corrosion mode is referred to as *micro-galvanic corrosion*. The underlying mechanisms and influencing factors are the same as for macroscopic galvanic corrosion, bearing in mind that the polarization response is a sum of all anodic and all cathodic reactions occurring on the same electrode surface. However, the study of the individual contributors of a micro-galvanic couple to the overall corrosion mechanism of a metal is owing to the size of the metallurgical features – typically in the nano- to micrometer range – and their co-existence on the same electrode surface incomparably more challenging.

Importance of purity

The high susceptibility to galvanic corrosion brings an important consequence for the material's requirement regarding purity. Most impurities possess a significantly higher electrochemical potential than Mg, thus accelerating the corrosion rate of Mg (Figure 1.11) by micro-galvanic coupling. Especially those that have a low solubility in Mg, such as Fe, Cu, Ni and Co, are detrimental because they easily precipitate and form highly active cathodic spots [21, 114]. Reported threshold for these elements are 170 ppm for Fe, < 1000 ppm for Cu and 5 ppm for Ni and Co [114]. These threshold values are significantly undercut for heat-treated or wrought Mg [97, 170]. For instance, Liu et al. [170] found that Fe may precipitate upon annealing already above a limit of 5 – 10 ppm. Also the presence of certain alloying elements may drastically decrease the threshold. For instance, with 7 wt.% Al the tolerance for Fe is reduced to about 5 ppm, an effect that was explained by the formation of an Fe–Al phase (FeAl$_3$) [95, 171].
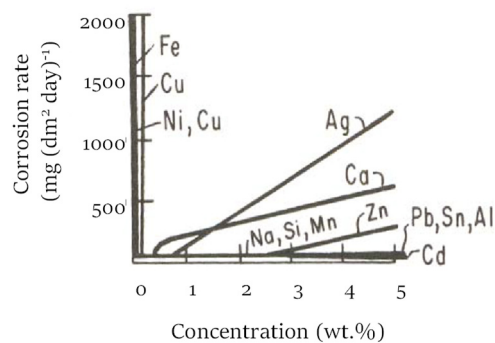
Figure 1.11: Impact of element addition on the corrosion rate of Mg [114, 172].

The detrimental impact of impurities on the corrosion resistance has been extensively studied and the necessity for high-purity Mg is well understood [97, 113, 114, 170, 171, 173]. It should be noted that high purity is not only relevant for Mg's industrial application but also crucial for the fundamental study of corrosion mechanisms acting on Mg and its alloys, which may be inaccessible when overshadowed by impurity-derived cathodes. For this reason, the materials used in this thesis to study the microstructure–corrosion-behavior correlations were produced with ultrahigh-purity (XHP, 99.999%) Mg, produced by vacuum distillation [96]. The content in all relevant impurity elements is in XHP Mg at ~2 ppm Fe, and < 1 ppm for Cu and Ni [82, 97] kept well below the reported threshold values allowing to safely prevent the formation of impurity-derived cathodes during thermomechanical processing.

Electrochemical considerations for ZX-lean alloys

Mg's standard reversible potential (E^o) is -2.37 V_{SHE}. In comparison the E^o of Zn, as the main alloying element in the ZX-lean alloys used in this thesis, is at -0.76 V_{SHE} and thus significantly more noble than Mg, while Ca is one of the very few representatives of suitable alloying element that have with -2.87 V_{SHE} an E^o that is even lower, i.e. it is less noble, than Mg (Table 1.4).

Table 1.4: Standard reversible potentials E^o for Mg and the alloying elements Zn and Ca composing the ZX-alloys.

Metal	E^o (V_{SHE})
Zn	-0.76
Mg	-2.37
Ca	-2.87

Information about the stability of zinc in aqueous media can be derived from the Pourbaix diagram in Figure 1.12. Anodic dissolution occurs at acidic to neutral pH values. For slightly alkaline pH values the formation of a quasi-passive $Zn(OH)_2$ film is thermodynamically favored. Owing to the amphoteric nature of zinc hydroxides, corrosion can also occur in strong alkaline conditions by dissolution of the $Zn(OH)_2$ to $HZnO_2^-$ and ZnO_2^{2-} [148], i.e. opposed to Mg there exist two stability areas for corrosion to occur in the Pourbaix diagram of Zn.

The influence of Zn and Ca on the corrosion resistance of the binary systems Mg–Zn and Mg–Ca, respectively, were presented already briefly above (see section 1.1.5. '*Mg–Zn–Ca system*'). In the following, the state-of-knowledge in literature on the impact of simultaneous addition of Zn and Ca on the corrosion susceptibility is outlined.

A comparison of Mg–Ca and Mg–Zn–Ca alloys showed that the addition of Zn to Mg–Ca can significantly reduce the macroscopic corrosion rate [84, 174, 175], while further Zn addition reverses the effect leading to accelerated corrosion rates [82, 83, 131]. The precise Zn content at which this reversal occurs differs between the studies reported and appears to be a function of both the overall alloying content and the Zn-to-Ca ratio. However, a common ground exists between these studies, which is that the change in corrosion susceptibility is rationalized by a change of the underlying microstructure [82-84, 131, 174, 175].
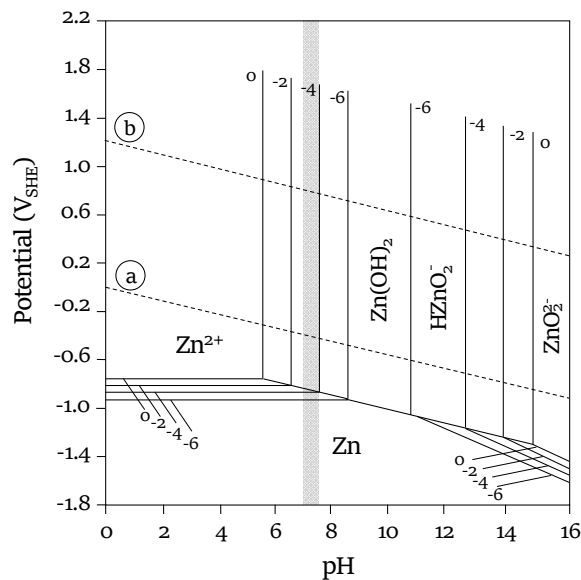
Figure 1.12: Pourbaix diagram for the zinc–water system at 25°C. Replotted from [148]. Between line (a) and (b) water is stable. Below line (a) decomposition of H2O into hydrogen and concomitant alkalization is favored. Above line (b) oxygen is evolved. The numbers adjacent to the lines separating the different stability areas indicate the logarithm of the Zn-ion concentration in solution. The grey bar marks the physiological pH region.

The low solubility of Ca in Mg (Table 1.2) favors precipitation of intermetallic phases in Mg–Zn–Ca already at very low alloying-element contents (see section 1.1.5. '*Mg–Zn–Ca system*'), which gives rise to micro-galvanic corrosion between the respective intermetallic phase and the α-Mg matrix. To infer on a phase's galvanic efficiency and its impact on the alloy's macroscopic degradation rate the composition of the phases that constitute the galvanic cell and their surface-area ratio need to be considered. In this context, it is reminded that in the lean-alloy regime (with the total alloying-element content ≤ 1 at.%) and temperature regime relevant for processing (250 – 350 °C), two intermetallic phases were predicted by thermodynamic calculations [33]: binary Mg_2Ca and a ternary Mg–Zn–Ca-rich IM1 phase with the predicted composition $Mg_6Zn_3Ca_2$ (Figure 1.4, Figure 1.5).

The ternary phase, which is reported to form when the nominal Zn content exceeds the one of Ca at a Zn-to-Ca ratio of ≥ 1.2 [174, 175], is suggested to be cathodic to Mg owing to its high Zn

content [164, 176]. Although the phase's corrosion potential has – to the best of our knowledge – not been determined in literature, its higher corrosion resistance compared to the Mg matrix was observed [84, 174]. In those studies, a larger volume fraction of the ternary phase was associated with a higher macroscopic degradation rate. However, the IM1 phase co-existed with the Mg_2Ca phase, which limits the access to understanding its individual role in the macroscopic corrosion behavior of ZX alloys.

The ability to transfer the results obtained in literature to the ZX-lean alloys studied in this thesis is furthermore limited by microstructural differences that may affect the extent of galvanic corrosion and uncertainties in the phases' composition. The former relates to the specific volume fraction, size and distribution of intermetallic phases, which are lower, smaller, and more finely and homogeneously distributed, respectively, in the ZX-lean alloys of this study (Figure 1.7) compared to the ones in literature [84, 174]. As for the detailed phase information, the stoichiometry and structure of the ternary intermetallic phase were not yet clearly identified (see section 1.1.5. '*Mg–Zn–Ca system*' and Chapter 2) and most often a range was stated for its composition with $Ca_3Mg_xZn_{15-x}$ (4.6 < x < 12) [140], as mentioned earlier. This uncertainty in composition is concomitant with an uncertainty of the potential difference and of the efficiency with which the hydrogen-reduction rate is facilitated, because $i_{o,H2/H+}$ is a function of the electrode's elemental composition. Facing the breadth of unknowns, the detailed corrosion behavior of the ternary phase and its specific role in the macroscopic degradation of ZX-lean alloys cannot be easily forecast. In fact, it is yet to be studied whether the ternary IMPs in the ZX-lean alloys at their nanometric size have at all an impact on the macroscopic corrosion behavior.

The binary Mg_2Ca phase was characterized for its corrosion potential in 0.1 M NaCl solution by Südholz et al. [164], who identified it to be anodic relative to pure Mg. As for the ZX system, the preferential dissolution of Mg_2Ca has indeed been observed [84, 103], and a large volume fraction of this anodic phase was associated with high macroscopic corrosion rates [175]. The addition of Zn may reduce the corrosion rate on the one hand by reducing the volume fraction of Mg_2Ca phase and on the other hand by incorporation of Zn into the Mg_2Ca phase. In fact, Mg_2Ca has a maximum solubility for Zn as high as 4.8 at.%, by substituting both Ca and Mg atoms [177]. Cha et al. [103] demonstrated that the addition of Zn to Mg_2Ca effectively reduces the potential difference between Mg_2Ca and pure Mg. An addition of Zn by ~3.1 at.% (7.1 wt.%) elevated the open circuit potential (E_{OCP}) of Mg_2Ca to a level close to the E_{OCP} of pure Mg, which resulted in comparable dissolution rates of these two phases and thus in a macroscopically homogeneous degradation front. Their results thus show that the Mg_2Ca phase can indeed be either anodic to Mg or 'galvanically inactive', depending on the Zn content. The precise composition of the binary-type IMPs in the ZX-lean alloys is so far

unknown, thus the phase's corrosion behavior cannot be predicted. Both, the composition and detailed corrosion behavior of the binary phase are addressed in this thesis.

Furthermore, it should be noted that Cha et al. came to their conclusions based on a study of single-phase specimens. This methodological choice limits the transferability of their results to ZX alloys with secondary phases, because it is the potential difference between the constituent phases that decides over the phase's polarity, i.e. whether it will present the anode or cathode or may not entail any galvanic activity, and the extent of micro-galvanic corrosion attack. It is thus required to take into account the solubility of Zn and Ca also in the Mg matrix. This, in turn, implies the necessity to consider besides the alloy's specific composition also its thermomechanical history, because the elemental solubility in the respective phases depends on the nominal composition [136] and on temperature [130].

In sum, a detailed analysis of the alloy's elemental distribution, and the volume fraction and distribution of intermetallic phases is required as a basis for an understanding of the microstructural role in the corrosion behavior.

Methods to study Mg corrosion

A high number of techniques is available for the study of Mg corrosion in aqueous environment, which can be used separately or combined. While presenting them all is outside the scope of this chapter, the interested reader is referred to the review article of Esmaily et al. [156], which includes a comprehensive overview of available methods for the study of Mg corrosion. A compact overview along with a critical assessment of the most common methods and their limitations is provided by Kirkland et al. [178].

In the following two methods are presented that are well established in the research community, and were applied complementary to transmission electron microscopy (TEM) studies in the framework of this thesis.

Hydrogen-evolution method. From the electrochemical reaction of Eq. 1.3 stated above, it is evident that the volume of generated hydrogen gas directly correlates with the mass of Mg metal dissolving, with 1 mol of dissolving Mg generating 1 mol of hydrogen gas. This relation is utilized in the hydrogen-evolution method introduced by Song et al. [179].

The experimental setup is simple and straightforward: the sample is placed under a funnel that is inserted into an inverted burette filled with the electrolyte. The gas emerging is collected in the burette, where it replaces the electrolyte volume, thus allowing for an easy quantification of its

volume [179]. Advantageous is the method's ability to provide information on-line over a long immersion time and thus on potentially time-dependent changes in the corrosion rate.

Limitations lie, on the one hand, in the method's inability to provide insights into underlying corrosion mechanisms and, on the other hand, in its accuracy. The latter arises from H_2-gas bubbles sticking to the funnel wall or dissolving in the electrolyte and thus cause an underestimation of the measured volume. This is, in relative terms, especially severe for either short test durations or for slowly degrading materials, in which cases the evolving gas volume is accordingly low. In these cases, the minor change in the burette's liquid level is easily overshadowed by fluctuations originating from atmospheric-pressure variations and changes in the electrolyte's gas solubility. To improve on the reliability, Hofstetter et al. [97] advanced the test setup, making it compatible for slowly degrading Mg samples. Their setup comprises reference burettes to correct for pressure fluctuations and gas solubility. This setup was also deployed in the framework of this thesis.

Furthermore, as for every immersion study, the control over the pH value is essential, because a change in electrolyte pH will ultimately alter the stability of corrosion products and in turn the substrate's corrosion susceptibility (Figure 1.8). From Eq. 1.3 it is obvious that Mg dissolution leads to the formation of hydroxide ions, which render the electrolyte more alkaline. An appropriate buffer system is thus required to stabilize the pH value. For biomedical applications a CO_2/$NaHCO_3$-buffer system is commonly employed, which is inspired by the physiological buffer system, and considered more appropriate for simulating the *in vivo* situation than the buffers Tris (tris(hydroxymethyl)-aminomethane) or HEPES (N-2-hydroxyethylpiperazine-N0-2-ethanesulfonic acid) [180, 181]. In the test setup mentioned above, which was developed by Hofstetter et al. [97] and is deployed in this thesis, an on-line CO_2-buffering system is included. The continuous buffering capabilities consistently stabilize the pH value at a desired value, e.g. at a physiological pH of 7.4. The *in vitro* degradation rates obtained with this setup were shown to indeed correlate closely with the *in vivo* degradation rates [97], thus showing the applicability of the method using this setup to predict *in vitro* the *in vivo* degradation performance of slowly-degrading Mg-based materials.

In order to correlate the hydrogen-evolution rate to a degradation rate expressed as the depth of corrosion attack per time unit, first the mass loss is correlated to a degradation depth considering Mg's density at 1.738 g cm^{-3}, resulting in:

$$DR = 2.10\, \Delta W \qquad\qquad\qquad \text{(Eq. 1.8)}$$

where *DR* is the degradation rate in mm year^{-1} and ΔW is the mass-loss rate in mg cm^{-2} day^{-1}. The mass-loss rate in Eq. 1.8 can then be replaced by the rate of evolving hydrogen-gas volume when

considering the relation of Mg mass (1 mol Mg corresponding to a mass of 24.31 g) to the hydrogen-gas volume (1 mol H_2 corresponding to a volume of 24.45 l at 25 °C and 1 atm), resulting in:

$$DR = 2.088 \, V_H \tag{Eq. 1.9}$$

where V_H is the hydrogen-evolution rate in ml cm^{-2} day^{-1}.

Electrochemical polarization method. Considering that corrosion processes are of electrochemical nature, it is not surprising that electrochemical methods are frequently used for their study. Among the electrochemical methods available, potentiodynamic polarization (PDP) is the most common one employed for the study of Mg corrosion [156, 178] and presented in the following.

PDP testing requires a potentiostat, which controls the potential of the sample as the working electrode, or more precisely the potential difference between the sample and a reference electrode (RE), by regulating the current flow between the sample and a counter electrode.

The polarization sweep is typically preceded by an equilibration step during which the potential is recorded that establishes without any applied perturbation (potential), the so-called open circuit potential (E_{OCP}). The duration of this step is chosen to reach a (near-)steady state for E_{OCP}. The PDP is then performed by linearly increasing the potential, typically starting from a potential that is negative, i.e. cathodic, to the E_{OCP} determined, and proceeding to potentials more positive, i.e. anodic, to the E_{OCP} determined. This sweep direction is usually chosen because anodic polarization induces the electrode's dissolution and causes irreversible changes to its surface. During the potential sweep, the current flow is monitored as a function of potential, resulting in polarization curves which are usually reported as semi-logarithmic plots, as schematically presented in Figure 1.9.

The potential at which polarity reversal occurs is the corrosion potential, E_{corr}. At E_{corr}, the anodic and cathodic reaction rates are equal and the net current is zero. For electrochemical reactions under activation control, polarization curves exhibit linear behavior in the semi-logarithmic plots. Extrapolation of these linear sections from both the anodic and cathodic branch allow in principle to determine at their intercept the corrosion current density, i_{corr} (Figure 1.9; see limitations below).

Besides E_{corr} and i_{corr}, with the latter potentially allowing to access kinetic information on the corrosion processes (see below), PDP testing can also reveal the relative anodic and cathodic contributions, and with that it allows access to mechanistic insights into the corrosion processes occurring. This presents a major advantage over the standard methods such as the hydrogen-evolution method mentioned above or mass-loss methods [178]. Advantageous is also the comparatively simple sample preparation, the relatively small destructive nature which makes

possible to re-use a sample after re-preparation, and the significantly shorter testing times compared to the common non-electrochemical methods mentioned.

Limitations associated with PDP testing are mainly related to the difficulties of interpreting the results. On the one hand, while the determination of i_{corr} is a reproducible method to derive the instantaneous corrosion rate of many metals, its applicability to Mg is not trivial. This is because of (i) Mg's non-polarizable nature, which leads to excessive current densities already at minimal anodic polarization [182]; (ii) local alkalization; (iii) the substantial H_2 evolution during anodic or cathodic polarization [95, 183], leading to an Ohmic potential drop is created in the proximity of the electrode surface that is difficult to compensate for [184]; and (iv) noble-element redeposition occurring on the Mg-electrode surface (see Chapter 4). As a result, Mg-based electrodes often do not show an ideal linear region in the anodic branch, thus not allowing for an accurate determination of i_{corr}.

On the other hand, the polarization response of an electrode delivers experimentally the summation of all anodically and all cathodically active areas on the electrode surface in accordance with the mixed-potential theory [162]. In the context of alloys containing intermetallic phases, as investigated in this thesis, the contributors of the polarization response to the mixed potential can only be deconvoluted when the relative area fractions and the electrochemical properties of each phase is known. However, accessing local phenomena, such as the corrosion behavior of intermetallic phases, would require an electrochemical cell with a surface area that is at the size of the feature of interest (for intermetallic phases typically in the nano- to micrometer range). The study of such local phenomena is thus not accessible with standard electrochemical cells, which have a surface area typically in the range of a few mm² to 1 cm².Furthermore, owing to the short testing period of PDP testing, it cannot serve for the prediction of long-term corrosion behavior.

Despite these limitations, PDP testing remains an invaluable tool in the study of Mg corrosion mainly due to its ability to determine relative changes in the anodic and cathodic reaction kinetics, arising for instance from alloying, impurities or electrolyte additives.

To sum up, owing to the limitations associated with the individual methods, a complementary approach that combines different experimental methods is essential to obtain a fundamental understanding of the corrosion mechanisms in Mg alloys.

Additionally to the methods described above, high-resolution transmission electron microscopy as a relatively new and experimentally demanding method to study Mg corrosion was extensively used in this thesis and is presented in the next chapter.

1.1.7   *Transmission electron microscopy in corrosion science*

Transmission electron microscopy (TEM) was extensively used to provide detailed insights into the local corrosion phenomena of ZX-lean alloys upon their immersion in simulated body fluid (SBF), and thus complements the methods presented in the previous section (see '*Methods to study Mg corrosion*' in 1.1.6).

In this section, the use of TEM in corrosion science in general and the state-of-the-art of its use in the study of Mg corrosion in specific are presented. Lastly, the basic principles of stereographic microscopy are demonstrated and its use in this thesis outlined

TEM in corrosion science – general

TEM has been of great benefit to corrosion science by providing access to the relationships between a material's microstructure plus composition and its corrosion behavior. Modern TEMs offer extraordinarily high magnification and resolution down to the atomic level. The capabilities are extended beyond imaging by high-resolution chemical analysis facilitated by the continuous advances in analytical TEM. In fact, different operational modes are available, which provide access to the simultaneous investigation of morphological (imaging mode), structural (electron diffraction) and chemical properties (high-angle annular dark field (HAADF) providing Z-contrast, energy-dispersive X-ray spectroscopy (EDS) or electron energy-loss spectroscopy (EELS) [185]). Such information can be acquired on the same specimen and even in the same area, provided that beam damage can be circumvented (see below). TEM also allows to obtain 3D information by electron tomography or to a certain extent by stereo imaging (see below).

Despite these advantages, it should be mentioned that TEM investigations are related with high acquisition costs of the microscope and with delicate and time-consuming sample preparation to achieve the electron transparency required. In the context of the latter, ion-beam techniques such as Focused-Ion Beam (FIB) or ion milling (precision-ion polishing, PIPS, or broad-ion-beam milling, BIB) are invaluable; especially for the demanding specimens of corroded Mg substrates, for which the combination of a rather soft metal substrate with a much stiffer corrosion-product layer present a high risk of mechanical disintegration.

Generally, the TEM-based techniques to study corrosion events can be divided in (i) *ex situ*, (ii) quasi-*in situ* and (iii) *in situ* investigations, and differ in the specimen's exposure to the corrosive environment to occur either outside or inside the microscope. They entail an increasing degree of the insights obtainable on the microstructural role in the corrosion processes but also an increasing complexity and demand on the experimental procedure.

Ex situ investigations refer to a "*post mortem*" analysis of the surface films and corrosion products. This simplest mode of investigation is typically realized in cross-sectional analysis and has been extensively deployed for all kinds of metals, for instance to characterize their respective surface films in various environments [145, 186-188], the impact of aggressive ions on the film stability [189], the origin of film-stability improvements via surface modifications [186, 190], or the details of stress-corrosion cracks [191] and pit formation [192]. However, the conclusions that can be drawn from *ex situ* analysis of the corrosion products on the role of the metal microstructure are limited.

Ex situ TEM analyses were also applied in the context of biocorrosion studies, in which they revealed details on the interface properties of permanent implants such as the role of a nanostructured Ti-oxide layer in osseointegration [193], or on the compositional changes of wear particles compared to Co–Cr–Mo or Ti–Al–V hip implants they originated from [194]. Attractive is the possibility to analyze simultaneously the biological side of the implant–tissue interface, provided that the tissue is appropriately prepared to give sufficient contrast in TEM [195].

Quasi-*in situ* analysis relates to the investigation of the same location in the same sample with potentially cumulative exposure times to a corrosive environment, while the exposure happens outside the microscope. The samples are typically investigated in planar view. Quasi-*in situ* protocols offer the advantage over *ex situ* analysis for their access to a correlation with the pristine metal microstructure and time-sequential insights of progressing corrosion attack; and over *in situ* analysis by their simplicity, because no special *in situ* equipment is necessary (see below). TEM-based quasi-*in situ* analyses were performed e.g on aluminum [196-198] and stainless steel [199]. In all cases, significant details on the local corrosion processes of the intermetallic phases contained and their specific impact on the matrix dissolution were observed on the nanometer scale.

In recent years, an increasing interest has been directed towards *in situ* investigations [200-203]. They enable the investigation of initiation processes of the corrosion attack and of the related structure, composition, and chemical state of the microstructure and corrosion products under realistic conditions. *In situ* analysis can circumvent the risk of potential artefacts associated with *ex situ* and quasi-*in situ* analyses arising from the specimen's dehydration in high vacuum, and enable accessing the very early stages of corrosion initiation occurring in sub-seconds. Specially designed TEM holders based on micro-electro-mechanical systems (MEMS) are required, which comprise a windowed environmental cell. Such "nanoreactors" allow for the specimen's exposure with corrosive gas or liquid in a static or flow mode during the TEM observations [200]. Despite the immense potential *in situ* corrosion studies have in answering fundamental questions related to local corrosion processes, the experimental effort should not be underestimated. In fact, such *in situ* studies are still in their infancy and so far limited to passive materials with comparably high corrosion resistance,

such as aluminum [201-203] or copper [202]. An overview on *in situ* TEM corrosion investigations is given in the review of Song and Xie [204].

TEM to understand Mg corrosion

The applicability of TEM for the corrosion studies of Mg is not trivial, and impaired by Mg's low atomic mass and high reactivity. More specifically, its low atomic mass and relatively low melting point make Mg particularly prone to beam damage. In fact, the displacement threshold energy, i.e. the energy above which displacement of atoms from the crystal lattice occurs, is relatively low for Mg so that knock-on damage occurs already at 100 kV [205]. As for electronically insulating corrosion products, beam damage may occur via radiolysis, i.e. ionization damage, at even lower energy [158, 185, 188]. Beam damage can affect the morphology or structure of a specimen, for instance by causing corrosion products to collapse [158] or otherwise amorphous oxides to crystallize [188], respectively, thus raising doubts on the validity of the observations made. A sufficiently low incident-beam energy is therefore crucial, while the loss in intensity can be compensated by the use of a high-brightness electron gun.

The low atomic mass of both Mg and the elements comprising the corrosion products present also a challenge for the analysis via EDS. The X-ray fluorescence yield is a function of atomic mass [185], which results in a low detection efficiency for these elements. High-efficiency EDS detectors are thus required to circumvent the necessity of excessive exposure times.

Mg's intrinsic high reactivity presents a major challenge for its TEM investigation, because it limits the time available for the observation before the TEM thin foil may be entirely dissolved (for quasi-*in situ* and *in situ* analyses) or the rapidly forming corrosion products reach an excessive thickness. Compared to the oxide layers on passive materials, which measure only a couple of nanometer in thickness, Mg's corrosion-product layers can reach a thickness of several tens to couple hundred of micrometer within minutes. An excessive thickness may limit the electron transparency in planar-view investigations and entails a risk for the specimen to mechanical disintegrate, especially in cross-sectional investigations [188]. The rapid release of corrosion products is particularly challenging for *in situ* investigations, in which an accumulation of corrosion products in the small electrolyte volume of the cell may affect the corrosion processes (see e.g. pH dependence in Figure 1.8) or the voluminous hydrogen gas may even damage the cell. For these reasons, corrosion studies on Mg have long been limited to *ex situ* analysis. In fact, no quasi-*in situ* or *in situ* characterization on Mg has been available at the start of this thesis project, and only a few quasi-*in situ* studies were documented very recently in 2018 [206, 207].

In an early study in 1992 Warner et al. [147] investigated in a cross-sectional TEM study the corrosion products formed on rapidly solidified Mg and an Mg–Al alloy, and observed a locally enhanced corrosion attack at the sites of precipitates and grain boundaries. Since then, and especially since the early 2010s, TEM has received increasing attention for the study of Mg-corrosion phenomena on the nanoscale [144-146, 158, 188, 208-210]. Different TEM modes – imaging, diffraction and chemical analysis – have been combined to achieve comprehensive insights into Mg-corrosion characteristics, e.g. that (i) a multilayer structure of the surface film forms upon immersion in pure water with an inner, dense MgO layer and an outer less dense $Mg(OH)_2$ layer [188, 208], (ii) the MgO forming upon atmospheric corrosion is amorphous [188] but nano-crystalline upon exposure to water [144, 188], (iii) an alloying-element rich layer is formed at the metal–corrosion-product-layer interface [145, 158, 209], and (iv) impurity-elements are embedded in the corrosion-product layer [146].

These investigations are limited to corrosive environments of little complexity, starting from atmospheric corrosion in air [188] and purified water [144, 188] to dilute saline [145, 147] and NaOH solutions [210]. Only Bowen et al. [208] made the attempt so far to study Mg's biocorrosion behavior via TEM. They characterized the corrosion products formed on pure Mg upon its implantation in the murine artery of rats, with a focus on the corrosion products' structural properties and revealed a duplex-layer structure with an inner nanocrystalline MgO layer and a nearly amorphous outer Mg-substituted hydroxyapatite layer. Despite the pioneering character of this investigation, a detailed characterization was limited by the susceptibility of the corrosion products to beam damage at high magnification. Further attempts to use TEM in the study of Mg's corrosion behavior in physiological conditions, i.e. upon exposure to complex biological fluids or even simulated body fluids, have not been pursued in literature up to now. The implementation of suitable protocols to allow for the study of the biocorrosion behavior of Mg-based alloys in *ex situ* and quasi-*in situ* TEM investigations is addressed in this thesis.

Stereographic-imaging technique

TEM imaging is intrinsically a two-dimensional projection of a 3D specimen. This may present a limitation if depth information is desired. In the specific context of this thesis, depth information is indeed required in the two following contexts:

(1) Estimation of the foil thickness in order to allow for the determination of the number density and volume fraction of intermetallic phases.
(2) Identification of microstructural features at free surfaces as those that are exposed to the corrosive environment.

To obtain depth information, stereo microscopy can be used. The principle of stereographic imaging, also termed stereo imaging or stereoscopic imaging, is equal to the 3D information the brain is capable to provide from two images of the same area acquired from both eyes (Figure 1.13a). The difference in viewing angle of the eyes causes a slight shift, termed the parallax shift p.
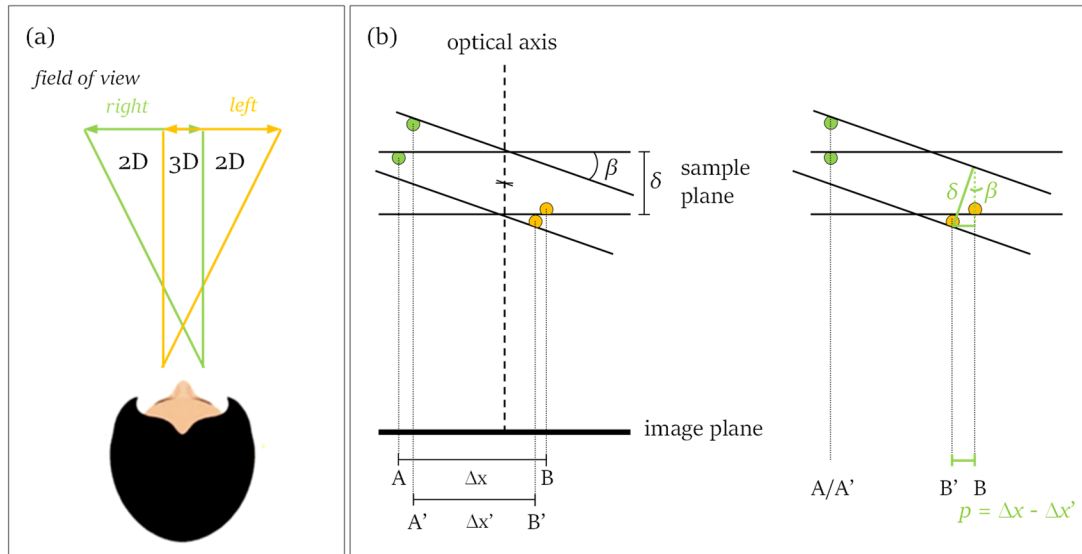
Figure 1.13: Principles of stereo microscopy. (a) Physiological stereo viewing. (b) By adjustment of the tilt angle β the parallax p is obtained, which can be used to estimate the sample thickness δ.

This principle can be transferred to TEM imaging [185], where two images are acquired at two different tilt angles. The sample is rotated around the holder axis by using a high-precision goniometer. When both 2D images are obtained, they are placed aside and viewed simultaneously. The brain then reconstructs a single image that reveals the depth information. The principle is schematically presented in Figure 1.13.

Although a stereo viewer or a trained operator is required to actually "see" in 3D based on only two images, this technique offers easy access to a 3D impression of the specimen and is especially attractive because of the significantly reduced amount of time it takes compared to TEM-based 3D tomography.

It should, however, be noted that stereo imaging can only be used for the imaging of features that show mass–thickness or diffraction contrast. Phase-contrast imaging, in contrast, is limited by a change of phase and projected-potential contrast upon tilting. A further limitation may arise from the difficulty to interpret the relative positions when the density of overlapping features in the TEM foil is excessive.

For an estimation of the TEM-foil thickness special care must be taken as to identify features on the top (marked with A in Figure 1.13b) and at the bottom surfaces (marked with B in Figure 1.13b), because the parallax p between them, with

$$p = \Delta x - \Delta x' \qquad \text{(Eq. 1.10)}$$

where Δx and $\Delta x'$ are the distances between A and B for a non-tilted and tilted specimen, respectively, defines the thickness δ according to:

$$\delta = \frac{p}{\sin \beta} \qquad \text{(Eq. 1.11)}$$

where β is the tilt angle. Targeted deposition or contamination spots, e.g. by focusing with a high beam current hydrocarbon contaminations are generated at both the top and the bottom surfaces, which may serve as suitable markers of the free surfaces. The stereo-imaging technique then provides an easy and relatively fast estimation of the specimen thickness and thus presents a valuable alternative to protocols based on EELS [211], which require the use of an EELS detector. However, it should be noted that stereo imaging is more prone for underestimation of the thickness and more subjective to the judgement by the operator compared to EELS.

Figure 1.14 provides an example of a typical stereo pair investigated in this study. It shows a ZX10 alloy heat treated at 250 °C with a microstructure containing ternary IMPs. The identified IMPs exposed at the top and bottom surfaces are marked with A and B, respectively.

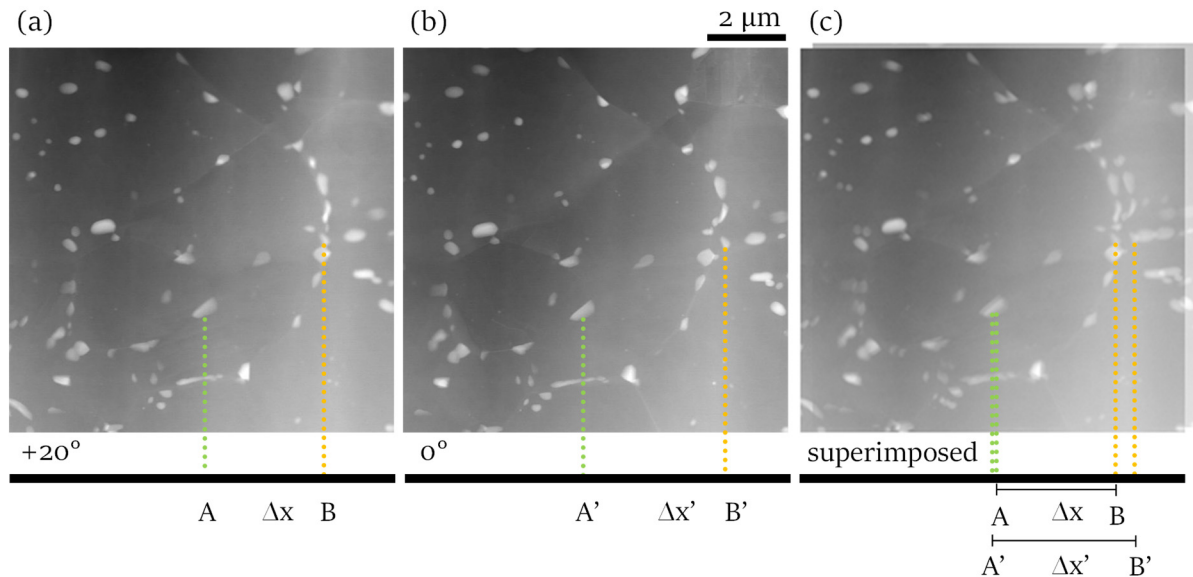**Figure 1.14**: A typical stereographic pair of images obtained in STEM-HAADF mode and at a tilt of (a) 0° and (b) +20°. Stereo viewing allows for a 3D impression of the TEM sample and thus reveals the relative depth of contained IMPs in the thin foil. With this the top (A) and bottom (B) precipitates can be identified. Superimposing the images gives the parallax with $p = \Delta x - \Delta x'$.

1.2 Aim of the project and outline of the thesis

This thesis aims to understand in detail the correlations between the microstructure of lean Mg-based alloys and their properties.

The specific aims were:

(listed in the order as addressed in the thesis)

1. To characterize the alloying-element distribution and intermetallic phases in lean Mg–Zn–Ca alloys and to assess the validity of the thermodynamic calculations, which underlie the alloying concept, regarding their prediction of intermetallic phases in these alloys.

2. To establish suitable experimental protocols for the *ex situ and* quasi-*in situ* TEM study of Mg corrosion on the nanoscale.

3. To assess locally the detailed dissolution behavior of the nanometric IMPs contained in Mg–Zn–Ca-lean alloys.

4. To identify the impact of nanometric IMPs on the macroscopic corrosion behavior of Mg–Zn–Ca-lean alloys as a function of their phase type.

5. To identify the specific microstructural contributors to the material strength of Mg–Zn–Ca-lean alloys, and assess their potential for age hardening.

6. To develop a new wrought Mg-based alloy with extended specific age-hardening potential.

The results of the thesis are structured as follows: **Chapter 2** investigates the validity of the simulated phase diagram as the basis of the alloying design of ZX alloys, and characterizes in detail the intermetallic phases contained in the lean ZX alloys. Local corrosion phenomena are studied on heat-treated specimens with a focus on the role of the two IMP types of interest (i.e. Mg_2Ca and IM1). The limitations of heat-treated specimens for the study of macroscopic corrosion behavior are also discussed. **Chapter 3** elucidates the detailed dissolution mechanisms acting on the cathodic ternary IM1 phase. Dealloying of the nanometric IMPs is identified to occur via preferential dissolution of Ca and concomitant enrichment of Zn, resulting in their ennoblement. While Chapter 2 and 3 focus on the local corrosion phenomena occurring in the first seconds to few hours of exposure to simulated body fluid, **Chapter 4** is directed towards understanding the corrosion behavior as a function of their IMP type on the macroscopic scale and the alloys' advanced dissolution. Model materials are deployed, each of them designed to host only one type of the IMPs of interest while the microstructure is otherwise comparable. The specific role of the IMP type is studied *in vitro* and validated *in vivo* in a small-animal model. This chapter also illustrates the concept of noble-element redeposition at the

origin of nanometric Zn-cluster formation observed, which can rationalize an observed dynamic increase of the cathodic activity of ZX-lean alloys with progressing degradation. For a comprehensive understanding of the microstructure–property correlations of ZX-lean alloys, their mechanical properties are assessed in **Chapter 5** and their microstructural characteristics (including nanoprecipitates) elucidated for their individual contribution to the material strength. The chapter also covers a brief investigation of the potential of ZX-lean alloys to age-harden. Identified limitations to age hardening of the ZX-lean alloys in Chapter 5 are tackled in **Chapter 6** by a new design concept that is based on the Mg–Al–Ca–Mn (AXM) system and developed towards a lean age-hardenable alloy (high tensile yield strength increase ΔTYS per at.% alloying elements). A detailed and multi-scale characterization of the material's nano- and microstructure reveals the microstructural contributors to the mechanical performance. **Chapter 7** finally summarizes the main findings of the thesis and presents possible future research directions.

1.3 References

[1] H. Davy, XXIII. Electro-chemical researches, on the decomposition of the earths; with observations on the metals obtained from the alkaline earths, and on the amalgam procured from ammonia, Philosophical Transactions of the Royal Society of London 98 (1808) 333-370.

[2] A.A. Bussy, Mémoire sur le Radical Métallique de la Magnésie, Annales de Chimie et de Physique 46 (1831) 434-437.

[3] H.E. Friedrich, B.L. Mordike, Magnesium Technology, Springer, Berlin, Germany, 2006.

[4] D. Zhao, F. Witte, F. Lu, J. Wang, J. Li, L. Qin, Current status on clinical applications of magnesium-based orthopaedic implants: A review from clinical translational perspective, Biomaterials 112 (2017) 287-302.

[5] A. Ditze, C. Scharf, Recycling of magnesium, Papierflieger Verlag, Clausthal-Zellerfeld, Germany, 2008.

[6] N.-E.L. Saris, E. Mervaala, H. Karppanen, J.A. Khawaja, A. Lewenstam, Magnesium: an update on physiological, clinical and analytical aspects, Clinica Chimica Acta 294(1-2) (2000) 1-26.

[7] O. Shaul, Magnesium transport and function in plants: the tip of the iceberg, Biometals 15(3) (2002) 307-321.

[8] W. Jahnen-Dechent, M. Ketteler, Magnesium basics, Clinical Kidney Journal 5 (2012) i3-i14.

[9] N.R. Council, Recommended dietary allowances, National Academies Press, Washington DC, USA, 1989.

[10] T. Kraus, S.F. Fischerauer, A.C. Hänzi, P.J. Uggowitzer, J.F. Löffler, A.M. Weinberg, Magnesium alloys for temporary implants in osteosynthesis: in vivo studies of their degradation and interaction with bone, Acta Biomaterialia 8(3) (2012) 1230-1238.

[11] C. Castellani, R.A. Lindtner, P. Hausbrandt, E. Tschegg, S.E. Stanzl-Tschegg, G. Zanoni, S. Beck, A.-M. Weinberg, Bone–implant interface strength and osseointegration: Biodegradable magnesium alloy versus standard titanium control, Acta Biomaterialia 7(1) (2011) 432-440.

[12] F. Witte, V. Kaese, H. Haferkamp, E. Switzer, A. Meyer-Lindenberg, C. Wirth, H. Windhagen, In vivo corrosion of four magnesium alloys and the associated bone response, Biomaterials 26(17) (2005) 3557-3563.

[13] K. Pichler, T. Kraus, E. Martinelli, P. Sadoghi, G. Musumeci, P.J. Uggowitzer, A.M. Weinberg, Cellular reactions to biodegradable magnesium alloys on human growth plate chondrocytes and osteoblasts, International Orthopaedics 38(4) (2014) 881-889.

[14] R.K. Rude, H.E. Gruber, Magnesium deficiency and osteoporosis: animal and human observations, The Journal of Nutritional Biochemistry 15(12) (2004) 710-716.

[15] E. Huse, A new ligature, Chicago Med J Exam 172(2) (1878).

[16] E. Payr, Beitrage zur Technik der Blutgesfass und Nervennaht nebst Mittheilungen die Verwendung eines Resorbierharen Metalles in der Chirurgie, Archiv für Klinische Chirurgie 62 (1900) 67-71.

[17] E. Payr, Blutgefäß-und Nervennaht (nebst Mittheilung über die Verwendung eines resorbirbaren Metalles in der Chirurgie) [Blood vessel and nerve suture (in addition to the use of a resorbable metal in surgery)], Centralblatt Chirurgie 28 (1901) 31-37.

[18]   E. Payr, Zur Verwendung des Magnesiums für resorbirbare Darmknöpfe und andere chirurgisch-technische Zwecke, Centralblatt Chirurgie 28(20) (1901) 513-515.

[19]   Y. Xin, T. Hu, P. Chu, In vitro studies of biomedical magnesium alloys in a simulated physiological environment: a review, Acta Biomaterialia 7(4) (2011) 1452-1459.

[20]   J. Walker, S. Shadanbaz, T.B. Woodfield, M.P. Staiger, G.J. Dias, Magnesium biomaterials for orthopedic application: a review from a biological perspective, Journal of Biomedical Materials Research Part B: Applied Biomaterials 102(6) (2014) 1316-1331.

[21]   K. Gusieva, C. Davies, J. Scully, N. Birbilis, Corrosion of magnesium alloys: the role of alloying, International Materials Reviews 60(3) (2015) 169-194.

[22]   Y. Ding, C. Wen, P. Hodgson, Y. Li, Effects of alloying elements on the corrosion behavior and biocompatibility of biodegradable magnesium alloys: a review, Journal of Materials Chemistry B 2(14) (2014) 1912-1933.

[23]   J.-W. Lee, H.-S. Han, K.-J. Han, J. Park, H. Jeon, M.-R. Ok, H.-K. Seok, J.-P. Ahn, K.E. Lee, D.-H. Lee, Long-term clinical study and multiscale analysis of in vivo biodegradation mechanism of Mg alloy, Proceedings of the National Academy of Sciences 113(3) (2016) 716-721.

[24]   F. Witte, The history of biodegradable magnesium implants: a review, Acta Biomaterialia 6(5) (2010) 1680-1692.

[25]   J.L. Gilbert, S.A. Mali, Medical implant corrosion: electrochemistry at metallic biomaterial surfaces, Degradation of Implant Materials, Springer, New York, NY, USA, 2012, 1-28.

[26]   M. Fernandez-Sampedro, C. Salas-Venero, C. Fariñas-Álvarez, M. Sumillera, L. Pérez-Carro, M. Fakkas-Fernandez, J. Gómez-Román, L. Martínez-Martínez, M.C. Fariñas, Postoperative diagnosis and outcome in patients with revision arthroplasty for aseptic loosening, BMC Infectious Diseases 15(1) (2015) 232.

[27]   J.L. Basko-Plluska, J.P. Thyssen, P.C. Schalock, Cutaneous and systemic hypersensitivity reactions to metallic implants, Dermatitis 22(2) (2011) 65-79.

[28]   D. Gilding, A. Reed, Biodegradable polymers for use in surgery—polyglycolic/poly (actic acid) homo-and copolymers: 1, Polymer 20(12) (1979) 1459-1464.

[29]   J.C. Middleton, A.J. Tipton, Synthetic biodegradable polymers as orthopedic devices, Biomaterials 21(23) (2000) 2335-2346.

[30]   O. Böstman, H. Pihlajamäki, Clinical biocompatibility of biodegradable orthopaedic implants for internal fixation: a review, Biomaterials 21(24) (2000) 2615-2621.

[31]   O. Böstman, Intense granulomatous inflammatory lesions associated with absorbable internal fixation devices made of polyglycolide in ankle fractures, Clinical Orthopaedics and Related Research 278 (1992) 193-199.

[32]   X.-N. Gu, Y.-F. Zheng, A review on magnesium alloys as biodegradable materials, Frontiers of Materials Science in China 4(2) (2010) 111-115.

[33]   J. Hofstetter, S. Rüedi, I. Baumgartner, H. Kilian, B. Mingler, E. Povoden-Karadeniz, S. Pogatscher, P.J. Uggowitzer, J.F. Löffler, Processing and microstructure–property relations of high-strength low-alloy (HSLA) Mg–Zn–Ca alloys, Acta Materialia 98 (2015) 423-432.

[34]   M.P. Staiger, A.M. Pietak, J. Huadmai, G. Dias, Magnesium and its alloys as orthopedic biomaterials: a review, Biomaterials 27(9) (2006) 1728-1734.

[35]   J. Nagels, M. Stokdijk, P.M. Rozing, Stress shielding and bone resorption in shoulder arthroplasty, Journal of Shoulder and Elbow Surgery 12(1) (2003) 35-39.

[36]   Y. Sul, P. Johansson, B. Chang, E. Byon, Y. Jeong, Bone tissue responses to Mg-incorporated oxidized implants and machine-turned implants in the rabbit femur, Journal of Applied Biomaterials and Biomechanics 3(1) (2005) 18-28.

[37]   Y.T. Sul, B.S. Kang, C. Johansson, H.S. Um, C.J. Park, T. Albrektsson, The roles of surface chemistry and topography in the strength and rate of osseointegration of titanium implants in bone, Journal of Biomedical Materials Research Part A 89(4) (2009) 942-950.

[38]   M. Haude, H. Ince, S. Kische, A. Abizaid, R. Tölg, P.L. Alves, N.M. Van, S. Verheye, E. Christiansen, W. Wijns, Sustained safety and clinical performance of a drug-eluting absorbable metal scaffold up to 24 months: pooled outcomes of BIOSOLVE-II and BIOSOLVE-III, EuroIntervention 13(4) (2017) 432-439.

[39]   H.-S. Han, S. Loffredo, I. Jun, J. Edwards, Y.-C. Kim, H.-K. Seok, F. Witte, D. Mantovani, S. Glyn-Jones, Current status and outlook on the clinical translation of biodegradable metals, Materials Today 23 (2019) 57-71.

[40]   M. Yazdimamaghani, M. Razavi, D. Vashaee, K. Moharamzadeh, A.R. Boccaccini, L. Tayebi, Porous magnesium-based scaffolds for tissue engineering, Materials Science and Engineering: C 71 (2017) 1253-1266.

[41]   J.M. Seitz, E. Wulf, P. Freytag, D. Bormann, F.W. Bach, The manufacture of resorbable suture material from magnesium, Advanced Engineering Materials 12(11) (2010) 1099-1105.

[42]   A.C. Hänzi, A. Metlar, M. Schinhammer, H. Aguib, T.C. Lüth, J.F. Löffler, P.J. Uggowitzer, Biodegradable wound-closing devices for gastrointestinal interventions: degradation performance of the magnesium tip, Materials Science and Engineering: C 31(5) (2011) 1098-1103.

[43]   K.-D. Kühn, A. Weinberg, P. Uggowitzer, S. Vogt, J. Löffler, Bio-absobable composite materials containing magnesium and magnesium alloys as well as implants made of said composites, U.S. patent US9700657B2, 2015.

[44]   H. Windhagen, K. Radtke, A. Weizbauer, J. Diekmann, Y. Noll, U. Kreimeyer, R. Schavan, C. Stukenborg-Colsman, H. Waizy, Biodegradable magnesium-based screw clinically equivalent to titanium screw in hallux valgus surgery: short term results of the first prospective, randomized, controlled clinical pilot study, Biomedical Engineering Online 12(62) (2013) 1-10.

[45]   R. Biber, J. Pauser, M. Geßlein, H.J. Bail, Magnesium-based absorbable metal screws for intra-articular fracture fixation, Case Reports in Orthopedics 2016 (2016) 1-4.

[46]   C. Plaass, S. Ettinger, L. Sonnow, S. Koenneker, Y. Noll, A. Weizbauer, J. Reifenrath, L. Claassen, K. Daniilidis, C. Stukenborg-Colsman, Early results using a biodegradable magnesium screw for modified chevron osteotomies, Journal of Orthopaedic Research 34(12) (2016) 2207-2214.

[47]   R. Biber, J. Pauser, M. Brem, H.J. Bail, Bioabsorbable metal screws in traumatology: a promising innovation, Trauma Case Reports 8 (2017) 11-15.

[48]   J.-M. Seitz, A. Lucas, M. Kirschner, Magnesium-based compression screws: a novelty in the clinical use of implants, JOM 68(4) (2016) 1177-1182.

[49]   ASTM, Standard Practice for Codification of Unalloyed Magnesium and Magnesium-Alloys, Cast and Wrought, B951 - 11, 2018.

[50]   K. Pichler, S. Fischerauer, P. Ferlic, E. Martinelli, H.-P. Brezinsek, P.J. Uggowitzer, J.F. Löffler, A.-M. Weinberg, Immunological Response to Biodegradable Magnesium Implants, JOM 66(4) (2014) 573-579.

[51]   F. Feyerabend, J. Fischer, J. Holtz, F. Witte, R. Willumeit, H. Drücker, C. Vogt, N. Hort, Evaluation of short-term effects of rare earth and other elements used in magnesium alloys on primary cells and cell lines, Acta Biomaterialia 6(5) (2010) 1834-1842.

[52]   A. Myrissa, S. Braeuer, E. Martinelli, R. Willumeit-Römer, W. Goessler, A.M. Weinberg, Gadolinium accumulation in organs of Sprague–Dawley® rats after implantation of a biodegradable magnesium-gadolinium alloy, Acta Biomaterialia 48 (2017) 521-529.

[53]   H.-S. Han, G.H. Jang, I. Jun, H. Seo, J. Park, S. Glyn-Jones, H.-K. Seok, K.H. Lee, D. Mantovani, Y.-C. Kim, Transgenic zebrafish model for quantification and visualization of tissue toxicity caused by alloying elements in newly developed biodegradable metal, Scientific Reports 8(1) (2018) 13818.

[54]   D. Zhao, S. Huang, F. Lu, B. Wang, L. Yang, L. Qin, K. Yang, Y. Li, W. Li, W. Wang, Vascularized bone grafting fixed by biodegradable magnesium screw for treating osteonecrosis of the femoral head, Biomaterials 81 (2016) 84-92.

[55]   A.M. Weinberg, CEO of BRI.Tech GmbH, Austria, personal communication, 2019.

[56]   BIOTRONIK SE & Co. KG Press Release: BIOTRONIK Announces CE Mark for Magmaris, the First Clinically-Proven Bioresorbable Magnesium Scaffold, (2) (2016).

[57]   R. Waksman, M.J. Lipinski, E. Acampado, Q. Cheng, L. Adams, S. Torii, J. Gai, R. Torguson, D.M. Hellinga, P.C. Westman, Comparison of acute thrombogenicity for metallic and polymeric bioabsorbable scaffolds: magmaris versus absorb in a porcine arteriovenous shunt model, Circulation: Cardiovascular Interventions 10(8) (2017) e004762.

[58]   E. Wittchow, N. Adden, J. Riedmüller, C. Savard, R. Waksman, M. Braune, Bioresorbable drug-eluting magnesium-alloy scaffold: design and feasibility in a porcine coronary model, EuroIntervention 8(12) (2013) 1441-1450.

[59]   M. Haude, H. Ince, A. Abizaid, R. Toelg, P.A. Lemos, C. von Birgelen, E.H. Christiansen, W. Wijns, F.-J. Neumann, C. Kaiser, Sustained safety and performance of the second-generation drug-eluting absorbable metal scaffold in patients with de novo coronary lesions: 12-month clinical results and angiographic findings of the BIOSOLVE-II first-in-man trial, European heart journal 37(35) (2016) 2701-2709.

[60]   A. Wlodarczak, L.A.I. Garcia, P.P. Karjalainen, A. Komócsi, F. Pisano, S. Richter, M. Lanocha, J.R. Rumoroso, K.F. Leung, Magnesium 2000 postmarket evaluation: Guideline adherence and intraprocedural performance of a sirolimus-eluting resorbable magnesium scaffold, Cardiovascular Revascularization Medicine 20(12) (2019) 1140-1145.

[61]   H. Sallmon, F. Berger, M.Y. Cho, B. Opgen-Rhein, First use and limitations of Magmaris® bioresorbable stenting in a low birth weight infant with native aortic coarctation, Catheterization and Cardiovascular Interventions 93 (2019) 1340–1343.

[62]   H. Yang, F. Zhang, J. Qian, J. Chen, J. Ge, Restenosis in Magmaris Stents Due to Significant Collapse, JACC: Cardiovascular Interventions 11(10) (2018) 77-78.

[63]   K.U. Kainer, Magnesium alloys and technologies, John Wiley & Sons, Weinheim, Germany, 2006.

[64]   C.L. Liu, J. Jiang, M. Wang, Y.J. Wang, P.K. Chu, W.J. Huang, In vitro degradation and biocompatibility of WE43, ZK60, and AZ91 biodegradable magnesium alloys, Advanced Materials Research 287 (2011) 2008-2014.

[65]   D. Crapper, S. Krishnan, A. Dalton, Brain aluminum distribution in Alzheimer's disease and experimental neurofibrillary degeneration, Science 180(4085) (1973) 511-513.

[66] A. Turyanskaya, M. Rauwolf, T. Grünewald, M. Meischel, S. Stanzl-Tschegg, J.F. Löffler, P. Wobrauschek, A.M. Weinberg, H. Lichtenegger, C. Streli, µXRF Elemental Mapping of Bioresorbable Magnesium-Based Implants in Bone, Materials 9(10) (2016) 811.

[67] F. Amerstorfer, S.F. Fischerauer, L. Fischer, J. Eichler, J. Draxler, A. Zitek, M. Meischel, E. Martinelli, T. Kraus, S. Hann, S.E. Stanzl-Tschegg, P.J. Uggowitzer, J.F. Löffler, A.M. Weinberg, T. Prohaska, Long-term in vivo degradation behavior and near-implant distribution of resorbed elements for magnesium alloys WZ21 and ZX50, Acta Biomaterialia 42 (2016) 440-450.

[68] J. Zhang, H. Li, W. Wang, H. Huang, J. Pei, H. Qu, G. Yuan, Y. Li, The degradation and transport mechanism of a Mg-Nd-Zn-Zr stent in rabbit common carotid artery: A 20-month study, Acta Biomaterialia 69 (2018) 372-384.

[69] S. Sandlöbes, S. Zaefferer, I. Schestakow, S. Yi, R. Gonzalez-Martinez, On the role of non-basal deformation mechanisms for the ductility of Mg and Mg–Y alloys, Acta Materialia 59(2) (2011) 429-439.

[70] T. Al-Samman, Comparative study of the deformation behavior of hexagonal magnesium–lithium alloys and a conventional magnesium AZ31 alloy, Acta Materialia 57(7) (2009) 2229-2242.

[71] T. Al-Samman, X. Li, Sheet texture modification in magnesium-based alloys by selective rare earth alloying, Materials Science and Engineering: A 528(10-11) (2011) 3809-3822.

[72] T. Sasaki, K. Yamamoto, T. Honma, S. Kamado, K. Hono, A high-strength Mg–Sn–Zn–Al alloy extruded at low temperature, Scripta Materialia 59(10) (2008) 1111-1114.

[73] B. Zhang, L. Geng, L. Huang, X. Zhang, C. Dong, Enhanced mechanical properties in fine-grained Mg–1.0 Zn–0.5 Ca alloys prepared by extrusion at different temperatures, Scripta Materialia 63(10) (2010) 1024-1027.

[74] G.S. Rao, Y. Prasad, Grain boundary strengthening in strongly textured magnesium produced by hot rolling, Metallurgical Transactions A 13(12) (1982) 2219-2226.

[75] A. Yamashita, Z. Horita, T.G. Langdon, Improving the mechanical properties of magnesium and a magnesium alloy through severe plastic deformation, Materials Science and Engineering: A 300(1-2) (2001) 142-147.

[76] M. Kai, Z. Horita, T.G. Langdon, Developing grain refinement and superplasticity in a magnesium alloy processed by high-pressure torsion, Materials Science and Engineering: A 488(1-2) (2008) 117-124.

[77] J. Koike, T. Kobayashi, T. Mukai, H. Watanabe, M. Suzuki, K. Maruyama, K. Higashi, The activity of non-basal slip systems and dynamic recovery at room temperature in fine-grained AZ31B magnesium alloys, Acta Materialia 51(7) (2003) 2055-2065.

[78] M. Barnett, Z. Keshavarz, A. Beer, D. Atwell, Influence of grain size on the compressive deformation of wrought Mg–3Al–1Zn, Acta Materialia 52(17) (2004) 5093-5103.

[79] M. Cihova, R. Schäublin, L.B. Hauser, S.S.A. Gerstl, C. Simson, P.J. Uggowitzer, J.F. Löffler, Rational design of a lean magnesium-based alloy with high age-hardening response, Acta Materialia 158 (2018) 214-229.

[80] F. Witte, N. Hort, C. Vogt, S. Cohen, K.U. Kainer, R. Willumeit, F. Feyerabend, Degradable biomaterials based on magnesium corrosion, Current Opinion in Solid State and Materials Science 12(5-6) (2008) 63-72.

[81] X.-N. Gu, S.-S. Li, X.-M. Li, Y.-B. Fan, Magnesium based degradable biomaterials: A review, Frontiers of Materials Science 8(3) (2014) 200-218.

[82] J. Hofstetter, M. Becker, E. Martinelli, A.M. Weinberg, B. Mingler, H. Kilian, S. Pogatscher, P.J. Uggowitzer, J.F. Löffler, High-strength low-alloy (HSLA) Mg–Zn–Ca alloys with excellent biodegradation performance, JOM 66(4) (2014) 566-572.

[83] H. Bakhsheshi-Rad, E. Hamzah, A. Fereidouni-Lotfabadi, M. Daroonparvar, M. Yajid, M. Mezbahul-Islam, M. Kasiri-Asgarani, M. Medraj, Microstructure and bio-corrosion behavior of Mg–Zn and Mg–Zn–Ca alloys for biomedical applications, Materials and Corrosion 65(12) (2014) 1178-1187.

[84] D. Zander, N.A. Zumdick, Influence of Ca and Zn on the microstructure and corrosion of biodegradable Mg–Ca–Zn alloys, Corrosion Science 93 (2015) 222-233.

[85] B. Zberg, P.J. Uggowitzer, J.F. Löffler, MgZnCa glasses without clinically observable hydrogen evolution for biodegradable implants, Nature Materials 8(11) (2009) 887-891.

[86] X. Gu, Y. Zheng, S. Zhong, T. Xi, J. Wang, W. Wang, Corrosion of, and cellular responses to Mg–Zn–Ca bulk metallic glasses, Biomaterials 31(6) (2010) 1093-1103.

[87] V. Wessels, G. Le Mené, S.F. Fischerauer, T. Kraus, A.M. Weinberg, P.J. Uggowitzer, J.F. Löffler, In Vivo Performance and Structural Relaxation of Biodegradable Bone Implants Made from Mg-Zn-Ca Bulk Metallic Glasses, Advanced Engineering Materials 14(6) (2012) 357-364.

[88] A. Castellero, D. Uhlenhaut, B. Moser, J.F. Löffler, Critical Poisson ratio for room-temperature embrittlement of amorphous Mg85Cu5Y10, Philosophical Magazine Letters 87(6) (2007) 383-392.

[89] H. Hornberger, S. Virtanen, A. Boccaccini, Biomedical coatings on magnesium alloys–a review, Acta Biomaterialia 8(7) (2012) 2442-2455.

[90] S. Hiromoto, A. Yamamoto, High corrosion resistance of magnesium coated with hydroxyapatite directly synthesized in an aqueous solution, Electrochimica Acta 54(27) (2009) 7085-7093.

[91] J. Li, P. Cao, X. Zhang, S. Zhang, Y. He, In vitro degradation and cell attachment of a PLGA coated biodegradable Mg–6Zn based alloy, Journal of Materials Science 45(22) (2010) 6038-6045.

[92] S. Fukumoto, K. Sugahara, A. Yamamoto, H. Tsubakino, Improvement of corrosion resistance and adhesion of coating layer for magnesium alloy coated with high purity magnesium, Materials Transactions 44(4) (2003) 518-523.

[93] S.-Y. Kim, Y.-K. Kim, M.-H. Ryu, T.-S. Bae, M.-H. Lee, Corrosion resistance and bioactivity enhancement of MAO coated Mg alloy depending on the time of hydrothermal treatment in Ca-EDTA solution, Scientific Reports 7(1) (2017) 9061.

[94] S. Fischerauer, T. Kraus, X. Wu, S. Tangl, E. Sorantin, A. Hänzi, J.F. Löffler, P.J. Uggowitzer, A. Weinberg, In vivo degradation performance of micro-arc-oxidized magnesium implants: a micro-CT study in rats, Acta Biomaterialia 9(2) (2013) 5411-5420.

[95] G.L. Song, A. Atrens, Corrosion mechanisms of magnesium alloys, Advanced Engineering Materials 1(1) (1999) 11-33.

[96] J.F. Löffler, P.J. Uggowitzer, C. Wegmann, M. Becker, H.K. Feichtinger, Process and apparatus for vacuum distillation of high-purity magnesium. European Patent Application PCT, EP 2013/000131–WO2013/1076442012, 2012.

[97] J. Hofstetter, E. Martinelli, A.M. Weinberg, M. Becker, B. Mingler, P.J. Uggowitzer, J.F. Löffler, Assessing the degradation performance of ultrahigh-purity magnesium in vitro and in vivo, Corrosion Science 91 (2015) 29-36.

[98]   Y. Liu, Y. Zheng, X.H. Chen, J.A. Yang, H. Pan, D. Chen, L. Wang, J. Zhang, D. Zhu, S. Wu, Fundamental Theory of Biodegradable Metals—Definition, Criteria, and Design, Advanced Functional Materials 29(18) (2019) 1805402.

[99]   M. Esmaily, D. Blücher, J.-E. Svensson, M. Halvarsson, L.-G. Johansson, New insights into the corrosion of magnesium alloys — The role of aluminum, Scripta Materialia 115 (2016) 91-95.

[100] O. Lunder, T.K. Aune, K. Nisancioglu, Effect of Mn additions on the corrosion behavior of mould-cast magnesium ASTM AZ91, Corrosion 43(5) (1987) 291-295.

[101] T. Gladman, Precipitation hardening in metals, Materials Science and Technology 15(1) (1999) 30-36.

[102] J.-F. Nie, Precipitation and hardening in magnesium alloys, Metallurgical and Materials Transactions A 43(11) (2012) 3891-3939.

[103] P.-R. Cha, H.-S. Han, G.-F. Yang, Y.-C. Kim, K.-H. Hong, S.-C. Lee, J.-Y. Jung, J.-P. Ahn, Y.-Y. Kim, S.-Y. Cho, Biodegradability engineering of biodegradable Mg alloys: Tailoring the electrochemical properties and microstructure of constituent phases, Scientific Reports 3 (2013) 2367.

[104] S.Y. Cho, S.W. Chae, K.W. Choi, H.K. Seok, Y.C. Kim, J.Y. Jung, S.J. Yang, G.J. Kwon, J.T. Kim, M. Assad, Biocompatibility and strength retention of biodegradable Mg-Ca-Zn alloy bone implants, Journal of Biomedical Materials Research Part B: Applied Biomaterials 101(2) (2013) 201-212.

[105] Y. Xia, B. Zhang, Y. Wang, M. Qian, L. Geng, In-vitro cytotoxicity and in-vivo biocompatibility of as-extruded Mg–4.0 Zn–0.2 Ca alloy, Materials Science and Engineering: C 32(4) (2012) 665-669.

[106] R.A. Bozym, F. Chimienti, L.J. Giblin, G.W. Gross, I. Korichneva, Y. Li, S. Libert, W. Maret, M. Parviz, C.J. Frederickson, Free zinc ions outside a narrow concentration range are toxic to a variety of cells in vitro, Experimental Biology and Medicine 235(6) (2010) 741-750.

[107] C. Bettles, M. Gibson, Current wrought magnesium alloys: strengths and weaknesses, JOM 57(5) (2005) 46-49.

[108] C. Boehlert, K. Knittel, The microstructure, tensile properties, and creep behavior of Mg–Zn alloys containing 0–4.4 wt.% Zn, Materials Science and Engineering: A 417(1-2) (2006) 315-321.

[109] S. Cai, T. Lei, N. Li, F. Feng, Effects of Zn on microstructure, mechanical properties and corrosion behavior of Mg–Zn alloys, Materials Science and Engineering: A 32(8) (2012) 2570–2577.

[110] C. Bettles, M. Gibson, K. Venkatesan, Enhanced age-hardening behaviour in Mg–4 wt.% Zn micro-alloyed with Ca, Scripta Materialia 51(3) (2004) 193-197.

[111] C. Cáceres, A. Blake, The strength of concentrated Mg–Zn solid solutions, Physica Status Solidi A 194(1) (2002) 147-158.

[112] S. Cai, T. Lei, N. Li, F. Feng, Effects of Zn on microstructure, mechanical properties and corrosion behavior of Mg–Zn alloys, Materials Science and Engineering: C 32(8) (2012) 2570-2577.

[113] J.E. Hillis, The effects of heavy metal contamination on magnesium corrosion performance, SAE Transactions 92 (1983) 553-559.

[114] J.D. Hanawalt, C.E. Nelson, J.A. Peloubet, Corrosion studies of magnesium and its alloys, Trans. AIME 147 (1942) 273-299.

[115] N.T. Kirkland, M.P. Staiger, D. Nisbet, C.H. Davies, N. Birbilis, Performance-driven design of biocompatible Mg alloys, JOM 63(6) (2011) 28-34.

[116] Y. Song, E.-H. Han, D. Shan, C.D. Yim, B.S. You, The effect of Zn concentration on the corrosion behavior of Mg–xZn alloys, Corrosion Science 65 (2012) 322-330.

[117] H.-Y. Ha, J.-Y. Kang, J. Yang, C.D. Yim, B.S. You, Limitations in the use of the potentiodynamic polarisation curves to investigate the effect of Zn on the corrosion behaviour of as-extruded Mg–Zn binary alloy, Corrosion Science 75 (2013) 426-433.

[118] Y.M. Kim, C.D. Yim, H.S. Kim, B.S. You, Key factor influencing the ignition resistance of magnesium alloys at elevated temperatures, Scripta Materialia 65(11) (2011) 958-961.

[119] N. Stanford, The effect of calcium on the texture, microstructure and mechanical properties of extruded Mg–Mn–Ca alloys, Materials Science and Engineering: A 528(1) (2010) 314-322.

[120] Y. Du, X. Qiao, M. Zheng, D. Wang, K. Wu, I. Golovin, Effect of microalloying with Ca on the microstructure and mechanical properties of Mg-6 mass% Zn alloys, Materials & Design 98 (2016) 285-293.

[121] X. Gao, S. Zhu, B. Muddle, J. Nie, Precipitation-hardened Mg–Ca–Zn alloys with superior creep resistance, Scripta Materialia 53(12) (2005) 1321-1326.

[122] A. Nayeb-Hashemi, J. Clark, The Ca– Mg (calcium-magnesium) system, Journal of Phase Equilibria 8(1) (1987) 58-65.

[123] C. Mendis, K. Oh-Ishi, K. Hono, Enhanced age hardening in a Mg–2.4 at.% Zn alloy by trace additions of Ag and Ca, Scripta Materialia 57(6) (2007) 485-488.

[124] N.T. Kirkland, N. Birbilis, J. Walker, T. Woodfield, G.J. Dias, M.P. Staiger, In-vitro dissolution of magnesium–calcium binary alloys: Clarifying the unique role of calcium additions in bioresorbable magnesium implant alloys, Journal of Biomedical Materials Research Part B: Applied Biomaterials 95(1) (2010) 91-100.

[125] Z. Li, X. Gu, S. Lou, Y. Zheng, The development of binary Mg–Ca alloys for use as biodegradable materials within bone, Biomaterials 29(10) (2008) 1329-1344.

[126] J. Oh, T. Ohkubo, T. Mukai, K. Hono, TEM and 3DAP characterization of an age-hardened Mg–Ca–Zn alloy, Scripta Materialia 53(6) (2005) 675-679.

[127] K. Oh-Ishi, R. Watanabe, C. Mendis, K. Hono, Age-hardening response of Mg–0.3 at.% Ca alloys with different Zn contents, Materials Science and Engineering: A 526(1) (2009) 177-184.

[128] J. Seong, W. Kim, Development of biodegradable Mg–Ca alloy sheets with enhanced strength and corrosion properties through the refinement and uniform dispersion of the Mg2Ca phase by high-ratio differential speed rolling, Acta Biomaterialia 11 (2015) 531-542.

[129] I.A. Anyanwu, Y. Gokan, S. Nozawa, S. Kamado, Y. Kojima, S. Takeda, T. Ishida, Heat resistant magnesium alloys for automotive powertrain applications, Materials Science Forum, Trans Tech Publications Ltd., Zurich-Uetikon, Switzerland, 2003, 445-450.

[130] A. Hänzi, A. Sologubenko, P. Gunde, M. Schinhammer, P.J. Uggowitzer, Design considerations for achieving simultaneously high-strength and highly ductile magnesium alloys, Philosophical Magazine Letters 92(9) (2012) 417-427.

[131] N.D. Nam, Role of zinc in enhancing the corrosion resistance of Mg-5Ca alloys, Journal of The Electrochemical Society 163(3) (2016) C76-C84.

[132] A.C. Hänzi, Development of biodegradable magnesium alloys for cardiovascular stent applications, PhD Thesis, ETH Zurich, Zurich, Switzerland, 2009.

[133] CompuTherm LLC, Pandat software package for calculating phase diagrams and thermodynamic properties of multi- component alloys, Madison, USA, www.computherm.com.).

[134] C. Zener, quoted by CS Smith, Trans. AIME 175 (1948) 15.

[135] J. Clark, Transmission electron microscopy study of age hardening in a Mg-5 wt.% Zn alloy, Acta Metallurgica 13(12) (1965) 1281-1289.

[136] J. Hofstetter, E. Martinelli, S. Pogatscher, P. Schmutz, E. Povoden-Karadeniz, A.M. Weinberg, P.J. Uggowitzer, J.F. Löffler, Influence of trace impurities on the in vitro and in vivo degradation of biodegradable Mg–5Zn–0.3 Ca alloys, Acta Biomaterialia 23 (2015) 347-353.

[137] J. Hofstetter, Development of high-strength low-alloy (HSLA) magnesium alloys for biomedical application, PhD thesis, ETH Zurich, Zurich, Switzerland, 2015.

[138] L.F. Porter, P.E. Repas, The evolution of HSLA steels, JOM 34(4) (1982) 14-21.

[139] MatCalc software package for computer simulation of phase transformation and microstructure evolution in metallic systems, Vienna, Austria, www.matcalc-engineering.com.

[140] Y.-N. Zhang, D. Kevorkov, J. Li, E. Essadiqi, M. Medraj, Determination of the solubility range and crystal structure of the Mg-rich ternary compound in the Ca–Mg–Zn system, Intermetallics 18(12) (2010) 2404-2411.

[141] S.V. Lamaka, J. Gonzalez, D. Mei, F. Feyerabend, R. Willumeit-Römer, M.L. Zheludkevich, Local pH and Its Evolution Near Mg Alloy Surfaces Exposed to Simulated Body Fluids, Advanced Materials Interfaces 5(18) (2018) 1800169.

[142] L. Rossrucker, A. Samaniego, J.-P. Grote, A.M. Mingers, C.A. Laska, N. Birbilis, G.S. Frankel, K.J.J. Mayrhofer, The pH dependence of magnesium dissolution and hydrogen evolution during anodic polarization, Journal of the Electrochemical Society 162(7) (2015) C333-C339.

[143] Y. Wang, M. Wei, J. Gao, J. Hu, Y. Zhang, Corrosion process of pure magnesium in simulated body fluid, Materials Letters 62(14) (2008) 2181-2184.

[144] M. Taheri, R. Phillips, J. Kish, G. Botton, Analysis of the surface film formed on Mg by exposure to water using a FIB cross-section and STEM–EDS, Corrosion Science 59 (2012) 222-228.

[145] M. Brady, G. Rother, L. Anovitz, K. Littrell, K. Unocic, H. Elsentriecy, G.-L. Song, J. Thomson, N. Gallego, B. Davis, Film breakdown and nano-porous Mg(OH)2 formation from corrosion of magnesium alloys in salt solutions, Journal of The Electrochemical Society 162(4) (2015) C140-C149.

[146] M. Taheri, J. Kish, N. Birbilis, M. Danaie, E. McNally, J. McDermid, Towards a physical description for the origin of enhanced catalytic activity of corroding magnesium surfaces, Electrochimica Acta 116 (2014) 396-403.

[147] T. Warner, N. Thorne, G. Nussbaum, W. Stobbs, A cross-sectional TEM study of corrosion initiation in rapidly solidified Mg-based ribbons, Surface and Interface Analysis 19(1-12) (1992) 386-392.

[148] M. Pourbaix, Atlas of electrochemical equilibria in aqueous solution, NACE 307 (1974).

[149] G. Makar, J. Kruger, Corrosion of magnesium, International Materials Reviews 38(3) (1993) 138-153.

[150] J. Kish, Y. Hu, J. Li, W. Zheng, J. McDermid, Examination of focused ion beam-sectioned surface films formed on AM60B Mg alloy in an aqueous saline solution, Corrosion 68(6) (2012) 468-474.

[151] G. Song, A. Atrens, D. St John, X. Wu, J. Nairn, The anodic dissolution of magnesium in chloride and sulphate solutions, Corrosion Science 39(10-11) (1997) 1981-2004.

[152] S. Zhang, J. Li, Y. Song, C. Zhao, X. Zhang, C. Xie, Y. Zhang, H. Tao, Y. He, Y. Jiang, In vitro degradation, hemolysis and MC3T3-E1 cell adhesion of biodegradable Mg–Zn alloy, Materials Science and Engineering: C 29(6) (2009) 1907-1912.

[153] H. Kuwahara, Y. Al-Abdullat, N. Mazaki, S. Tsutsumi, T. Aizawa, Precipitation of magnesium apatite on pure magnesium surface during immersing in Hank's solution, Materials Transactions 42(7) (2001) 1317-1321.

[154] L. Wang, B.-P. Zhang, T. Shinohara, Corrosion behavior of AZ91 magnesium alloy in dilute NaCl solutions, Materials & Design 31(2) (2010) 857-863.

[155] P.-W. Chu, E.A. Marquis, Linking the microstructure of a heat-treated WE43 Mg alloy with its corrosion behavior, Corrosion Science 101 (2015) 94-104.

[156] M. Esmaily, J. Svensson, S. Fajardo, N. Birbilis, G. Frankel, S. Virtanen, R. Arrabal, S. Thomas, L. Johansson, Fundamentals and Advances in Magnesium Alloy Corrosion, Progress in Materials Science 89 (2017) 92–193.

[157] M. Taheri, M. Danaie, J. Kish, TEM examination of the film formed on corroding Mg prior to breakdown, Journal of The Electrochemical Society 161(3) (2014) C89-C94.

[158] K.A. Unocic, H.H. Elsentriecy, M.P. Brady, H. Meyer, G. Song, M. Fayek, R.A. Meisner, B. Davis, Transmission electron microscopy study of aqueous film formation and evolution on magnesium alloys, Journal of The Electrochemical Society 161(6) (2014) C302-C311.

[159] R. Willumeit, J. Fischer, F. Feyerabend, N. Hort, U. Bismayer, S. Heidrich, B. Mihailova, Chemical surface alteration of biodegradable magnesium exposed to corrosion media, Acta Biomaterialia 7(6) (2011) 2704-2715.

[160] A.J. Davenport, C. Padovani, B.J. Connolly, N.P. Stevens, T.A. Beale, A. Groso, M. Stampanoni, Synchrotron X-ray microtomography study of the role of Y in corrosion of magnesium alloy WE43, Electrochemical and Solid-State Letters 10(2) (2007) C5-C8.

[161] J. Sullivan, S. Mehraban, J. Elvins, In situ monitoring of the microstructural corrosion mechanisms of zinc–magnesium–aluminium alloys using time lapse microscopy, Corrosion Science 53(6) (2011) 2208-2215.

[162] F. Mansfeld, Area relationships in galvanic corrosion, Corrosion 27(10) (1971) 436-442.

[163] G. Song, A. Atrens, Understanding magnesium corrosion—a framework for improved alloy performance, Advanced Engineering Materials 5(12) (2003) 837-858.

[164] A. Südholz, N. Kirkland, R. Buchheit, N. Birbilis, Electrochemical properties of intermetallic phases and common impurity elements in magnesium alloys, Electrochemical and Solid-State Letters 14(2) (2011) C5-C7.

[165] M.-J. Liang, G.-H. Wu, W.-J. Ding, W. Wei, Effect of inclusion on service properties of GW103K magnesium alloy, Transactions of Nonferrous Metals Society of China 21(4) (2011) 717-724.

[166] O. Lunder, K. Nisancioglu, R.S. Hansen, Corrosion of die cast magnesium-aluminum alloys, SAE Technical Paper, 1993.

[167] E. Ghali, W. Dietzel, K.-U. Kainer, General and localized corrosion of magnesium alloys: a critical review, Journal of Materials Engineering and Performance 13(1) (2004) 7-23.

[168] S. Tiwari, R. Balasubramaniam, M. Gupta, Corrosion behavior of SiC reinforced magnesium composites, Corrosion Science 49(2) (2007) 711-725.

[169] N.N. Aung, W. Zhou, C.S. Goh, S.M.L. Nai, J. Wei, Effect of carbon nanotubes on corrosion of Mg–CNT composites, Corrosion Science 52(5) (2010) 1551-1553.

[170] M. Liu, P.J. Uggowitzer, A. Nagasekhar, P. Schmutz, M. Easton, G.-L. Song, A. Atrens, Calculated phase diagrams and the corrosion of die-cast Mg–Al alloys, Corrosion Science 51(3) (2009) 602-619.

[171] W. Loose, L. Pidgeon, J. Mathes, N. Woldmen, Corrosion and protection of magnesium, ASM Int., Materials Park, OH (1946) 173.

[172] N.D. Tomashov, Theory of corrosion and protection of metals, The Macmillian Company, New York, 1965.

[173] N. Birbilis, A. King, S. Thomas, G. Frankel, J. Scully, Evidence for enhanced catalytic activity of magnesium arising from anodic dissolution, Electrochimica Acta 132 (2014) 277-283.

[174] H. Bakhsheshi-Rad, M. Abdul-Kadir, M. Idris, S. Farahany, Relationship between the corrosion behavior and the thermal characteristics and microstructure of Mg–0.5 Ca–xZn alloys, Corrosion Science 64 (2012) 184-197.

[175] H. Du, Z. Wei, X. Liu, E. Zhang, Effects of Zn on the microstructure, mechanical property and bio-corrosion property of Mg–3Ca alloys for biomedical application, Materials Chemistry and Physics 125(3) (2011) 568-575.

[176] T. Cain, L. Bland, N. Birbilis, J. Scully, A compilation of corrosion potentials for magnesium alloys, Corrosion 70(10) (2014) 1043-1051.

[177] Y.-N. Zhang, D. Kevorkov, F. Bridier, M. Medraj, Experimental study of the Ca–Mg–Zn system using diffusion couples and key alloys, Science and Technology of Advanced Materials 12(2) (2011) 025003.

[178] N.T. Kirkland, N. Birbilis, M. Staiger, Assessing the corrosion of biodegradable magnesium implants: a critical review of current methodologies and their limitations, Acta Biomaterialia 8(3) (2012) 925-936.

[179] G. Song, A. Atrens, D. St John, An hydrogen evolution method for the estimation of the corrosion rate of magnesium alloys, in: J.N. Hryn (Ed.) Magnesium Technology 2001, TMS, New Orleans, LA, USA, 2001, 254-262.

[180] N.T. Kirkland, J. Waterman, N. Birbilis, G. Dias, T.B. Woodfield, R.M. Hartshorn, M.P. Staiger, Buffer-regulated biocorrosion of pure magnesium, Journal of Materials Science: Materials in Medicine 23(2) (2012) 283-291.

[181] N.I.Z. Abidin, A.D. Atrens, D. Martin, A. Atrens, Corrosion of high purity Mg, Mg2Zno. 2Mn, ZE41 and AZ91 in Hank's solution at 37 C, Corrosion Science 53(11) (2011) 3542-3556.

[182] A. King, N. Birbilis, J. Scully, Accurate electrochemical measurement of magnesium corrosion rates; a combined impedance, mass-loss and hydrogen collection study, Electrochimica Acta 121 (2014) 394-406.

[183] G. Song, A. Atrens, D. Stjohn, J. Nairn, Y. Li, The electrochemical corrosion of pure magnesium in 1 N NaCl, Corrosion Science 39(5) (1997) 855-875.

[184] M. Curioni, F. Scenini, T. Monetta, F. Bellucci, Correlation between electrochemical impedance measurements and corrosion rate of magnesium investigated by real-time hydrogen measurement and optical imaging, Electrochimica Acta 166 (2015) 372-384.

[185] D.B. Williams, C.B. Carter, Transmission Electron Microscopy - A Textbook for Materials Science, Plenum Press, New York, USA, 1996.

[186] C.-C. Shih, C.-M. Shih, Y.-Y. Su, L.H.J. Su, M.-S. Chang, S.-J. Lin, Effect of surface oxide properties on corrosion resistance of 316L stainless steel for biomedical applications, Corrosion Science 46(2) (2004) 427-441.

[187] Y.-J. Kim, Analysis of oxide film formed on type 304 stainless steel in 288 C water containing oxygen, hydrogen, and hydrogen peroxide, Corrosion 55(1) (1999) 81-88.

[188] J.H. Nordlien, S. Ono, N. Masuko, K. Nis, Morphology and structure of oxide films formed on magnesium by exposure to air and water, Journal of the Electrochemical Society 142(10) (1995) 3320-3322.

[189] P. Ghods, O. Isgor, G. Carpenter, J. Li, G. McRae, G. Gu, Nano-scale study of passive films and chloride-induced depassivation of carbon steel rebar in simulated concrete pore solutions using FIB/TEM, Cement and Concrete Research 47 (2013) 55-68.

[190] Y. Fu, X. Wu, Y. Wang, B. Li, S.-z. Yang, Study of corrosion resistance property and microstructure of TiNi shape memory alloy modified by pulsed high-energy density plasma, Applied Surface Science 157(3) (2000) 167-177.

[191] W. Nisbet, G. Lorimer, R. Newman, A transmission electron microscopy study of stress corrosion cracking in stainless steels, Corrosion Science 35(1-4) (1993) 457-469.

[192] J. Paillier, C. Mickel, P.F. Gostin, A. Gebert, Characterization of corrosion phenomena of Zr–Ti–Cu–Al–Ni metallic glass by SEM and TEM, Materials Characterization 61(10) (2010) 1000-1008.

[193] A. Palmquist, K. Grandfield, B. Norlindh, T. Mattsson, R. Brånemark, P. Thomsen, Bone–titanium oxide interface in humans revealed by transmission electron microscopy and electron tomography, Journal of the Royal Society Interface 9(67) (2011) 396-400.

[194] P.F. Doorn, P.A. Campbell, J. Worrall, P.D. Benya, H.A. McKellop, H.C. Amstutz, Metal wear particle characterization from metal on metal total hip replacements: transmission electron microscopy study of periprosthetic tissues and isolated particles, Journal of Biomedical Materials Research 42(1) (1998) 103-111.

[195] A.M. Glauert, P.R. Lewis, Biological specimen preparation for transmission electron microscopy, Princeton University Press, Princeton NJ, USA, 2014.

[196] R.P. Wei, C.-M. Liao, M. Gao, A transmission electron microscopy study of constituent-particle-induced corrosion in 7075-T6 and 2024-T3 aluminum alloys, Metallurgical and Materials Transactions A 29(4) (1998) 1153-1160.

[197] S. Malladi, F. Tichelaar, Q. Xu, M. Wu, H. Terryn, J. Mol, F. Hannour, H. Zandbergen, Quasi in situ analytical TEM to investigate electrochemically induced microstructural changes in alloys: AA2024-T3 as an example, Corrosion Science 69 (2013) 221-225.

[198] S. Kairy, P. Rometsch, C. Davies, N. Birbilis, On the Electrochemical and Quasi In Situ Corrosion Response of the Q-Phase (AlxCuyMgzSiw) Intermetallic Particle in 6xxx Series Aluminum Alloys, Corrosion 73(1) (2016) 87-99.

[199] B. Zhang, J. Wang, B. Wu, Y. Zhou, X. Ma, Quasi-in-situ ex-polarized TEM observation on dissolution of MnS inclusions and metastable pitting of austenitic stainless steel, Corrosion Science 100 (2015) 295-305.

[200] F.M. Ross, Liquid Cell Electron Microscopy, Cambridge University Press, Cambridge, UK, 2016.

[201] S. Chee, R. Hull, F. Ross, Liquid cell TEM of the corrosion of metal films in aqueous solutions, Microscopy and Microanalysis 18(S2) (2012) 1110-1111.

[202] S.W. Chee, S.H. Pratt, K. Hattar, D. Duquette, F.M. Ross, R. Hull, Studying localized corrosion using liquid cell transmission electron microscopy, Chemical Communications 51(1) (2015) 168-171.

[203] S. Malladi, C. Shen, Q. Xu, T. de Kruijff, E. Yücelen, F. Tichelaar, H. Zandbergen, Localised corrosion in aluminium alloy 2024-T3 using in situ TEM, Chemical Communications 49(92) (2013) 10859-10861.

[204] Z. Song, Z.-H. Xie, A literature review of in situ transmission electron microscopy technique in corrosion studies, Micron 112 (2018) 69-83.

[205] K. Urban, Radiation-induced processes in experiments carried out in-situ in the high-voltage electron microscope, Physica Status Solidi (a) 56(1) (1979) 157-168.

[206] X. Zhang, S. Kairy, J. Dai, N. Birbilis, A closer look at the role of nanometer scale solute-rich stacking faults in the localized corrosion of a magnesium alloy GZ31K, Journal of The Electrochemical Society 165(7) (2018) C310-C316.

[207] Y. Zhang, P. Gore, W. Rong, Y. Wu, Y. Yan, R. Zhang, L. Peng, J.-F. Nie, N. Birbilis, Quasi-in-situ STEM-EDS insight into the role of Ag in the corrosion behaviour of Mg-Gd-Zr alloys, Corrosion Science 136 (2018) 106-118.

[208] P.K. Bowen, C.T. McNamara, O.P. Mills, J. Drelich, J. Goldman, FIB-TEM Study of Magnesium Corrosion Products after 14 Days in the Murine Artery, ACS Biomaterials Science & Engineering 1(10) (2015) 919-926.

[209] R. Phillips, J. Kish, Nature of surface film on matrix phase of Mg alloy AZ80 formed in water, Corrosion 69(8) (2013) 813-820.

[210] M. Taheri, J. Kish, Nature of surface film formed on Mg exposed to 1 M NaOH, Journal of The Electrochemical Society 160(1) (2013) C36-C41.

[211] K. Iakoubovskii, K. Mitsuishi, Y. Nakayama, K. Furuya, Thickness measurements with electron energy loss spectroscopy, Microscopy Research and Technique 71(8) (2008) 626-631.

2 Microstructure and early-stage biocorrosion in ZX10 alloy with tailored intermetallic phases

Applying heat treatments to alter the microstructure of multi-component alloys is a common approach to generate distinct phases and microstructures while preserving the nominal composition. The materials generated in this way allow studying the impact of the characteristic microstructure on the associated properties of interest, here the corrosion susceptibility, to come to a deeper understanding of the corresponding microstructure–property correlations.

In this chapter, heat treatments guided by thermodynamical calculations were applied to tailor the phase type of intermetallic particles in the ZX10 alloy, here either the binary phase rich in Mg and Ca, or the ternary phase rich in Mg, Zn and Ca. The resulting microstructure was assessed by transmission electron microscopy to inspect the validity of the calculations, followed by a study to investigate the role which the various phases play in the corrosion processes, using methods based on electron microscopy and electrochemistry.

2.1 Introduction

This chapter presents a detailed investigation of the microstructure of the ZX10 alloy, with a specific focus on the contained intermetallic particles (IMPs), and the role they have in the alloy's corrosion behavior.

In order to tailor the phase-type of these IMPs, extruded Zx10 was exposed to specific heat treatments, guided by thermodynamic calculations. This approach allows to keep the nominal composition constant, while it still allows to generate various microstructures that are dominated by a specific phase type, here either a binary phase rich in Mg and Ca, or a ternary one rich in Mg, Zn and Ca.

Thus far, however, there is no information available on the validity of the calculated phase diagram on which the alloy design of ZX-lean alloys builds on [1, 2]. This phase diagram was presented by Hofstetter et al. [1] and results from calculations using the Pandat software (CompuTherm, Madison, WI) [3], a simulation tool for multicomponent phase diagram calculations, and the data base MatCalc mc_mg_v1.006 [4]. Using these calculations the authors predicted that the IMPs' phase in as-extruded ZX10 is Mg_2Ca, but no experimental proof was provided. The applicability of the calculations to predict the microstructure of extruded materials may indeed be questioned, considering that the calculations assume thermodynamic equilibrium, which may not be reached following extrusion because of the finite time the material is exposed to the extrusion temperature. The validity of the data base at the origin of the calculations has also not been confirmed experimentally. For that reason, it remains to be experimentally shown whether the predicted phases, namely Mg_2Ca for the binary phase and $Ca_2Mg_6Zn_3$ for the ternary phase [1], are valid.

The first part of this chapter thus presents an assessment of the ZX10 microstructure as a function of heat treatments guided by the phase diagram available from Hofstetter et al. and by considering the diffusivity of the alloying elements, here Ca and Zn, in Mg. It is hypothesized that following extrusion a heat treatment at or below 275 °C generates a phase transformation from the binary to the ternary phase. To test this hypothesis, the microstructure following heat treatments was assessed using transmission electron microscopy (TEM) and TEM-based energy dispersive X-ray spectroscopy (EDS) for chemical analysis. Based on this a critical evaluation of the calculated phase diagram including the two predicted key phases, i.e. the binary and the ternary phase, is presented.

In the second part of this chapter the ZX10 alloy that was heat treated to host solely one type of intermetallic phase, i.e. either the binary or the ternary one, was deployed for an investigation of the corrosion behavior in simulated-body conditions as a function of the IMP type. The hypothesis that

the type of nanometric IMPs [2] can control the macroscopic corrosion rate of ZX10 is thoroughly scrutinized. To that end, the corrosion behavior was first investigated locally using TEM in quasi-*in situ* corrosion conditions, and then macroscopically using electrochemical protocols and SEM imaging of cross-sections following immersion in SBF. The corresponding results are presented here, followed by a discussion on the validity of the hypothesis.

2.2 Experimental details

2.2.1 ZX10 alloy with engineered intermetallic phases

The alloy with nominal composition Mg–Zn1.0(0.37)–Ca0.3(0.18) (in wt.% (at.%)), referred to as ZX10, was produced using distilled, ultra-high purity (XHP) Mg (99.999% [5]), and high-purity Zn (99.99%) and Ca (99.5%). The alloying was performed at 750 °C under a protective gas mixture (Ar with 1 vol.% SF_6). The ingot was cast into a graphite crucible and then machined into a billet of 50 mm in diameter and 120 mm in length. The billet was homogenized (350 °C/ 12 h plus 450 °C/ 8 h) and then exposed to isothermal holding at 250 °C for 0.5 h, in a similar fashion as described in Ref. [2]. Subsequently, the billet was heated to 300 °C and then indirectly extruded at an exit speed of 3.75 mm s^{-1} into rods of 10 mm diameter, corresponding to an extrusion ratio of 25.

As to examine the validity of the calculated phase diagram, the microstructure of samples heat treated at different temperatures to thermodynamic equilibrium was investigated. The as-extruded material was exposed to a series of isothermal heat treatments, between 250 and 375 °C in 25 °C increments, to control the secondary phases while keeping the overall alloying composition constant. The heat-treatment time was chosen in such a way that each treatment generated the same diffusion distance L for the slowest diffusing species, here Zn. Zn diffusion in Mg was indeed assumed to be the rate-determining step, because its activation energy is higher and thus its diffusion coefficient in Mg lower compared to Ca [6]. The formation of intermetallic phases containing Zn is thus controlled by the diffusion of Zn according to the Arrhenius equation:

$$D = D_0 \exp\left(\frac{-Q}{RT}\right)$$ (Eq. 2.1)

where Q is the activation energy taken for Zn in Mg at ~133 kJ mol^{-1} [7], R is the gas constant, T is the absolute temperature (in K), and D_0 is a temperature-independent pre-exponential factor (in m^2 s^{-1}). Using the diffusion coefficient D, the time t across the different heat treatments was chosen following $L = \sqrt{D(T)\,t} = constant$, with a heat treatment of 375 °C for 1 h used as a benchmark for all heat treatments. The latter was found from previous experiences to generate an equilibrium microstructure in the ZX10 alloy. The calculated equivalent heat-treatment times are included in Table 2.3.

The effect of heat treatments on the microstructure, specifically on their intermetallic phases, was again analyzed by STEM-EDS. The samples are labelled with 'HT-', short for *heat treated*,

followed by the heat-treatment temperature; for example, 'HT-250' presents the sample annealed at 250 °C.

2.2.2   *Grain-size analysis*

For the grain-size analysis, samples in the as-extruded and heat-treated conditions were cut perpendicularly to the extrusion axis, and prepared by mechanical grinding and polishing followed by etching with picric acid to reveal the grain boundaries in light microscopy. The grain size was analyzed by applying the linear-intercept method using the Lince® software (TU Darmstadt).

2.2.3   *Transmission electron microscopy*

TEM samples were prepared from the as-extruded and heat-treated rods by cutting and mechanically grinding them to a thickness of about 80 µm. They were then punched into standard TEM 3 mm disks. Electron transparency was achieved by Ar^+-ion milling using a Precision Ion Polishing System (PIPS™ II from Gatan, Inc.) at 3.5 ° incident angle and an acceleration voltage of 4 kV. Ion milling was performed at liquid-nitrogen temperature to avoid changes to the microstructure.

TEM imaging was performed in an FEI Talos™ F200X operated at 80 kV mainly in scanning TEM (STEM) mode with a high-angle annular dark-field (HAADF) detector for atomic-mass (Z) contrast. Quantitative chemical information was obtained by means of energy dispersive X-ray spectroscopy (EDS) using a wide-angle detector. The instrument is equipped with a high-brightness X-FEG Schottky field-emission gun (FEI X-FEG) and four-quadrant Super-X silicon drift EDS detectors (FEI Super-X detector), which can produce ultrahigh X-ray count rates. Each acquisition was performed for at least 15 min at a dwell time of 10 µs, and the spectra were quantified using the QMap function in Cliff-Lorimer mode in ESPRIT software from Bruker. Special care was taken for the analysis of the intermetallic-phase composition as to only consider those particles which occupied the entire TEM foil thickness, thus excluding the contribution of the Mg matrix.

The number density N of IMPs was evaluated by manual counting of the particles in a given area and their size was determined by manually measuring the diameter d in ImageJ software. The TEM foil thickness, necessary to estimate N, was determined using stereographic pairs of images taken at +15 ° and -15 °. The IMP volume fraction f was obtained from N and d, assuming spherical particles.

For a detailed analysis of the ternary phase, ultra-high-resolution STEM imaging with the corresponding atomically resolved STEM-EDS chemical mapping was performed using a double Cs-corrected FEI Titan Themis™, operated at 80 kV. The instrument is equipped with the X-FEG Super-X detector for X-rays. Thanks to the Cs correction in STEM mode a spatial resolution of about 1 Å is

reached, which, coupled to the Super-X detector, enables atomically resolved chemical mapping. Acquisition was performed using the FEI VELOX™ software. The analysis of the ternary IMPs was performed in sample areas thin enough to avoid Mg-matrix contribution to the signal. Visualization of the ternary-phase candidate crystal structures was performed using VESTA software [8].

2.2.4   Analysis of early-stage corrosion processes

The initial corrosion processes were studied by TEM following short-time immersion and pre- and post-investigation of the same locations before and after corrosion attack. We refer to this protocol in the following as *SABACO* method, stemming from the '*S*ame *A*rea *B*efore and *A*fter *Co*rrosion'. The details of this method, along with its potential and limitations are presented in Chapter 3. In short, the changes in the microstructure upon corrosion attack and potential corrosion-product formation are imaged in STEM mode with a strong focus on chemical mapping using STEM-EDS. Complementary acquisition of stereographic image pairs taken at different tilt angles allow to obtain a 3D impression from the 2D-projected images intrinsic to TEM. Visual inspection of the stereo pairs allows for a quick identification of those microstructural features exposed at the free surfaces of the TEM thin foil.

Corrosion attack was provoked by immersing the electron-transparent TEM disk in simulated body fluid (SBF) (Table 2.1, Table 2.2) [9] under physiological temperature and pH. The latter was adjusted by constant flushing of the SBF with air containing 6.7 vol.% CO_2, a concentration that was chosen based on the ionic strength of the SBF used to achieve the pH value desired. To terminate the corrosion attack, the specimens were carefully rinsed sequentially in water and ethanol, each for 5 s.

Table 2.1: Salts for the preparation of the simulated body fluid used in this study in the order of mixing [9].

Reagent	Concentration (mg l^{-1})
KCl	298.2
NaCl	5844
NaHCO$_3$	2268.5
MgSO$_4 \cdot$ 7H$_2$O	246.5
CaCl$_2$	367.5
KH$_2$PO$_4$	136.1

Table 2.2: Concentration of species in the simulated body fluid used in this study.

Species	Concentration (mmol l^{-1})
Na$^+$	127
K$^+$	5
Mg^{2+}	1
Ca^{2+}	2.5
Cl$^-$	109
HCO$_3^-$	27
HPO$_4^{2-}$	1
SO$_4^{2-}$	1

2.2.5 Electrochemical characterization

Specimens were electrically contacted using a Cu wire soldered to the back of the specimens and subsequently embedded in 2-component epoxy (RenLam® LY 113 / Ren® HY 97-1). Immediately preceding insertion into the electrochemical cell, the samples were mechanically ground using SiC2500 grinding paper and ethanol as a lubricant, followed by thorough rinsing with ethanol and compressed-air drying.

The electrochemical investigations were conducted using a standard three-electrode electrochemical cell (flat cell with V = 300 ml) equipped with a Pt-mesh counter electrode and an Ag/AgCl reference electrode. All potentials are reported relative to the standard-hydrogen electrode (SHE). Measurements were carried out with a PGSTAT101 potentiostat (Metrohm Autolab).

Potentiodynamic polarization (PDP) sweeps, preceded by an open circuit potential (E_{OCP}) immersion period of 300 s, were performed from -250 mV to +400 mV with respect to the E_{OCP} at 300 s ($E_{OCP,300}$) or until a steep current increase was observed. A scan rate of 1 mV s^{-1} was applied. PDP sweeps were conducted under simulated-body conditions as defined above. The entire electrochemical cell was housed in a cell-culture incubator (HeraCell® 150 CO$_2$ incubator, Heraeus) with the atmosphere adjusted to 6.7 vol.% CO$_2$ to maintain an SBF pH of 7.4 ± 0.05. The pH value was controlled online with an external pH meter and never exceeded 7.5.

2.2.6 Cross-sectional SEM analysis of the corrosion-product layer

For an estimation of the depth of corrosion attack via scanning electron microscopy (SEM), cross-sectional SEM (xSEM) specimens were prepared from as-extruded and selected heat-treated samples after their immersion in SBF for 48 h. The corresponding samples were mechanically ground and polished to a mirror-like surface finish using ethanol as a lubricant to avoid excessive oxidation. Prior to immersion, a part of the surface was covered with water-impermeable and peelable varnish (Lacomit, Agar Scientific Ltd) to prevent its corrosion attack (Figure 2.1). Here, the same immersion conditions as for the SABACO experiment were used. Following the immersion, the samples were rinsed subsequently in water and ethanol to terminate the corrosion attack. The varnish was then carefully removed to expose the non-corroded surface area, which corresponds to the original sample surface and thus serves as a reference height to estimate the corrosion depth and corrosion-product-layer thickness.

Each corroded sample was glued onto an XHP-Mg plate using a vacuum- and electron-beam compatible glue (G1 from Gatan, Inc.) to obtain a sandwich assembly with the corrosion-product layer as the region of interest facing the XHP-Mg plate. Cross-sections of this sandwich assembly

were cut with a diamond wire saw. Improved surface quality of the cross section was achieved by mechanical grinding and polishing, followed by a final surface polishing via Ar$^+$-ion milling using a Broad-Ion Beam (BIB) polishing system (IM4000, Hitachi) at an acceleration and discharge voltage of 3 kV and 1.5 kV, respectively. The cross-sections were finally sputter-coated with gold and imaged using an SEM SU70 Hitachi at 15 kV in backscattered electron (BSE) mode. The corrosion-product-layer thickness was measured in the SEM micrographs using ImageJ software.
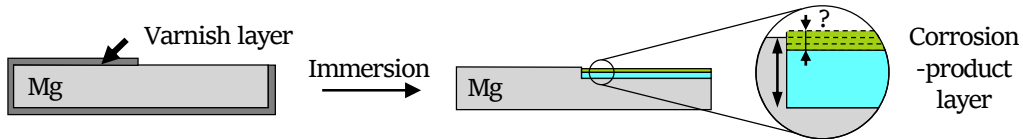

Figure 2.1: Schematics of the experimental procedure for cross-sectional SEM analysis of the corroded ZX alloys. A peelable varnish protects part of the surface from corrosion, thus preserving the original sample surface. The experiment is designed to reveal the depth of corrosion attack and the volume of corrosion products forming.

2.3 Results and discussion

2.3.1   Microstructure of as-extruded and heat-treated ZX10 alloy

Figure 2.2 shows the STEM-EDS chemical maps of Zn (in red) and Ca (in green) for ZX10 in its as-extruded condition and following various heat-treatments in relation to the phase fractions obtained by the thermodynamic calculations. Note that the yellow color in the chemical maps for 250 – 325 °C results from the superimposed signal for Zn and Ca. Only Ca and Zn but not Mg are shown in these maps to reflect the composition of the intermetallic phases only, but not that of the matrix.
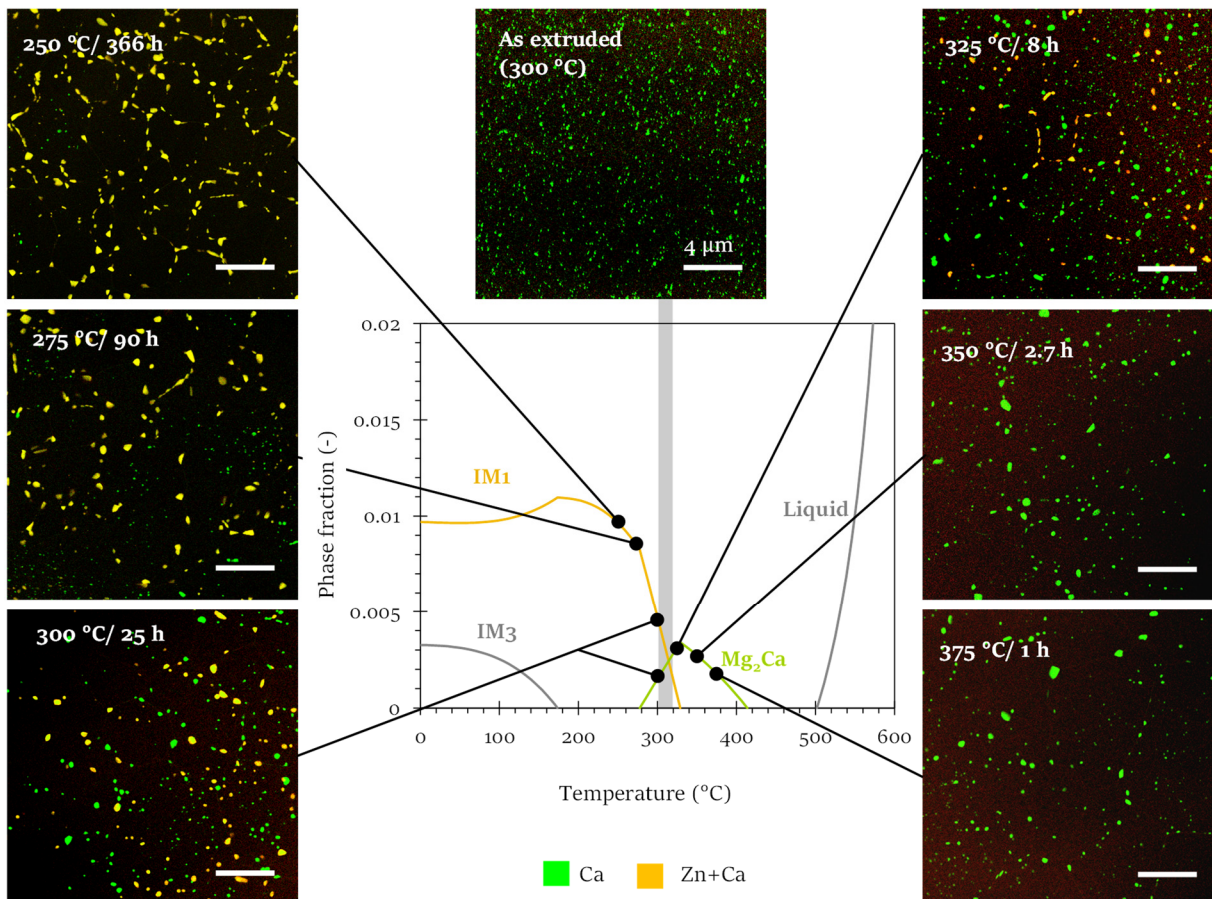

Figure 2.2: STEM-EDS chemical maps for Ca and Zn in ZX10 in relation to phase fractions derived from the thermodynamic calculations as a function of temperature. The EDS maps reveal the presence of the binary Mg–Ca-rich intermetallic phase in green and ternary Mg–Zn–Ca-rich intermetallic phase in yellow for various thermomechanical processing conditions.

The alloy indirectly extruded at 300 °C (Figure 2.2, center top) hosts nanometric intermetallic particles (IMPs) with a high number density, and exhibits a fine-grained microstructure with a grain size of about 2.31 ± 0.30 µm (Table 2.3). The STEM-EDS chemical map reveals that only one type of intermetallic phase is present in the microstructure and that this phase is rich in Ca, forming an Mg–Ca-rich binary phase. While this information does not suffice to yet conclude on the precise phase, it should be noted that the presence of a binary Mg–Ca-rich phase is generally in agreement with the phase diagram, which suggests Mg_2Ca phase, and thus follows what was postulated by Hofstetter et al. [2]. Note further that the phase diagram predicts the exclusive presence of the binary Mg–Ca-rich phase only for temperatures ≥ 325 °C, which may indicate that the real temperature during extrusion, set to 300 °C, was slightly higher owing to heat generated by friction and deformation [10]. Alternatively, the calculated phase diagram may not be accurate.

The chemical maps for low-temperature heat treatments of ≤ 325 °C reveal the presence of an intermetallic phase that is rich in Zn and Ca (Figure 2.2, IMPs in yellow contrast), forming an Mg–Zn–Ca-rich ternary phase. Its phase fraction increases with decreasing heat-treatment temperature (see Figure 2.2, left and f derived from the TEM-image analysis in Table 2.3), in agreement with the calculated ternary phase field (center of Figure 2.2, referred to as 'IM1'), and represents almost 100% of the IMPs present in the HT-250 sample (Figure 2.2, top left). As to the higher end of this temperature range, i.e. at 325 °C, the ternary phase still appears to be stable at this temperature, although outnumbered by the binary one (Figure 2.2, top right). This is again in good agreement with the calculations. This is also interesting when comparing this equilibrium microstructure to the one following extrusion, where the lower temperature of extrusion compared to that of the HT-325 condition would imply a larger fraction of the ternary phase in the as-extruded state, according to the calculated phase field. From its absence in the as-extruded condition it can thus be concluded that the thermodynamic equilibrium was not reached upon extrusion, i.e. the process did not allow for sufficient time to form the ternary phase.

Finally, the absence of this ternary intermetallic phase at temperatures larger than 325 °C (HT-350 and HT-375 in Figure 2.2, right) is also in agreement with the calculations, which predicted its phase fraction to recede completely from about 330 °C. At this temperature and above, the binary Mg–Ca-rich phase is stable and its phase fraction decreases with temperature (see Figure 2.2, right and f in Table 2.3), again following closely the trend predicted computationally.

For all heat treatments applied, the IMPs' size coarsened compared to the as-extruded state, while their number density declined (Table 2.3). This is opposed to the behavior of the matrix grain size: it remained constant following the low-temperature heat treatments at 250 and 275 °C and only

marginally grew at 300 °C. From 325 °C grain coarsening occurred. The grain size and the type and number density N of the IMPs resulting from the various thermomechanical treatments are summarized in Table 2.3.

Table 2.3: Grain size D, number density N, IMP size d, and resulting volume fraction f of binary and ternary IMPs resulting from extrusion and various heat treatments. D was obtained by light microscopy, and N, d and f by TEM analysis. f was calculated with the average value for d and assuming spherical particles.

Condition	D (µm)	IMP type	N (m⁻³)	d (nm)	f^* (-)
As extruded	2.31 ± 0.30	binary	4.46×10^{18}	67 ± 23	0.70×10^{-3}
		ternary	-	-	-
HT-250°C/366h	2.54 ± 0.21	binary	0.09×10^{18}	-	-
		ternary	1.13×10^{18}	180 ± 81	3.45×10^{-3}
HT-275°C/90h	3.14 ± 0.44	binary	1.03×10^{18}	76 ± 31	0.24×10^{-3}
		ternary	0.46×10^{18}	227 ± 103	2.82×10^{-3}
HT-300°C/25h	4.23 ± 0.53	binary	0.39×10^{18}	126 ± 74	0.41×10^{-3}
		ternary	0.26×10^{18}	225 ± 90	1.55×10^{-3}
HT-325°C/8h	8.59 ± 1.41	binary	2.72×10^{18}	103 ± 49	1.56×10^{-3}
		ternary	0.23×10^{18}	187 ± 70	0.79×10^{-3}
HT-350°C/3h	8.39 ± 1.46	binary	1.01×10^{18}	122 ± 64	0.96×10^{-3}
		ternary	0.06×10^{18}	-	-
HT-375°C/1h	10.2 ± 1.65	binary	1.06×10^{18}	118 ± 64	0.91×10^{-3}
		ternary	-	-	-

Figure 2.3 summarizes the experimentally obtained phase fractions for the two intermetallic phases of interest, i.e. the binary Mg–Ca phase (labelled Mg$_2$Ca) and ternary Mg–Zn–Ca phase (labelled IM1), which are plotted as a function of heat-treatment temperature. It includes also the phase fractions obtained for the as-extruded state. Based on the heat-treatment times chosen to reach thermodynamic equilibrium (see experimental section 2.2.1), the graph can be considered an 'experimentally obtained phase diagram' and thus allows a direct comparison to the one computationally obtained in Figure 2.2. In the temperature regime experimentally investigated, 250 – 375 °C, the general trends of phase fractions fit strikingly well to the ones predicted, including the gradually declining phase fraction of the Mg–Zn–Ca ternary phase from 250 °C to 325 °C and its absence from 350 °C, and the increasing phase fraction of the Mg–Ca binary phase from 275 °C and then again its decline for temperatures from 325 °C.
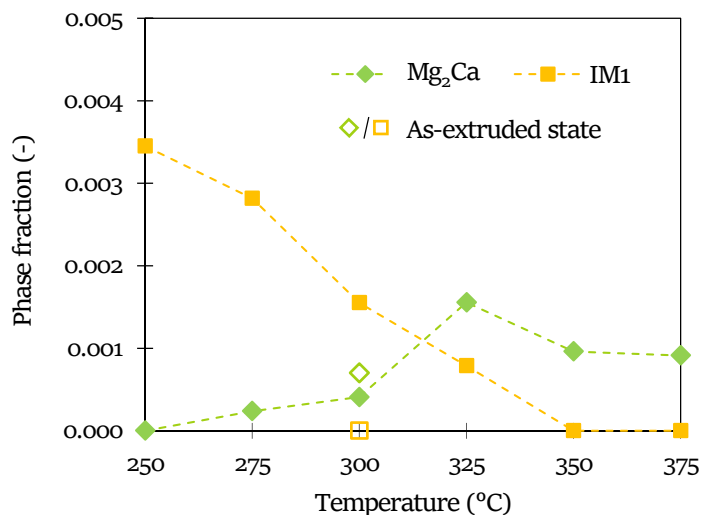
Figure 2.3: Experimentally obtained phase fractions for the binary Mg$_2$Ca and ternary IM1 phase at temperatures between 250 and 375 °C. The phase fractions of both phases obtained for ZX10 upon extrusion at 300 °C are also shown.

The largest apparent discrepancy is the level of the experimentally obtained volume fractions that is overall lower than the predicted one. This deviation is attributed to elemental segregation of Zn and Ca to grain boundaries (see Figure 2.7 further below), which is not accounted for in the calculations. The discrepancy could also relate to the limited spatial resolution of TEM at the magnifications used, which do not allow to account for potentially present smallest precipitates of less than 5 – 10 nm. Besides, it may also be noted that the thermodynamic calculations predict the theoretical equilibrium that occurs at an infinitely long annealing time, which cannot be reached experimentally.

2.3.2 Detailed phase analysis

The low-magnification EDS chemical maps have revealed that the intermetallic phases are either composed of Mg and Ca (binary phase) or of Mg, Zn and Ca (ternary phase). For the identification of their precise composition, however, a more detailed analysis is required.

Figure 2.4 shows EDS spectra obtained from binary and ternary intermetallic particles. As mentioned above special care was taken to only consider those IMPs that occupied the entire TEM-foil thickness as to prevent the contribution of the Mg matrix to the signal.

The composition of the binary IMPs contained in the as-extruded condition was determined to 68.0 ± 2.1 at.% and 31.7 ± 2.1 at.% for Mg and Ca, respectively. A small amount of Zn at about 0.4 at.% was also detected in this phase. The Mg-to-Ca ratio of ~2.1 suggests this phase to be indeed the Mg$_2$Ca phase and is thus in good agreement with the thermodynamic calculations (Figure 2.2,

66

([2]), which predicted Mg_2Ca as the predominant secondary phase for temperatures above 300 °C, before receding from about 410 °C.
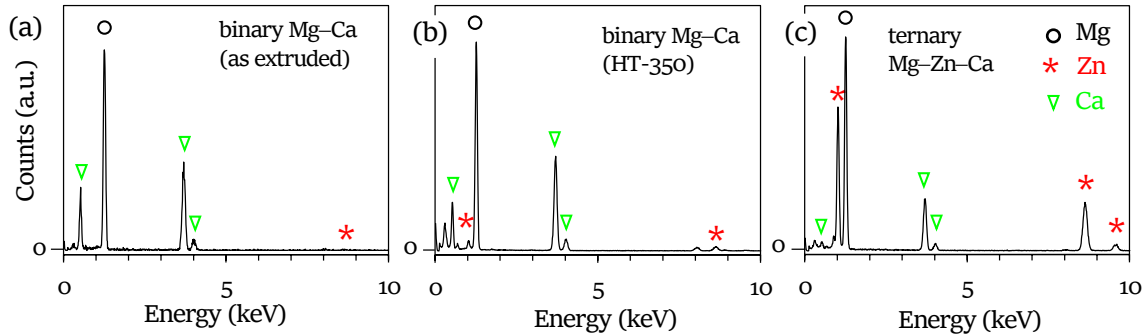

Figure 2.4: EDS spectra of the intermetallic phases in ZX10. (a) Binary phase contained in the as-extruded state; (b) binary phase in HT-350; (c) ternary phase in HT-250. The elements' label is given in (c).

In order to evaluate if the binary phase observed in the as-extruded condition is identical to the phase observed in the heat-treated condition at 350 °C (HT-350), the phase of the IMPs in the ZX10 alloy heat treated at 350 °C was additionally analyzed (Figure 2.4b). Note that the phase in the HT-350 condition is assumed to be the equilibrium phase while thermodynamic equilibrium cannot be assumed for the as-extruded state because of the significantly shorter exposure time to the extrusion temperature. Its composition was determined to be 65.4 ± 0.9 at.% for Mg and 32.5 ± 1.1 at.% for Ca, respectively, giving an Mg-to-Ca ratio of ~2.0, and thus again confirming the Mg_2Ca phase predicted by the calculations. The concentration of dissolved Zn was about 2.2 at.% and thus substantially higher compared to the binary phase in the as-extruded state.

Considering that in literature there is little if any ambiguity on the structure and composition of this phase [11-13], the EDS analysis presented here is assumed to be sufficient to conclude that the binary phase in ZX10 is Mg_2Ca, the solubility of which varies with temperature or size.

In contrast, the ternary phase structure is subject of a long-lasting debate in literature:

The first results on the Mg–Zn–Ca ternary system were presented in 1933 by Paris [14] who used 189 different alloys and identified one ternary compound, $Ca_2Mg_5Zn_5$, with a melting point of 495 °C. No crystallographic data was provided. In 1961, Clark [15] presented a 335 °C isothermal section of the Mg–Zn–Ca phase diagram using 76 key alloys. Using X-ray diffraction and metallography two ternary phases were observed, namely β ($Ca_2Mg_6Zn_3$) and ω ($Ca_2Mg_5Zn_{13}$), both of which differ from the one reported in [14]. Despite the fact that no structural data was provided, the two phases were incorporated to the Joint Committee on Powder Diffraction Standards (JCPDS) as Card 12-0266. In 2001, Larinova et al. [16] investigated several melt-spun Mg–Zn–Ca alloys at varying Zn and Ca

amounts (Zn at 1.25 – 4.25 at.%, Ca at 0.83 – 3.19 at.%) and concluded that the XRD reflections of a ternary phase matched $Ca_2Mg_6Zn_3$ based on the hexagonal structure of CaMgZn [17]. Around 2002, Jardim et al. [18, 19] studied the ternary phase in melt-spun Mg–Zn6–Ca1.5 (in wt.%). Even though its composition determined by EDS was close to $Ca_2Mg_4Zn_3$, the authors concluded that the phase was $Ca_2Mg_6Zn_3$ based on a selected area electron diffraction pattern (SADP) analysis in the TEM, and attributed the 20% difference in composition to the incertitude of the EDS analysis. They then related its structure to a compound of similar sized atoms and same stoichiometry, namely $Si_2Te_6Mn_3$, which has a trigonal structure and the space group $P\bar{3}1c$ [20]. Due to the good match between the simulated and experimental diffraction patterns they concluded that $Ca_2Mg_6Zn_3$ has the same structure and space group. Motivated by previous studies in which the reported crystal structure and the compositional range of the $Ca_2Mg_6Zn_3$ compound were contradictory, see e.g. Ref. [21], Zhang et al. [22] conducted a study in 2010 based on the diffusion-couple method. They concluded that the ternary compound has a compositional range of $Ca_3Mg_xZn_{15-x}$ ($4.6 \leq x \leq 12$) at 335 °C, and named it IM1 (for 'intermetallic compound'). The prototype chosen for their analysis was $Sc_3Ni_{11}Si_4$, which has a hexagonal structure with $P6_3/mmc$ (194) space group. Note that the $Ca_2Mg_6Zn_3$ compound is in terms of its stoichiometry approximately, but not accurately, incorporated in this compositional range. Finally. the structure was again challenged in 2016 by Cao et al. [23] who analyzed an alloy with a nominal composition close to $Mg_{58}Zn_{29}Ca_{12}$. The composition was chosen to lie in the $Ca_2Mg_5Zn_5$, $Ca_2Mg_6Zn_3$, and IM1 phase fields according to the respective Mg–Zn–Ca phase diagrams published by Paris [14], Clark [15] and Zhang [22]. Based on EDS and structural refinement using X-ray diffraction they concluded that the compound is $Ca_2Mg_5Zn_5$ with a hexagonal structure and $P6_3/mmc$ (194) space group.

In summary, for the ternary phase three candidate crystal structures were identified in the literature: (i) $Ca_2Mg_6Zn_3$ with a trigonal structure [18], (ii) $Ca_3Mg_{11}Zn_4$ with a hexagonal structure [22], and (iii) $Ca_2Mg_5Zn_5$ with a hexagonal structure [23]. A detailed description of these candidate crystal structures is outside the scope of this chapter, but the interested reader is directed to our related study, published as Schäublin et al. [24], in which we present an in-depth evaluation of the candidate structures for their match with experimentally obtained electron-diffraction patterns, ultra-high resolution STEM images and correlative STEM-EDS chemical maps.

Here, in order to identify the structure of the ternary phase in ZX10, EDS analysis combined with ultra-high resolution microscopy was performed. The analysis of the EDS spectrum (Figure 2.4b) gives an IMP composition of 61.2 ± 1.1 at.%, 22.6 ± 1.3 at.%, and 16.3 ± 0.2 at.% for Mg, Zn and Ca, respectively, which is equivalent to $Ca_3Mg_{11.4}Zn_{4.3}$.

Figure 2.5 shows ultra-high-resolution STEM-HAADF images obtained along two different zone axes, (a) $< \bar{1}2\bar{1}0]$ and (e) $< \bar{1}100]$, with corresponding atomic-resolution elemental EDS mapping for Mg (blue), Zn (red), and Ca (green) (b-d, f-h). With the above-mentioned candidate structures for the IM1 phase, and taking into account the composition of the precipitates determined by STEM-EDS as $Ca_3Mg_{11.3}Zn_{4.1}$, the prototype structure $Sc_3Ni_{11}Si_4$ with $P6_3/mmc$ symmetry as suggested by Zhang et al. [22] was considered. The atomic structural model of $Ca_3Mg_{11}Zn_4$ projected along the $< \bar{1}2\bar{1}0]$ and $< \bar{1}100]$ directions is overlaid on the STEM-HAADF images in Figure 2.5e, respectively, showing an excellent match.

The good visual match for both zone axes between the projection of the proposed simulated structure and the experimental image – with respect to (i) the atomic positions, (ii) the nominal phase composition, and (iii) the allocation of elements – suggests that the ternary phase in ZX10 is indeed the denominated IM1 phase, with a composition at the upper end of Mg (with $x = 11$) for the range proposed for this phase, i.e. $Ca_3Mg_xZn_{15-x}$ ($4.6 \leq x \leq 12$) [22].
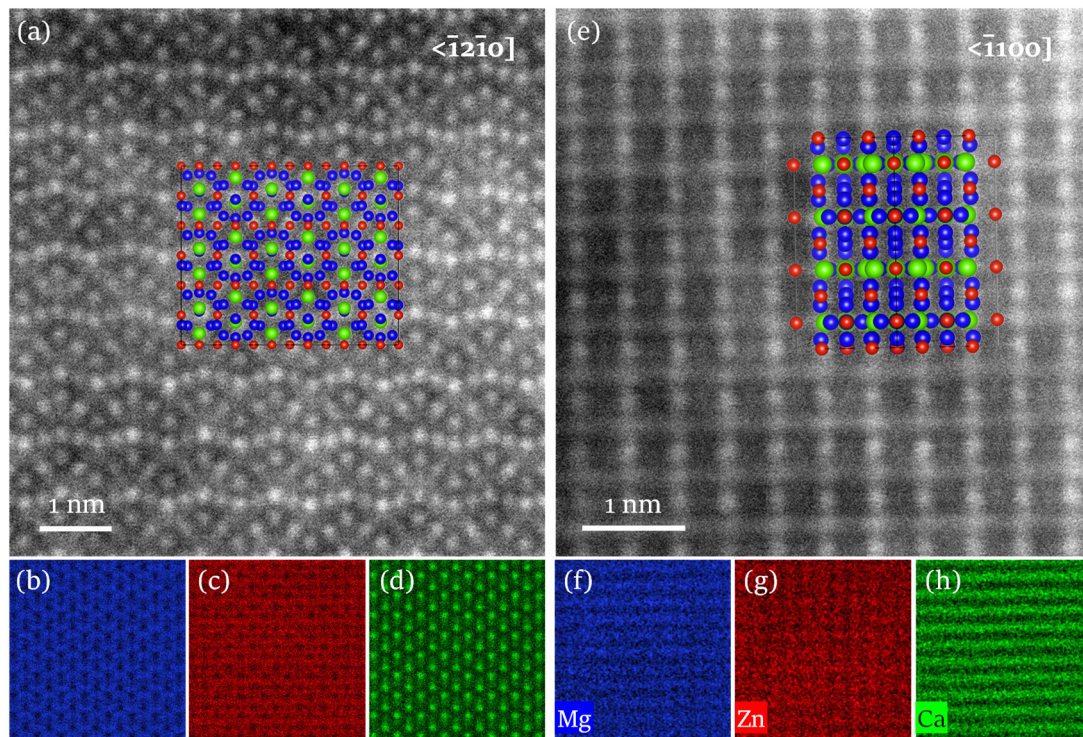
Figure 2.5: (a, e) Ultra-high resolution HAADF STEM images and (b-d, f-h) corresponding EDS chemical maps of the ternary intermetallic phase in ZX10 heat treated at 250 °C. The superimposed lattice structure in the STEM images corresponds to $Ca_3Mg_{11}Zn_4$. The structure matches the STEM images as well as the chemical maps. The crystal orientations are (a-d) $< \bar{1}2\bar{1}0]$ and (e-h) $< \bar{1}100]$. The color code is indicated in (f-h).

It should be noted that the identified phase is *not* in line with the thermodynamic calculations, which predicts the ternary phase to be $Ca_2Mg_6Zn_3$ according to Jardim et al. [4, 19]. The present

results should thus give an impetus for refining the input parameters of the thermodynamic calculations in the MatCalc database [4], by considering $Ca_3Mg_{11}Zn_4$ instead of $Ca_2Mg_6Zn_3$ as the equilibrium ternary phase.

Based on the detailed microstructural information obtained, three thermomechanical conditions were selected to study the influence of microstructure on the corrosion behavior:

- *As-extruded state*: contains only binary-type IMPs at a small grain size.
- *Heat-treated at 250 ℃* (HT-250): contains only ternary-type IMPs, which are coarsened; matrix grain size comparable to that of the as-extruded state.
- *Heat-treated at 350 ℃* (HT-350): contains only binary-type IMPs, which are coarsened (and comparable to HT-250); matrix grain size is also coarsened and thus significantly larger than that of the as-extruded state.

In the following, a more detailed description of the ZX10 microstructure with the elemental spatial distribution of Zn and Ca characteristic to these thermomechanical conditions is presented in greater detail, setting the basis for a detailed understanding of the microstructure–corrosion-susceptibility correlations. Then, the samples' early local corrosion events in relation to their IMPs are scrutinized, applying a quasi-*in situ* protocol. Lastly the role of IMPs on the macroscopic corrosion behavior is documented.

2.3.3   *Elemental distribution*

Figure 2.6 shows STEM-HAADF images (Figure 2.6a, c and e) along with corresponding STEM-EDS chemical maps for Zn and Ca (Figure 2.6b, d and f) for the three selected thermomechanical conditions in their pristine state, i.e. before corrosion attack. In this image mode the grain structure is visible together with the size, shape and spatial distribution of the IMPs, which are apparent in brighter *Z*-contrast owing to the presence of elements heavier than Mg. They relate, as mentioned before, to either the binary Mg_2Ca phase in the as-extruded (Figure 2.6b) and HT-350 (Figure 2.6f) states, or the ternary IM1 phase in the HT-250 state (Figure 2.6d).

In addition, the spatial distribution of the IMPs relative to the grain structure is apparent: in the as-extruded state (Figure 2.6a), the IMPs are homogeneously distributed within the grains and at the grain boundaries. The particles have an average size of about 80 nm and a roughly globular morphology. Upon extended heat treatment at 250 ℃ (Figure 2.6c), not only are the IM1-type IMPs significantly coarsened, with an average size of about 50 – 200 nm, but they are mainly located at the grain boundaries with hardly any IMPs remaining within the grains. Their morphology appears to follow the grain boundaries, often with an elongated shape along the boundaries between two

grains and a triangular shape at triple junctions. Upon heat treatment at 350 °C (Figure 2.6e), the binary Mg$_2$Ca-type IMPs coarsen and reach an average particle size of about 180 nm, with a large distribution ranging from 50 nm to 500 nm. They are present within the grains and at the grain boundaries. The grain size for this thermomechanical condition is clearly larger compared to the other conditions.
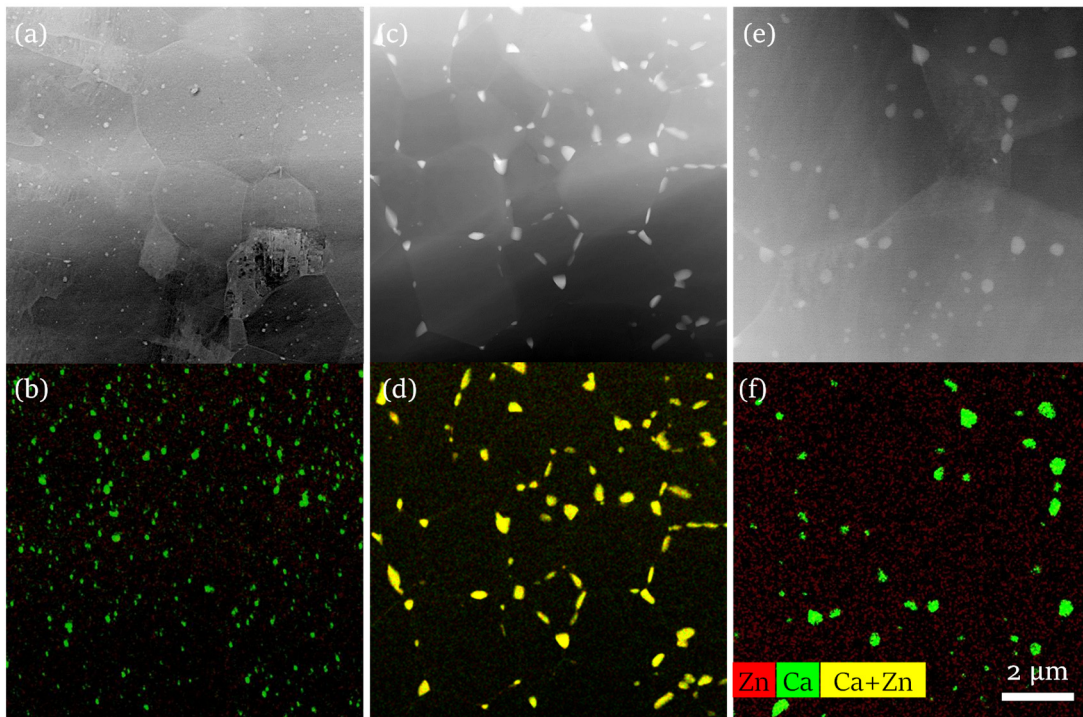
Figure 2.6: ZX10 microstructure in three selected thermomechanical conditions: (a-b) as-extruded state, (c-d) HT-250 condition, and (e-f) HT-350 condition. (a,c,e) STEM-HAADF images and (b,d,f) corresponding STEM-EDS chemical maps for Zn and Ca. The scale bar and elemental color code are indicated in (f). Note that the yellow color in (d) is a result of the superimposed Zn- (red) and Ca- (green) elemental map.

Figure 2.7 shows magnified STEM-EDS maps superimposed for Zn and Ca for the three selected thermomechanical conditions, revealing the respective IMPs and grain boundaries. Representative quantitative line profiles for Zn and Ca obtained across grain boundaries are additionally shown in these maps. Segregation of Zn and Ca at the grain boundaries is detected in all cases, with the concentration of Zn exceeding that of Ca. However, in relative terms, compared to their concentration in the Mg matrix, the accumulation of Zn at the grain boundaries is lower than that of Ca, especially for the thermomechanical conditions which contain the binary-type IMP (i.e., as-extruded state, Figure 2.7a and HT-350 condition, Figure 2.7c).

The elemental contents of Mg, Zn and Ca in the IMPs and the matrix are summarized in Table 2.4 for the three selected thermomechanical treatments.

Figure 2.7: Magnified STEM-EDS maps of (a) as-extruded ZX10, (b) HT-250, and (c) HT-350, revealing IMPs and grain-boundary elemental segregat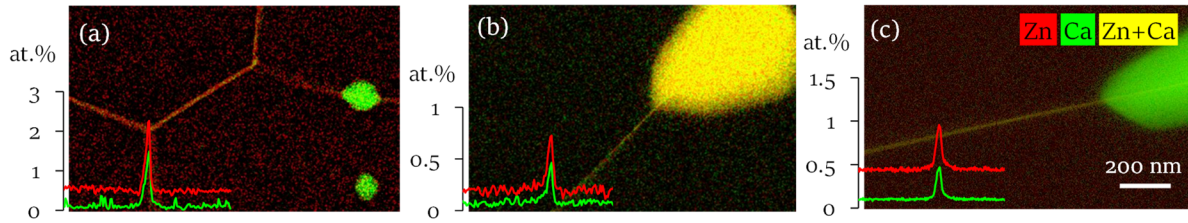ion. Line composition profiles for Zn (red) and Ca (green) are taken across grain boundaries. The color code and scale bar are indicated in (c).

Table 2.4: Thermomechanical process parameters of ZX10 in the three thermomechanical conditions investigated and the composition of the respective intermetallic particles and matrix, obtained by STEM-EDS.

Condition	Processing temperature (°C)	Time of heat treatment (h)	Type of primary IMP	Elemental concentration in at.%					
				IMP			Matrix		
				Mg	Zn	Ca	Mg	Zn	Ca
As extruded	300	–	$(Mg,Zn)_2Ca$	68.0 ± 2.1	0.4 ± 0.1	31.7 ± 2.1	Bal.	0.54	0.14
HT-250	250	366	Ternary IM1	61.2 ± 1.1	22.6 ± 1.3	16.3 ± 0.2	Bal.	0.18	0.02
HT-350	350	3	$(Mg,Zn)_2Ca$	65.4 ± 0.9	2.2 ±0.5	32.5 ±1.1	Bal.	0.39	0.06

2.3.4 Early-stage corrosion events

Figure 2.8 shows in planar view the samples in the three selected thermomechanical conditions and presents the identical area in the pristine state (Figure 2.8a-c) and after corrosive attack induced by SBF immersion for 5 s (Figure 2.8d-i). A detailed view of the post-corrosion state is provided in the high-magnification HAADF images with corresponding elemental maps for oxygen in Figure 2.9.

ZX10 in the *as-extruded* state shows at lower magnification a largely homogeneous corrosion attack, expressed in the STEM-HAADF image (Figure 2.8d) as a homogeneous surface roughening and in the STEM-EDS chemical map as a homogeneous distribution of oxygen (Figure 2.8e). A closer look, however, reveals the presence of distinct cavities (insets to Figure 2.8d marked by arrows in the main figure) which have a size comparable to the IMPs characteristic of this thermomechanical condition (Figure 2.6a-b). The direct comparison to the pristine microstructure (Figure 2.8a) allows to deduce that the cavities are indeed the sites of former IMPs (see arrows). Their preferential dissolution occurred thus rapidly, i.e. within only 5 s of immersion time. It seems worth
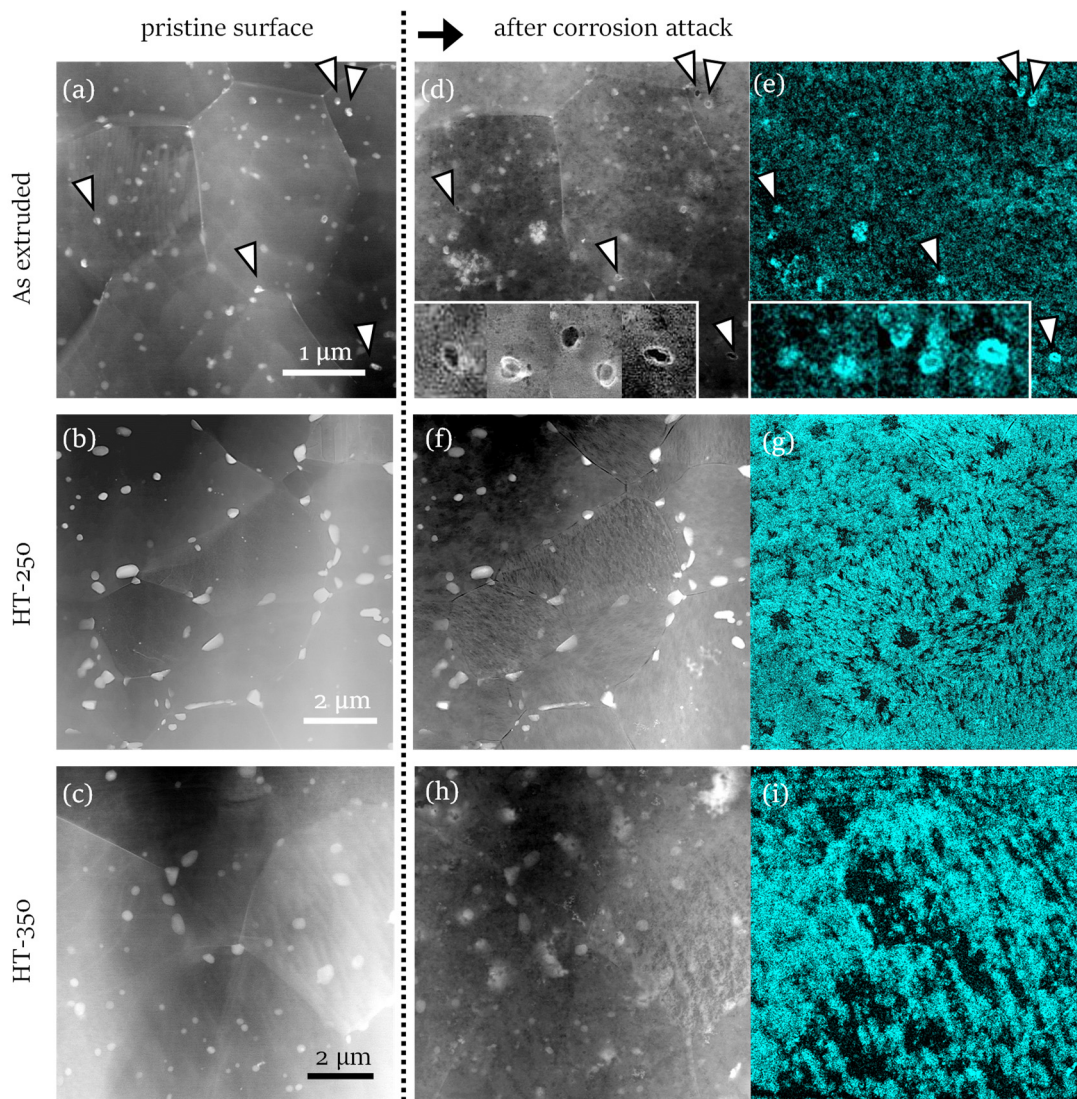
Figure 2.8: Quasi-*in situ SABACO* experiment on ZX10 alloy. (a-c, d,f,h) STEM-HAADF images of the same area (a,b,c) before and (d - i) after corrosion attack in SBF for 5 s for the (a,d,e) as-extruded, (b,f,g) HT-250, and (c,h,i) HT-350 condition. (e,g,i) Corresponding chemical maps for oxygen after corrosion attack. Insets to (d,e): magnified view on the sides of prior IMPs (marked by white arrow heads). The respective scale bar for each condition is shown in the HAADF images (a-c).

emphasizing that not all IMPs visible in the HAADF image were affected but only those exposed at the free surfaces of the TEM sample. This underlines the importance of stereographic imaging as part of the *SABACO* protocol, which allows identifying those IMPs that are emerging at the surfaces. The results clearly demonstrate the anodic nature of the Mg_2Ca-type IMPs and show that, due to their rapid dissolution, the Mg matrix is exposed to a largely uniform corrosion attack virtually unaffected by the presence of the IMPs. This demonstrates a clear advantage of the ZX10 alloy in this

thermomechanical state over related alloys with greater volume fractions of this anodic intermetallic phase, for which the incongruent dissolution leads to a laterally heterogeneous corrosion front [25].
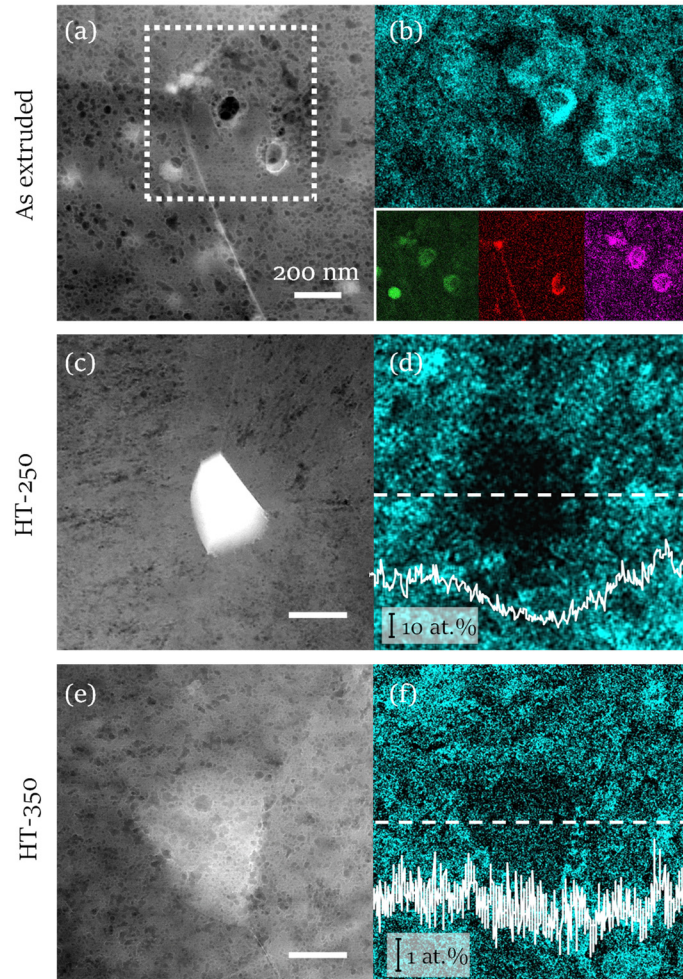
Figure 2.9: High-resolution imaging of intermetallic particles in ZX10, respectively their remnants, after corrosion attack. (a,c,e) STEM-HAADF and (b,d,f) corresponding STEM-EDS chemical maps for oxygen of individual intermetallic particles after corrosion attack for (a-b) as-extruded, (c-d) HT-250, and (e-f) HT-350 conditions. The inset to (b) also shows the chemical maps for (left to right) Ca (green), Zn (red) and P (magenta). The scale bar corresponds to 200 nm. The line profiles in (d) and (f) give the quantified oxygen concentration across the respective particle, taken along the dashed white line.

The STEM-EDS map for oxygen (Figure 2.8e) reveals an enhanced oxygen signal at the edges around the cavities formed by the dissolved IMPs. Ca and P appear to be also enriched at the same locations (inset to Figure 2.9b and Figure 2.8d), indicating that a calcium-phosphate compound had formed. Calcium phosphates are indeed known to precipitate from solutions of biological fluids onto the surface of Mg substrates [26, 27], and are observed to spread across the entire Mg substrate for longer immersion [28] (see also Chapter 3) or implantation times [26]. The precipitation of this Ca–

P–O-rich compound is assumed to be facilitated by the combination of a locally enhanced Ca availability, provided by the dissolved Ca-rich precipitates, and the locally elevated pH value, resulting from the cathodic reaction occurring around the dissolving precipitates (Eq. 1.2 in section 1.1.6). The local analysis at short immersion times of the SABACO experiment thus reveals that the IMPs act as nucleation sites for the precipitation of this compound.

Interestingly, not all IMPs dissolved entirely, but occasionally a shell-shaped remnant remained, which appears in brighter contrast in the HAADF images (Figure 2.8d and Figure 2.9a), thus indicating the presence of heavier elements. STEM-EDS revealed that the shell is rich in Zn (see Zn map in Figure 2.9b). It is assumed that the local Zn accumulation results from electrochemical redeposition [29, 30], a phenomenon further discussed in Chapter 4. Further investigation is required to understand the decisive mechanisms that lead to either the complete dissolution of the Mg_2Ca particles or the (subsequent) formation of Zn-rich redeposits at or around their former location upon dissolution.

The *HT-250* sample (Figure 2.8b, f and g) containing the ternary IM1-phase IMPs shows likewise a distinct correlation of the underlying microstructure with the corrosion attack: at the sites of IMPs exposed at the surface, no or a drastically reduced oxygen signal is detected compared to the adjacent Mg matrix (Figure 2.8g). This is best visible from the quantified line scan for oxygen taken across an IMP (Figure 2.9d). Moreover, the magnified imaging presented in Figure 2.9c and d reveals that indeed the vicinity of the IMPs and not the IMPs themselves are attacked, as indicated by surface roughening of the matrix whereas the surface of the IMP remained smooth. This observation supports the assumption that the IM1-phase precipitates function as local cathodes. Their detailed dissolution behavior is further discussed in Chapter 3.

The *HT-350* sample, which hosts the binary-type IMPs at a size comparable to those in the HT-250 sample, shows a generally homogeneous corrosion attack across both the matrix and IMPs (Figure 2.8h and i). In fact, no correlation with the underlying pristine microstructure (Figure 2.8c) can be derived, neither from the HAADF contrast nor the oxygen map. At higher magnification (Figure 2.9f) a trend towards slightly reduced oxidation rate of the IMP compared to the matrix is observed, though the difference is minor. In fact, a quantified line scan across the precipitate (Figure 2.9f) shows that the oxygen distribution on the surface of the HT-350 sample is largely homogeneous without any significant depletion at the IMP's location. The morphology of both the IMPs and the matrix, presented in the HAADF image of Figure 2.9e, appears spongy and comparable for both locations. The observation of similar corrosion resistance of IMP and matrix is at first surprising considering that the IMPs are composed of the same intermetallic phase as those contained in the as-extruded ZX alloy, namely Mg_2Ca, which were shown to dissolve rapidly and preferentially.

A possible explanation is found in the slightly greater Zn content of the IMPs in the HT-350 condition compared to that of the as-extruded state (Table 2.4). Zn is expected to elevate the overall electrochemical potential of the otherwise anodic Mg_2Ca phase, possibly sufficiently high to reach a level that is comparable to that of the Mg matrix. This assumption is supported by observations of Cha et al. [25], who illustrated in a study on a single-crystal Mg_2Ca phase that its open-circuit potential can be tailored by Zn addition to closer match that of pure Mg. They also showed that by choosing a sufficiently high Zn concentration a similar oxidation susceptibility of the $(Mg,Zn)_2Ca$ phase and Mg matrix can be achieved in a two-phase alloy, resulting in a significant improvement of the homogeneity of corrosion attack.

However, besides the slight chemical variations of the Mg_2Ca phase between the HT-350 and as-extruded condition, it should be also kept in mind that the size of their IMPs differed (Figure 2.6 and Table 2.3). The coarsened IMPs in the HT-350 samples result locally in a modified anode-to-cathode area ratio and in a larger spacing between the IMPs due to their reduced number density. Both parameters are known to critically influence the efficiency of micro-galvanic coupling [31, 32] and may thus contribute to the greater corrosion resistance of the Mg_2Ca phase observed for the HT-350 condition compared to that in the as-extruded state. However, at this stage of the present study, it is not possible to conclude on whether it is the number density and spacing or the chemical variations that predominantly influences the electrochemical behavior of the IMPs. An investigation which allows to decouple these parameters would be required to answer this question.

Figure 2.10 presents micrographs and chemical maps of attacked ZX10 with a focus on the grain boundaries. The figure shows apparent preferential dissolution along the grain boundaries after immersion for 5 s. In this figure, samples from the HT-250 condition are exemplarily shown, but the grain-boundary attack occurred for all samples of all conditions to a comparable degree, irrespective of their thermomechanical history. In some cases, the locally accelerated corrosion attack even caused entire grain fall-out from the TEM thin-foil (not shown). However, while at lower magnification (Figure 2.10a) the attack appears as grain-boundary etching, i.e. via intergranular corrosion, higher-magnification HAADF images (Figure 2.10c) and corresponding STEM-EDS chemical mapping (Figure 2.10d-f) show clearly that it is not the grain boundaries but the matrix in their direct vicinity that experienced accelerated dissolution. The grain boundaries, in contrast, remained unaffected and were exposed as thin walls, as evident in the inset to Figure 2.10c, which shows the grain boundary as a line with a width of a few nanometers. The chemical maps for Ca and Zn in Figure 2.10e and f, respectively, confirm the integrity of the grain boundaries, which in this chapter refer to an extended volume that also comprises the segregated region along them.

The observation of near-grain boundary etching is explained by the grain-boundary chemistry (Figure 2.7). The greater concentration of Zn detected compared to Ca at the grain boundaries renders them more noble than the surrounding Mg matrix. On this ground, the grain boundaries are expected to act as local cathodes, thus accelerating the matrix dissolution in their vicinity via micro-galvanic coupling.
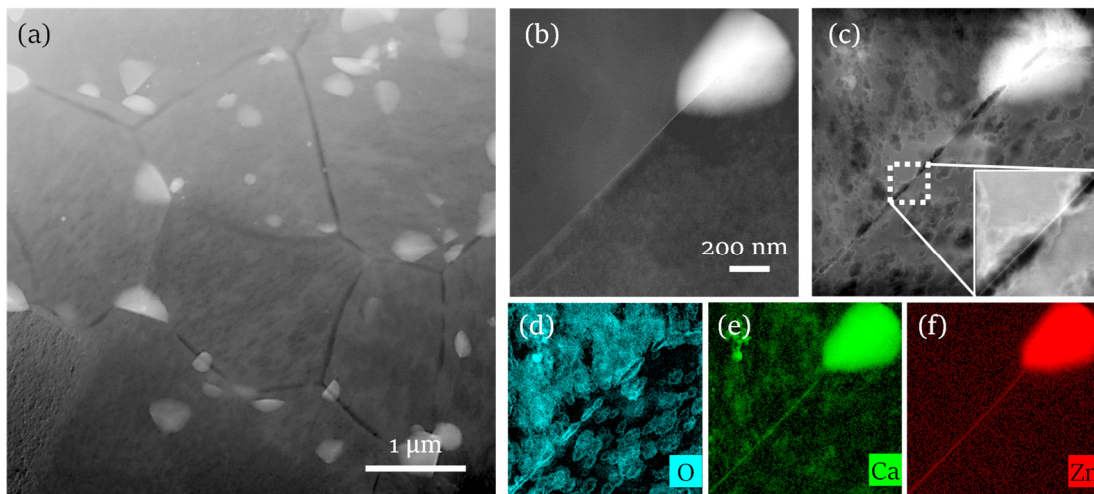

Figure 2.10: Preferential dissolution of the matrix at the direct vicinity of grain boundaries. (a) Overview HAADF image after corrosion attack. (b, c) HAADF images of a grain boundary (b) before and (c) after corrosion attack. (d-f) Corresponding STEM-EDS chemical maps after corrosion attack for (d) oxygen, (e) calcium, and (f) zinc.

Only a few studies have addressed this form of localized corrosion attack in Mg alloys [33-35] because other types of corrosion such as general, galvanic and micro-galvanic, or stress corrosion have been identified to have a significantly higher impact on these materials. Even more so, the common assumption is that 'Magnesium and magnesium alloys are virtually immune to intercrystalline attack', as stated by Song and Atrens in 1999 in their highly cited review paper [36]. The immunity is attributed to the low nobility of Mg which entails cathodic sites for segregated areas or secondary-phase precipitation at grain boundaries composed of almost all elements. This comes indeed with only few exceptions, such as segregation or precipitation of particles composed of Ca or Li, which are less noble than Mg [37, 38]. The results presented here show that while intercrystalline corrosion *sensu stricto* is indeed not a concern for ZX-lean alloys, the segregation of Zn and Ca causes preferential near-grain boundary dissolution, which results in local trenching to both sides of the nm-thin grain-boundary regions (Figure 2.10). It must be considered that the trenching may eventually cause mesoscopic mechanical disintegrity that can develop into corrosion fatigue as known for intercrystalline corrosion [39, 40]. Further studies should thus aim at understanding the impact

of near-grain boundary attack, starting with investigating how far into the material's bulk the trenching can proceed to answer if entire grains can be undercut and finally fall out.

2.3.5 Electrochemical response

The local analysis of the corrosion events has revealed a distinct difference between the two types of IMPs in ZX10. The question therefore arises how the IMP type affects the macroscopic corrosion behavior of these alloys and specifically their degradation rate.
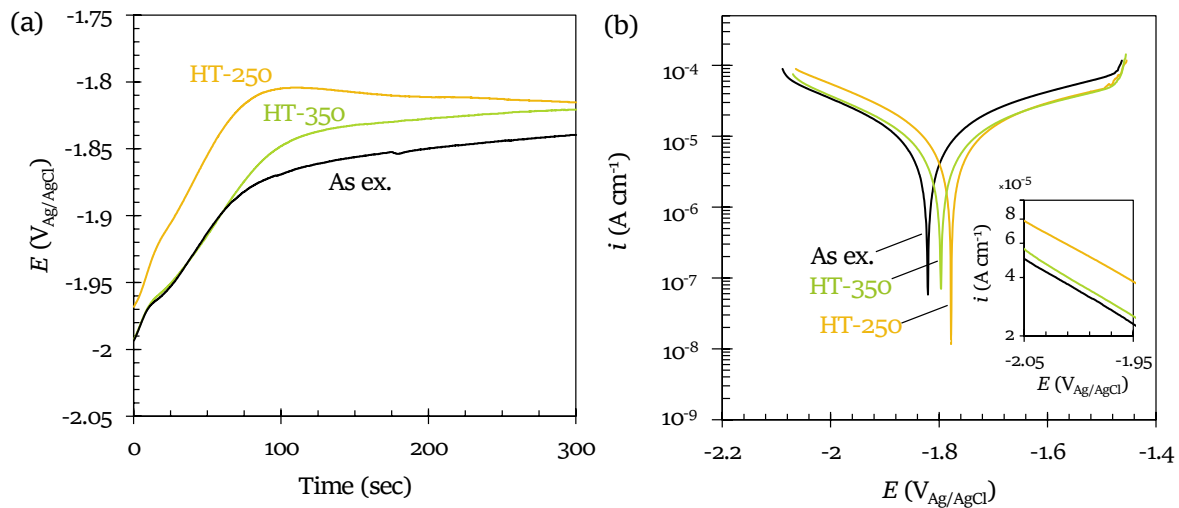
Figure 2.11: Electrochemical response of ZX10 for the conditions investigated, studied under simulated body conditions: (a) open circuit potential over time, and (b) polarization curves under potentiodynamic conditions. The inset in (b) shows a magnified view of the cathodic branch.

Figure 2.11 shows the electrochemical response of ZX10 for the selected thermomechanical conditions upon their immersion in SBF. The electrode surface was 1 cm^2, which implies, considering the grain size and the IMPs' size, that the signal measured corresponds to the integrated signal of a number of local anodes and local cathodes on the surface. The open circuit potential (E_{OCP}) (Figure 2.11a) increased rapidly for all sample conditions and stabilized after 300 s at -1.84 ± 0.01, -1.81 ± 0.01 and -1.82 ± 0.00 V$_{Ag/AgCl}$ for the as-extruded, HT-250 and HT-350 sample, respectively. Interestingly, despite an about equal potential at the start of immersion for the as-extruded and HT-350 sample, the latter polarized slightly more and stabilized at a more positive E_{OCP}, almost approaching the value for E_{OCP} of the HT-250 sample.

The subsequent polarization (Figure 2.11b) yielded a corrosion potential E_{corr} at -1.82 ± 0.00, -1.77 ± 0.01 and -1.79 ± 0.01 V$_{Ag/AgCl}$ for the as-extruded, HT-250 and HT-350 sample, respectively. The inset to Figure 2.11b provides a close-up of the cathodic branch and reveals a slightly increasing cathodic current density in the order of *as extruded* < HT-350 < HT-250. The increasing cathodic

activity is assumed to be responsible for the E_{corr} shift towards higher potentials, which is observed to follow the same order. Taking into account the microstructural information obtained for these specimens, it can thus be assumed that the ternary-type IMPs, contained in the HT-250 samples, impose an increased cathodic activity on the ZX10 alloy. The lower E_{corr} value for the as-extruded state, on the other hand, follows the observation described above, namely that the binary-type IMPs dissolve rapidly as local anodes. Lastly, the E_{corr} value of the HT-350 samples lies in between those of the other two conditions, indicating that the Mg_2Ca phase at larger size and slightly higher Zn content possesses some cathodic activity. This supports the observation made in the analysis of the early-stage corrosion events (Figure 2.9) that showed a slightly reduced oxygen coverage on the surfaces of the IMPs compared to those of the Mg matrix.

In order to evaluate the macroscopic corrosion rate, the corrosion current density (i_{corr}) was determined and revealed values of 11.98 ± 0.51, 10.32 ± 1.53 and 9.58 ± 1.01 µA cm^{-2} for the as-extruded, HT-250 and HT-350 sample, respectively. Considering the intra-sample variations, no significant differences between the samples can be identified. It may thus be assumed that the IMPs do not influence the corrosion rate at a macroscopic scale. Drawing such a conclusion, however, may be premature due to the methodological limitations. In fact, the determination of i_{corr} may not allow for a reliable estimate of the corrosion rate, as discussed in section '*Methods to study Mg corrosion*' in Chapter 1. Moreover, for all electrochemical measurements it needs to be kept in mind, that the short measuring time (typically on the order of minutes to ≤ 1 h immersion) may not be representatively reflecting the corrosion rates establishing for prolonged immersion or implantation times.

All electrochemical parameters obtained are summarized in Table 2.5.

Table 2.5: Electrochemical parameters of ZX10 obtained from open-circuit and polarization measurements under simulated body conditions.

	$E_{\text{OCP,300}}$ (V$_{\text{Ag/AgCl}}$)	E_{corr} (V$_{\text{Ag/AgCl}}$)	i_{corr} (µA cm^{-2})
As extruded	-1.84 ± 0.01	-1.82 ± 0.00	11.98 ± 0.51
HT-250	-1.81 ± 0.01	-1.77 ± 0.01	10.32 ± 1.53
HT-350	-1.82 ± 0.00	-1.79 ± 0.01	9.58 ± 1.01

For that reason, a complementary immersion study was performed to probe the corrosion behavior of ZX10 at longer immersion times and is presented in the following.

2.3.6 Cross-sectional analysis of the corrosion-product layer

The hydrogen-evolution method [41] is one of the common methods for the investigation of the macroscopic degradation rate of Mg-based materials [42]. Here it was applied on the three selected alloy conditions (not shown), but it could not yield conclusive results in terms of their characteristic degradation rate related to the IMP type. The hydrogen-evolution method, while appreciated for the ease of its protocol, is known to be prone to experimental artefacts caused by environmental pressure variations, fluctuating gas solubility in the electrolyte, or difficulties in capturing the gas in the electrolytes that are subjected to turbulent flow. In fact, artefacts were reported to especially occur for short immersion times and slow-degrading materials [42]. While special care was taken to account for environmental factors, the low gas volume liberated for the slowly-degrading ZX10 alloy may indeed have limited the reliability of this method.

For that reason an immersion study at prolonged immersion time was performed as an alternative method, aiming at determining the corrosion depth, which provides a direct measure of the degradation rate. To that end, part of the sample surface was covered with a water-impermeable varnish to protect it from corrosion attack. A cross-section view prepared across the boundary between the area protected from and the one affected by the corrosion attack then provides information about the depth of dissolution. Figure 2.12 shows SEM-BSE images of such cross sections for the three tested sample conditions. In these images, the corrosion-product layer appears in darker contrast, indicating the presence of lighter elements or of a lower density compared to the metallic substrate. Interestingly, the interface between the corrosion-product layer and the electrolyte is at the same height as the original surface of the metallic sample, or in other words, the corrosion-product layer occupies fairly accurately the same volume as the dissolved metallic substrate. This preservation of the Mg's original volume – while the metal is gradually replaced by the poorly soluble $Mg(OH)_2$ and a Ca–P–O-rich compound – is in line with previously reported observations *in vitro* and *in vivo* [43, 44]. This seems surprising when considering that the main corrosion product is porous $Mg(OH)_2$ (Eq. 1.4, and Figure 3.4 and Figure 3.5b in Chapter 3), which should occupy a much larger volume than the original metallic Mg. It demonstrates, however, that a good fraction of dissolving Mg ions is released into the electrolyte rather than being consumed for the formation of the corrosion-product layer. This agrees with observations made in various studies that monitored changes in the electrolyte's Mg concentration to deduce the material dissolution [45-47].

In terms of the depths of the corrosion attack, values of $26 \pm 3\,\mu m$, $27 \pm 5\,\mu m$ and $28 \pm 4\,\mu m$ were determined for the as-extruded, HT-250 and HT-350 sample, respectively. Considering the intra-sample variation, no significant difference between the sample conditions could thus be identified.
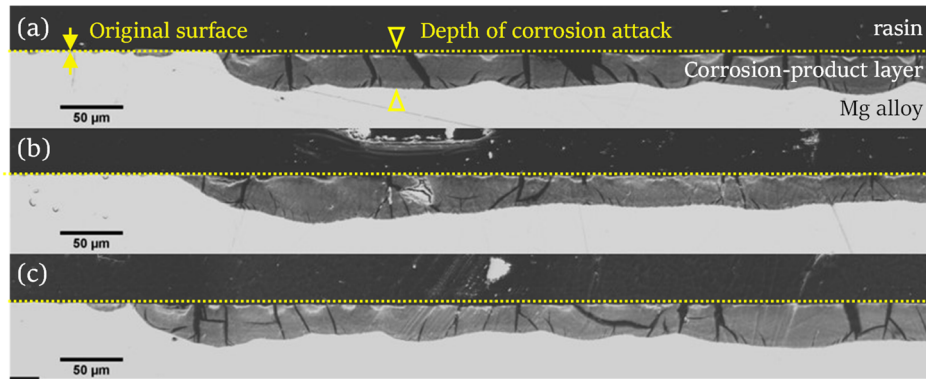
Figure 2.12: Cross-sectional BSE-SEM images of the corroded Mg alloy ZX10 in (a) as-extruded condition and (b,c) following heat treatments at (b) 250 °C and (c) 350 °C. The dotted yellow line marks the original surface. The yellow arrow heads illustrate the depth of corrosion attack. For all conditions the cross sections reveal an inward-growing corrosion front and preservation of the original surface level. No significant difference in the depth of corrosion attack is detected between the samples.

2.3.7   *Evaluation of the study hypothesis*

As the outset of this study it was hypothesized that (i) the IMP type can be tailored by specific heat treatments, which in turn (ii) can govern the rate of material dissolution.

As for (i), the detailed microstructural analysis showed that indeed the primary intermetallic phase in the ZX alloy can be switched completely from the binary Mg_2Ca phase in the as-extruded condition to the ternary IM1 phase via heat treatment at 250 °C.

As for (ii), based on the compiled data presented here, comprising electrochemical investigation and immersion studies, it needs to be concluded that the heat-treatment-induced characteristic microstructures do *not* result in significantly different macroscopic corrosion rates although a difference locally at the nanometer level has been observed. The absence of the hypothesized correlation indicates that the IMPs' size or the difference of their chemistry and concomitant electrochemical potential are sub-critical as to impact the macroscopic corrosion behavior. However, it is important to realize that the characteristic microstructures resulting from the heat treatments differ not only in their IMP type, but also in their IMP size and number density and their grain size (Figure 2.2, Table 2.3). The coarsening of IMPs alters the spacing between them as well as the anode–to–cathode area ratio. Both parameters are known to critically influence the efficiency of micro-galvanic coupling [31, 32]. The grain size is also thought to influence the corrosion resistance of Mg alloys [48]. While improved corrosion resistance for fine-grained Mg has been observed for most alloys [48, 49] – attributed to superior protection via the forming corrosion-product layer [50] – for some materials there is an ambiguity about it as they show an inverse correlation [51]. As for ZX

alloys, Lu et al. [52] observed for an Mg–Zn3–Ca0.3 alloy (in wt.%) that the corrosion rate increases with increasing grain size.

It was further observed in this study that the composition of the IMPs varies with their size, concomitant with a higher heat-treatment temperature: the larger IMPs (HT-350 condition) contained a substantially greater amount of Zn compared to their fine counterparts (as-extruded condition) (Table 2.4).

To sum up, despite the aforementioned limitations to study *macroscopic* properties, the presented materials allowed to investigate the local phenomena related to the IMPs' dissolution behavior in ZX alloys. The results presented here demonstrate on the nanoscale that binary-type Mg_2Ca IMPs with minor Zn content dissolve rapidly and preferentially to the Mg matrix (Figure 2.9a-b), while the same intermetallic type at a larger size and with a slightly higher Zn content dissolves at a similar rate as the Mg matrix (Figure 2.9e-f). Opposed to that, the ternary-type IM1 phase IMPs seem protected from dissolution while the Mg matrix surrounding them oxidizes preferentially (Figure 2.9c-d). The detailed dissolution of the IM1 phase will be addressed in greater detail in Chapter 3.

At the macroscopic level, the initial hypothesis on the tailoring of the corrosion rate based on an engineered microstructure can at this point neither be rejected nor confirmed. In fact, the presented approach of applying heat treatments to tailor the microstructure, although commonly used to study the impact of microstructure on the macroscopic corrosion behavior [32, 51, 52], induces simultaneous multi-parameter changes on the microstructure and thus appears to not provide a good model material for extracting information on the specific role that sub-micrometer sized IMPs play in the macroscopic corrosion processes. In fact, suitable model materials should differ in their IMP type only, while the other microstructural parameters should be kept constant.

2.4 Conclusions

In this chapter the microstructure of ZX10 was investigated in its as-extruded and heat-treated states to experimentally determine the main intermetallic phases in light of the predictions presented by thermodynamic calculations. A selection of specimens with heat-treatment-induced tailored microstructures was used to study the role of intermetallic-particle type – binary Mg_2Ca vs. ternary IM1 phase – in the early-stage biocorrosion processes. The main conclusions drawn are as follows:

- The ZX10 alloy in its as-extruded state ($T_{extrusion}$ = 300 °C) hosts nanometric IMPs exclusively made of the binary Mg_2Ca phase.

- Prolonged heat-treatment at 250 °C switches the IMP type completely to a ternary Mg–Zn–Ca-rich phase.

- The ternary phase was experimentally determined to have a $Ca_3Mg_{11}Zn_4$ structure, which opposes the structure of $Ca_2Mg_6Zn_3$ proposed by thermodynamic calculations, and thus urges to refine the data base at the basis of the calculations.

- Local quasi-*in situ* TEM analysis showed that the IMPs made of the binary Mg_2Ca phase rapidly dissolve within a few seconds of immersion when its Zn content is minor (0.4 at.%) and the anode-to-cathode area ratio is minute.

- The binary phase contained in ZX10 following heat treatment at 350 °C dissolves at a similar rate as the Mg matrix, presumably owing to its slightly elevated Zn content at 2.2 at.% and/or their coarsened size.

- IMPs composed of the ternary phase act as cathodic spots.

- Cross-sectional SEM analysis revealed that the type of IMPs, despite their distinct difference in local dissolution behavior, does not evoke a difference in the corrosion-product layer thickness, indicating that they do not induce a differing macroscopic corrosion rate.

- The coarsening of both IMPs and grain size upon excessive heat exposure appears to be responsible for the non-conclusive macroscopic corrosion behavior. Suitable model materials to study the role of IMP type in the corrosion processes of ZX10 alloys should only differ in their IMP type while other microstructural features that influence the corrosion processes should remain constant.

2.5 Acknowledgements

2.6 References

[1]   J. Hofstetter, M. Becker, E. Martinelli, A.M. Weinberg, B. Mingler, H. Kilian, S. Pogatscher, P.J. Uggowitzer, J.F. Löffler, High-strength low-alloy (HSLA) Mg–Zn–Ca alloys with excellent biodegradation performance, JOM 66(4) (2014) 566-572.

[2]   J. Hofstetter, S. Rüedi, I. Baumgartner, H. Kilian, B. Mingler, E. Povoden-Karadeniz, S. Pogatscher, P.J. Uggowitzer, J.F. Löffler, Processing and microstructure–property relations of high-strength low-alloy (HSLA) Mg–Zn–Ca alloys, Acta Materialia 98 (2015) 423-432.

[3]   CompuTherm LLC, Pandat software package for calculating phase diagrams and thermodynamic properties of multi- component alloys, Madison, USA, www.computherm.com.).

[4]   MatCalc software package for computer simulation of phase transformation and microstructure evolution in metallic systems, Vienna, Austria, www.matcalc-engineering.com.

[5]   J.F. Löffler, P.J. Uggowitzer, C. Wegmann, M. Becker, H.K. Feichtinger, Process and apparatus for vacuum distillation of high-purity magnesium. European Patent Application PCT, EP 2013/000131–WO2013/1076442012, 2012.

[6]   B.-C. Zhou, S.-L. Shang, Y. Wang, Z.-K. Liu, Diffusion coefficients of alloying elements in dilute Mg alloys: A comprehensive first-principles study, Acta Materialia 103 (2016) 573-586.

[7]   S.K. Das, Y.-M. Kim, T.K. Ha, I.-H. Jung, Investigation of anisotropic diffusion behavior of Zn in hcp Mg and interdiffusion coefficients of intermediate phases in the Mg–Zn system, Calphad 42 (2013) 51-58.

[8]   K. Momma, F. Izumi, VESTA 3 for three-dimensional visualization of crystal, volumetric and morphology data, Journal of Applied Crystallography 44(6) (2011) 1272-1276.

[9]   A.C. Hänzi, P. Gunde, M. Schinhammer, P.J. Uggowitzer, On the biodegradation performance of an Mg–Y–RE alloy with various surface conditions in simulated body fluid, Acta Biomaterialia 5(1) (2009) 162-171.

[10]   M. Jiang, C. Xu, T. Nakata, H. Yan, R. Chen, S. Kamado, High-speed extrusion of dilute Mg-Zn-Ca-Mn alloys and its effect on microstructure, texture and mechanical properties, Materials Science and Engineering: A 678 (2016) 329-338.

[11]   J. Nie, B. Muddle, Precipitation hardening of Mg-Ca (-Zn) alloys, Scripta Materialia 37(10) (1997) 1475-1481.

[12]   A. Finkel, L. Shepeleva, M. Bamberger, E. Rabkin, The effect of exposure to elevated temperatures on the microstructure and hardness of Mg–Ca–Zn alloy, Zeitschrift für Metallkunde 97(1) (2006) 64-71.

[13] J. Oh, T. Ohkubo, T. Mukai, K. Hono, TEM and 3DAP characterization of an age-hardened Mg–Ca–Zn alloy, Scripta Materialia 53(6) (2005) 675-679.

[14] M.R. Paris, Sur les alliages ternaires magnésium-zinc-calcium, Comptes Rendus des Séances de Lacadémie des Sciences 197 (1933) 1634-1636.

[15] J. Clark, The solid constitution in the magnesium-rich region of the Mg-Ca-Zn phase diagram, Transactions of the Metallurgical Society of AIME 221(3) 1961, 644-645.

[16] T.V. Larionova, W.-W. Park, B.-S. You, A ternary phase observed in rapidly solidified Mg-Ca-Zn alloys, Scripta Materialia 45(1) (2001) 7-12.

[17] G. Schulze, J. Wieting, Über Bauprinzipien des CaZn2-Gitters, Zeitschrift für Metallkunde 52(11) (1961) 743-746.

[18] P.M. Jardim, G. Solórzano, J.B. Vander Sande, Precipitate crystal structure determination in melt spun Mg-1.5 wt% Ca-6wt% Zn alloy, Microscopy and Microanalysis 8(6) (2002) 487-496.

[19] P. Jardim, G. Solorzano, J. Vander Sande, Second phase formation in melt-spun Mg–Ca–Zn alloys, Materials Science and Engineering: A 381(1-2) (2004) 196-205.

[20] J. Daams, P. Villars, J. van Vucht, Atlas of crystal structure types for intermetallic phases, ASM Intrenational, Materials Park, OH, USA 3 (1991) 4937-4939.

[21] K. Oh-Ishi, R. Watanabe, C. Mendis, K. Hono, Age-hardening response of Mg–0.3 at.% Ca alloys with different Zn contents, Materials Science and Engineering: A 526(1) (2009) 177-184.

[22] Y.-N. Zhang, D. Kevorkov, J. Li, E. Essadiqi, M. Medraj, Determination of the solubility range and crystal structure of the Mg-rich ternary compound in the Ca–Mg–Zn system, Intermetallics 18(12) (2010) 2404-2411.

[23] J.D. Cao, T. Weber, R. Schäublin, J.F. Löffler, Equilibrium ternary intermetallic phase in the Mg–Zn–Ca system, Journal of Materials Research 31(14) (2016) 2147-2155.

[24] R. Schäublin, M. Becker, M. Cihova, S.S.A. Gerstl, D. Deiana, C. Hébert, S. Pogatscher, P.J. Uggowitzer, J.F. Löffler, Precipitation in the Mg–Zn–Ca alloy ZX20, in preparation.

[25] P.-R. Cha, H.-S. Han, G.-F. Yang, Y.-C. Kim, K.-H. Hong, S.-C. Lee, J.-Y. Jung, J.-P. Ahn, Y.-Y. Kim, S.-Y. Cho, Biodegradability engineering of biodegradable Mg alloys: Tailoring the electrochemical properties and microstructure of constituent phases, Scientific Reports 3 (2013) 2367.

[26] F. Witte, V. Kaese, H. Haferkamp, E. Switzer, A. Meyer-Lindenberg, C. Wirth, H. Windhagen, In vivo corrosion of four magnesium alloys and the associated bone response, Biomaterials 26(17) (2005) 3557-3563.

[27] L. Li, J. Gao, Y. Wang, Evaluation of cyto-toxicity and corrosion behavior of alkali-heat-treated magnesium in simulated body fluid, Surface and Coatings Technology 185(1) (2004) 92-98.

[28] H. Bakhsheshi-Rad, E. Hamzah, A. Fereidouni-Lotfabadi, M. Daroonparvar, M. Yajid, M. Mezbahul-Islam, M. Kasiri-Asgarani, M. Medraj, Microstructure and bio-corrosion behavior of Mg–Zn and Mg–Zn–Ca alloys for biomedical applications, Materials and Corrosion 65(12) (2014) 1178-1187.

[29] N. Birbilis, A. King, S. Thomas, G. Frankel, J. Scully, Evidence for enhanced catalytic activity of magnesium arising from anodic dissolution, Electrochimica Acta 132 (2014) 277-283.

[30] A. El Warraky, A. El-Aziz, K.A. Soliman, Copper redeposition and surface enrichment during the dissolution of Al-Cu alloys in different concentrations of NaCl solution. Part 2–spectroscopic analysis measurements, Anti-Corrosion Methods and Materials 54(3) (2007) 163-172.

[31] L. Bland, N. Birbilis, J. Scully, Exploring the effects of intermetallic particle size and spacing on the corrosion of Mg-Al alloys using model electrodes, Journal of The Electrochemical Society 163(14) (2016) C895-C906.

[32] L.G. Bland, J. Bhattacharyya, S. Agnew, J. Scully, Effect of Intermetallic Particle Size and Distribution on the Corrosion of an Mg-Al Alloy, Meeting Abstracts, The Electrochemical Society, 2016, 1327-1327.

[33] T. Valente, Grain boundary effects on the behavior of WE43 magnesium castings in simulated marine environment, Journal of Materials Science Letters 20(1) (2001) 67-69.

[34] W. Zhou, T. Shen, N.N. Aung, Effect of heat treatment on corrosion behaviour of magnesium alloy AZ91D in simulated body fluid, Corrosion Science 52(3) (2010) 1035-1041.

[35] G. Makar, J. Kruger, Corrosion of magnesium, International Materials Reviews 38(3) (1993) 138-153.

[36] G.L. Song, A. Atrens, Corrosion mechanisms of magnesium alloys, Advanced Engineering Materials 1(1) (1999) 11-33.

[37] A. Südholz, N. Kirkland, R. Buchheit, N. Birbilis, Electrochemical properties of intermetallic phases and common impurity elements in magnesium alloys, Electrochemical and Solid-State Letters 14(2) (2011) C5-C7.

[38] R.-C. Zeng, L. Sun, Y.-F. Zheng, H.-Z. Cui, E.-H. Han, Corrosion and characterisation of dual phase Mg–Li–Ca alloy in Hank's solution: The influence of microstructural features, Corrosion Science 79 (2014) 69-82.

[39] J. Galvele, S. de De Micheli, Mechanism of intergranular corrosion of Al-Cu alloys, Corrosion Science 10(11) (1970) 795-807.

[40] J.L. Gilbert, C.A. Buckley, J.J. Jacobs, K.C. Bertin, M.R. Zernich, Intergranular corrosion-fatigue failure of cobalt-alloy femoral stems. A failure analysis of two implants, Journal of Bone and Joint Surgery 76(1) (1994) 110-115.

[41] G. Song, A. Atrens, D. St John, An hydrogen evolution method for the estimation of the corrosion rate of magnesium alloys, in: J.N. Hryn (Ed.) Magnesium Technology 2001, TMS, New Orleans, LA, USA, 2001, 254-262.

[42] N.T. Kirkland, N. Birbilis, M. Staiger, Assessing the corrosion of biodegradable magnesium implants: a critical review of current methodologies and their limitations, Acta Biomaterialia 8(3) (2012) 925-936.

[43] E. Wittchow, N. Adden, J. Riedmüller, C. Savard, R. Waksman, M. Braune, Bioresorbable drug-eluting magnesium-alloy scaffold: design and feasibility in a porcine coronary model, EuroIntervention 8(12) (2013) 1441-1450.

[44] J. Zhang, H. Li, W. Wang, H. Huang, J. Pei, H. Qu, G. Yuan, Y. Li, The degradation and transport mechanism of a Mg-Nd-Zn-Zr stent in rabbit common carotid artery: A 20-month study, Acta Biomaterialia 69 (2018) 372-384.

[45] L. Rossrucker, K.J.J. Mayrhofer, G.S. Frankel, N. Birbilis, Investigating the real time dissolution of Mg using online analysis by ICP-MS, Journal of the Electrochemical Society 161(3) (2014) C115-C119.

[46] N. Ott, P. Schmutz, C. Ludwig, A. Ulrich, Local, element-specific and time-resolved dissolution processes on a Mg–Y–RE alloy–Influence of inorganic species and buffering systems, Corrosion Science 75 (2013) 201-211.

[47] J.-H. Jo, B.-G. Kang, K.-S. Shin, H.-E. Kim, B.-D. Hahn, D.-S. Park, Y.-H. Koh, Hydroxyapatite coating on magnesium with MgF 2 interlayer for enhanced corrosion resistance and biocompatibility, Journal of Materials Science: Materials in Medicine 22(11) (2011) 2437-2447.

[48]   K. Ralston, N. Birbilis, Effect of grain size on corrosion: a review, Corrosion 66(7) (2010) 075005-13.

[49]   M. Alvarez-Lopez, M.D. Pereda, J. Del Valle, M. Fernandez-Lorenzo, M. Garcia-Alonso, O.A. Ruano, M. Escudero, Corrosion behaviour of AZ31 magnesium alloy with different grain sizes in simulated biological fluids, Acta Biomaterialia 6(5) (2010) 1763-1771.

[50]   R. Ambat, N.N. Aung, W. Zhou, Evaluation of microstructural effects on corrosion behaviour of AZ91D magnesium alloy, Corrosion Science 42(8) (2000) 1433-1455.

[51]   K. Kutniy, I. Papirov, M. Tikhonovsky, A. Pikalov, S. Sivtzov, L. Pirozhenko, V. Shokurov, V. Shkuropatenko, Influence of grain size on mechanical and corrosion properties of magnesium alloy for medical implants, Materialwissenschaft und Werkstofftechnik: Entwicklung, Fertigung, Prüfung, Eigenschaften und Anwendungen technischer Werkstoffe 40(4) (2009) 242-246.

[52]   Y. Lu, A. Bradshaw, Y. Chiu, I. Jones, Effects of secondary phase and grain size on the corrosion of biodegradable Mg–Zn–Ca alloys, Materials Science and Engineering: C 48 (2015) 480-486.

3 Detailed dissolution phenomena of the ternary IM1 phase

Intermetallic phases that are cathodic to the Mg matrix require special attention, because they can control the corrosion processes via micro- or nano-galvanic coupling. As such they can have a detrimental impact for the material integrity by causing locally heterogeneous corrosion attack or considerably accelerated matrix dissolution. Understanding the detailed dissolution phenomena associated with these cathodically active intermetallics on the local scale thus sets the basis for the understanding of the alloy's overall microscopic corrosion behavior. This chapter addresses the detailed corrosion mechanisms of ZX-lean alloys containing the ternary intermetallic phase IM1.

Evidence for dealloying of nanometric intermetallic particles

Biodegradable magnesium alloys generally contain intermetallic phases on the micro- or nanoscale, which can initiate and control the local corrosion processes via micro-galvanic coupling. However, the experimental difficulties in characterizing active degradation on the nanoscale so far limits the understanding of how these materials degrade in complex physiological environments. Here, a quasi-*in situ* experiment based on transmission electron microscopy (TEM) has been designed, which enables accessing the initial corrosion attack at nanometric particles within the first seconds of immersion. Combined with high-resolution *ex situ* cross-sectional TEM analysis of a well-developed corrosion-product layer, mechanistic insights into Mg-alloys' degradation on the nanoscale are provided over a large range of immersion times. Applying this methodology to lean Mg–Zn–Ca alloys and following in detail the dissolution of their nanometric Zn- and Ca-rich particles the *in statu nascendi* observation of intermetallic-particle dealloying is documented for magnesium alloys, where electrochemically active Ca and Mg preferentially dissolve and electropositive Zn enriches, inducing the particles' gradual ennoblement. Based on electrochemical theory, the manuscript presents the concept of cathodic-polarization-induced dealloying, which controls the dynamic microstructural changes. It also discusses the general prerequisites for this new dealloying mechanism to occur in multicomponent alloys and its distinction to other dealloying modes.

3.1 Introduction

Mechanically stronger than polymers and with the benefit of bioresorption capabilities over stainless steel and titanium, magnesium (Mg) and its alloys may become the new standard for temporary implant applications in the treatment of cardiovascular [1, 2] and musculoskeletal [3, 4] conditions. Key to a successful clinical outcome is a tightly controllable and predictable degradation behavior of these alloys in physiological environment. Owing to Mg's large reactivity, it is highly susceptible to galvanic corrosion. Especially those alloys containing intermetallic phases that are considered cathodic to the Mg matrix require particular attention. This is because these intermetallic phases may be the cause of laterally heterogeneous corrosion attack or may induce enhanced matrix dissolution through micro-galvanic coupling [5-7]. Both processes can result in detrimental implant failure when the implant loses its mechanical integrity [8], or in critical tissue irritation when corrosion products are released too rapidly [9, 10]. In comparison, intermetallic phases that are anodic to the Mg matrix, especially those that are nanometric in size and contained in a low volume fraction, are considered harmless for the alloy's corrosion susceptibility, because they would simply dissolve preferentially without causing the mentioned acceleration impact on the Mg matrix [6, 11].

Mg alloys containing zinc (Zn) and calcium (Ca), denominated ZX alloys, have received special attention [3, 9, 11-19] because they are composed of elements essential for the human body, making them biologically safe [20], and because of their favorable combination of adequate mechanical properties [12, 13] and slow and homogeneous corrosion [9, 16]. This alloy system's microstructure [11, 12, 21] and its relation to corrosion [11, 14, 15, 17] were thus broadly investigated and immense efforts were devoted to optimize these alloys. In fact, implants made from this alloying system have meanwhile, after promising pre-clinical validation [9, 13, 16, 17], reached the state of translational clinical trials [2-4]. Nevertheless, an in-depth understanding of the corrosion mechanisms at play in physiological environment remains fragmentary. Mg's intrinsically high electrochemical reactivity and the fragile nature of the corrosion products forming make such studies on Mg-alloys indeed challenging; in fact much more challenging than comparable investigations on passivating alloys (such as Al alloys or stainless steel) or generally less reactive materials.

The main cathodic intermetallic phase in the ZX alloy of this study (i.e. ZX10, see experimental section 3.2.1) is a ternary phase denoted IM1, which has a reported compositional range of $Ca_3Mg_xZn_{15-x}$ with $4.6 \leq x \leq 12$ [21]. First attempts to reveal this phase's corrosion behavior were conducted on either a single-phase specimen with IM1 composition, i.e. in isolation from the Mg matrix [18], or indirectly by studying alloys containing this phase via either electrochemical methods, such as polarization sweeps and electrochemical impedance spectroscopy [14, 15, 22, 23], or simple

immersion methods, such as the hydrogen-gas evolution method [15, 22, 23] or by monitoring the evolution of the electrolyte's pH [14]. However, the artificial condition of a single phase and the limited spatial resolution of the methodologies chosen so far did not allow a detailed description of the corrosion mechanisms. Accessing this information is especially difficult for lean-alloyed ZX compositions (where the overall alloying content is below 1 at.%), as the IM1 phase is present as precipitates of nanometric size [12]. Their small size combined with the high reactivity and dissolution rate of Mg makes studies of their corrosion behavior even more challenging.

In this study we were able to cope with this challenge by investigating the detailed dissolution of the nanometric IM1 precipitates *in situ,* i.e. in their natural state in terms of their size and composition and embedded in the α-Mg matrix, using advanced, high-resolution transmission electron microscopy (TEM)-based methods. To this end, we developed a new TEM-based method here referred to as *SABACO* (stemming from *S*ame *A*rea *B*efore and *A*fter *CO*rrosion), which is a quasi-*in situ* analysis method, which combines high-magnification 'morphological imaging', low-dose 'chemical imaging', and stereomicroscopy. Only by combining these three methodologies was it possible to gain detailed micro- and nanoscale insights into the initial corrosion processes and corrosion products formed. We complemented this method by cross-sectional TEM analysis, which can provide information on the prolonged corrosion behavior after the formation of a mature, i.e. spatially comprehensive, micrometer-thick corrosion-product layer. By applying both analytical characterization methods, we were able to resolve the details of the early-stage dissolution of the IM1 phase at the nanometer scale, and of the role this phase plays in micro- and nano-galvanic coupling in ZX alloys. More specifically, this novel high-resolution methodology allowed us to directly observe dealloying of nanometric IMPs, which generates a dynamic change in their electrochemical activity. While dealloying of intermetallic phases is well-described and identified as a key corrosion mechanism in *passive* materials, such as in aluminum alloys [24-26], we report here dealloying to occur in magnesium alloys, which as *active* materials entail a fundamentally different corrosion behavior. The dealloying observed here for Mg is thus considered to be a new mechanism identified via the nanoscale methodology described above. This methodology thus reveals active corrosion mechanisms in Mg alloys down to the nanometer scale and can be applied to other active alloy systems to provide further evidence for the generality of this phenomenon.

3.2 Experimental details

3.2.1   *Material and material preparation*

The alloy with nominal composition Mg–Zn1.0(0.37)–Ca0.3(0.18), in wt.% (at.%), referred to as ZX10, was prepared by melting distilled, ultra-high purity Mg (99.999% [27]), and high-purity Zn (99.99%) and Ca (99.5%) in a graphite crucible at 750 °C in a protective gas mixture (Ar with 1 vol.% SF_6). The crucible was cooled to room temperature on a water-cooled copper block to achieve directional solidification and avoid precipitation during cooling. The ingot was machined into a billet of 50 mm in diameter and 120 mm in height. The billet was homogenized (350 °C/ 12 h plus 450 °C/ 8 h) and then exposed to isothermal holding at 250 °C for 0.5 h, following the procedure described in Ref. [12]. The billet was subsequently heated to 300 °C and then indirectly extruded at an exit speed of 3.75 mm s⁻¹ into rods of 10 mm diameter, corresponding to an extrusion ratio of 25.

The as-extruded material, with the binary Mg_2Ca phase as the thermodynamically predicted primary secondary phase [12], was isothermally heat-treated to generate the IM1-type secondary phase with reported compositional range of $Ca_3Mg_xZn_{15-x}$ where $4.6 \leq x \leq 12$ [21]. The temperature and time to achieve this phase transformation were chosen based on the calculated phase diagram reported in Ref. [12], and estimated by taking the diffusivity of Zn as the diffusion-limiting element into account. To this end, the samples were cut, heat-treated at 250 °C for 366 h, and then water-quenched to preserve the microstructure.

3.2.2   *TEM investigation*

All TEM samples were prepared as standard 3 mm discs. Specimens for microstructural analysis and *SABACO* experiments were cut from the extruded and heat-treated rod and mechanically ground to a thickness of about 70 µm. Specimens for *ex situ* cross-sectional TEM analysis of the corrosion-product layer (xTEM) were prepared as described below. Electron transparency was achieved for all specimens by Ar⁺-ion milling using a Precision Ion Polishing System (PIPS™ II from Gatan, Inc.). Double-sided Ar⁺-ion milling was chosen for the TEM-foil preparation to remove potential mechanically deformed surface area originating from the preceding mechanical sample preparation. Ion milking was performed at an incident angle of 3.5° and an acceleration voltage of 4 kV. Ion milling was performed at liquid-nitrogen temperature to prevent changes in the microstructure.

TEM imaging was performed in an FEI Talos™ F200X operated at 80 kV in scanning TEM (STEM) mode with a high-angle annular dark-field (HAADF) detector for *Z*-contrast. Quantitative chemical information was obtained by means of energy-dispersive X-ray spectroscopy (EDS) using a

large collection-angle detector (FEI Super-X detector, made of Silicon Drift Detectors (SDDs)). Each acquisition was performed for at least 15 min at a dwell time of 10 µs, and the spectra were quantified using the QMap function in Cliff-Lorimer mode using ESPRIT software from Bruker. The combination of a high-brightness Schottky field emission gun (FEG) source with a high-sensitivity TEM system and a high-efficiency EDS detector ensured short acquisition times at a low electron dose during EDS analysis. This proved to be an essential prerequisite for the study of the fragile corrosion products that formed on the Mg substrates without causing beam damage. For the chemical analysis of the intermetallic phase, special care was taken to only consider those particles that entirely occupied the TEM thin foil, thus excluding the contribution of the Mg matrix to the signal.
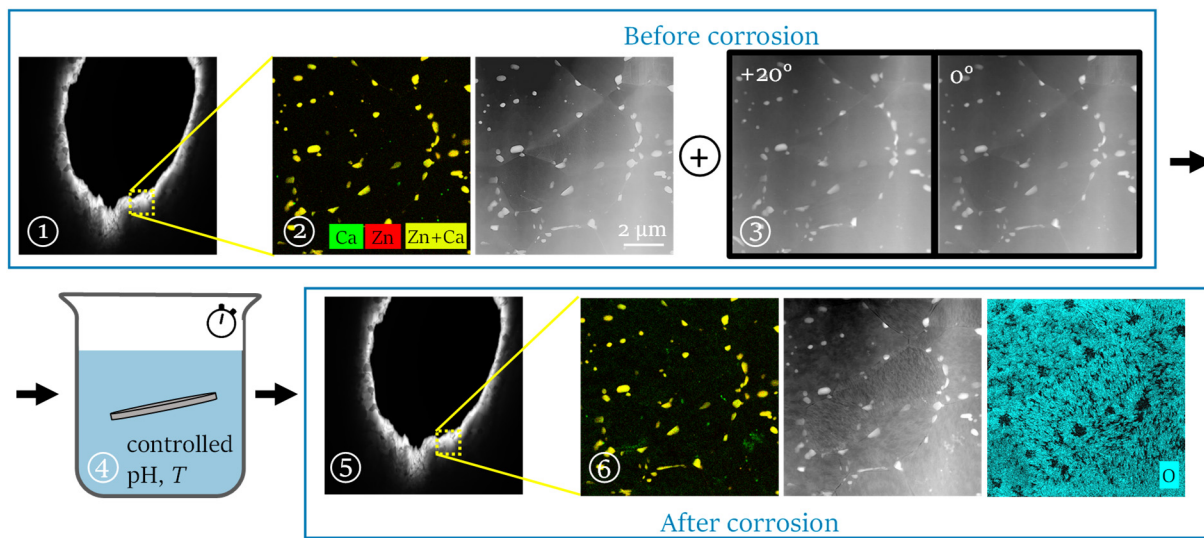
Figure 3.1: Schematic presentation of the TEM-based *SABACO* method, which allows nano- to microscale investigation of corrosion attack and corrosion-product formation. 1: A TEM disc prepared via precision-ion polishing generates a hole, the edges of which are electron transparent. 2: In the TEM, regions of interest (ROIs) are defined and their micro- and nanostructure pre-corrosion is analyzed in detail using STEM-EDS and STEM-HAADF for chemical and morphological information, respectively. 3: Stereographic pairs of images acquired at two different tilt angles provide a 3D impression of the TEM thin foil. Using these stereopairs of images, micro- and nanostructural features facing the surface (top or bottom) are identified. This information is crucial considering that corrosion is a surface process. 4: The TEM disc is immersed outside the microscope in an electrolyte (in this study: simulated body fluid) and under a controlled pH value and temperature. 5: The ROIs are relocated in the TEM. 6: The microstructure and corrosion products are investigated post-corrosion on the micro- and nanoscale, allowing both direct correlation of the alloy's microstructure and corrosion behavior and observation of potential microstructural changes induced by corrosion processes.

The microstructure before and after corrosion attack was characterized in STEM imaging mode with a strong focus on the chemical information obtained by STEM-EDS. Prior to immersion, stereographic pairs of images, which give a 3D impression of the 2D projection intrinsic to TEM, were taken at +20° and 0°. The stereographic pairs were visually inspected to identify the surface-facing

IMPs. This inspection is essential because only those IMPs located at the surface are affected by corrosion.

3.2.3 Immersion

Biocorrosion was initiated by immersing the TEM discs for 5 s in simulated body fluid (SBF) [28] at 37 °C and at pH 7.4. The pH was maintained by flushing the SBF with an Air–CO2 mixture containing 6.7% CO_2, adjusted to the ionic strength of the electrolyte used. Following the immersion period, the corrosion attack was immediately terminated by rinsing the sample sequentially in deionized water and in ethanol, for 5 s each.

3.2.4 Cross-sectional TEM

Cross-sectional TEM (xTEM) specimens were prepared using the cross-section kit from Gatan to allow for an evaluation of the active biocorrosion attacks at prolonged immersion durations of up to 12 h. Plates of about 1 mm thickness were cut from the heat-treated rods, ground, and polished down to ¼ µm diamond paste using ethanol as a lubricant to avoid extensive oxidation. The samples were immersed under physiological conditions as described above for 10 min, 5 h, and 12 h, respectively. To terminate the corrosion processes at the immersion time desired, the samples were sequentially rinsed in deionized water and ethanol, for 5 s each. Two Mg-alloy plates were glued with their respective corrosion-product layer as the region of interest facing each other, thus forming a sandwiched assembly. Cross-sections of these sandwiches were cut, and 3 mm TEM samples were ion-milled to electron transparency following the protocol presented above. TEM imaging with EDS mapping was performed with the settings described above.

3.3 Results and discussion

3.3.1 Primary biocorrosion events

The initiation of corrosion processes was studied quasi-*in situ* via TEM. Biocorrosion was simulated by immersing the material in simulated body fluid (SBF) and its impact studied by investigating the microstructure at the same locations before and after immersion along with a potential corrosion-product formation. Applying TEM for this protocol allows the investigation of both microstructure and corrosion-product formation of the *S*ame *A*rea *B*efore and *A*fter *Co*rrosion (referred here as *SABACO*) down to the nanometer scale (Figure 3.1). Applying this method representative regions of interest (ROIs) are identified and their micro- and nanostructure characterized by TEM imaging and chemical mapping, setting the basis for a detailed understanding of the microstructure–corrosion-susceptibility correlations. While before-and-after corrosion-attack investigations have already been reported for various materials, the *SABACO* method presented here stands out by the scale of investigation achievable and the concurrent information that can be obtained regarding both morphology (in STEM mode) and chemistry (in STEM-EDS mode). The latter also allows to access information on the fragile corrosion products forming on Mg substrates provided that an appropriate low-electron dosage TEM and advanced EDS-detector system are used that provide chemical information without causing beam damage (see experimental section 3.2.2). Furthermore, the *SABACO* method comprises the acquisition of stereographic image pairs, which provide a 3D impression of the samples from 2D projections intrinsic to TEM imaging. This allows identifying those intermetallic particles that are at the surface and are thus exposed to the corrosive environment (see '*Stereographic-imaging technique*' in section 1.1.7). This information is crucial, considering that corrosion is a surface effect.

Figure 3.2 presents the typical outcome of such a *SABACO* experiment, revealing the IM1 nature of the intermetallic particles and their noble nature relative to the α-Mg matrix during the initial biocorrosion attack.

STEM-HAADF imaging of the pristine sample (Figure 3.2a) shows the intermetallic particles (IMPs) in brighter *Z*-contrast, indicating the presence of elements heavier than Mg. (Note that a thickness variation at the lateral scale of the IMPs as a contributor to the HAADF intensity can be excluded thanks to the sample-preparation technique of precision-ion polishing, which is performed at a low incident angle.) The IMPs exhibit a roughly globular morphology, are about 50 to 200 nm in diameter, and have a number density of about 10^{18} m^{-3}. They mainly decorate the grain boundaries but are also contained within the grains. The IMPs are composed of the ternary phase rich in Zn and

Ca, with $Ca_3Mg_{11}Zn_4$ structure, as a detailed analysis based on STEM-EDS and ultra-high resolution microscopy had revealed (see Chapter 2). The phase composition of the IMPs in ZX10 is thus at the upper boundary of Mg content (and lower boundary of Zn) compared to the composition range of the IM1 phase proposed by Zhang et al. [21] as $Ca_3Mg_xZn_{15-x}$ ($4.6 \leq x \leq 12$).

The pristine sample exhibits a smooth surface (Figure 3.2a) and a homogeneous oxygen distribution with no detectable correlation to the underlying microstructure. The latter is visible from the oxygen map in Figure 3.2b and the quantified line scan across one IMP in Figure 3.2d. This observation is essential, as possible atmospheric corrosion may otherwise bias the subsequent corrosion mechanisms acting during SBF immersion.

After immersion in SBF for only 5 s (Figure 3.2e-h), considerable corrosion-product formation is prevalent, characterized by a roughened surface of the grains in the HAADF contrast (Figure 3.2e), and by a strong oxygen signal in the EDS chemical map (Figure 3.2f). More importantly, both the surface texture and oxygen signal show distinct dependence on the microstructure: the former remains smooth (inset to Figure 3.2e) and the latter is depleted (Figure 3.2f and g) at the sites of the IMPs that are exposed at the surface (see stereographic pair of images in section 1.1.7). The depletion of oxygen at the sites of the IMPs is also evident from the quantified line scan (Figure 3.2 h) across the same IMP as before the corrosion attack. Note that the distribution of Ca is not plotted in this line scan due to the presence of Ca in the electrolyte and consequently in the corrosion products formed, thus not allowing to distinguish its origin from that of the alloy. Compared to the situation before corrosion attack (Figure 3.2d), the oxygen signal is significantly elevated after corrosion attack (Figure 3.2h), clearly showing the presence of corrosion products. These observations show clearly that the IMPs are spared from the oxidation and corrosive attack, a fact that can be explained by their more noble nature compared to the Mg matrix. The IMPs are thus evidently identified as cathodically protected spots on the surface. This observation is not surprising, considering the IMPs' chemical composition, and can be attributed to their significant content of electrochemically more noble Zn compared to Mg.
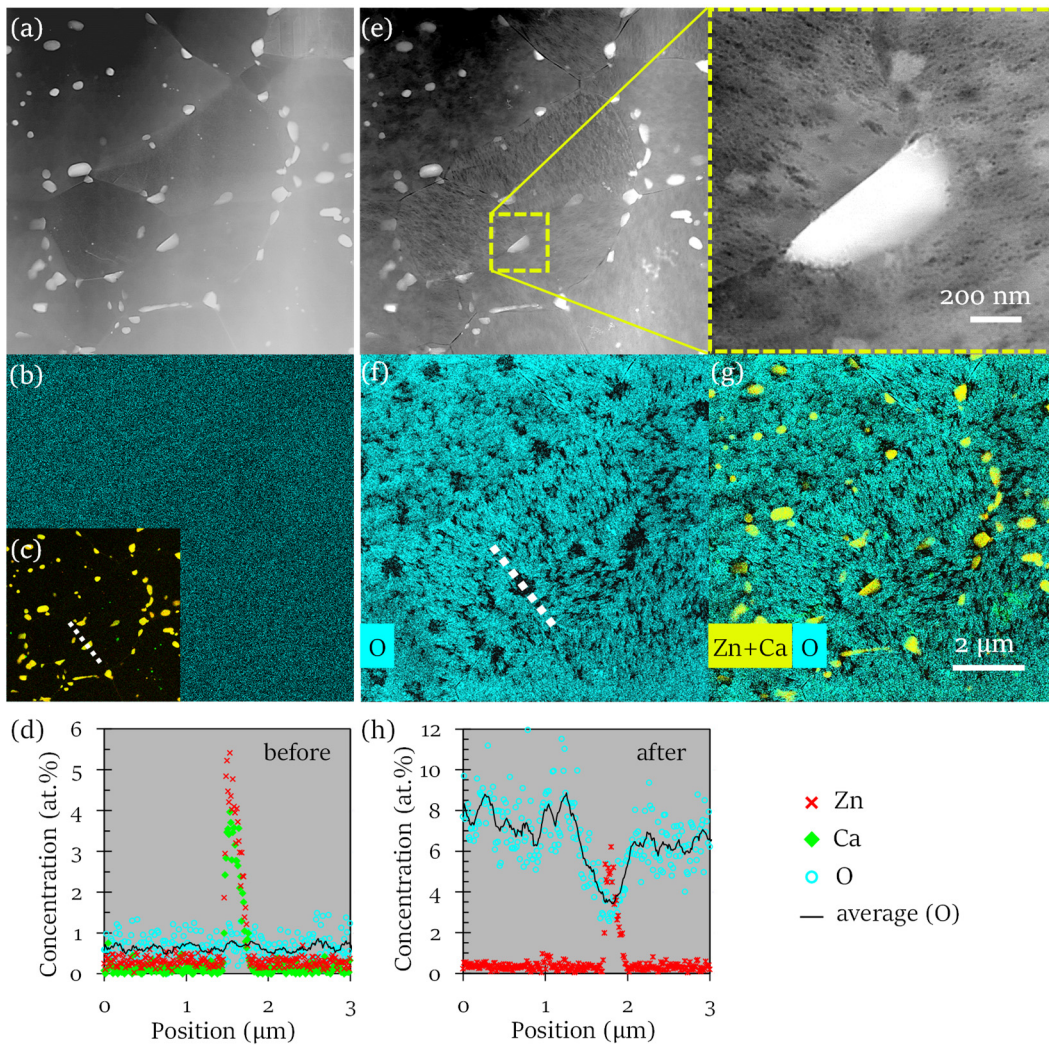
Figure 3.2: Initial corrosion behavior revealed by the TEM-based SABACO method. The STEM-HAADF (a, e) and corresponding STEM-EDS chemical maps (b, c, f, g) show the Same Area (a - c) Before and (e - g) After COrrosion attack upon exposure to simulated body fluid for 5 s. (a) The pristine sample surface appears smooth. (b) The STEM-EDS chemical map for oxygen reveals a homogeneous distribution with no correlation to the underlying microstructure, which contains IMPs rich in Zn and Ca, as shown in (c). (d) EDS line scans across an individual IMP for the pristine surface; the scan line is indicated in (c). No correlation of the oxygen signal to the underlying IMP is detected and the oxygen content is generally very low; see turquoise symbols in (d) and the corresponding average (black line). (e) After immersion in SBF the matrix grains are clearly attacked, as evident from the topographical roughening observed. Inset to (e): the magnified view of an IMP confirms that corrosion attack only occurred at its vicinity, whereas its surface remains smooth, thereby supporting the hypothesis that the IMPs are cathodically protected. (f) The distribution of oxygen is laterally heterogeneous and clearly follows the underlying microstructure, with a depleted oxygen coverage at the location of the IMPs that are exposed at the surface; the scale bar is indicated in (g). (g) The oxygen-depleted zones appear larger than the IMPs and roughly circular in shape, supporting the hypothesis that the IMPs are the sites of hydrogen-gas formation and of high pH. (h) EDS line scans across an individual IMP at the surface after corrosion attack; the line across the individual particle is marked in f, respectively. The overall level of oxygen is significantly higher compared to the pristine surface (d) and a clear correlation to the microstructure is observed, with a distinct oxygen depletion at the site of the IMP.

The Mg matrix, in contrast, experiences active dissolution, identifying it as the effective anode in this micro-galvanic couple. Interestingly, the oxygen-depleted area at the IMP sites appears circular irrespective of the IMPs' shape and slightly larger than their size (Figure 3.2g and black-grey striped pattern in the schematics shown in Figure 3.3); this supports the hypothesis that the IMPs are the sites of cathodic hydrogen-gas bubble formation with a subsequent local pH increase possibly resulting in the formation of a protective or semi-protective oxide or hydroxide on the surrounding Mg matrix [5]. Figure 3.3 shows a schematic presentation of events, which underlie the observation of an oxygen-depleted zone around the IMPs in the *SABACO* experiment.
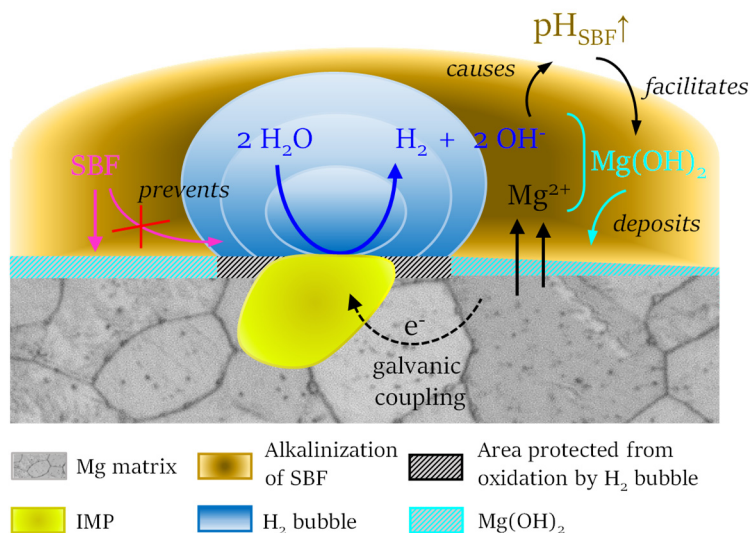
Figure 3.3: Schematic presentation of hydrogen-gas formation on the IMPs' surface. The formation and growth of a gas bubble hinders the corrosive environment to reach the metallic surface of the IMP and of the surrounding Mg matrix, thus preventing its oxidation. Only in areas in direct contact with the corrosive environment (here: SBF) can oxidation and thus conversion to Mg(OH)$_2$ occur. The protection of the near-IMP area only persists for very short immersion times until the bubble reaches a critical size at which it escapes from the surface.

3.3.2   *Evolution of corrosion-product layer over time*

While the *SABACO* method proves very valuable in providing detailed insights into early-stage corrosion processes at the nanoscale, it is limited to initial oxidation processes, which occur rapidly owing to the high reactivity of Mg. Feasible immersion times typically comprise just a few seconds, before either the built-up of corrosion products limits the electron transparency or the high oxidation rate results in a complete dissolution of the thin TEM foil.

For this reason we complementarily performed a cross-sectional analysis of the mature corrosion-product layer. This extends the mechanistic investigation to significantly longer immersion

times and thus provides valuable information on the progressing material dissolution. The cross-sectional analysis of the corrosion-product layer in the TEM, referred to as xTEM, enables to obtain simultaneous information on morphology (in STEM-HAADF mode) and chemistry (in STEM-EDS mode), down to the nanometer scale.

Figure 3.4 shows xTEM images of corrosion-product layers formed at an immersion time of 10 min (Figure 3.4a), 5 h (Figure 3.4b) and 12 h (Figure 3.4c), thus revealing how the corrosion attack progresses. Two distinct layers constituting the corrosion products are revealed, which differ in their morphology, thickness and chemical composition. IMPs are embedded in the corrosion-product layer, indicative for an inward-growing corrosion-product-film formation. Note that the corrosion-product-film growth occurs without volume expansion despite the conversion from Mg to $Mg(OH)_2$, thus preserving the original surface and in turn the shape of the sample (see xSEM experiment in Chapter 2). The presence of IMPs in the corrosion-product film also indicates that the cathodic protection of IMPs persists beyond the initial corrosion process studied for 5 s of immersion time in the *SABACO* experiment.

A thin Ca-, P- and O-rich product-precipitation layer forms within a few minutes of immersion in SBF. This layer, which is generated at the interface between the corrosion-product layer and the electrolyte (Figure 3.4a, yellow arrows), is about 30 to 50 nm in thickness and rather dense in its morphology. Its origin stems from the Ca and P ions present in body fluids, which precipitate as the pH increases as a result of the Mg dissolution and hydrogen reduction [10, 29]. This Ca/P/O-rich layer is therefore characteristic of Mg biocorrosion in physiological environments. The layer's rather dense nature provides a significant corrosion protection [10, 30] and its chemical similarity to bone minerals is ascribed a contribution to the good osseointegration behavior of Mg-based implant materials [10, 31, 32].

Subjacent to the Ca/P/O-layer and separated by a sharp chemical interface, a highly spongy layer forms, which extends to the metal–corrosion-product-layer interface (see dotted lines in the Mg and Zn chemical maps). This layer is composed of $Mg(OH)_2$ evident from the corresponding Mg-to-O atomic ratio of 1-to-2 obtained from EDS analysis (Figure 3.5b, line profiles to the right of *if2*). While the Ca/P/O-layer remains approximately constant in thickness at about 30 to 50 nm, the spongy $Mg(OH)_2$ layer propagates inward into the Mg alloy with increasing immersion time, reaching a thickness of 125 ± 50 nm after 10 min (Figure 3.4a), and further extending to 800 ± 200 nm after 5 h (Figure 3.4b), and 1400 ± 250 nm after 12 h (Figure 3.4c) of immersion. This inward-growing corrosion front appears to be facilitated by the spongy nature of the $Mg(OH)_2$ layer, allowing electrolyte to ingress and reach the metal–corrosion-product-layer interface. At this interface,
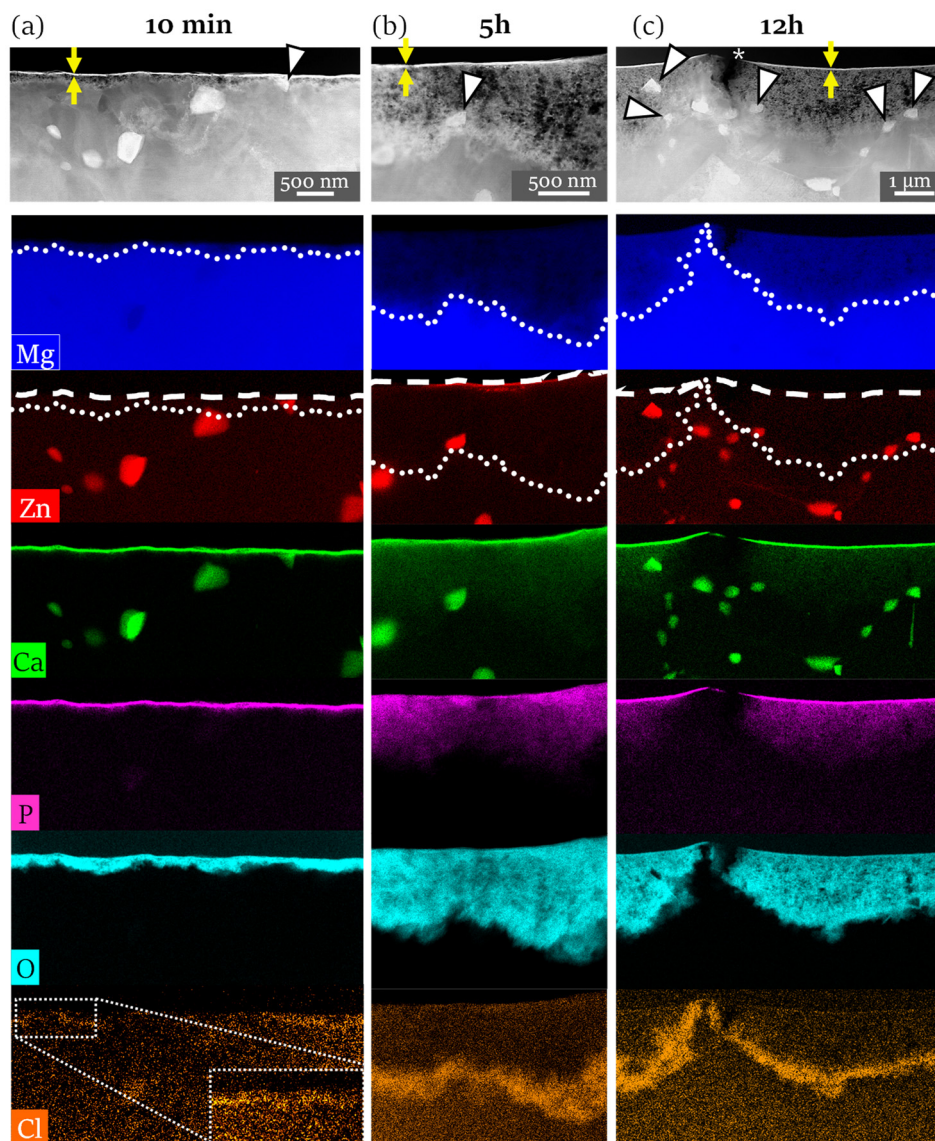
Figure 3.4: Cross-sectional view and interface chemistry of the growing corrosion-product layers as a function of immersion time in SBF. Cross-sectional STEM-HAADF images (top row) and corresponding STEM-EDS chemical maps (from second row) of the growing corrosion-product layer after immersion in SBF for (a) 10 min, (b) 5 h and (c) 12 h. The white arrow heads in the STEM-HAADF images point to the IMPs embedded in the corrosion-product layer. The dotted lines in the chemical maps represent the metal–corrosion-product-layer interface and the dashed lines indicate the interface to the Ca/P/O-rich layer for the various immersion times. While after 10 min the IMPs are still integrated in the matrix, the IMPs are undermined by the inward-growing corrosion front with progressing corrosion attack and are eventually separated from the matrix. Whereas the Ca/P/O-rich layer, precipitated on the outer interface towards the electrolyte, forms rapidly and remains at a constant thickness for longer immersion times (yellow arrows), the subjacent $Mg(OH)_2$ layer with a spongy morphology progressively increases in thickness. The corrosion front propagates inwards, presumably facilitated by the presence of chloride ions at the metal–corrosion-product-layer interface. The absence of outward-growing corrosion-product formation preserves the original sample shape, which is steadily replaced by spongy $Mg(OH)_2$.

chlorine (Cl) accumulates (Figure 3.4, bottom row), presumably present as Cl⁻ and driven by charge compensation to the cation-enriched near-metal-surface zone, to form $MgCl_2$. While the specific interfacial chemistry and the chloride interaction mechanisms remain a subject of ongoing research, it is widely assumed that chlorine plays a key role in maintaining an active dissolution of the Mg alloy [5, 33]. With the corrosion-product-layer–metal interface maintained active, the corrosion front can continuously grow inward, but with increasing layer thickness, the risk of crack formation (Figure 3.4c, asterisk) increases owing to accumulated stresses present between the Mg metal and $Mg(OH)_2$ [34]. Cracks tend particularly to impair the desired homogeneous material dissolution because they facilitate a locally enhanced electrolyte exchange within the corrosion-product layer and at the metal–corrosion-product-layer interface. This in turn alters the corrosion behavior locally.

IMPs are clearly visible in the HAADF images (Figure 3.4, top row), owing to their brighter *Z*-contrast, and in the corresponding EDS chemical maps for Zn and Ca (Figure 3.4, third and fourth row). The IMPs are detected not only in the bulk material, but with progressing corrosion attack are also found to protrude at the metal–corrosion-product-layer interface (Figure 3.4a-c, white arrow heads). This shows their greater dissolution resistance compared to the surrounding Mg matrix. With further corrosion attack, the IMPs are eventually embedded in the corrosion-product layer, undermined by the inward-growing corrosion front, and finally separated from the metallic bulk material (Figure 3.4c, white arrow heads).

High-resolution TEM analysis, and specifically the ability of nanoscale chemical analysis using STEM-EDS, allow to zoom in on the detailed dissolution mechanisms acting on the IMPs.

3.3.3   *Dealloying of the intermetallic phase*

In the following, the dissolution mechanisms acting on the ternary IM1 phase are described: the intermetallic phase composed of Mg, Zn and Ca experiences dealloying expressed by preferential dissolution of Ca and Mg, generating a gradual enrichment of Zn in IM1 and thereby IM1's ennoblement.

Figure 3.5a displays a magnified view of IMPs at the metal–corrosion-product-layer interface at different stages of their dissolution sequence: (I) shows an IMP protruding into the corrosion-product layer but still electrically coupled to the Mg matrix. The adjacent matrix dissolution is enhanced at the matrix–IMP interface (Figure 3.5a, white arrows), producing trenches surrounding the IMP; (II) shows an IMP that has just been undermined by the inward-growing corrosion front and is thus separated from the Mg matrix; (III) shows an IMP which has been completely undermined by the formerly bypassing corrosion front and is now well embedded in the $Mg(OH)_2$ layer. This later stage corresponds to a partially dissolved particle, i.e. a remnant of an IMP.
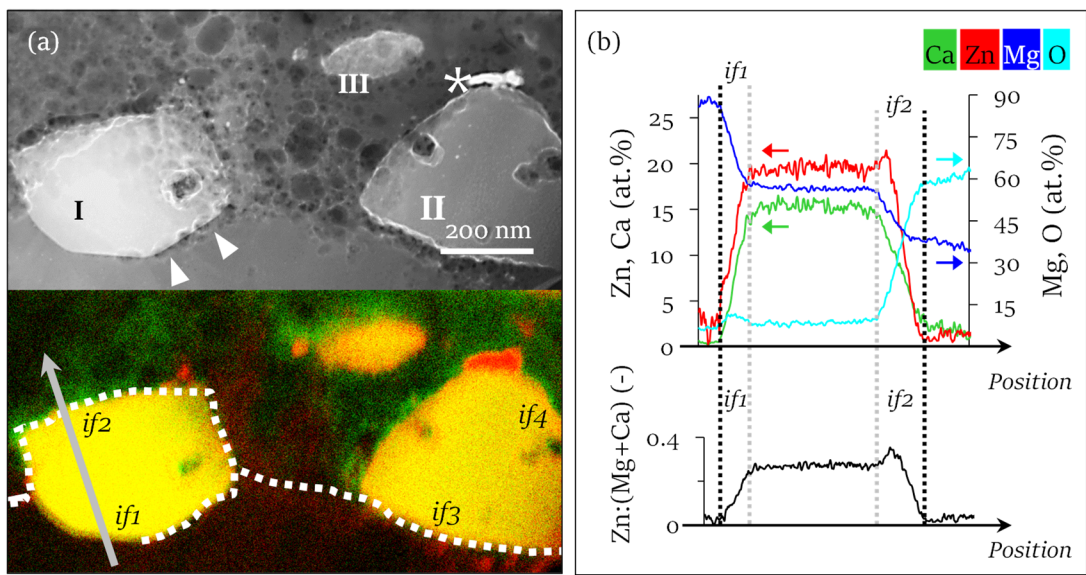
Figure 3.5: Dealloying of the IM1 phase. (a) Cross-sectional view of a ZX alloy immersed in SBF for 5 h showing IMPs exposed at the metal–corrosion-product-layer interface (dotted line); top: STEM-HAADF image; bottom: corresponding STEM-EDS chemical map. I: IMP integrated in the matrix; II: IMP separated and thus electrically decoupled from the matrix; III: Zn-enriched IMP remnant; *: Zn redeposition; *if*: interface. (b) Quantified STEM-EDS line scan across an IMP marked by the grey arrow in (a) to reveal the interfacial chemistry. Top: Line profiles for Mg, Zn, Ca and O showing depletion of Ca and Mg and enrichment of Zn in the IMP periphery (*if2*), and enhanced presence of Ca in the corrosion-product layer adjacent to the IMP; bottom: Zn-to-(Mg+Ca) ratio along the same scan line emphasizes the compositional change at the IMP–corrosion-product-layer interface (*if2*) resulting from dealloying. The Mg-matrix–IMP interface (*if1*) serves as a reference interface without detectable compositional change.

The STEM-EDS chemical map (Figure 3.5a, bottom image) allows to extract essential information on the dynamic chemical distribution of the alloying elements as a function of the dissolution stages. An increased concentration of Ca is present in the IMPs' surrounding, diffusively reaching into the spongy $Mg(OH)_2$ layer. A quantified line scan across the IMP–corrosion-product-layer interface (*if2* in Figure 3.5b; line indicated as a solid grey arrow in Figure 3.5a, bottom) confirms not only the enrichment in Ca in the IMP vicinity but also its depletion within the IMP periphery. The detection of Ca depletion at the IMP periphery is essential because it supports the perception that the diffuse Ca accumulation in the IMP vicinity indeed stems from the dissolving IMP and not from the Ca contained in the electrolyte. The line profile also reveals the simultaneous depletion of Mg across the same interface. Zn, in contrast, presents a substantially different distribution: no Zn accumulation in the corrosion products around the IMPs is detected, which would indicate its dissolution. Conversely, its content at the IMP periphery is even increased compared to the IMP-bulk content (see *if2* in Figure 3.5b), thus forming a Zn-rich shell. A direct comparison of this attacked interface with the pristine one between the Mg matrix and IMP of the same intermetallic particle (*if1*) demonstrates clearly the modified interfacial chemical distribution emerging from the

corrosion attack: while *if2* suffers from preferential dissolution of Ca and Mg, the IMP composition at *if1* location is largely constant (see the absence of Mg depletion and the constant Zn-to-Ca ratio across *if1* in Figure 3.5b, top). Note that the width of *if1* in the line profile arises because the scan line across this interface is not perpendicular (as for *if2*) but inclined relative to the interface (see direction of the grey arrow in Figure 3.5a, bottom), and is not due to a gradual composition change in the IMP periphery. The *if1* inclination is also demonstrated in Figure 3.5b by an increasing Mg contribution towards the matrix. The associated relative Zn enrichment at the attacked interface (*if2*) and its absence at the intact interface (*if1*), are explicit in the elemental ratio of Zn to the sum of Mg and Ca derived across the same line profile (Figure 3.5b, bottom).

Comparing the different IMP-dissolution stages I to III in Figure 3.5a, it appears that the Ca and Mg content of the IM1-phase periphery steadily decreases and its Zn content significantly increases (more red color, bottom image of Figure 3.5a) with progressing dissolution. The shift in the IMP composition is accompanied by morphological changes at the IMP–corrosion-product-layer interface, apparent in the HAADF image in Figure 3.5a (top image): the corrosion attack, while initially present only at the interface (Figure 3.5a, I-II), advances into the IMP and eventually leaves a porous remnant of significantly smaller size (Figure 3.5a, III; Figure 3.8).

The question thus arises as to what drives the preferential Ca and Mg dissolution and the Zn enrichment in the IMPs.

Considering first the case of IMPs integrated in the Mg matrix and exposed to the metal–corrosion-product-layer interface (particle I in Figure 3.5a and step 1 in Figure 3.6), a scenario arises that also applies to the planar-view examination employing the *SABACO* method. In this situation the IMPs are polarized cathodically (Figure 3.2), at the galvanic potential of the alloy they populate. The establishing effective (polarized) potential on the IMP is close to the potential of the α-Mg matrix, owing to the active dissolution and therefore non-polarizable nature of Mg [35-37] and the high surface ratio of anodic Mg matrix to cathodic nanometric IMPs. For physiological conditions, an open circuit potential on the order of -1.5 to -1.2 V_{SHE} is usually measured [6, 16], though the real potential at the Mg-metal–corrosion-product-layer interface, while experimentally not accessible because of the presence of the corrosion products, may be even significantly lower. In this potential regime, which is considerably more negative than the reversible potential of the Zn/ Zn^{2+} reaction, Zn oxidation is thermodynamically not possible [38] (see Pourbaix diagram for Zn in Figure 1.12, section 1.1.6 '*Magnesium corrosion*'). In other words, Zn is cathodically protected via polarization by the active corroding α-Mg matrix. Ca and Mg, in contrast, oxidize at this potential and pH [38], resulting in their active dissolution (Figure 3.6, step 2). As a consequence of this preferential Ca and Mg dissolution, dealloying of the IM1 phase occurs in conjunction with a relative enrichment in Zn.

Considering the underlying mechanism, which involves cathodic protection of the nobler element, we refer to it as *cathodically polarized dealloying*.

The resulting enrichment in metallic Zn, concomitant with the ennoblement of the IMP, renders the IMPs even more effective cathodic spots. An increased hydrogen-gas-formation activity at the IMP surface results, owing to a greater exchange-current density for hydrogen reduction on Zn compared to Mg or Ca and owing to a higher discharge efficiency on a metallic compared to an oxidized surface (indicated by the double blue arrow in Figure 3.6, step 2). Their elevated cathodic activity is expected to provoke severe deterioration of the material's overall corrosion resistance and thus because of drastic laterally heterogeneous corrosion when increased peripheral matrix dissolution via micro-galvanic coupling sets in (Figure 3.6, step 3). The peripheral matrix dissolution proceeds until the inward-growing corrosion front (time-resolved xTEM in Figure 3.4) eventually bypasses, and thus undermines the IMP, causing its separation from the Mg matrix (Figure 3.6, step 4).
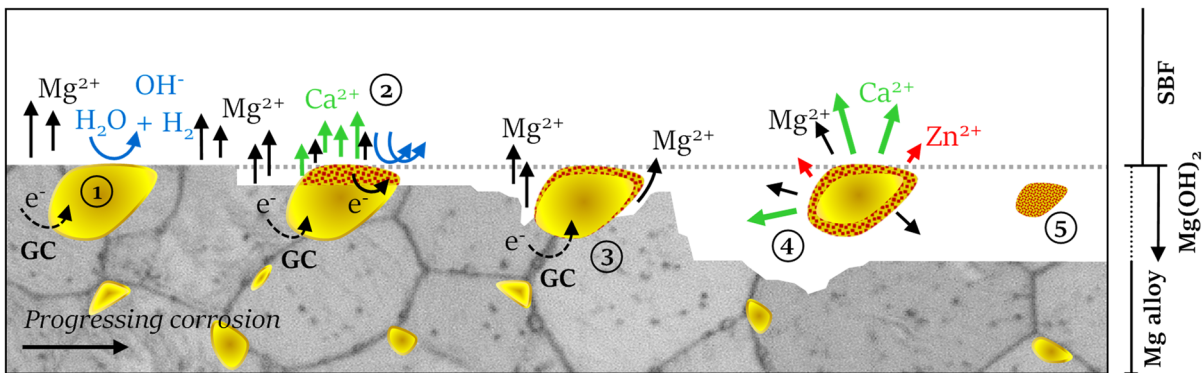
Figure 3.6: Schematic presentation of the individual dealloying stages for the IM1 phase. 1 - 3: *Cathodically polarized dealloying*. 1: galvanic protection of the IMP as the site of hydrogen-gas formation; 2: preferential dissolution of Ca and Mg while Zn is galvanically protected (GC: galvanic coupling); metallic Zn enrichment as a consequence of preferential dissolution of Ca and Mg supports the cathodic hydrogen-gas formation more efficiently, as indicated by the double blue arrow; 3: the increasing nobility of the IMP leads to enhanced peripheral matrix dissolution surrounding the IMP. 4 - 5: *Kinetic dealloying*. 4: the IMP is undermined and separated from the matrix, so that the dissolution rate becomes independent from the matrix. However, due to their difference in corrosion rates supported by the hydrogen reduction, the dissolution rate at this open-circuit condition is highest for Ca and lowest for Zn. 5: The IMP remnants are increasingly enriched in Zn. The dotted grey line in (c) marks the original metal surface.

It should be emphasized here that even when individual IMPs become electrically decoupled from the matrix, the overall alloy corrosion continues to be governed by the IMP-induced galvanically accelerated dissolution of the peripheral Mg matrix. This applies on account of the high number density of IMPs in ZX10, which ensures that new, subjacent IMPs come to be exposed at the metal–corrosion-product-layer interface with the progressing inward-growing corrosion front.

Upon complete separation from the Mg matrix (particles II and III in Figure 3.5a), the loss of direct electrical contact between matrix and IMP cannot be compensated by the spongy $Mg(OH)_2$. Consequently, because no sufficient electron flux is provided to assist micro-galvanic corrosion, the separated IMP is no longer polarized. It will establish its own free corrosion potential, independent of the Mg-alloy composition and microstructure. Under these non-polarized, or open-circuit, conditions, both Ca and Mg still appear to continuously dissolve preferentially (Figure 3.6, step 5). This is evident from the diffusive Ca signal in the IMPs' vicinity (around particles II and III in Figure 3.5a) and from their progressing enrichment in Zn (Figure 3.5a, particles I-III). These chemical changes at different stages of the IMP dissolution after being undermined by the inward-growing corrosion front (Figure 3.5a, particles II-III) are further analyzed by EDS line profiles compiled across various interfaces of an IMP and IMP remnant, respectively, and the corrosion-product layer (Figure 3.7).
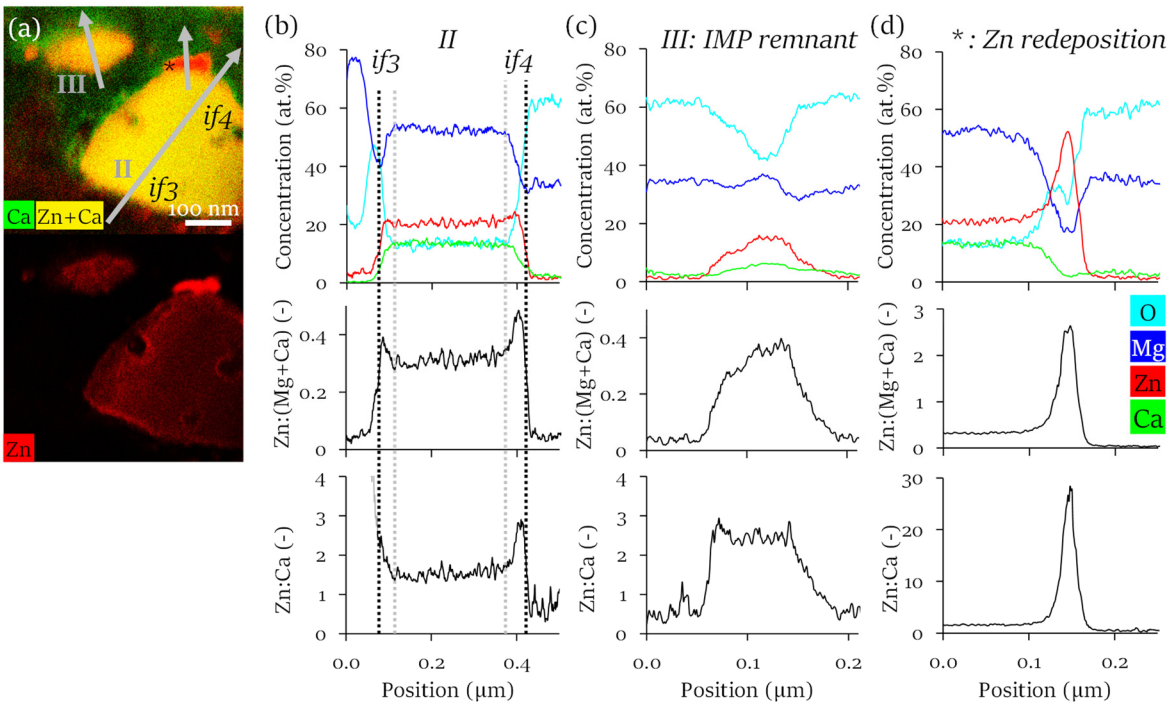
Figure 3.7: Interfacial chemistry of IMPs decoupled from the Mg matrix. a) Top: STEM-EDS chemical map, superimposed for Ca and Zn; the interfaces between IMP II and the corrosion-product layer are marked; *if*: interface. Bottom: STEM-EDS chemical map of the same area for Zn. (b-d) Quantified EDS-line scan along the grey arrows marked in (a); for particle II, the interface boundaries are marked with dotted lines. (b-d) Top: line profiles for Mg, Zn, Ca and O; center: Zn-to-(Mg + Ca) ratio, and bottom: Zn-to-Ca ratio.

Figure 3.7a depicts the chemical distribution of Zn and Ca in and around the separated IMP and the IMP remnant. Around them, an enhanced diffusive Ca signal is detected in the corrosion-product layer, comparable to the case of a polarized IMP (Figure 3.5a, particle I). The isolated chemical map

for Zn (Figure 3.7a, bottom) further reveals a slightly enhanced Zn content at the IMP–corrosion-product-layer interfaces for particle II. A quantified line scan across particle II (Figure 3.7b; all interfaces (*if*), across which line scans were compiled, are marked in Figure 3.7a) supports these observations: not only does it show that the corrosion product has intruded into the former Mg-matrix–IMP interface *if3*, but also that Zn is enriched at both interfaces, *if3* and *if4*, where the effect is more pronounced for the *if4* interface, which was longer in contact with the solution within the porous corrosion products. The relative Zn enrichment is unambiguously apparent from the spatial ratios of Zn:(Mg+Ca) (Figure 3.7b, center row) and Zn:Ca (Figure 3.7b, bottom row) derived along this line profile. Both ratios emphasize the modified interfacial composition resulting from dealloying for both interfaces *if3* and *if4* while the IMP interior remains unaffected (constant Zn:Ca ratio). Note that the Zn enrichment detected here for the separated IMP is comparable to that of the integrated particle I (see Figure 3.5b) at the corrosion-product layer interface (*if2*) but was not detected at the intact Mg-matrix–IMP interface (*if1*). Because *if3* is only exposed to physiological solution once undermined, the detection of Zn enrichment at this location supports the fact that dealloying also initially occurs under OCP conditions. Note that the high Zn-to-Ca ratio detected at the sites of the Mg-matrix (greyed out in Figure 3.7b, bottom) is not the result of excessive Zn enrichment but of almost total Ca depletion.

Particle III in Figure 3.7a represents a particle remnant formed after being separated from the Mg matrix for a longer time compared to particle II. The postulated advanced Zn enrichment of the remnant (Figure 3.6, steps 4-5) is not easily apparent at first from the quantified line profiles in Figure 3.7c. This is because of the remnant's relatively small size, which does not occupy the entire TEM-foil thickness. Consequently, the corrosion-product layer makes a significant contribution to the signal (refer to the high level of Mg and O), suppressing the Zn and Ca signals. The well-advanced Ca depletion accompanied by Zn enrichment can, however, well be recognized in the Zn-to-Ca ratio of Figure 3.7c (bottom row): at about 2.5 for the remnant it is greater than the ratio of about 1.4 for the pristine IMP. Note that this experimentally obtained value presumably represents a significant underestimate owing to the presence of Ca ions in the corrosion-product layer, which originate from the electrolyte and surrounding dealloyed IMPs.

This persisting preferential Ca and Mg dissolution beyond Mg-matrix separation can be explained by the elements' individual electrochemical reactivity, which entails intrinsically higher dissolution kinetics for Ca compared to Mg and for both higher ones compared to Zn in physiological conditions, owing to their (standard) reversible potentials at -0.76, -2.38 and -2.87 V_{SHE} for Zn, Mg and Ca, respectively. This relates to an increasing overpotential to the hydrogen-reduction reaction on the order of Zn << Mg < Ca. The persisting preferential Ca and Mg dissolution in turn inevitable

causes continuous Zn enrichment, continuously leading to gradual ennoblement of the IMP remnants (Figure 3.6, step 5). Taking into account that the underlying mechanism is solely attributed to different dissolution kinetics of the alloying elements at open circuit conditions, we refer to it as *kinetic dealloying*.

Finally, Figure 3.7d presents a quantified line scan across the Zn-rich cluster (marked with * in Figure 3.7a). The high content of Mg in the elemental profile shows clearly that the cluster is embedded in the corrosion-product layer. It also reveals that the cluster is significantly depleted in Ca and has a large Zn-to-Ca ratio of about 28. The real value, however, is again expected to be significantly greater considering the contribution of Ca ions in the corrosion-product layer which originate from the electrolyte and neighboring dealloyed IMPs. The Zn cluster is presumably metallic in nature and formed via electrochemical reduction on the IMP surface [39, 40]. Such reduction appears possible due to the high reversible potential of Zn and is described in detail in Chapter 4, '*Zn-cluster act as additional* nano-cathodes'.

Morphological changes appear to accompany the chemical changes during dealloying. Figure 3.8 presents magnified HAADF images of individual particles at the IMP–corrosion-product-layer interface, which reveal an intensity variation at the IMP periphery visible as a network-like pattern.
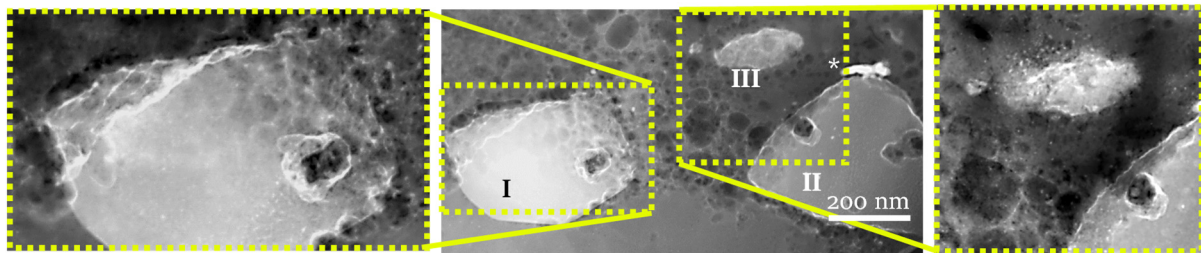
Figure 3.8: STEM-HAADF image of IM1-phase IMPs in their different dissolution stages. The insets show magnified views on the particle–corrosion-product-layer interfaces of particles I, II and III.

Considering the intensity I of HAADF contrast to be a function of thickness t and atomic number Z, with $I \propto tZ^2$, and taking into account the sample-preparation technique of precision-ion polishing at a low incident angle (which leads to a virtually constant thickness at the scale of the IMPs), the magnified views suggest the outer periphery of the IMP to be porous, with a darker HAADF contrast resulting from material voids. Porosity appears to be a result of both stages of IMP dissolution, i.e. while integrated in and when separated from the Mg matrix. It further appears that the porosity advances into the IMP and eventually leads to a porous remnant, which is not only enriched in Zn (see Zn-to-Ca ratio in Figure 3.7d, bottom row) but also significantly smaller in size (Figure 3.5a and Figure 3.8, III).

The morphology of the IMP remnant is assumed to depend on the IMP composition and especially on the proportion of the noble element Zn: an IMP with a high Zn content is likely to result in a Zn-rich network-like remnant with significant porosity. This is expected when the Zn content is sufficiently high, such that its atoms percolate in the pristine IMP structure. In contrast, a low Zn content is likely to result in complete dissolution of the remnant, potentially accompanied by redeposition of Zn on the Mg surface. Further investigations on the intermetallic phase with varying Zn content are required to test the validity of these expectations.

While it remains unresolved how far inward the IMP dealloying can advance before diffusion limitation dominates, it is likely that with the IMPs' increasing porosity, their mechanical integrity will decline and eventually cause them to collapse. Emerging TEM-based atomically-resolved analyses may provide detailed insights into the remaining structure.

The entire dealloying mechanism described, comprising both modes, for IMPs integrated in and separated from the Mg matrix, is schematically presented in Figure 3.6.

The relevance of these dealloying phenomena for local corrosion processes becomes apparent when reaching out to other metallic systems, such as to analogies in aluminum alloys: the preferential dissolution of Mg from the S-phase composed of Al_2CuMg [24, 41], the selective dissolution of Al from the θ-phase composed of Al_2Cu [25], or the selective dissolution of Si and Mg from the Q-phase composed of $Al_xCu_yMg_zSi_w$ [26] all eventually cause local enrichment and redistribution or redeposition of the electropositive elements contained in the intermetallic phase, in this case Cu [42, 43]. Because Al is a *passive* material, the local enrichment in and redeposition of Cu are detrimental, as they are responsible for an increased cathodic activity inducing the initiation of severe localized corrosion [44] and present a key challenge in the corrosion control of commercial Al alloys.

Although Mg alloys are *active* materials and therefore reveal a fundamentally different corrosion behavior compared to passive materials, the IMP dealloying is still expected to have an equally high significance for the local corrosion processes, in which now the ennobled IMPs and the accumulation of noble elements control the micro- and nano-galvanic coupling. Nonetheless, dealloying of IMPs and noble-element redeposition has so far only been sparsely described. Observations so far have concerned mainly Mg-alloy compositions containing Al [45, 46], in which selective Al dissolution from the IMP was observed. In such alloys, the selective Al dissolution is explained by the intrinsically opposed passivating behaviors of Mg and Al at alkaline conditions, where the latter is a consequence of the Mg-matrix dissolution [5]. While Mg dissolution significantly slows down as the pH becomes more alkaline due to the increasing stabilization of $Mg(OH)_2$ and possibly of MgO, Al dissolution is enhanced at these conditions because of the destabilization of alumina [38]. This local *environment-*

induced dealloying, which is fundamentally different from the here described mechanism of cathodically polarized dealloying, is solely a chemical dissolution mechanism, in which micro-galvanic coupling and cathodic protection of one element over another play no role.

It is only recently that the corrosion processes acting on intermetallic phases in Al-free Mg alloys have become a focus of investigations: Gharbi and Birbilis [47] described the dissolution behavior of the Mg_2Si phase, and Han and Ogle [48] that of the $MgZn_2$ phase. While in both cases preferential dissolution of Mg as the less noble element was indeed observed, the respective intermetallic phase was studied as a bulk single phase, isolated from the Mg matrix. Such a single-phase analysis, however, disregards the possible mechanistic impact of the Mg matrix on the active corrosion mechanisms via micro-galvanic coupling, such that cathodically polarized dealloying could not be observed. In other words, such studies are limited to the investigation of incongruent dissolution either via what is here referred to as environmentally induced or kinetic dealloying, but could not investigate cathodically polarized dealloying.

In contrast, we report here on the *in statu nascendi* observation of dealloying acting on nanometric IMPs in their *in situ* state, that is as they are embedded in the Mg matrix; and thus present the mechanism of intermetallic-phase dealloying to occur also in active Mg alloys. The cathodically polarized dealloying mechanism, identified here for the ternary IM1 phase, is expected to be widely applicable, and to occur not only for various intermetallic phases in the Mg–Zn–Ca system studied here but also in other metallic systems and for other electrolytes. A prerequisite for the occurrence of cathodically polarized dealloying is the presence of a secondary phase composed of at least two elements. One of them is either Mg or an alloying element which, in the pH regime relevant to the intended application, features a higher electrochemical activity than Mg, e.g. Ca or Li [6]. The other element must be electropositive compared to Mg. When these conditions are met, cathodically polarized dealloying is expected to take place as the element possessing the higher electrochemical activity dissolves preferentially, while the more noble element remains cathodically protected via matrix-induced polarization. It should be noted that the IMP's noble-element content is predominantly decisive for its integrity and stability upon corrosion attack, leading either to its dealloying or to its complete dissolution [49]. As mentioned above, dealloying is expected when the noble-element content is sufficiently high such that the atoms can percolate in the pristine IMP structure [49], resulting in a porous remnant. Decomposition, in contrast, is expected at a low noble-element content, potentially accompanied by noble-element redeposition on the Mg surface. While the results presented here suggest that the Zn content of the IM1 phase of ~23 at.% is certainly above the required threshold for dealloying to occur, further analysis is needed to determine this

compositional threshold and clarify the detailed remnant structure as a function of the pristine IMP composition.

The identification of IMP dealloying has important implications for the choice of methodology to study the microstructure–corrosion-behavior correlations of Mg-based alloys and multicomponent alloys in general. Many studies describe the microstructure in the alloy's pristine state as a basis for the understanding of the subsequently investigated corrosion behavior. The corrosion behavior is most commonly characterized either via electrochemical methods or immersion studies. The latter evaluates the material's corrosion susceptibility by mass loss or hydrogen-gas evolution [50]. However, neither approach reveals further insights into the microstructural evolution upon material dissolution. In other words, these common methodological approaches *assume* the microstructure to remain unchanged throughout the alloy's dissolution. Dealloying, however, causes a dynamic change in the IMP composition with progressing dissolution. This dynamic compositional change in turn generates a dynamic change in the IMPs' electrochemical activity. More specifically, enrichment of noble-element content causes the IMPs' cathodic activity to increase, leading to a higher efficiency in the hydrogen-reduction reaction and micro-galvanically accelerated matrix dissolution, and thus to a higher risk of laterally heterogeneous corrosion attack. In an extreme case, dealloying may even result in polarity reversal, i.e. in a complete switch of initial local anodes to cathodes when the enrichment in noble elements peaks [51].

Dealloying, with the dynamically changing microstructure it induces, may therefore provide a rationalization for the mechanistic origin of Mg-alloys' dynamically changing corrosion behavior. It is likely to be an important reason for differences in the corrosion behavior observed *in vitro* and *in vivo*, which could not be rationalized on the basis of the microstructural information available. For this reason, modification of the commonly used methodological protocols towards careful consideration of post-corrosion microstructures seems inevitable. Novel analytical techniques can greatly assist in such realizations and provide insights into prevalent corrosion processes down to the nanoscale. Finally, it should be mentioned that although the simulated body fluid used as electrolyte in this study may not reflect the full complexity of real biological fluids, it presents a first step towards an understanding of biocorrosion phenomena at the nanometer scale. Furthermore, the key mechanisms related to intermetallic dealloying identified here are expected to equally occur in simple aqueous solutions, such as dilute sodium chloride solutions, and are thus also of great relevance for general corrosion phenomena in a non-biological context.

3.4 Conclusions

In summary, we employed two complementary TEM-based methods, namely the developed *SABACO* method, which comprises high-resolution planar quasi-*in situ* morphological and chemical investigations of both the microstructure and corrosion products formed coupled with stereographic imaging, and the *ex situ* cross-sectional method xTEM, to understand in detail the dissolution behavior of the ternary IM1 phase in Mg–Zn–Ca alloys. Applying both methods in concert, we were able to unveil key fundamental mechanistic information on the microstructure's role on early-stage corrosion processes. In fact, we revealed the cathodic protection of the IM1 phase on the nanoscale, and documented *in statu nascendi* observation of IMP dealloying in Mg alloys, leading to a dynamic IMP ennoblement via Zn enrichment. We describe this mechanism as *cathodically polarized dealloying*, and illustrate that this dealloying mode acts in the material in conjunction with *kinetic dealloying*, which occurs under non-polarized conditions. This new concept, presented here for the Mg–Zn–Ca system, is likely to be applicable to other alloying systems and intermetallics phases. These findings not only shed light on the possible origins of local corrosion processes and dynamic changes in corrosion behavior, but also provide guidelines for the experimental design of emerging *in situ* corrosion studies of Mg-based alloys at the nanometer scale.

3.5 Acknowledgements

3.6 References

[1]   M. Haude, H. Ince, S. Kische, A. Abizaid, R. Tölg, P.L. Alves, N.M. Van, S. Verheye, E. Christiansen, W. Wijns, Sustained safety and clinical performance of a drug-eluting absorbable metal scaffold up to 24 months: pooled outcomes of BIOSOLVE-II and BIOSOLVE-III, EuroIntervention 13(4) (2017) 432-439.

[2]   H.-S. Han, S. Loffredo, I. Jun, J. Edwards, Y.-C. Kim, H.-K. Seok, F. Witte, D. Mantovani, S. Glyn-Jones, Current status and outlook on the clinical translation of biodegradable metals, Materials Today 23 (2019) 57-71.

[3]   J.-W. Lee, H.-S. Han, K.-J. Han, J. Park, H. Jeon, M.-R. Ok, H.-K. Seok, J.-P. Ahn, K.E. Lee, D.-H. Lee, Long-term clinical study and multiscale analysis of in vivo biodegradation mechanism of Mg alloy, Proceedings of the National Academy of Sciences 113(3) (2016) 716-721.

[4]   D. Zhao, F. Witte, F. Lu, J. Wang, J. Li, L. Qin, Current status on clinical applications of magnesium-based orthopaedic implants: A review from clinical translational perspective, Biomaterials 112 (2017) 287-302.

[5]   M. Esmaily, J. Svensson, S. Fajardo, N. Birbilis, G. Frankel, S. Virtanen, R. Arrabal, S. Thomas, L. Johansson, Fundamentals and Advances in Magnesium Alloy Corrosion, Progress in Materials Science 89 (2017) 92–193.

[6]   K. Gusieva, C. Davies, J. Scully, N. Birbilis, Corrosion of magnesium alloys: the role of alloying, International Materials Reviews 60(3) (2015) 169-194.

[7]   H. Feng, S. Liu, Y. Du, T. Lei, R. Zeng, T. Yuan, Effect of the second phases on corrosion behavior of the Mg-Al-Zn alloys, Journal of Alloys and Compounds 695 (2017) 2330-2338.

[8]   M.B. Kannan, R.S. Raman, In vitro degradation and mechanical integrity of calcium-containing magnesium alloys in modified-simulated body fluid, Biomaterials 29(15) (2008) 2306-2314.

[9]   J. Hofstetter, M. Becker, E. Martinelli, A.M. Weinberg, B. Mingler, H. Kilian, S. Pogatscher, P.J. Uggowitzer, J.F. Löffler, High-strength low-alloy (HSLA) Mg–Zn–Ca alloys with excellent biodegradation performance, JOM 66(4) (2014) 566-572.

[10]   F. Witte, V. Kaese, H. Haferkamp, E. Switzer, A. Meyer-Lindenberg, C. Wirth, H. Windhagen, In vivo corrosion of four magnesium alloys and the associated bone response, Biomaterials 26(17) (2005) 3557-3563.

[11]   D. Zander, N.A. Zumdick, Influence of Ca and Zn on the microstructure and corrosion of biodegradable Mg–Ca–Zn alloys, Corrosion Science 93 (2015) 222-233.

[12]   J. Hofstetter, S. Rüedi, I. Baumgartner, H. Kilian, B. Mingler, E. Povoden-Karadeniz, S. Pogatscher, P.J. Uggowitzer, J.F. Löffler, Processing and microstructure–property relations of high-strength low-alloy (HSLA) Mg–Zn–Ca alloys, Acta Materialia 98 (2015) 423-432.

[13]   S.Y. Cho, S.W. Chae, K.W. Choi, H.K. Seok, Y.C. Kim, J.Y. Jung, S.J. Yang, G.J. Kwon, J.T. Kim, M. Assad, Biocompatibility and strength retention of biodegradable Mg-Ca-Zn alloy bone implants, Journal of Biomedical Materials Research Part B: Applied Biomaterials 101(2) (2013) 201-212.

[14]   H. Bakhsheshi-Rad, E. Hamzah, A. Fereidouni-Lotfabadi, M. Daroonparvar, M. Yajid, M. Mezbahul-Islam, M. Kasiri-Asgarani, M. Medraj, Microstructure and bio-corrosion behavior of Mg–Zn and Mg–Zn–Ca alloys for biomedical applications, Materials and Corrosion 65(12) (2014) 1178-1187.

[15]   N.D. Nam, Role of zinc in enhancing the corrosion resistance of Mg-5Ca alloys, Journal of The Electrochemical Society 163(3) (2016) C76-C84.

[16] P.-R. Cha, H.-S. Han, G.-F. Yang, Y.-C. Kim, K.-H. Hong, S.-C. Lee, J.-Y. Jung, J.-P. Ahn, Y.-Y. Kim, S.-Y. Cho, Biodegradability engineering of biodegradable Mg alloys: Tailoring the electrochemical properties and microstructure of constituent phases, Scientific Reports 3 (2013) 2367.

[17] Y. Jang, Z. Tan, C. Jurey, Z. Xu, Z. Dong, B. Collins, Y. Yun, J. Sankar, Understanding corrosion behavior of Mg–Zn–Ca alloys from subcutaneous mouse model: Effect of Zn element concentration and plasma electrolytic oxidation, Materials Science and Engineering: C 48 (2015) 28-40.

[18] K. Hagihara, S. Shakudo, K. Fujii, T. Nakano, Degradation behavior of Ca–Mg–Zn intermetallic compounds for use as biodegradable implant materials, Materials Science and Engineering: C 44 (2014) 285-292.

[19] B. Zberg, P.J. Uggowitzer, J.F. Löffler, MgZnCa glasses without clinically observable hydrogen evolution for biodegradable implants, Nature Materials 8(11) (2009) 887-891.

[20] Y. Liu, Y. Zheng, X.H. Chen, J.A. Yang, H. Pan, D. Chen, L. Wang, J. Zhang, D. Zhu, S. Wu, Fundamental Theory of Biodegradable Metals—Definition, Criteria, and Design, Advanced Functional Materials 29(18) (2019) 1805402.

[21] Y.-N. Zhang, D. Kevorkov, J. Li, E. Essadiqi, M. Medraj, Determination of the solubility range and crystal structure of the Mg-rich ternary compound in the Ca–Mg–Zn system, Intermetallics 18(12) (2010) 2404-2411.

[22] Y. Lu, A. Bradshaw, Y. Chiu, I. Jones, Effects of secondary phase and grain size on the corrosion of biodegradable Mg–Zn–Ca alloys, Materials Science and Engineering: C 48 (2015) 480-486.

[23] C. Zhang, S. Zhu, L. Wang, R. Guo, G. Yue, S. Guan, Microstructures and degradation mechanism in simulated body fluid of biomedical Mg–Zn–Ca alloy processed by high pressure torsion, Materials & Design 96 (2016) 54-62.

[24] R. Buchheit, R. Grant, P. Hlava, B. McKenzie, G. Zender, Local dissolution phenomena associated with S phase (Al2CuMg) particles in aluminum alloy 2024-T3, Journal of the Electrochemical Society 144(8) (1997) 2621-2628.

[25] X. Zhang, T. Hashimoto, J. Lindsay, X. Zhou, Investigation of the de-alloying behaviour of θ-phase (Al2Cu) in AA2024-T351 aluminium alloy, Corrosion Science 108 (2016) 85-93.

[26] S. Kairy, P. Rometsch, C. Davies, N. Birbilis, On the Electrochemical and Quasi In Situ Corrosion Response of the Q-Phase (AlxCuyMgzSiw) Intermetallic Particle in 6xxx Series Aluminum Alloys, Corrosion 73(1) (2016) 87-99.

[27] J.F. Löffler, P.J. Uggowitzer, C. Wegmann, M. Becker, H.K. Feichtinger, Process and apparatus for vacuum distillation of high-purity magnesium. European Patent Application PCT, EP 2013/000131–WO2013/1076442012, 2012.

[28] A.C. Hänzi, P. Gunde, M. Schinhammer, P.J. Uggowitzer, On the biodegradation performance of an Mg–Y–RE alloy with various surface conditions in simulated body fluid, Acta Biomaterialia 5(1) (2009) 162-171.

[29] L. Li, J. Gao, Y. Wang, Evaluation of cyto-toxicity and corrosion behavior of alkali-heat-treated magnesium in simulated body fluid, Surface and Coatings Technology 185(1) (2004) 92-98.

[30] H. Kuwahara, Y. Al-Abdullat, N. Mazaki, S. Tsutsumi, T. Aizawa, Precipitation of magnesium apatite on pure magnesium surface during immersing in Hank's solution, Materials Transactions 42(7) (2001) 1317-1321.

[31] L. Xu, G. Yu, E. Zhang, F. Pan, K. Yang, In vivo corrosion behavior of Mg-Mn-Zn alloy for bone implant application, Journal of Biomedical Materials Research Part A 83(3) (2007) 703-711.

[32] E. Zhang, L. Xu, G. Yu, F. Pan, K. Yang, In vivo evaluation of biodegradable magnesium alloy bone implant in the first 6 months implantation, Journal of Biomedical Materials Research Part A 90(3) (2009) 882-893.

[33] M. Brady, G. Rother, L. Anovitz, K. Littrell, K. Unocic, H. Elsentriecy, G.-L. Song, J. Thomson, N. Gallego, B. Davis, Film breakdown and nano-porous Mg(OH)2 formation from corrosion of magnesium alloys in salt solutions, Journal of The Electrochemical Society 162(4) (2015) C140-C149.

[34] P. Schmutz, V. Guillaumin, R. Lillard, J. Lillard, G. Frankel, Influence of dichromate ions on corrosion processes on pure magnesium, Journal of The Electrochemical Society 150(4) (2003) B99-B110.

[35] N. Kirkland, J. Lespagnol, N. Birbilis, M. Staiger, A survey of bio-corrosion rates of magnesium alloys, Corrosion Science 52(2) (2010) 287-291.

[36] T. Cain, L. Bland, N. Birbilis, J. Scully, A compilation of corrosion potentials for magnesium alloys, Corrosion 70(10) (2014) 1043-1051.

[37] A. Südholz, N. Birbilis, C. Bettles, M. Gibson, Corrosion behaviour of Mg-alloy AZ91E with atypical alloying additions, Journal of Alloys and Compounds 471(1-2) (2009) 109-115.

[38] M. Pourbaix, Atlas of electrochemical equilibria in aqueous solution, NACE 307 (1974).

[39] N. Birbilis, A. King, S. Thomas, G. Frankel, J. Scully, Evidence for enhanced catalytic activity of magnesium arising from anodic dissolution, Electrochimica Acta 132 (2014) 277-283.

[40] D. Höche, C. Blawert, S.V. Lamaka, N. Scharnagl, C. Mendis, M.L. Zheludkevich, The effect of iron re-deposition on the corrosion of impurity-containing magnesium, Physical Chemistry Chemical Physics 18(2) (2016) 1279-1291.

[41] R. Buchheit, M. Martinez, L. Montes, Evidence for Cu Ion Formation by Dissolution and Dealloying the Al2CuMg Intermetallic Compound in Rotating Ring-Disk Collection Experiments, Journal of The Electrochemical Society 147(1) (2000) 119-124.

[42] T. Hashimoto, X. Zhang, X. Zhou, P. Skeldon, S. Haigh, G. Thompson, Investigation of dealloying of S phase (Al 2 CuMg) in AA 2024-T3 aluminium alloy using high resolution 2D and 3D electron imaging, Corrosion Science 103 (2016) 157-164.

[43] S. Lebouil, J. Tardelli, E. Rocca, P. Volovitch, K. Ogle, Dealloying of Al2Cu, Al7Cu2Fe, and Al2CuMg intermetallic phases to form nanoparticulate copper films, Materials and Corrosion 65(4) (2014) 416-424.

[44] A. El Warraky, A. El-Aziz, K.A. Soliman, Copper redeposition and surface enrichment during the dissolution of Al-Cu alloys in different concentrations of NaCl solution. Part 2–spectroscopic analysis measurements, Anti-Corrosion Methods and Materials 54(3) (2007) 163-172.

[45] M. Danaie, R.M. Asmussen, P. Jakupi, D.W. Shoesmith, G.A. Botton, The cathodic behaviour of Al–Mn precipitates during atmospheric and saline aqueous corrosion of a sand-cast AM50 alloy, Corrosion Science 83 (2014) 299-309.

[46] R. Asmussen, W. Binns, R. Partovi-Nia, P. Jakupi, D. Shoesmith, The stability of aluminum-manganese intermetallic phases under the microgalvanic coupling conditions anticipated in magnesium alloys, Materials and Corrosion 67(1) (2016) 39-50.

[47] O. Gharbi, N. Birbilis, Clarifying the Dissolution Mechanisms and Electrochemistry of Mg2Si as a Function of Solution pH, Journal of The Electrochemical Society 165(9) (2018) C497-C501.

[48] J. Han, K. Ogle, Editors' Choice—Dealloying of MgZn2 Intermetallic in Slightly Alkaline Chloride Electrolyte and Its Significance in Corrosion Resistance, Journal of The Electrochemical Society 164(14) (2017) C952-C961.

[49] Q. Chen, K. Sieradzki, Mechanisms and morphology evolution in dealloying, Journal of The Electrochemical Society 160(6) (2013) C226-C231.

[50] N.T. Kirkland, N. Birbilis, M. Staiger, Assessing the corrosion of biodegradable magnesium implants: a critical review of current methodologies and their limitations, Acta Biomaterialia 8(3) (2012) 925-936.

[51] C. Luo, S.P. Albu, X. Zhou, Z. Sun, X. Zhang, Z. Tang, G.E. Thompson, Continuous and discontinuous localized corrosion of a 2xxx aluminium–copper–lithium alloy in sodium chloride solution, Journal of Alloys and Compounds 658 (2016) 61-70.

4 The role of Zn and intermetallic-particle type in the macroscopic biocorrosion behavior of ZX-lean alloys

The local corrosion phenomena associated with the binary and ternary intermetallic phases in ZX-lean alloys were described in the previous chapters, revealing that the former dissolved rapidly and preferentially while the latter is cathodically protected and undergoes dealloying. However, coarsening of the ternary phase occurred due to the fabrication path of the samples involving extensive heat treatment. Because the size and number density of intermetallic phases may have an impact on the global corrosion behavior, the heat-treated ZX10 sample, while suitable to study local corrosion phenomena, does not constitute a suitable model material to investigate the role of IMP type in the macroscopic corrosion behavior.

In this chapter the design of two suitable model materials is therefore described, based on thermodynamic calculations towards microstructures that differ solely in their IMP type while other microstructural features that are known to influence corrosion processes are kept largely constant. With these model materials, the role of the nanometric IMPs' phase type in the macroscopic corrosion process is studied in vitro and in vivo.

The role of zinc in the biocorrosion behavior of resorbable Mg–Zn–Ca alloys

Zinc- and calcium-containing magnesium alloys, denominated ZX alloys, excel as temporary implant materials because of their composition made of physiologically essential minerals and lack of commonly used rare-earth alloying elements. This study documents the specific role of nanometric intermetallic particles (IMPs) on the *in vitro* and *in vivo* biocorrosion behavior of two ZX-lean alloys, Mg–Zn1.0–Ca0.3 (ZX10) and Mg–Zn1.5–Ca0.25 (ZX20) (in wt.%). These alloys were designed according to thermodynamic considerations by finely adjusting the nominal Zn content towards microstructures that differ solely in the type of phase composing the IMPs: ZX10, with 1.0 wt.% Zn, hosts binary Mg_2Ca-phase IMPs, while ZX20, with 1.5 wt.% Zn, hosts ternary IM1-phase IMPs. Electrochemical methods and the hydrogen-gas evolution method were deployed and complemented by transmission electron microscopy analyses. These techniques used in concert reveal that the Mg_2Ca-type IMPs anodically dissolve preferentially and completely, while the IM1-type IMPs act as nano-cathodes, facilitating a faster dissolution of ZX20 compared to ZX10. Additionally, a dynamically increasing cathodic reactivity with progressing dissolution was observed for both alloys. This effect is explained by redeposits of Zn on the corroding surface, which act as additional nano-cathodes and facilitate enhanced cathodic reaction kinetics. The higher degradation rate of ZX20 was verified *in vivo* via micro-computed tomography upon implantation of both materials into femurs of Sprague Dawley® rats. Both alloys were well integrated with direct bone–implant contact observable 4 weeks *post operationem*, and an appropriately slow and homogeneous degradation could be observed with no adverse effects on the surrounding tissue. The results suggest that both alloys qualify as new temporary implant materials, and that a minor adjustment of the Zn content may function as a lever for tuning the degradation rate towards desired applications.

4.1 Introduction

Biodegradable alloys made from magnesium (Mg) with additions of zinc (Zn) and calcium (Ca) represent new biomaterials for the temporary treatment of cardiovascular and musculoskeletal conditions [1-8]. These denominated ZX alloys are especially attractive in light of their biological safety. This is a fundamental prerequisite for every biomaterial, but is even more so for those that are designed to degrade in the body. Because all constituents, i.e. Mg, Zn and Ca, exist in the human body as essential minerals, the organism already has the pathways required to safely metabolize the implant [9]. Among the three elements, Zn alone is a trace element in the human body, while Mg and Ca are mass elements. This means that the release of Zn must be more closely controlled than that of Mg and Ca. With both the Zn alloy content and its release, concomitant with the degradation rate of the overall alloy, kept low, there is, however, no reason for concern, and artificial distribution or accumulation can be prevented [9].

The above alloys differ from a variety of Mg-based alloys that contain rare-earth elements (REE) or other non-physiological elements such as aluminum (Al). While supposedly suitable for biomedical applications, the biological fate of such elements is at best unknown. Increasing awareness thereof is visible in recent reports, which show that REE elements accumulate in organs [9, 10] and bone tissue [11, 12]. The body clearance of Al is also a topic of debate, because Al is suspected of having adverse effects on the nervous system and may be implicated in Alzheimer's disease [13]. The use of such alloying elements in degradable biomaterials is therefore discussed controversially.

The deployment of ZX alloys circumvents these biosafety concerns, but the challenges common to Mg-based implant materials still apply. These involve the difficulty of attaining simultaneous control over the rate and homogeneity of material degradation while assuring sufficient mechanical strength and ductility. Lean ZX alloys, characterized by an alloying-element content as low as or below 1 at.%, satisfy this combination of properties desired, by combining high strength and high ductility with a slow and homogeneous dissolution [5]. The mechanical performance of these lean ZX alloys relies critically on the presence of nanometric intermetallic particles, hereafter referred to as IMPs [14]. The precipitation of these IMPs is tuned by processing means [14] towards a large number density and small size. In this fine dispersion, the IMPs can effectively function during hot forming as obstacles to grain-boundary motion [15] and thus ensure a fine-grained microstructure, which is crucial for simultaneous occurrence of high strength and ductility.

In terms of corrosion processes, the chemical composition, i.e. the phase type, of these IMPs needs to be considered. Two types of intermetallic phase are relevant in this alloy system and in the

temperature regime relevant to its processing (roughly 250 – 350 °C): a binary Laves-type Mg_2Ca phase and a ternary IM1 phase with a reported composition range of $Ca_3Mg_xZn_{15-x}$ (4.6 ≤ x ≤ 12, in at.%) [7, 16, 17]. With Ca being less and Zn more electropositive than Mg, respectively, the former IMP type generally presents the local anode relative to Mg, and the latter the local cathode [3, 4, 7, 18]. In fact, the preferential dissolution of Mg_2Ca in ZX-alloys has been observed [3, 7], and a large volume fraction of this anodic phase was associated with high macroscopic corrosion rates [1]. Cha et al. [3] showed that the presence of Zn in Mg_2Ca can effectively reduce the potential difference between this intermetallic phase and pure Mg, which entails a change in the dissolution behavior of the Mg_2Ca phase from anodic characteristics to a dissolution rate that is comparable to that of the matrix phase. Consequently, a macroscopically homogeneous degradation front was observed [3]. These results demonstrate the importance for a detailed understanding of the elemental distribution in the various phases of an alloy. Here, the elemental distribution of Zn is especially important in order to understand and describe the role of the Mg_2Ca phase in the macroscopic degradation behavior.

The ternary IM1 phase is suggested to be cathodic to Mg owing to its high Zn content [19, 20]. Although the phase's corrosion potential has – to the best of our knowledge – not been determined in literature, its higher corrosion resistance compared to the Mg matrix has been reported [7, 18]. We recently expanded this understanding through a TEM-based study that unveiled the detailed dissolution processes of the IM1 phase on the nanoscale [21]. IM1-phase dissolution is characterized by cathodically polarized dealloying, manifested in the preferential dissolution of Ca and Mg and simultaneously retained Zn, generating a gradual ennoblement of the IM1 phase with progressing dissolution [21]. However, due to the local scale of these observations, obtained by TEM on individual nanometric IMPs, their impact on the macroscopic degradation behavior, specifically the resulting rate of dissolution, cannot be easily forecast. Literature [7, 18] suggests that a larger volume fraction of the ternary phase can be associated with a higher macroscopic degradation rate. However, in such studies the IM1 phase co-existed with the Mg_2Ca phase, which limits the access for an understanding of its individual role in the macroscopic corrosion behavior of ZX alloys. With regard to the lean ZX alloys of this study, it is in fact unknown to date whether the nanometric size and the low volume fraction of either the Mg_2Ca- or IM1-type IMPs may be even subcritical as to make an impact on the overall material degradation.

It was thus the aim of this study to investigate the specific role that these two types of IMP and Zn play in the *macroscopic* corrosion behavior, i.e. at the scale relevant to implant applications. In the course of this study we also aimed at answering the question of whether by variation of the

nominal Zn content, and thereby in turn by tuning the phase type of the nanometric IMPs, the global degradation rate can be controlled.

Identifying model materials suitable to study the influence of individual microstructural features on the macroscopic corrosion behavior is indeed challenging. A common approach to governing a distinct intermetallic-phase type is heat treatment. This, however, often causes coarsening of grains or of the intermetallic phases, leading to different levels of solid solubility in the matrix or to segregation at grain boundaries [22]. Likewise, modifying the nominal chemical composition, while it can produce the desired difference in the primary intermetallic phase, also often generates a change in grain size, the volume fraction of phases, or their distribution (along grain boundaries vs. interior of the grains) [6, 18]. Because all of these microstructural characteristics are known to impact local corrosion processes in Mg alloys [23], it is difficult to separate their role from that of intermetallic phases in their effects on the macroscopic corrosion behavior. Lastly, the co-presence of different intermetallic phases makes it challenging to disentangle the individual roles of each IMP phase type.

To this end, on the basis of thermodynamic calculations we designed two alloys, which differ only in their IMP type while other microstructural characteristics were kept virtually constant. The *in vitro* degradation behavior of the resulting alloys was investigated using the hydrogen-gas evolution method and electrochemistry protocols. Complementary high-resolution microscopy based on TEM, with spatially resolved chemical information, was employed to reveal the phenomena at the origin of the biodegradation behavior. The relevance of the *in vitro* observations made to the *in vivo* situation was explored by implanting the alloys into the femurs of a small-animal model and monitoring their degradation via micro-computed tomography (μCT). The results show that nanometric IM1-type IMPs act as nano-cathodes and thus accelerate global implant degradation compared to a ZX alloy containing Mg_2Ca-type IMPs. In both alloys, solute Zn redeposits in the form of nanometric metallic clusters, which act as additional nano-cathodes to dynamically increase the cathodic reaction kinetics.

4.2 Experimental details

4.2.1 Thermodynamic calculations

Thermodynamic calculations of possible phases in ZX were performed using the Pandat™ software package for multicomponent systems, Pandat_2018 [24], taking input from the MatCalc database mc_mg_v1.009 [25]. The calculations assume thermodynamic equilibrium.

4.2.2 Material processing

Ingots of two Mg–Zn–Ca-lean alloys with nominal composition Mg–Zn1.0(0.37)–Ca0.3(0.18) (in wt.% (at.%)), referred to as ZX10, and Mg–Zn1.5(0.56)–Ca0.25(0.15) (in wt.% (at.%)), referred to as ZX20, were alloyed and cast in graphite crucibles. For both alloys distilled, ultrahigh-purity (XHP) Mg (99.999%) [26], and high-purity Zn (99.999%) and Ca (99.99%) were used to avoid precipitation of impurity-derived cathodic intermetallics [27]. The ingots (with a diameter of 55 mm and a length of 150 mm) underwent a homogenization heat treatment at 350 °C/ 12 h plus 450 °C/ 8 h, were air-cooled, and finally aged at 250 °C for 0.5 h in order to precipitate the IM1 phase.

The ingots were shaped into 6 mm rods by indirect extrusion at an extrusion ramp speed of 18 mm min^{-1}. An extrusion temperature of 330 °C was chosen for both alloys based on the thermodynamic calculations conducted in this study, which exclusively predicted the binary Mg$_2$Ca phase for the ZX10 alloy and exclusively the ternary IM1 phase for the ZX20 alloy at this temperature. The nominal composition of the alloys was determined by inductively-coupled plasma atomic-emission spectrometry (ICP-AES), which entails a relative error of 5% (instrument uncertainty). The impurities were quantified by glow-discharge mass spectrometry (GDMS), which entails a relative error of 20% (instrument uncertainty).

XHP Mg without the addition of alloying elements was extruded to 6 mm rods and used as a reference material for the hydrogen-gas-evolution analysis and electrochemical characterization.

4.2.3 Transmission Electron Microscopy

All samples for transmission electron microscopy (TEM) were prepared as standard disks of 3 mm diameter.

Specimens for microstructural investigation were prepared from the bulk extruded bars via cutting discs of about 1 mm in thickness. The discs were mechanically ground to about 80 μm thickness, followed by Ar$^+$-ion milling to obtain electron transparency (PIPS™ II from Gatan.). Ion milling was performed at liquid-nitrogen temperature to prevent changes to the microstructure.

TEM imaging and chemical analysis of the microstructure were performed in an FEI Talos™ F200X operated at 80 kV in bright-field (BF) TEM or scanning TEM (STEM) mode with a high-angle annular dark-field (HAADF) detector for atomic-number (Z) contrast. Quantitative chemical information was obtained by energy-dispersive X-ray spectroscopy (EDS) using a large collection-angle detector (FEI Super-X detector). The spectra of intermetallic particles were acquired in thin areas of the TEM foil to assure that the respective IMP occupied the entire TEM-foil thickness, thus avoiding the contribution of Mg matrix to the signal. The spectra obtained were analyzed using the QMap function in Cliff-Lorimer mode using the ESPRIT software from Bruker. The number density N of the IMPs was evaluated by manual counting of the precipitates in a given area and their size was determined by manually measuring the diameter d in ImageJ software. The TEM-foil thickness, necessary to estimate N of the IMPs, was determined from stereographic pairs of images taken at $-15°$ and $+15°$. The volume fraction of the IMPs was estimated from N and d, assuming spherical morphology.

To characterize the corrosion-product layer forming on the corroding Mg alloys, bulk specimens were mechanically polished (¼ µm diamond paste with ethanol used as a lubricant) and immersed in simulated body fluid (SBF) under physiological temperature and pH of 37 °C and 7.4, respectively (for the composition of the SBF see Table 2.1, Table 2.2, and Ref. [28]). The pH was adjusted by constantly flushing the SBF with 6.7% CO_2 (rest air). The CO_2 concentration of 6.7% was chosen based on the ionic strength of the SBF used to achieve the pH value desired. Following an immersion time of 24 h, the corrosion attack was terminated by carefully rinsing the specimens first in water and then in ethanol, each for 5 s. Cross-sectional TEM (xTEM) specimens of the corrosion-product layer were prepared using the Gatan cross-section kit. Here, two Mg-alloy plates were glued (G1 epoxy glue, Gatan) with their corrosion-product layers facing each other, forming a sandwiched assembly. Cross-sections of these sandwiches were cut, resulting in disks of 3 mm diameter, which were mechanically thinned and finally Ar^+-ion milled to obtain electron transparency. TEM imaging and chemical mapping of the corrosion products formed were performed in the same way as stated above.

4.2.4 *Hydrogen-gas evolution*

The corrosion rate was quantified via the hydrogen-gas (H_2) evolution method [29] using a setup suitable for slow-degrading Mg samples as described in [27]. Immersion was conducted in the SBF described above. An online pH-buffering system was used with a controlled gas inlet for pure CO_2 to maintain the pH at 7.40 ± 0.05 during the entire immersion time. Prior to immersion, the specimens ($n = 3$) with a surface of 4.13 ± 0.14 cm² were mechanically ground with SiC4000 paper and rinsed with ethanol. A volume of at least 100 ml SBF per cm² sample surface was used, thereby well

exceeding the minimum value defined by ASTM G 31–72 [30]. The H_2 evolution was related to the respective sample-surface area, giving the specific gas volume $v_{H2,ZX}$ in units of ml cm^{-2}. All data points were corrected for gas solubility and atmospheric pressure fluctuations, as described in Ref. [27], and $v_{H2,ZX}$ was normalized to the specific H_2 volume evolving for XHP Mg [27], $v_{H2,XHP-Mg}$. To that end, the H_2-evolution data as a function of immersion time were linearly fitted for XHP Mg via separate fits for 0 – 30 h and 30 – 340 h to account for the significant change in slope after 30 h of immersion. The data for ZX10 and ZX20 were then normalized with respect to the linear fits of XHP Mg. The error bars reported correspond to the standard deviations of the three samples tested, considering also the R^2 value of the linear fit for XHP Mg.

4.2.5 *Electrochemistry*

Specimens were electrically contacted using a Cu wire soldered to the back of the specimens and subsequently embedded in 2-component epoxy (RenLam® LY 113 / Ren® HY 97-1). Immediately preceding insertion into the electrochemical cell, the samples were mechanically ground using SiC2500 grinding paper and ethanol as a lubricant, followed by thorough rinsing with ethanol and compressed-air drying.

The electrochemical investigations were conducted using a standard three-electrode electrochemical cell (flat cell with V = 300 ml) equipped with a Pt-mesh counter electrode and an Ag/AgCl reference electrode. All potentials are reported relative to the standard-hydrogen electrode (SHE). Measurements were carried out with a PGSTAT101 potentiostat (Metrohm Autolab).

Figure 4.1: Polarization strategy for the investigation of cathodic reactivity evolution with progressing material degradation.

Potentiodynamic polarization (PDP) sweeps in the anodic direction, preceded by an open circuit potential (E_{OCP}) immersion period of 300 s to achieve a near-steady state, were performed from -250 mV to +400 mV with respect to the E_{OCP} at 300 s ($E_{OCP,300}$) or until a steep current increase was observed. A scan rate of 1 mV s^{-1} was applied. PDP sweeps were conducted under simulated-body

conditions as defined above. The pH of the SBF was controlled to 7.40 ± 0.05 by adjusting the atmosphere of a cell-culture incubator (HeraCell® 150 CO_2 incubator, Heraeus) to 6.7% CO_2, with the incubator housing the entire electrochemical cell. The pH value was controlled online with an external pH meter and never exceeded 7.50.

Potentiodynamic polarization sweeps in the cathodic direction were preceded by a defined sequence of (i) E_{OCP} period for 1800 s ($E_{OCP,1800}$) to achieve a near-steady state, and (ii) anodic potentiostatic polarization at a potential of +100 mV with respect to $E_{OCP,1800}$ for various polarization times between 0 and 30 min (Figure 4.1). It is important to note that the polarization potential value during potentiostatic polarization was for all materials well below the reversible potential of Zn/Zn^{2+} [31]. Cathodic PDP sweeps (iii) were performed from +100 mV to -500 mV with respect to $E_{OCP,1800}$ at a scan rate of 1 mV s^{-1}. During the potentiostatic polarization, the anodic current density i and charge density q transferred across the working-electrode surface were recorded. Cathodic PDP sweeps were conducted in 0.1 M NaCl at a pH of 6.00 ± 0.02 (adjusted by HCl) at room temperature. MiliQ water ($\geq$ 18 MΩ cm^{-1} at RT) was used to prepare the electrolyte. The cathodic polarization strategy was defined as a model experiment to study the role of local cathodes on the surfaces of ZX alloys in detail. For this model experiment NaCl combined with a slightly acidic pH was chosen over SBF to prevent the formation of a dense corrosion-product film (Ca–P–O-containing film characteristic of Mg corroding in body fluids [32, 33]) and to minimize the formation of a thick magnesium hydroxide ($Mg(OH)_2$) surface film, respectively. This choice allows to probe the electrochemical response closer to the metal–corrosion-product layer interface.

4.2.6 *In vivo evaluation*

18 male Sprague Dawley® rats of 140 to 160 g weight and 5 weeks of age were deployed. These animals were divided into 2 groups: 9 animals treated with ZX10, and 9 animals treated with ZX20.

Both alloys were machined into pins of cylindrical shape with a diameter of 1.6 mm and a length of 8 mm. Following fabrication, the implants were cleaned in ethanol in an ultrasonic bath, packaged sterile, and sterilized with gamma radiation of 51 kGy. The outer packaging prevented corrosion attack prior to implantation. The cylindrical implants were inserted transcortically into the femoral bones (overall, 18 implants per alloy) under general anesthesia. The entire surgical procedure and *post operationem* (post-op) treatment are described in Ref. [8]. All animals tolerated the operation well and showed unrestricted weight-bearing post-surgery. No rats died during the surgical procedure and all animals gained normal weight throughout the study period. The animal experiments were performed according to approved ethical standards and were authorized by the

Austrian Ministry of Science and Research (accreditation number BMWFW-66.010/0122-WF/V/3b/2014).

Micro-focused computed tomography (µCT) scans were performed after euthanization at predefined times of 4, 26 and 52 weeks post-op. To this end, the explanted bones were embedded as described below and scanned using a Siemens Inveon™ Research Workplace with Acquisition 1.2.2.2 software. A high-resolution protocol performed at 80 kV, 500 µA and an exposure time of 1050 ms was applied. The effective pixel size was 18.93 µm [10].

4.2.7   Histology

After euthanization at 4, 26, and 52 weeks post-op, the explanted implant–bone samples were embedded in Technovit 9100 New® (Heraeus Kulzer, Wehrheim, Germany) according to the protocol described by Willbold and Witte [34]. Samples were fixed in 3.7% formalin at 4 °C for 48 h. Following dehydration in increasing grades of isopropanol (70%, 96% and 100%) and xylol, the samples were infiltrated (3 days in a pre-infiltration solution plus 7 days in an infiltration solution according to the manufacturer's instructions), and finally polymerized in methyl-methacrylate (MMA) (Technovit 9100 New®).

The bone samples were cut in 5 µm thick slices using a rotation microtome (Histocom, HM 355 S, Vienna, Austria) with a D tungsten carbide knife (Histocom, 152,120, Vienna, Austria) and dried at 37 °C for 3 days [35]. The slices were then deplastified using xylol and 2-methoxyethyl acetate and rehydrated in decreasing grades of isopropanol (100%, 96%, 70%) and distilled water. The rehydrated slices were stained with 0.1% toluidine blue O (Sigma, Vienna, Austria) to reveal the general bone morphology, and to follow the bone remodeling and potential body reaction upon implant placement. The slices were submerged in the staining solution for 40 s, washed in distilled water, dehydrated with a series of isopropanol and xylol and mounted in Eukitt® (Sigma-Aldrich Handels-GmbH, Vienna, Austria). The entire staining procedure took place at room temperature. The histological slices were imaged in an Aperio ScanScope scanner (Aperio Technologies, Vista, Calif., USA), and six slices per material and time point were prepared.

4.2.8   Statistical analysis

A statistical analysis of the *in vivo* degradation at different times was performed using Mann-Whitney U tests, comparing two independent samples per time point via the IBM SPSS® Statistics 20 program (SPSS Inc., Chicago, USA). All further data are reported as average ± standard deviation calculated by Microsoft Excel® 2010 (Microsoft Corporation, Redmond, USA).

4.3 Results

4.3.1   Alloy design for model materials

Figure 4.2 shows the phase diagrams generated by thermodynamic calculations for the designed alloys Mg–Zn1.0(0.37)–Ca0.3(0.18) (in wt.% (at.%)), denominated ZX10, and Mg–Zn1.5(0.56)–Ca0.25(0.15) (in wt.% (at.%)), denominated ZX20. These material compositions are the result of the alloy design, which aimed at two materials each with only one intermetallic-phase type, i.e. exclusively either the binary Mg_2Ca or the ternary IM1 phase. It seems worth emphasizing that these two alloys differ in their nominal Zn content by only as little as 0.5 wt.%, equivalent to 0.19 at.%. Note that a minor adjustment of the Ca content by as little as 0.05 wt.%, equivalent to 0.03 at.%, was required to achieve the best balance of the change in phase type with the simultaneous desire to generate a comparable volume fraction of the IMPs and the possibility of constant thermomechanical processing conditions for both materials.

As a boundary condition for the calculations, the maximum total alloying content was set to 1 at.%, following our lean-alloy concept [5, 36, 37]. This allows for a solution-heat-treatment window for the relevant elements constituting the primary intermetallic phase, which is beneficial to avoid coarse precipitation [38] and to ease material formability [39]. Additionally, the Zn content was chosen to be as high as possible to benefit improved mechanical properties via solid-solution strengthening [2]. Lastly, a processing temperature of 300 – 350 °C was envisaged, limited to the lower end by increasing extrusion forces, and to the higher end by grain growth detrimental to the mechanical performance [14, 40].

With these boundary conditions in mind, a process temperature of 330 °C was chosen, balancing an appropriate extrusion speed and small grain size. At this temperature, ZX10 is predicted to host exclusively the binary Mg_2Ca phase, whereas ZX20 is predicted to host exclusively the ternary IM1 phase (Figure 4.2). The predicted phase fractions as a function of temperature in Figure 4.2a and the isothermal cut at 330 °C in Figure 4.2b reveal that either a slight temperature shift or a slight compositional change would result in a mixture of the intermetallic-phase types of interest and would thus be undesirable for this study. It is important to realize that thermodynamic equilibrium is the basis of these calculations. With this in mind, it was yet to be experimentally investigated whether these simulations might successfully predict the microstructure resulting from extrusion, with the latter process possibly offering too little time at elevated temperature to achieve equilibrium. For this reason a thorough microstructural analysis using TEM preceded the corrosion studies.
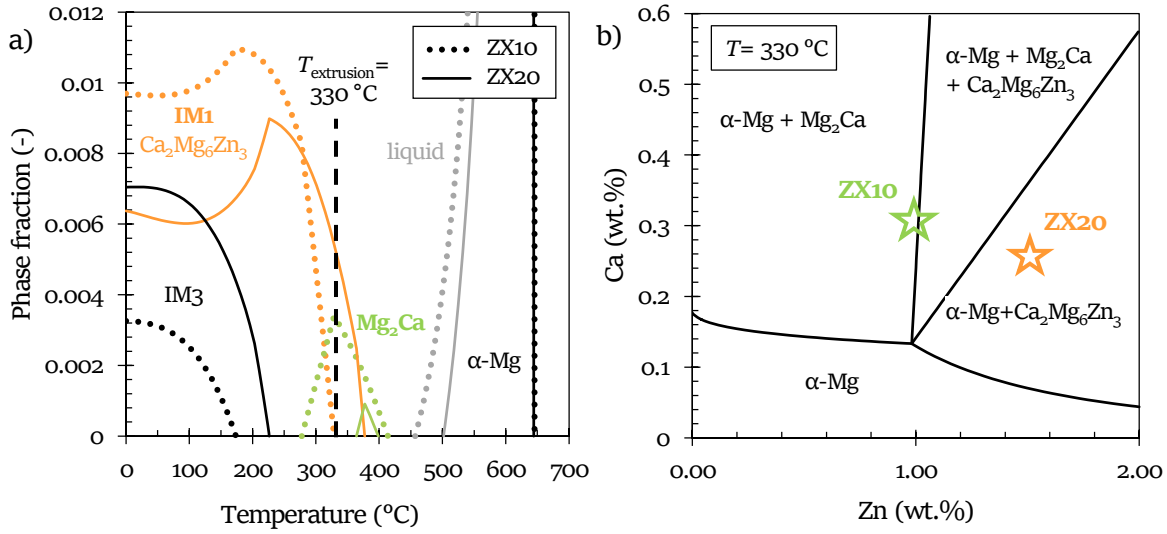
Figure 4.2: Thermodynamic calculations at the basis of the alloy design. (a) Phase fraction as a function of temperature for the two alloys, ZX10 and ZX20 designed. The extrusion temperature ($T_{extrusion}$) chosen at 330 °C is marked. (b) Isothermal cut of the phase diagram at 330 °C for varying Ca and Zn content, where ZX10 and ZX20 are marked with stars. Their composition was chosen based on the simulations, which predict the intermetallic phase formed as either binary Mg_2Ca phase (ZX10) or ternary IM1 ($Ca_2Mg_6Zn_3$) phase (ZX20).

4.3.2 Material microstructure

Table 4.1: Chemical compositions of ultrahigh-purity ZX10 and ZX20. The values given in ppm are by weight.

	Zn	Ca	Mn	Si	Fe	Cu	Ni
	(wt.% (at.%))	(wt.% (at.%))	(ppm)	(ppm)	(ppm)	(ppm)	(ppm)
ZX10	0.96 (0.36)	0.32 (0.20)	1.9	2.0	1.0	0.32	0.07
ZX20	1.48 (0.56)	0.24 (0.15)	2.1	1.7	0.88	0.28	0.04

Table 4.1 gives the effective compositions determined by atomic absorption spectrometry (Zn and Ca) and by glow discharge mass spectrometry (other elements), and reveals the close match with the respective target compositions. Figure 4.4 presents the microstructure characteristic of the extruded ZX10 and ZX20 alloys. Both consist of the primary α-Mg phase and globular secondary-phase particles of nanometric dimensions. The TEM bright-field (BF) images in Figure 4.4a and b reveal the alloys' grain morphology, which is roughly equiaxed, and their grain size, which is comparable for both materials at an almost fully recrystallized microstructure, with 2.0 ± 0.2 μm for

ZX10 and 2.2 ± 0.3 µm for ZX20, as determined from complementary light-microscopy images in Figure 4.3.

In the TEM-BF images, nanometric particles are visible. They appear to be both homogeneously distributed within the grains and also present at the grain boundaries. Complementary STEM-EDS chemical maps (Figure 4.4c and d) reveal that the particles in ZX10 are enriched in Ca, visible in green in Figure 4.4c, and that those in ZX20 are enriched in Ca and Zn, visible in yellow in Figure 4.4d. The yellow color results from the chromatic superimposed signal for Ca (green) and Zn (red). Mg is not included in these maps for the sake of legibility, as the signal would be dominated by Mg considering the small amounts of Ca and Zn in these lean alloys. It is worth emphasizing that – as targeted – only one type of IMP is present in each alloy's respective microstructure. Only occasionally, individual IMPs with altered compositions were detected. However, the number count of these "foreign" IMPs was negligibly low, with an approximate fraction of a few per mill (‰) relative to the main IMP type.
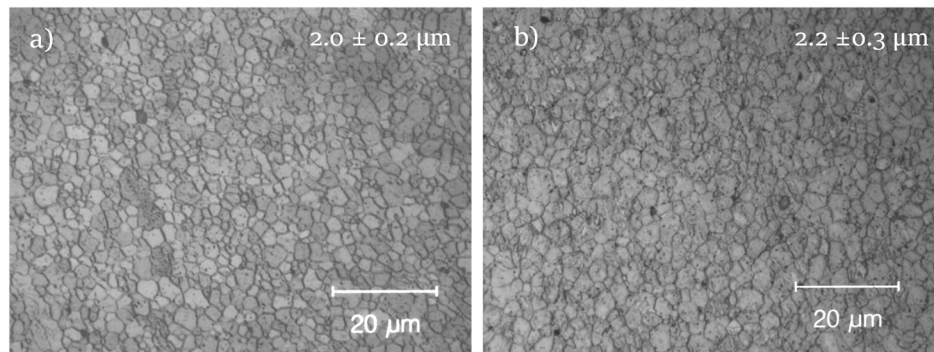
Figure 4.3: Light micrographs revealing the grain sizes and morphology of (a) ZX10 and (b) ZX20. The average grain size for each alloy is indicated on the top right.

The insets to Figure 4.4c and d show that the IMPs have approximately globular morphology and sizes of 80 ± 35 nm in diameter for ZX10 and 100 ± 39 nm for ZX20. The IMPs in both materials were non-coherent with the Mg matrix. Quantified EDS spectra (Figure 4.4 e and f) allowed identifying and assigning the phases: with 68 ± 2 and 32 ± 2 at.% for Mg and Ca, respectively, the primary intermetallic phase in ZX10 was confirmed to be the binary Mg_2Ca phase, as predicted by the calculations (Figure 4.2). Only a small amount of Zn, as small as 0.35 ± 0.05 at.%, was detected as solute in this phase. Regarding ZX20, the IMPs are composed of a ternary phase made of Mg, Zn and Ca, as predicted by the calculations (Figure 4.2). The ternary IM1 phase is, according to literature [16], known to have a compositional range that originates from a variation of the Mg-to-Zn ratio. In ZX20, the IMPs' composition was determined to be 60 ± 2, 25 ± 2 and 15 ± 2 at.% for Mg, Zn and Ca, respectively. This is roughly equivalent to $Ca_3Mg_{12.3}Zn_{5.1}$, and agrees well with the phase IM1 proposed
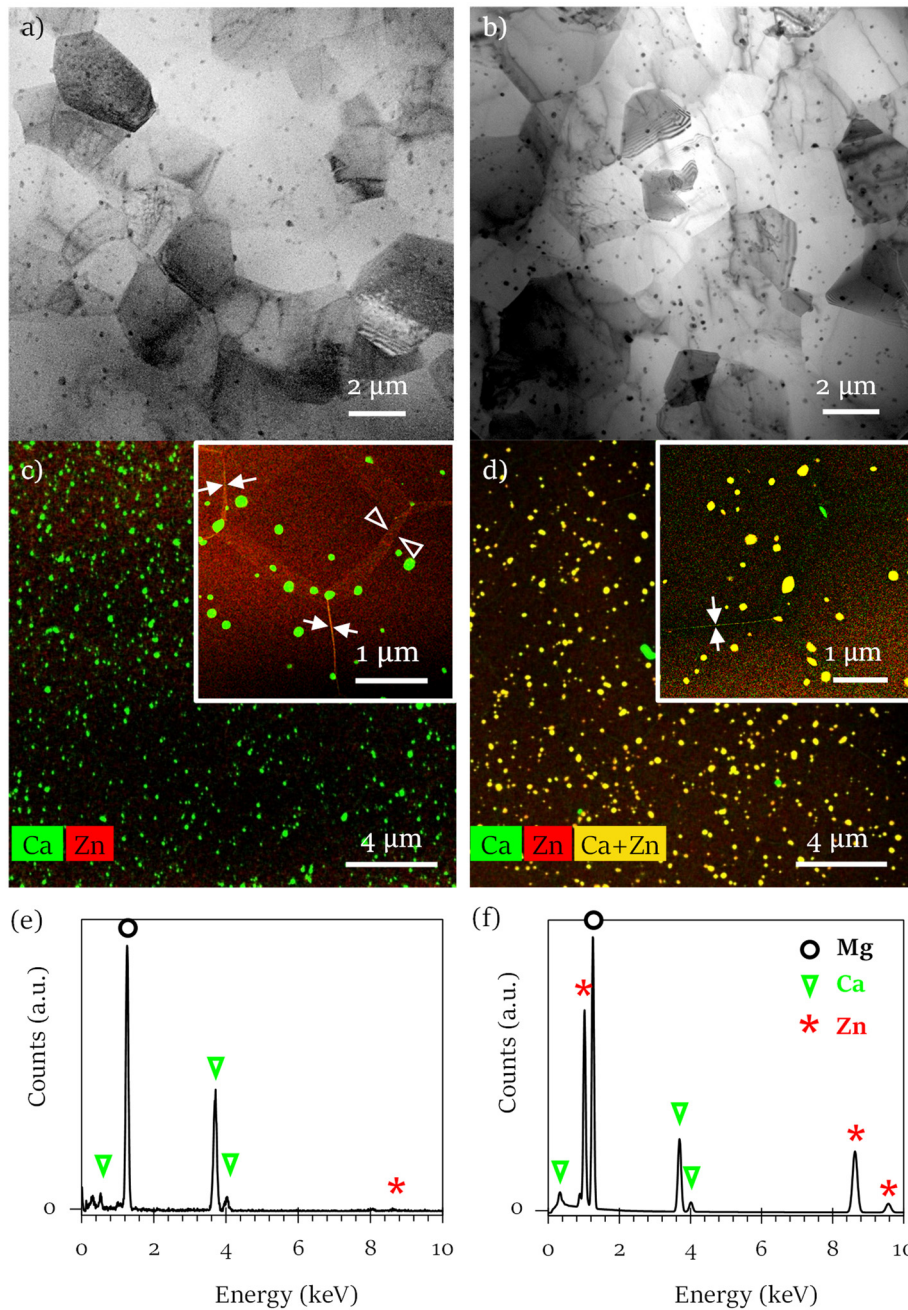
Figure 4.4: Microstructure of ZX10 and ZX20. (a, b) TEM bright-field images showing the grains and dispersion of precipitates in (a) ZX10 and (b) ZX20. (c, d) STEM-EDS chemical maps revealing that the intermetallic phases in (c) ZX10 are rich in Ca, and in (d) ZX20 are rich in Zn and Ca. The insets to (c) and (d) show the elemental segregation at grain boundaries (white arrows). While those grain boundaries that are edge-on to the plane of view appear sharp (solid arrows), inclined grain boundaries appear blurred and broadened (empty arrow heads). (e, f) Quantified EDS spectra for the respective intermetallic phases reveal that the IMPs in (e) ZX10 are made of the binary Mg_2Ca phase and in (f) ZX20 are made of the ternary IM1 phase.

in [16], which had a compositional range given by $Ca_3Mg_xZn_{15-x}$ ($4.6 \leq x \leq 12$) as determined by electron-probe micro analysis (EPMA) with a reported estimated error of about 2 at.%. The slightly higher Mg content determined in both Mg_2Ca and IM1 phase relative to their expected content may be due to stray electrons originating from the Mg matrix.

For a full picture of elemental distribution within these alloys, the Mg-matrix composition was also quantified: while the matrix appeared to be almost entirely depleted in Ca in both materials, the Zn-solute content was at a comparable level of about 0.4 at.%. The elemental distribution within the respective primary IMP type and matrix is summarized for both alloys in Table 4.2.

Table 4.2: Nominal compositions of ZX10 and ZX20, and elemental compositions of their respective primary intermetallic particles (IMPs) and of their matrices, as determined by STEM-EDS. The Zn:Ca ratio in the nominal compositions relates to the atomic ratio.

	Nominal		IMP				Matrix			
		Zn:Ca	Mg	Zn	Ca	Zn:Ca	Mg	Zn	Ca	Zn:Ca
	wt.% (at.%)	(-)		(at.%)		(-)		(at.%)		(-)
ZX10	Mg–Zn1.0(0.37)–Ca0.3(0.18)	2.1	68 ± 2	0.35 ± 0.05	32 ± 2	0.01	bal.	0.37 ± 0.04	0.05 ± 0.01	7.4
ZX20	Mg–Zn1.5(0.56)–Ca0.25(0.15)	3.7	60 ± 2	25 ± 2	15 ± 2	1.7	bal.	0.44 ± 0.04	0.04 ± 0.01	11.0

Both Zn and Ca were found in enhanced concentrations at the grain boundaries (white arrows in the insets to Figure 4.4c and d). Despite this grain-boundary segregation, no additional phases precipitated at the grain boundaries.

4.3.3 Hydrogen-gas evolution

Monitoring the hydrogen-gas (H_2) formation upon immersion allows to access the corrosion rate of materials that have the hydrogen-gas evolution reaction as the primary cathodic reaction. As for Mg, 1 mol of oxidizing Mg generates 1 mol of H_2, which can be collected and quantified [29].

Figure 4.5 presents the cumulative H_2 volume collected by Hofstetter [36] for ZX10 and ZX20 upon their immersion in SBF. The data are plotted normalized to the gas volume evolving from XHP Mg and previously published in [27]. Figure 4.5 illustrates clearly that the H_2-evolution reaction strongly depends on the Zn content, as manifested in an increasing gas evolution with increased Zn content.

The difference in evolving gas volume between ZX10 and XHP Mg (corresponding to the dashed black line in Figure 4.5) is small, and only at about 1.5 times that of XHP Mg. In contrast, a significantly greater gas-release rate is established for ZX20 compared to ZX10 and XHP Mg already after a short immersion time, and this is maintained for the entire immersion period. In fact, the specific gas volume for ZX20 is initially about 3.5 times that of XHP Mg and steadily increases to a factor of 6.5 after about 2 weeks of immersion. With respect to the ZX20 vs. ZX10 ratio, the *in vitro* gas-release rate of ZX20 is about 1.3 times that of ZX10 in the beginning of the immersion and increases steadily to a factor of 4 after 2 weeks. These results thus allow to obtain an estimation of the *in vitro* dissolution rate, which for ZX20 significantly exceeds that of ZX10 (and XHP Mg). We refrain from a quantitative assessment of the *in vitro* degradation rate from the hydrogen-gas evolution method, which is known to be subject of large fluctuations [41]. The methodology of H_2 evolution does also not enable access to the corrosion mechanisms underlying the observed differences in dissolution rate. More specifically, it is not possible to derive from these data whether the higher nominal Zn content in ZX20 changes the anodic dissolution rates or whether the IMP type – adjusted by the Zn content – and thus the local cathodic activity is responsible for the increased dissolution rate. To this end, the alloys' electrochemical responses were studied under open-circuit potential and polarization conditions.
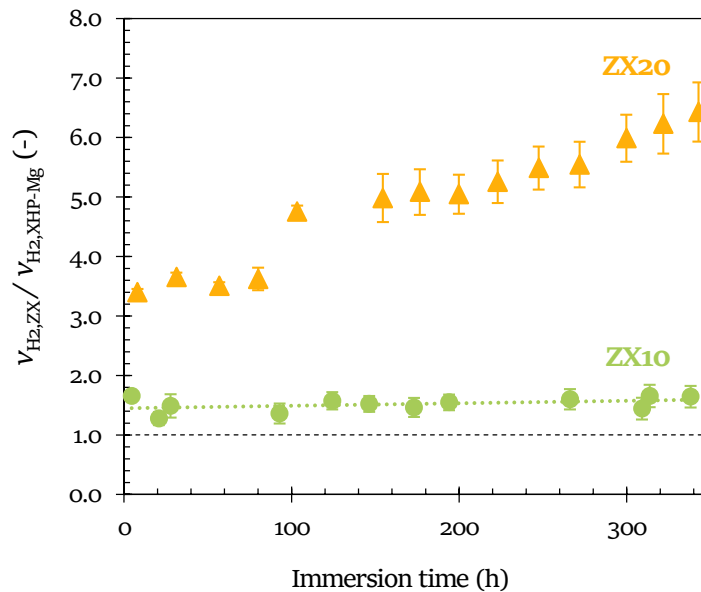
Figure 4.5: Cumulative hydrogen-gas (H_2) evolution as a function of immersion time under simulated body conditions. The specific gas volumes for ZX10 and ZX20 ($v_{H2,ZX}$) are reproduced from [36] and plotted normalized to that of XHP Mg ($v_{H2,XHP-Mg}$) [27]. The dotted line for ZX10 presents a linear trend, showing a slight increase of the normalized specific gas volume with immersion time. The dashed black line relates to the normalized gas volume of XHP Mg.

4.3.4 Electrochemical behavior in SBF

Figure 4.6 reveals the electrochemical responses of XHP Mg, ZX10, and ZX20 upon their immersion in SBF. The free-corrosion potential shifts towards more noble (i.e. higher) values with increased Zn content.

Figure 4.6a shows the evolution of the open circuit potential (E_{OCP}) over the course of 300 s. For all materials an initial steep increase followed by stabilization of the E_{OCP}, setting in rapidly after about 100 s of immersion, can be attributed to the formation of a surface corrosion-product film. The E_{OCP} at 300 s ($E_{OCP,300}$) shows an increasingly higher value for higher nominal Zn content, with an E_{OCP} of -1.67 ± 0.02, -1.63 ± 0.01 and -1.53 ± 0.01 V_{SHE} for XHP Mg, ZX10 and ZX20, respectively.
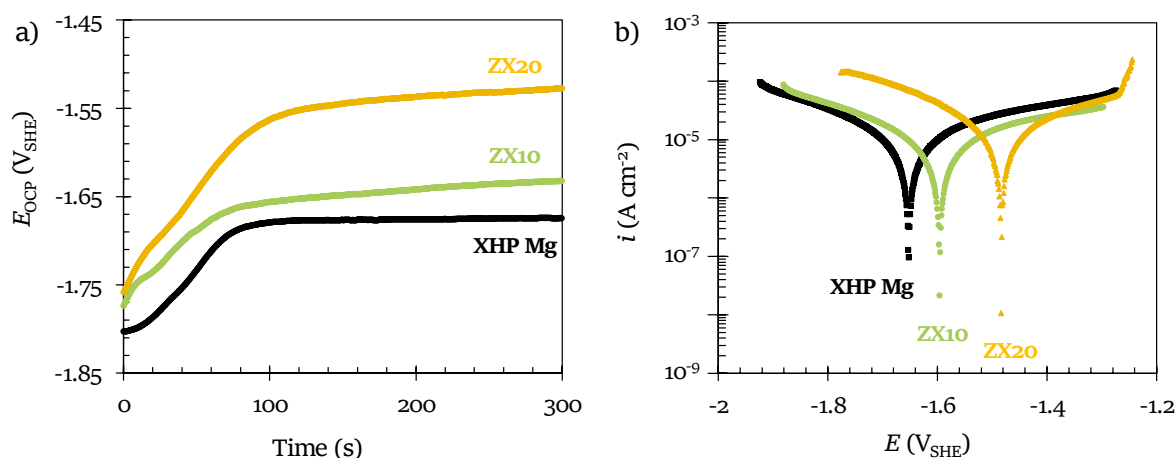
Figure 4.6: Electrochemical response of ZX10 and ZX20 under simulated body conditions. (a) Evolution of open-circuit potential, E_{OCP}, and (b) potentiodynamic polarization curves. XHP Mg was investigated as reference.

Figure 4.6b shows the evolution of the potentiodynamic polarization current response obtained after the stabilization time at E_{OCP} presented in Figure 4.6a. XHP Mg, included as a reference, was found to have the lowest corrosion potential (E_{corr}) (at ~-1.64 ± 0.03 V_{SHE}) among the materials tested. Adding Zn raised the corrosion potential to more positive values, with E_{corr} amounting to ~-1.59 ± 0.02 V_{SHE} for ZX10 and ~-1.48 ± 0.01 V_{SHE} for ZX20. While this E_{corr} shift indicates that the increasing Zn addition renders ZX20 presumably more 'noble' (i.e. less active) than ZX10 (and both more 'noble' than XHP Mg), the electrochemically more plausible explanation is found in the current shift of the cathodic branches observed for higher Zn content. In fact, the higher cathodic current density for ZX20 compared to ZX10 hypothesizes that larger hydrogen-reduction-reaction kinetics in ZX20 are the origin of the E_{corr} shift. In comparison, the cathodic branch of XHP Mg and ZX10 are almost congruent, and only marginally shifted towards higher cathodic current densities for ZX10.

The hypothesis that ZX20's electrochemical behavior is under cathodic control cannot be understood from the macroscopic PDP measurements alone because of the methodological limitation on providing mechanistic insights into the local reactive sites. In fact, PDP sweeps yield an electrochemical response according to mixed-potential theory, i.e. the potential measured integrates all local anodes and all local cathodes on the electrode surface. For this reason, complementary microscopical characterization was conducted, which makes possible the direct observation of the impact of corrosion attack on microstructure evolution and corrosion-product formation and composition.

4.3.5 *Cross-sectional TEM analysis of the corrosion-product layer*

Figure 4.7 displays the corrosion-product films formed on ZX10 (Figure 4.7a and b) and on ZX20 (Figure 4.7c and d) after 24 h of immersion in SBF. The white dotted lines mark the interface between the metal and the corrosion-product layer. The STEM-HAADF images in Figure 4.7 a and c reveal a two-layered corrosion-product film as previously described in [21]: the majority of corrosion product is composed of sponge-like, porous $Mg(OH)_2$ (for EDS chemical maps of Mg and O see Figure 4.8). On top of this spongy layer, at the interface with the electrolyte, a significantly thinner layer composed of Ca, O and P is present, and indicated by arrow heads in Figure 4.7a and c (for EDS chemical maps of O and P see Figure 4.8). The simultaneous presence of Ca, O and P in this layer indicates that it is composed of a calcium phosphate (CaP). The precipitation of CaP from biological fluids is characteristic of Mg biocorrosion [32, 33]. It should be also noted that the thickness of the corrosion-product layer is different in ZX10 compared to ZX20. However, the corrosion-product layer thickness cannot provide a direct measure of the corrosion rate, because it presents the net sum of corrosion-product formation and its dissolution in the electrolyte, with the latter being dependent on the corrosion-product stability. At the current stage it cannot be excluded that the different Zn contents in ZX10 and ZX20 entail differences in the corrosion-product resistance. Further studies on the effect of Zn on the properties of the corrosion-product layers forming on ZX-lean alloys are required to allow inferring the corrosion rate from the layer thickness.

The IMPs in ZX10 are revealed in the alloy's bulk. They are visible in the STEM-EDS chemical map of Figure 4.7b, but only faintly visible in the STEM-HAADF contrast (Figure 4.7a). This weak contrast is caused by the relatively small atomic-mass difference between Mg and Ca, the predominant Mg content in the Mg_2Ca phase, and the relatively high amount of Ca and P, both higher in Z than Mg, in the Ca–P–O-rich layer in the same image, which diminishes the contrast within the metallic area. Importantly, no evidence of IMPs or IMP remnants were found in the corrosion-product layer, neither in HAADF nor EDS mode. Their absence is proof that the dissolution rate of binary IMPs composed of Mg_2Ca is similar or even greater than that of the Mg matrix.
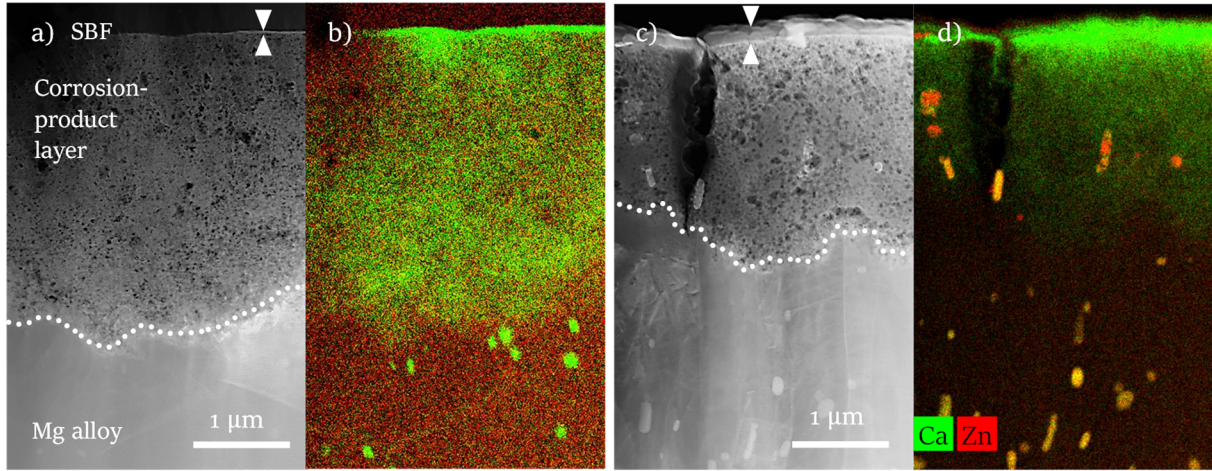
Figure 4.7: Cross-sectional imaging (xTEM) of the corrosion-product layer formed after 24 h of immersion under simulated body conditions for (a,b) ZX10 and (c,d) ZX20. (a,c) STEM-HAADF images revealing the morphology of the mature corrosion-product layer. The white dotted lines mark the interface between the Mg alloy and the corrosion-product layer. The white arrow heads mark the thickness of the Ca–P–O-rich precipitation layer; (b,d) show corresponding chemical maps of Zn and Ca.
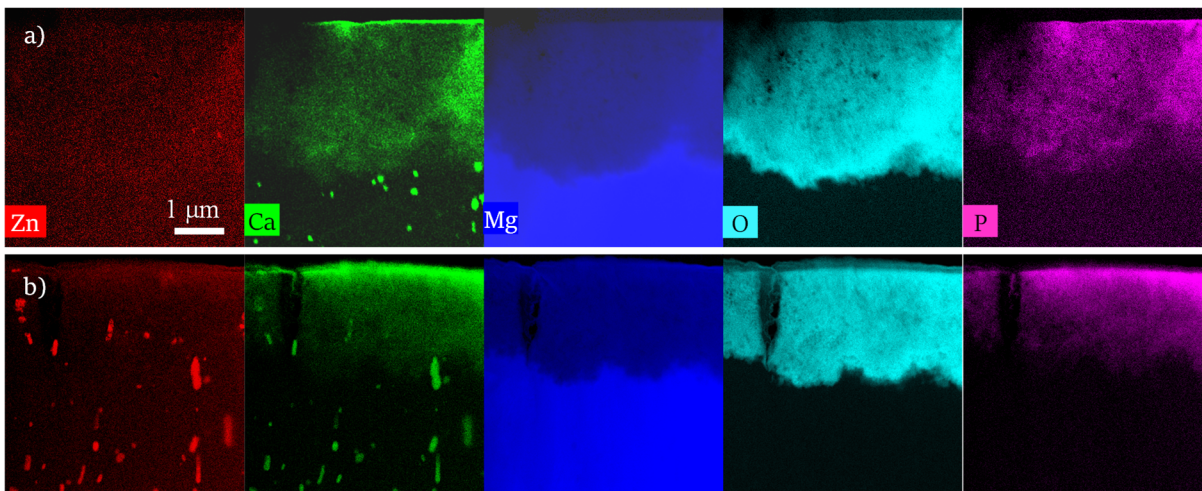
Figure 4.8: STEM-EDS chemical maps of the corrosion-product layer in cross-section, formed on (a) ZX10 and (b) ZX20. The scale bar and elemental color code are marked in (a).

The IMPs in ZX20 are likewise revealed in the alloy's bulk and visible in both the STEM-HAADF image in Figure 4.7c and in the corresponding STEM-EDS chemical map for Zn and Ca in Figure 4.7d. In both STEM modes, IMPs are also found embedded in the corrosion-product layer. Their size and morphology appears comparable to those in the bulk. Their presence proves that IMPs composed of the ternary IM1 phase have a higher corrosion resistance than the Mg matrix, presumably acting as local cathodes via nano-galvanic coupling as observed for a closely related ZX-lean alloy [21]. The presence of IMPs in the $Mg(OH)_2$ layer also indicates an inward-growing corrosion-product-film mechanism. Furthermore, from the STEM-EDS chemical analysis it is apparent that the IMPs in the corrosion-product layer differ in their chemical composition from those in the alloy's bulk. More specifically, IMPs present in the corrosion-product layer appear to be enriched in Zn, which is visible from a higher intensity of red, corresponding to the EDS signal chosen for Zn.

4.3.6 *Cathodic reactivity investigation with polarization strategy*

The role of local cathodes on the surface of ZX alloys was investigated in greater detail by means of electrochemical polarization experiments, with a focus on the cathodic reaction kinetics upon progressing material dissolution in a 0.1 M NaCl solution.

Figure 4.9a shows the evolution of E_{OCP} over the course of 1800 s prior to the polarization sequence. For both ZX alloys, an initial steep increase followed by a gradual stabilization of the E_{OCP}. In contrast, the increase E_{OCP} of XHP Mg was significantly less pronounced. Note the difference to the behavior observed in SBF (Figure 4.6a) where the E_{OCP} stabilizes rapidly after about 100 s, thus supporting that a (semi-)protective layer forms (presumably corresponding to the deposition of the Ca–P–O-rich layer (Figure 4.7 and Figure 4.8)) in SBF but – as expected and intended – absence of such in 0.1 M NaCl. As for the measurement in SBF, the E_{OCP} at 1800 s ($E_{OCP,1800}$) shows an increasingly higher value for higher nominal Zn content, with an E_{OCP} of -1.68 ± 0.01, -1.57 ± 0.01 and -1.47 ± 0.01 V_{SHE} for XHP Mg, ZX10 and ZX20, respectively. Interestingly, the onset potential at the beginning of immersion was for ZX10 at -1.74 ± 0.01 V_{SHE} slightly lower than for XHP Mg at -1.73 ± 0.01 V_{SHE} (Figure 4.9b).

An increasing degree of material dissolution was stimulated by potentiostatic polarization for various times at +100 mV relative to the $E_{OCP,1800}$ (Figure 4.9a). During this small anodic polarization, the current density i_{anod} (Figure 4.10a) and cumulative charge density q (Figure 4.10b) passing through the corroding interface were monitored as an indication of the dissolution rate under these conditions. i_{anod} increased first for about 200 s for XHP Mg, and about 300 s for both ZX10 and ZX20, before it progressively declined with further polarization time. Nevertheless, no polarity reversal occurred and i_{anod} was positive for the entire polarization time of up to 30 min, showing that all

materials for all times underwent anodic dissolution as intended. The values detected for i_{anod} were greater at all times for ZX20 compared to ZX10, and those of ZX10 were in turn greater than for XHP Mg. Concomitantly, a significantly greater total charge density q passed through the surface of ZX20 (amounting to about 0.07 C cm^{-2} after 30 min) compared to ZX10 ($q \approx 0.05$ C cm^{-2}), which in turn was greater compared to XHP Mg ($q \approx 0.04$ C cm^{-2}). This observation implies faster dissolution with increasing nominal Zn content under small anodic polarized conditions. This observation is in line with the greater amount of H$_2$ evolved for ZX20 (Figure 4.5) under open-circuit potential conditions.

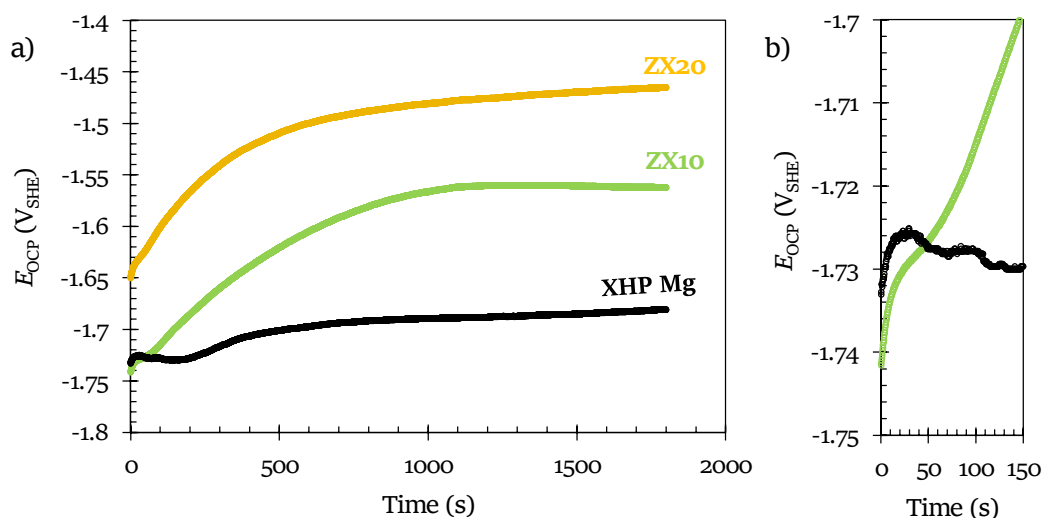**Figure 4.9**: (a) Evolution of the open circuit potential (E_{OCP}) in 0.1M NaCl prior to cathodic polarization for ZX10, ZX20, and XHP Mg. (b) Magnified view of the first 150 s immersion time for XHP Mg and ZX10.
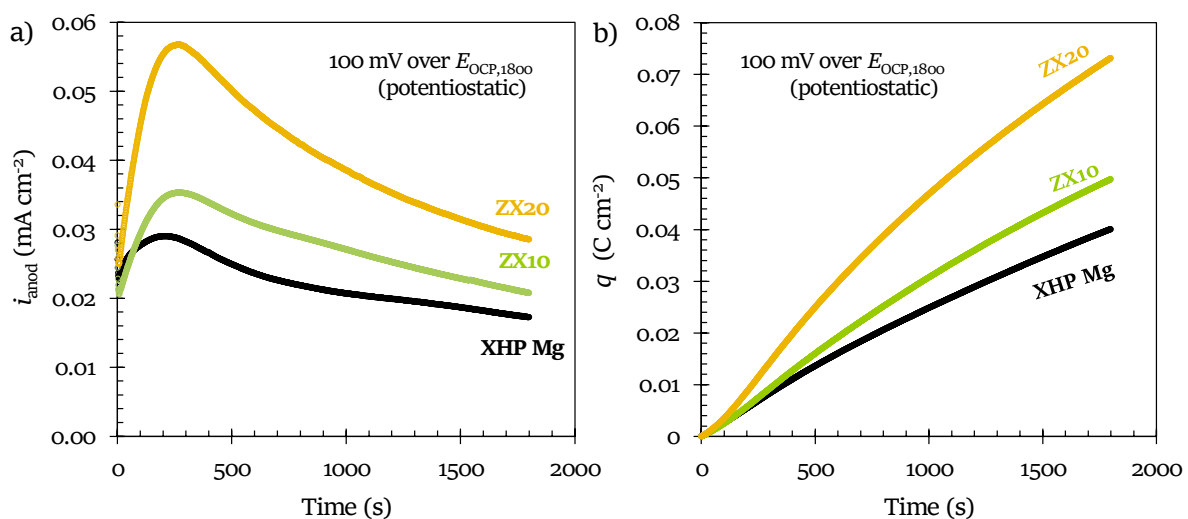
Figure 4.10: (a) Current density i and (b) corresponding cumulated charge density q as a function of time measured during small anodic potentiostatic polarization at 100 mV over $E_{OCP,1800}$ in 0.1 M NaCl.

Subsequently, a cathodic potentiodynamic polarization sweep was run from +100 mV to -500 mV vs. $E_{OCP,1800}$. The potential regime scanned (-1.4 to -2 V_{SHE}) still lies within the relevant potential domain for corroding Mg electrodes [42]. The precise potential established at the corrosion front, however, depends strongly on the Ohmic drop across the corrosion-product layer, and is experimentally not accessible. For this reason, a potentiodynamic sweep, which covers a rather large potential regime, was chosen over a potentiostatic polarization. Following this protocol the material can be polarized to a potential regime in that IMPs (or other microstructural features) are polarized if acting as cathodes in a nano-galvanic couple on the corroding surface.
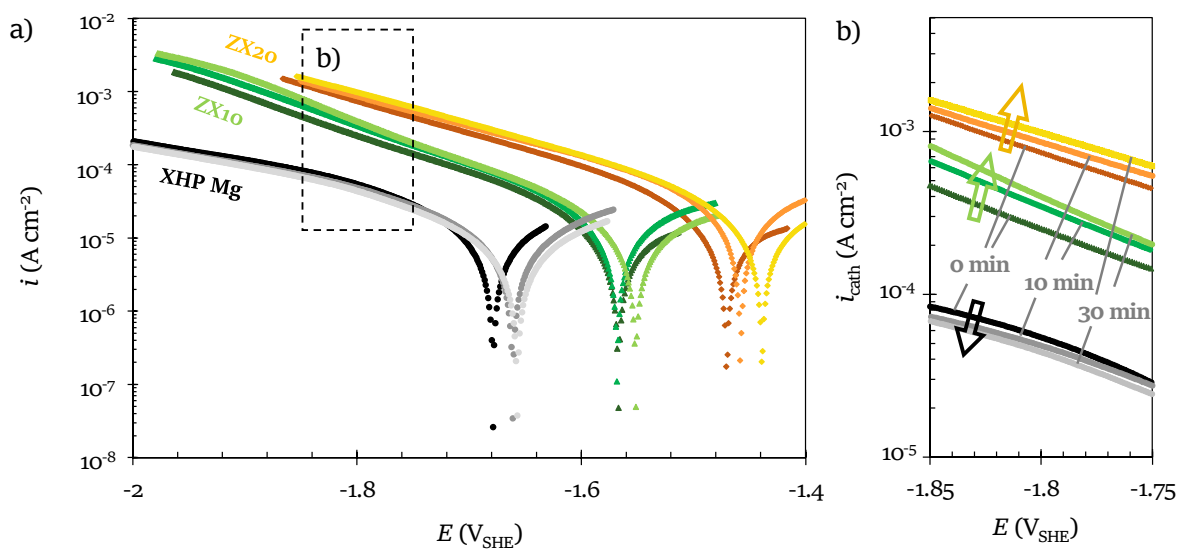
Figure 4.11: (a) Cathodic polarization response of ZX10, ZX20 and XHP Mg in 0.1 M NaCl following a small anodic potentiostatic polarization at 100 mV over $E_{OCP,1800}$ for 0, 10 and 30 min. The respective color intensity corresponds to the duration of anodic polarization and is indicated in (b). (b) Magnified view of the cathodic branch (see dashed rectangle in (a)). For ZX10 and ZX20 it shows a shift towards higher reaction kinetics with increasing immersion time, whereas the opposite trend is observed for XHP Mg.

Figure 4.11a presents the cathodic polarization curves obtained for XHP Mg, ZX10 and ZX20 without preceding anodic polarization (labelled with 0 min in Figure 4.11b) and after 10 and 30 min of potentiostatic polarization at +100 mV. The electrochemical response of the three material surfaces in 0.1 M NaCl at pH = 6 was qualitatively comparable with that obtained in SBF at physiological pH (Figure 4.6b): both the E_{corr} and the cathodic reaction rates increased with increasing nominal Zn content, i.e. in the order XHP < ZX10 < ZX20. With increasing potentiostatic polarization time, concomitant with progressing material dissolution, E_{corr} shifted towards more noble potentials for all materials, presumably due to the formation of a surface corrosion-product film. The increasing E_{corr} values are in line with the decreasing i_{anod} monitored during polarization,

with i_{anod} declining as a result of the evolution of E_{corr}. With E_{corr} successively increasing, the effective overpotential at potentiostatic conditions is in fact lower than 100 mV, resulting in a successively lower i_{anod}. In terms of the cathodic reaction rates, the difference between XHP Mg and ZX10, while almost non-detectable in SBF, is considerably amplified in 0.1 M NaCl.

Importantly, for both ZX-lean alloys a time-dependent increase in the cathodic reaction rate is observed with the time at potentiostatic polarization (Figure 4.11b, indicated by arrows). This upward shift of the cathodic current density i_{cath} is an indication of progressively increasing cathodic-site reactivity or area. Its extent appears comparable between both alloys. In contrast, a slight opposite trend is observed for XHP Mg.

Complementary high-resolution (HR) STEM imaging combined with chemical analysis sheds light on the origin of the observed dynamically increasing cathodic activity of the ZX-lean alloys, as will be presented in the following.

4.3.7   STEM analysis zoomed-in into the corrosion-product layer

STEM-HAADF imaging of the spongy $Mg(OH)_2$ layer (Figure 4.12a) reveals at high magnification the presence of globular clusters (Figure 4.12b). These clusters are present in large number densities in both materials ZX10 and ZX20 in sizes ranging from a few nanometers to about 10 nm.
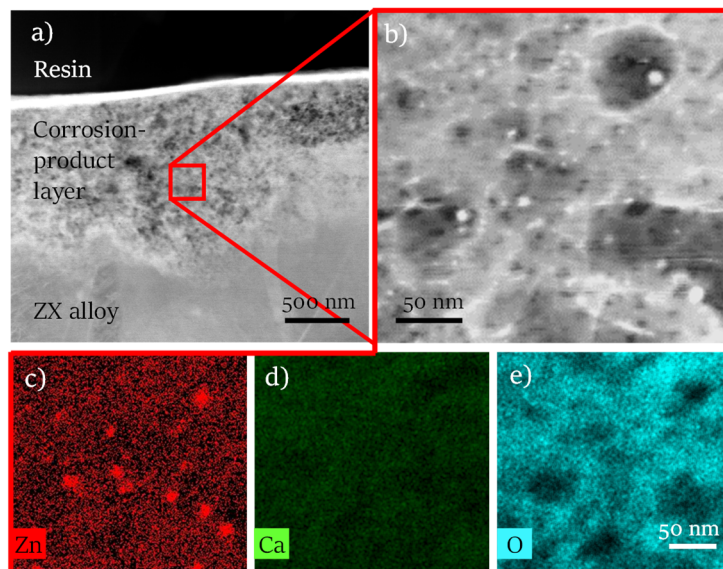
Figure 4.12: Nanometric Zn clusters in the corrosion-product layer. (a) STEM-HAADF image of the corrosion-product layer in cross-section. The red box marks the corrosion-product layer as the region of interest for (b) a magnified STEM-HAADF image of the spongy $Mg(OH)_2$ layer, which reveals nanometric globular clusters. Chemical mapping by STEM-EDS for (c) Zn, (d) Ca, and (e) O of the area shown in (b) provides evidence that the clusters are rich in Zn but not in Ca or O. All images of this figure are shown for ZX10, but they are also representative for ZX20.

Although not quantified in this study, no obvious difference in size or number density was observed between the Zn clusters found in the corrosion-product layers of ZX10 and ZX20. The bright contrast in STEM-HAADF mode indicates that these clusters are enriched in a high *Z*-number element. Corresponding STEM-EDS chemical maps (Figure 4.12c-e) reveal that they are composed of Zn (Figure 4.12c). No Ca signal is detected at their locations (Figure 4.12d), making these clusters clearly distinguishable from the IMPs of both types, i.e. those composed of Mg_2Ca and IM1 phase. Moreover, no O signal is detected at their locations (Figure 4.12e), meaning that the clusters are not composed of oxides.

At this stage, the study covered a detailed investigation of the *in vitro* reactivity, emphasizing the role and corrosion mechanisms related to the presence of Zn in the alloy. In a further step, the observations were to be validated in more complex environments found *in vivo*.

4.3.8 *High-resolution micro-focused computed tomography*

Both alloys were implanted in the femurs of juvenile rats to investigate their *in vivo* degradation behavior. Figure 4.13 (a,c and e) depicts micro-CT (µCT) reconstructions obtained after 4, 26 and 52 weeks of implantation time for ZX10 and ZX20. The degradation behaviors of ZX10 and ZX20 noticeably differ, following the same trends as those observed *in vitro*. In fact, ZX10 (Figure 4.13, left) degrades more slowly overall compared to ZX20 (Figure 4.13, right): within the first 4 weeks post-op, the volume loss amounted to a maximum of 4% and an average of 5 ± 3% of the initial implant volume for ZX10 and ZX20, respectively, and advanced further to 10 ± 3% and 27 ± 2%, respectively, after 26 weeks and 25 ± 8% and 36 ± 8%, respectively, after 52 weeks of implantation. To allow comparison with the *in vitro* situation, the degradation rate $DR_{\mu CT,i}$ was calculated from the µCT data according to:

$$DR_{\mu CT,i} = \frac{\Delta V_i}{\Delta t \, S_{av}}$$

(Eq. 4.1)

where ΔV_i is the volume loss during the time period Δt (between time point i and i-1) and S_{av} is the average implant surface of the time points i and i-1. The initial implantation time of i = 4 weeks was considered to allow the closest comparison with the *in vitro* characterization, which had been obtained for an immersion time of about 2 weeks. With V and S obtained from µCT data (Table 4.3), an average *in vivo* degradation rate of 34 ± 136 µm year^{-1} and 225 ± 119 µm year^{-1} was determined for ZX10 and ZX20, respectively, for the first 4 weeks post-op. Following the same approach, an average degradation rate can be determined for the entire implantation period of i = 52 weeks (i-1 = 0 weeks), which results in 91 ± 32 µm year^{-1} and 123 ± 25 µm year^{-1} for ZX10 and ZX20, respectively. Although the values obtained, which are based on the assumption of a homogeneous

corrosion front and constant degradation rate, are clearly only a rough estimation, the µCT-derived information confirms that *in vivo* ZX20 degrades faster than ZX10, as already observed *in vitro*.
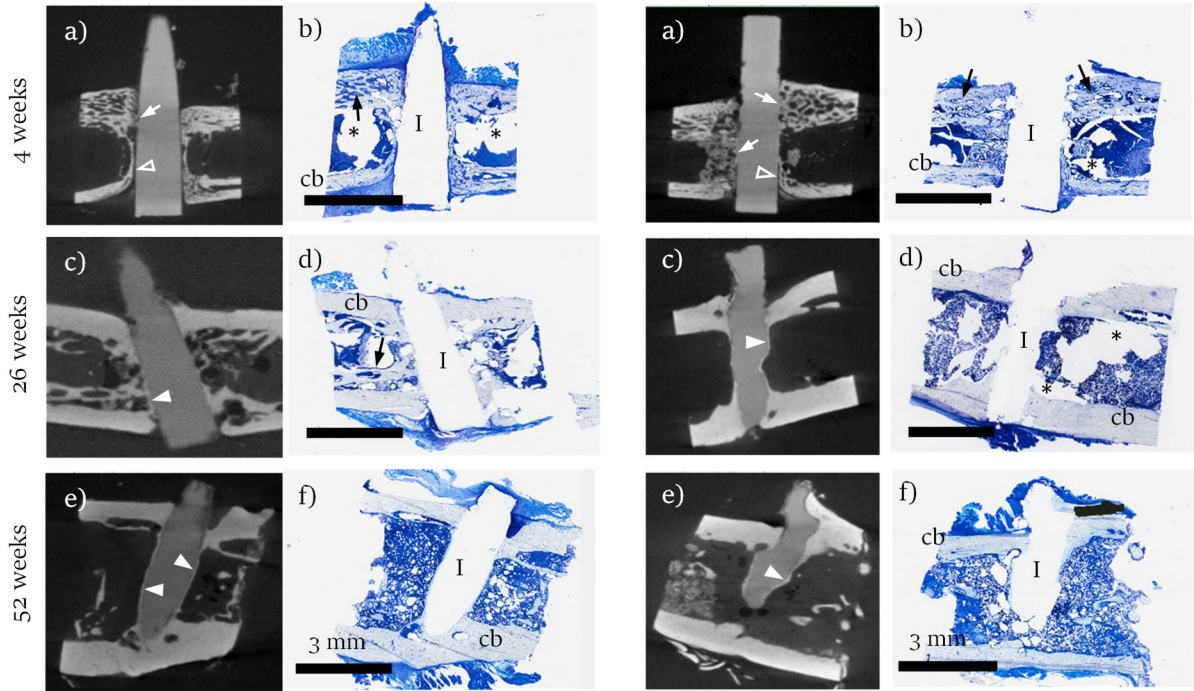
Figure 4.13: Micro-CT and histological investigation of (left) ZX10 and (right) ZX20. (a,c,e) Micro-computer tomograms of ZX-alloy implanted in rat femurs for (a) 4, (c) 26, and (e) 52 weeks. The white arrows in (a) point at direct tissue-to-implant contacts, the empty arrow heads point to a thin layer of dark contrast surrounding the implant, corresponding to fibrous tissue. The solid arrow heads in (c, e) point at a layer of bright contrast surrounding the implant, corresponding to new-bone deposition. (b,d,f) Corresponding histological slices stained with toluidine blue. (I) site of implant, (cb) cortical bone, (arrows) trabecular bone, and (*) preparation artefact.

In terms of the homogeneity of the corrosion attack, both alloys feature largely homogeneous degradation across the implant surface for the first 4 weeks of implantation at the scale observable in µCT (Figure 4.13a). As implantation time progresses, the corrosion rate depends on the implantation site: for both materials, enhanced degradation is detected in contact with soft tissue from 4 weeks on (Figure 4.13a), occasionally accompanied by signs of laterally inhomogeneous corrosion attack. For ZX20, relatively slow degradation is observed in locations where the material was in early direct contact with cortical bone (Figure 4.13c and e). In contrast, increased material dissolution is noticeable in those locations that were subjected to strong remodeling, i.e. the interface of bone marrow to cortical bone; were subjected to mechanical stimuli, i.e. the interface of cortical bone to soft tissue and muscles [43]; or were within the medullary cavity. This difference can be

simply explained by the elevated vascularization of bone marrow and has been observed previously [8]. It should be emphasized that implant integrity is clinically required during the initial fracture-healing period in order to allow for sufficient stability to hold the replaced fracture. Inhomogeneous degradation and implant disintegration can then be tolerated beyond this period when the bone tissue is able to carry a progressively increasing load.

Table 4.3: Evolution of implant volume and implant surface for ZX10 and ZX20 over an implantation time of 52 weeks obtained by µCT.

		0 weeks	4 weeks	26 weeks	52 weeks
ZX10	Volume (mm^3)	16.08	15.96 ± 0.43	14.56 ± 0.47	12.11 ± 1.22
	Surface (mm^2)	44.23	46.83 ± 1.27	50.35 ± 4.1	36.06 ± 3.53
ZX20	Volume (mm^3)	16.08	15.28 ± 0.40	11.81 ± 0.23	10.37 ± 1.13
	Surface (mm^2)	44.23	47.79 ± 1.89	56.00 ± 5.10	48.21 ± 5.47

Direct bone–implant contact is observed in places on the surfaces of both materials at 4 weeks post-op (Figure 4.13a, white arrows). In other places, a thin layer of dark contrast surrounded the implants made of either material, and separated the implant from bone tissue (see white arrow heads). This dark layer vanished with progressing implantation times. From 26 weeks on (Figure 4.13c and e) a tight connection between cortical bone and implant was established for both materials, revealing good osseointegration of the implants. New bone formation was also observed on the implant surface in the medullary cavity, visible in the tomograms as a thin layer of bright contrast around the implants (see white solid arrow heads). Important for the implant performance is besides its integration into the bone also an appropriately low H_2 evolution. *Ex vivo* µCT investigations cannot provide reliable information on the *in vivo* H_2 volume owing to potential artefacts arising from the embedding protocol. In a subsequent publication, we will provide this information in a complementary *in vivo* µCT study conducted on both alloys over an implantation time of up to 78 weeks [43]. There it is shown that the gas volume observed is low for both materials throughout the study, and well tolerated by the adjacent tissue.

4.3.9   Histology

Figure 4.13 (b, d and f) shows histological slices corresponding to the 2D-reconstructed tomograms for ZX10 and ZX20 in Figure 4.13 (a, c and e, respectively). Magnified views of the implant–tissue interfaces at 4 and 52 weeks post-implantation are also presented in Figure 4.14. Toluidine Blue-O staining reveals the general bone morphology in a histological slice: fibrous tissue and the cell nuclei are strongly stained in blue, young bone in light blue and compact or older bone cells in slightly bluish.

At 4 weeks after implantation (Figure 4.13b) trabecular bone surrounding the implant is observed, reaching into the medullary cavity. The new bone formation in the medullary cavity appears slightly enhanced in ZX20 (Figure 4.13, right) compared to ZX10 (Figure 4.13, left). It merits comment that the trabecular "spongy" bone characteristic of this investigation time (Figure 4.13b, arrows) corresponds to the normal bone morphology of juvenile rodents used in this study, and beyond bone trauma the bone morphology does not seem to be adversely affected by the presence of the Mg implant [35, 44].
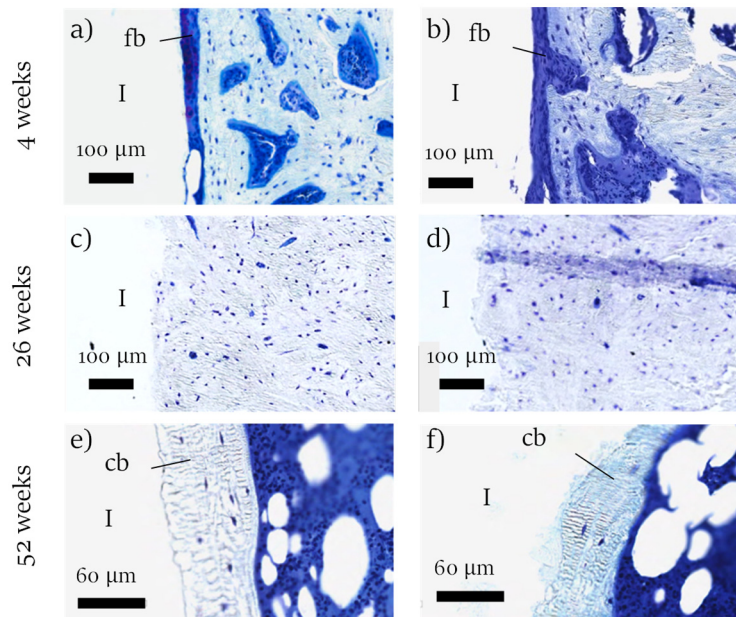
Figure 4.14: Histological investigation of the implant–bone interface for (left) ZX10 and (right) ZX20. Enlarged view of the tissue in direct contact with (a,c,e) ZX10 and (b,d,f) ZX20, stained with toluidine blue after *in vivo* implantation for (a, b) 4 weeks, (c, d) 26 weeks and (e, f) 52 weeks. (I) Site of implant, (fb) fibrous tissue, and (cb) compact bone.

At larger magnification (Figure 4.14a and b), a thin fibrous layer around the implant is observed in the histological slices of both implant materials, corresponding to the dark layer observed in the tomograms. The layer is visible in dark blue and is, with a thickness of about $42 \pm 12\ \mu m$ and $32 \pm 8\ \mu m$ for ZX10 and ZX20, respectively, approximately similar for both materials. This fibrous layer receded completely with implantation time and is not observed anymore at 26 weeks (Figure 4.14c and d) around either material.

With implantation time, and the rodent's concurrent growth, trabecular bone calcified progressively and compact bone developed, accompanied by a continuous recession of trabecular bone from the medullary cavity. New-bone formation showed close contact with the implant surface at both the cortical and medullary-cavity sites.

After 52 weeks (Figure 4.14 e and f) a thin layer of compact bone is apparent, deposited intramedullary on the surface of both materials. It corresponds to the bright layer observed in the tomograms, consists of three cell layers, derived from the count of cell nuclei, and amounts to a comparable layer thickness of 56 ± 13 µm for ZX10 and 63 ± 19 µm for ZX20. A clear transition zone is recognized from ordered compact bone at the implant interface – characterized by parallel alignment of cell layers – to spongy, trabecular bone further away from the implant – characterized by disordered, round arrangement of the cells. No noticeable difference was observed between the two materials.

Furthermore, it should be noted that neither material showed any adverse reactions or signs of inflammation at any time. The *in vivo* local and systemic body response to ZX10 and ZX20 will be followed up in a further investigation [43].

4.4 Discussion

The objective of this study was to evaluate the role of nanometric intermetallic particles on the macroscopic degradation behavior of ZX-lean alloys. The data demonstrate that the IMP type can be adjusted by minor changes in the nominal Zn content, and that this significantly modifies the degradation rate of ZX-lean alloys *in vitro* and *in vivo*.

4.4.1   *Microstructural engineered lean alloys are obtained via Zn adjustment*

Thermodynamic calculations were performed to design model materials suitable for addressing the specific role nanometric IMPs play in the biodegradation behavior of ZX-lean alloys. The alloy design carefully balanced the nominal chemical composition and the processing temperature with respect to both processability and temperature-dependent elemental distribution within the IMPs and Mg matrix (Figure 4.2).

The microstructural analysis based on TEM-EDS (Figure 4.4) revealed that the ZX10 alloy designed, with a Zn content of 1 wt.% (0.37 at.%) and a Zn-to-Ca atomic ratio of ~2.1, hosts IMPs that are made nearly exclusively of the binary Mg_2Ca phase (Figure 4.4c). This finding regarding the IMPs' composition confirms what was previously postulated by Hofstetter et al. [5] from computational results on this alloy (see also Figure 4.2). A minor increase in the nominal Zn content in ZX20 to 1.5 wt.% (0.56 at.%) at a Zn-to-Ca atomic ratio of ~3.7 was sufficient to generate a complete change of the primary IMP type to the ternary IM1 phase (Figure 4.4d), with an experimentally determined composition of $Ca_3Mg_{12.3}Zn_{5.1}$. This composition, while it fits rather well the compositional range reported in literature [16], deviates from that predicted by thermodynamic calculations at $Ca_2Mg_6Zn_3$ (Figure 4.2), corresponding to $Ca_3Mg_9Zn_{4.5}$. The larger Mg content in the experimental data can be explained by the measuring of stray electrons that originate from the Mg matrix. Further analysis is required to obtain the precise composition and structure of the ternary phase composing the nanometric IMPs in ZX20, and will be reported in Ref. [45]. Note that the Zn distribution is substantially different in the intermetallic and matrix phases of ZX10 and ZX20, but in both alloys a comparable matrix solute content of about 0.4 at.% is retained (Table 4.2).

The Zn-to-Ca ratio of both alloys is well above the threshold value of 1.2 frequently stated for cast Mg–Zn–Ca alloys [1, 18], below which the eutectic (α-Mg + Mg_2Ca + IM1) phase would form, and above which the IM1 phase would form as the sole intermetallic phase. More recently Zander et al. [7] and Li et al. [17] reported on the stability of the Mg_2Ca phase in lean cast Mg–Zn–Ca alloys with a total alloying content of about 1 at.% and 0.35 at.%, respectively, and larger Zn-to-Ca ratios (1.84 and 1.9). However, in those two studies the binary Mg_2Ca phase co-existed with the IM1 phase, which

makes it difficult to break down their individual roles in macroscopic corrosion behavior. To our best knowledge, only ternary alloys with a greater Ca content and a Zn-to-Ca ratio << 1 are reported to possess a microstructure comprising only primary α-Mg and the Mg_2Ca phase [3, 46, 47]. However, their alloying content exceeded the solubility limit for Ca in Mg [48], negating the possibility of a solution-heat treatment (*sht*).

The possibility of *sht* is essential to the lean alloying concept [14, 37]: the precipitation of IMPs from solid solution enables their nucleation in a high number density and, thus, nanometric size. By setting a *sht* window for both alloy compositions (Figure 4.2) and applying the identical processing protocol, a similar nanometric size, number density, and similar volume fraction of IMPs were successfully achieved for ZX10 and ZX20 (Figure 4.4a-d). From these similarities in IMP characteristics it is easily understood that the alloys exhibit a comparable grain size (Figure 4.3), considering that the IMPs are able to control grain size via grain-boundary pinning [15] at elevated extrusion temperature.

The volume fraction of the primary intermetallic phase is obtained from the IMP number density at 4.1×10^{18} m^{-3} and 3.2×10^{18} m^{-3} and their average size at 80 nm and 100 nm for ZX10 and ZX20, respectively. The resulting volume fraction is 1.1×10^{-3} and 1.7×10^{-3} for ZX10 and ZX20, respectively, when a spherical morphology is assumed. Comparing these experimental data with the simulated volume fractions at the extrusion temperature of 330 °C (~3.4×10^{-3} for ZX10 and ~5.4×10^{-3} for ZX20; Figure 4.2a), the trend of a slightly larger value for ZX20 compared to ZX10 is retained. However, the experimental values are lower overall by a factor of three than what was predicted by the thermodynamic calculations. This discrepancy can be explained by the segregation of Zn and Ca to grain boundaries, which is not taken into account by the simulations. Segregation reduces the alloying element amounts available for secondary-phase precipitation, thus reducing its volume fraction. Solute co-segregation of Zn and Ca to the grain boundaries, as seen in the insets to Figure 4.4c and d (white arrows), was also previously reported to occur in a ZX00 alloy with Mg–0.3Zn–0.1Ca (in wt. %) composition [49]. More important in the context of this study, however, is the prediction regarding temperature-dependent phase stabilities. In fact, the respective simulation of the primary IMP type characteristic for ZX10 and ZX20 was astonishingly accurate for both materials under the processing conditions chosen. The close match of predicted phases as a function of temperature once more underlines the suitability of thermodynamic calculations as a tool for the rational design of Mg-lean alloys.

4.4.2   *Nanoscale IMP type governs macroscale alloy degradation*

The microstructurally engineered IMPs of nanometric size function as a lever for the control of the biodegradation rate at the macroscale.

Based on the phase concentration of electropositive Zn and electrochemically active Ca (both relative to Mg), the expected electrochemical potential of the considered phases, according to [19, 20], decreases in the following order: IM1 phase > α-Mg > Mg_2Ca. On this basis, in a micro- or nano-galvanic couple with α-Mg, the IM1 phase should represent the local cathode, while Mg_2Ca phase should dissolve as the local anode. Indeed, the higher corrosion resistance of the former and the preferential dissolution of the latter was previously reported [3, 4, 7, 18]. However, in those studies, the Mg_2Ca phase co-existed with the IM1 phase, and thus its individual role in the macroscopic corrosion behavior of ZX alloys remains unclear. The respective phase was also present in a volume fraction larger than in the ZX-lean alloys of this study, and precipitated mainly along the grain boundaries with a coarse or even percolated morphology. This relatively coarse morphology combined with a coarse distribution, and thus resulting intrinsic incongruent dissolution, generated a laterally inhomogeneous corrosion front and network-like cracks [4], which are both undesirable for the application as an implant material.

The lean-alloy compositions in this study host the respective intermetallic phase as nanoparticles that are immensely different in size to that of the matrix grain and have a notably low volume fraction. In fact, the maximum surface area of an IMP of average size is roughly 500 times smaller than that of an average matrix grain. It is generally recognized that besides the chemical composition of each phase (i.e. IMP and matrix), which sets its electrochemical potential in contact with a given environment, the total-area ratio of anode(s) and cathode(s) also plays a distinct role in the micro/nano-galvanic-coupling-induced corrosion acceleration.

For the ZX10 alloy, the large cathode-to-anode ratio of micrometer-sized Mg-matrix grains and nanometric Mg_2Ca-type IMPs expectedly causes the rapid dissolution of the latter. Its preferential dissolution also cannot be influenced by the low level of dissolved Zn in Mg_2Ca (~0.35 at.%, Table 4.2), which is about the same as that in the α-Mg matrix (~0.37 at.%, Table 4.2). Only with considerably greater Zn content, concomitant with an elevated electrochemical potential of $(Mg,Zn)_2Ca$, would dissolution at a similar rate to that of α-Mg be possible, as demonstrated by Cha et al. [3]. In ZX10 the Mg_2Ca phase appears to dissolve completely with no detectable remnants (Figure 4.7a and b). Fortunately, due to their minute size, the voids generated by the dissolved globular IMPs (on average 80 nm in diameter) are at such a small scale that they do not affect the desired homogeneity of material dissolution at a scale relevant for implant application. This is a

considerable advantage compared to those ZX alloys that host the Mg_2Ca phase at larger sizes and volume fractions and with a percolating morphology [3, 7]. The latter, in particular, enables incongruent dissolution to advance deep into the material's bulk, with the resulting risk of material disintegration and early implant failure, in particular under fatigue load. In contrast, the corrosion front characteristic of ZX10 observed *in vitro* (Figure 4.7a and b) and *in vivo* (Figure 4.13, left) can safely be described as laterally homogeneous at the relevant scale, even though µCT with a resolution of slightly below 20 µm cannot resolve the preferential dissolution of the Mg_2Ca phase, which is at a scale of < 100 nm. It is understood that because of the rapid dissolution of the anodic IMPs from ZX10, the α-Mg dissolves virtually unaffected. This may also explain why the corrosion rate of ZX10 *in vitro* even approaches the low level of XHP Mg (Figure 4.5). As for its electrochemical response, the slight upward shift in E_{corr} relative to the XHP Mg observed (Figure 4.6b) can be explained by the solubility of Zn in the α-Mg phase, which elevates the matrix's electrochemical potential [19], and by Zn redeposits acting as nano-cathodes, as discussed later.

For the ZX20 alloy, the IM1 phase-type IMPs have a higher corrosion resistance than the Mg matrix and may also be cathodically protected at the corroding surface, as evident from their presence in the corrosion-product layer (Figure 4.7c and d). We recently also observed in a high-resolution quasi-*in situ* TEM study [21] that the IM1 phase-type IMPs act as active local nano-cathodes upon short-term immersion under simulated body conditions, and showed that their dissolution occurred via dealloying with preferential dissolution of Ca and Mg. Thus a relative enrichment of Zn results, which entails a gradual ennoblement of these IMPs. The local insights into the early-stage corrosion attack from that study are expanded here to address the macroscopic electrochemical response of ZX20. The shift in E_{corr} and the simultaneous increase in the cathodic reaction rates, both relative to ZX10 (Figure 4.6b and Figure 4.11), clearly demonstrate the cathodic activity of the IM1-type IMPs. Importantly, because the immersed surface area in the electrochemical cell used was 1 cm^2, the electrochemical response presents the macroscopic response according to mixed-potential theory [50], and thus demonstrates that the nanoscale IMPs have a distinct 'upscale' impact on the macroscopic degradation behavior. The distinct difference in E_{corr} between ZX10 and ZX20 may at first be surprising, considering the non-polarizable nature of Mg [19, 51] and the small size and volume fraction of the IMPs. However, we argue here that the IMPs have a decisive electrochemical impact precisely because of their minute size: Bland et al. [52, 53], for example, showed that the size and spacing of IMPs as local cathodes play an important role in their efficiency in facilitating the H_2-evolution reaction. By using model electrodes, they demonstrated that a high number of small cathodes was more effective in facilitating micro-galvanic-coupling-induced acceleration of matrix dissolution than larger cathodes did at the same surface fraction. Their findings suggest that in ZX20

it is indeed the nanometric size of IM1-type IMPs ($d \approx 100$ nm), plus their homogeneous distribution (the average spacing results with $N = 3.2 \times 10^{18}$ m^{-3} to $\frac{1}{\sqrt{2Nd}} \approx 1250$ nm), which control the effectively high macroscopic degradation rate, exceeding what would be expected for the small volume fraction of the IM1 phase. Further investigation is required to elaborate on the possible role played by the spacing of the cathodically active IM1-type IMPs in the corrosion rate of ZX-lean alloys. It is worth emphasizing that because of their nanometric size the IMPs are rapidly undermined by the inward-growing corrosion front. At the same time, new IMPs of the same type are consistently exposed at the active metal–corrosion-product-layer interface. This has two important consequences: first, a laterally homogeneous degradation front is established. Second, the IMP-induced enhanced matrix dissolution persists even for extended degradation times. The role of IMPs as nano-cathodes thus explains the greater overall material dissolution of ZX20 compared to ZX10, evident in the increased H$_2$ evolution (Figure 4.5), the larger current and charge transient (Figure 4.10), and the larger volume loss *in vivo* for long implantation periods of up to 52 weeks (Figure 4.13 and [43]). It merits comment that despite the fact that only estimates of the degradation rates can be obtained from *in vitro* degradation studies owing to the limitations intrinsic to the hydrogen-gas evolution method [41], the degradation rates observed for ZX10 and ZX20 follow the same trend of a higher *DR* for ZX20 compared to ZX10, as observed *in vivo*, and lie in the same order of magnitude. In fact, both investigations reveal a similar ratio, with a *DR* of up to 4 times larger for ZX20 than ZX10 determined *in vitro*, and about 6.6 times larger *in vivo*. At longer implantation times the ratio of *in vivo* degradation rates between the alloys declines and for the entire implantation time of 52 weeks the *DR* reaches values only about 1.4 times larger for ZX20 than for ZX10. However, despite the declining ratio, the generally higher *DR* for ZX20 persisted throughout the entire study period.

The role Zn plays in governing the corrosion rate of ZX alloys has been addressed in multiple studies [1, 3-5, 7, 18, 54], and was concisely summarized by Zander and Zumdick in [7]. In these studies, a beneficial impact of Zn addition on the corrosion resistance of binary Mg–Ca alloys was reported [1, 3, 4, 7, 18, 54]. The decrease in corrosion rate observed was attributed partially to Zn dissolved in the Mg$_2$Ca phase, which reduced the potential difference between the (Mg,Zn)$_2$Ca phase and the α-Mg matrix and thus increased the corrosion resistance of (Mg,Zn)$_2$Ca. Another explanation was based on the reduced volume fraction of the same phase. Nevertheless, the beneficial effect was limited to small Zn amounts, and reversed with further element addition [3-5, 54, 55]. No conclusive threshold value above which Zn generates an increased corrosion rate has been agreed upon in literature, because this varies greatly between the different alloys that comprise differing total alloying amounts, differing Zn distributions, and differing Zn-to-Ca ratios. In fact, the total alloying amount of Zn ranged from 1 wt.% for Mg–5Ca–*x*Zn [54] and Mg–0.3Ca–*x*Zn [5, 55], over 1.25 wt.%

for Mg–1Ca–xZn [4], to 3 wt.% for Mg–0.5Ca–xZn [18] and Mg–5Ca–xZn [3]. Despite the non-agreement in defining a Zn threshold, it appears to be commonly accepted that beyond a certain threshold, the increasing corrosion rate observed with increasing Zn content can be attributed to the formation [5] and increasing volume fraction of the IM1 phase [3, 4, 7, 22, 54, 55] at the expense of increasingly destabilized Mg_2Ca phase [4, 18]. It was thus postulated that the volume fraction of the IM1 phase should be minimized [7] or avoided altogether [5, 55] when slow and homogeneous degradation is desired.

In the present study, however, our results show that when the volume fraction of the IM1 phase is sufficiently reduced ($\leq 1.5 \times 10^{-3}$) and precipitated at a high number density (order of $\geq 10^{18}$ m^{-3}) and low size ($\leq \sim 100$ nm), an implant material (such as ZX20) results that not only degrades sufficiently slow but also exhibits the required laterally homogeneous corrosion front during the time period that is clinically relevant to facilitate fracture healing.

The biological response was comparable for ZX10 and ZX20, with only minor formation of fibrous-tissue layer at the early implantation stage of 4 weeks (Figure 4.14a and b), which vanished completely over time. The formation and subsequent complete clearance of the fibrous tissue relates to healthy healing. Additionally, both materials supported neoformation of bone tissue on their surface (Figure 4.14e and f) and facilitated direct bone–implant contact at 4 weeks post-implantation (Figure 4.13a). These promising results on the biological response are further supported by the low gas-formation rate observed for both materials [43]. The gas volume was clinically tolerable for both materials, indicating that in both cases the surrounding tissue can absorb most of the generated gas. Based on these results both materials qualify as suitable temporary bone-implant materials. In fact, depending on the specific application – involving a specific implant size, implantation site, patient age and underlying pathophysiology – the degradation rate of ZX10 or that of ZX20 may indeed be preferred.

A central finding of this study was the identification of the decisive role that the chemistry of the nanometric IMPs plays in the global degradation characteristics of ZX-lean alloys. Because other microstructural features that are known to influence corrosion processes were kept nearly constant between ZX10 and ZX20, the results show unambiguously that, despite their nanometric dimensions and low volume fraction, the type of IMPs alone can control the global degradation rate, both short- (electrochemical characterization) and medium-term *in vitro* (H_2-evolution study) and transmitted long-term *in vivo*. Under all conditions examined, ZX20 comprising the ternary IM1-type IMPs degraded significantly faster than ZX10 comprising binary Mg_2Ca-type IMPs. It is expected that at a given IMP volume fraction, size, and number density, a mixture of both IMP types, Mg_2Ca and IM1

phase, can be deployed to achieve a degradation rate that is in fact between that of ZX10 and ZX20, enabling a true degradation rate on demand.

However, an apparent inconsistency still remains to be discussed. While the cathodically active IM1-type IMPs can rationalize the larger cathodic reaction rates in ZX20 compared to ZX10 (Figure 4.6 and Figure 4.11), they cannot explain the time-dependent shift of the cathodic current density observed for both ZX-lean alloys (Figure 4.11b). Complementary high-resolution microscopy (Figure 4.12) provided an answer by revealing Zn redeposits, which function as additional nano-cathodes. Their effect on dynamic changes in the electrochemical reaction rate is described in the following section.

4.4.3 Zn-cluster act as additional nano-cathodes

Noble-element redeposition has long been recognized to impede the corrosion resistance of Al alloys with e.g. the redeposition of copper (Cu) [56, 57] and only recently got the needed attention in the Mg-research community [58-67]. Noble-element redeposition is hitherto mostly discussed in the context of impurities; first and foremost for iron [58-62], due to its long realized detrimental impact on the corrosion performance of Mg and its alloys. More recently, noble-element redeposition and accumulation in Mg were reported also for silver [63], Al [64, 65] and Cu [66]. All elements have in common that their reversible potential is well above the potential established for Mg, which is generally reported to be at about -1.5 to -1.2 V_{SHE} in physiological conditions [42]. The local electrochemical potential at the interface between Mg metal and the corrosion-product layer is, while experimentally difficult to access due to the rapid formation of corrosion products, most likely even lower, i.e. the overpotential to noble-element reduction even larger. In this potential domain, oxidation of the nobler element is thermodynamically not possible. Instead the Mg (alloy) itself can act as a "reducing electrode", facilitating not only the redeposition as metallic compounds [59, 67] but also their cathodic protection. Cathodic protection is granted as long as redeposits are in electrical contact to the Mg substrate. Naturally, these metallic spots will be much more efficient in facilitating the electron transfer needed for the hydrogen-reduction reaction than neighboring oxidized surfaces, and therewith drastically accelerate the degradation rate [58, 59]. An enhanced effect of the noble-element redeposition on the hydrogen-evolution rate also stems from the exchange current densities for the hydrogen-reduction reaction $i_{0,H2/H+}$, which are for most metals higher than for Mg. Consequently, a greater H_2 evolution can be observed [59, 61] and a progressively increasing cathodic current density manifests [59-61] when noble-element enrichment occurs, both the greater the more noble-element redeposits accumulate.

In this study, the polarization strategy in diluted NaCl solution, presented in Figure 4.11b, revealed indeed an increasing cathodic current density with progressing material dissolution for both ZX-lean alloys. Impurity-derived noble-element accumulation at its origin can, however, be safely excluded, because these alloys are made from ultrahigh-purity (XHP) Mg, which has an Fe-impurity content of about 1 ppm only and a total impurity content at the few ppm level ([27] and Table 4.1). Instead, Zn accumulation in the form of nanometric clusters in the corrosion-product layer was observed via high-resolution imaging and chemical mapping (Figure 4.12). High-magnification TEM-EDS also revealed that the Zn signal does not correlate, neither with the signal for Ca nor O, thus ruling out that these clusters originate from IMPs or present oxides, respectively. Instead, these Zn clusters are assumed to form via the electrochemical interfacial deposition described above. The assumption that an electrochemical reduction of Zn ions on the Mg surface (Figure 4.15, step 2) occurs is premised on the reversible potential of the Zn/Zn^{2+} reaction (see Pourbaix diagram for Zn in Figure 1.12, section 1.1.6 '*Magnesium corrosion*'). Its potential is well above the interfacial potential of Mg (alloys) [31], thus the same processes as described previously for transition metals [58-60, 63, 66] are presumed to occur.

The redeposited Zn is assumed to originate mainly from solute atoms in the dissolving α-Mg phase, but may also originate from the Zn contained in the rapidly dissolving Mg_2Ca-type IMPs (Figure 4.15, step 1). In contrast, the Zn originating from the IM1-type IMPs is unlikely to be a major contributor to the cluster formation because under physiological conditions its oxidation can only occur once the cathodically protected IMPs have been undermined and decoupled from the Mg substrate [21].

High-resolution imaging and corresponding EDS mapping revealed that the Zn deposits in ZX-lean alloys are present as nanometric, isolated clusters (Figure 4.12). Even apparently minute in size, the amount of solute atoms required to form a cluster should not be underestimated: for illustration, a globular cluster of only 5 nm (10 nm) in diameter is composed of ~4000 Zn (>3×10^4 Zn) atoms, if it is assumed that they are dense and made solely of metallic Zn. In the ZX-lean alloys only ~0.4 at.% Zn are dissolved in the Mg matrix, i.e. only for every 250th Mg atom that dissolves, one Zn atom will become available for the Zn-cluster formation (Figure 4.15, step 1). With these numbers in mind, it is easily understood that for nanometric Zn clusters to form, the sparsely present and spatially separated Zn atoms need to accumulate. This may occur either via Zn-adatom surface diffusion or by preferential reduction of Zn ions on pre-existing Zn atoms via a nucleation and growth mechanism on the surface (Figure 4.15, steps 3 and 4). In this scenario, both, nucleation and growth are facilitated by the electrochemical reduction reaction of divalent Zn ions to metallic Zn (Figure 4.15, step 2). It should be noted that "surface" in this context refers to the corrosion front, i.e. the interface

between the Mg metal and the corrosion-product layer. While the details of the underlying cluster-formation processes remain to be studied, it seems unambiguous that cluster growth is possible only as long as the cluster is in electrical contact with the Mg substrate. In this state, the redeposited cluster is assumed to cause accelerated peripheral matrix dissolution via nano-galvanic coupling (Figure 4.15, step 5). Once decoupled, the Zn cluster loses the cathodic protection and will dissolve under open-circuit conditions (Figure 4.15, step 6), in physiological conditions eventually completely [31, 68]. In other words, cluster growth competes with the progressing Mg dissolution. In fact, when the clusters accelerate as nano-cathodes the Mg-matrix dissolution, it is logical to assume that the cluster size and number density become self-limiting. That the Zn cluster can still reach an appreciable size before they are finally deactivated can be rationalized by the inherent rate difference between the cluster formation and growth as electrochemical processes and the conversion of Mg to $Mg(OH)_2$ as a chemical process.

The cluster morphology and minute size observed here for the ZX-lean alloys are opposed to deposits observed on alloys with larger alloying-element contents. In such alloys lateral propagation of the noble elements contained or even their coalescence seems possible, which results in a thin – presumably dense – layer detected at the metal–corrosion-product-layer interface [62, 64, 65, 67]. As such, this layer may act as a large cathode, which could drastically accelerate the Mg-matrix dissolution. In contrast, coalescence of Zn at the metal–corrosion-product-layer interface was not observed for the ZX-lean alloys in this study. In fact, it requires further investigation to determine a possible threshold Zn-matrix content, above which coalescence may occur. Our understanding of the cluster formation via an interfacial dissolution-precipitation mechanism is schematically presented in Figure 4.15.

Considering that the Zn-matrix content is with about 0.4 at.% (Table 4.2) similar in both ZX alloys, similar degrees of redeposited Zn can be expected for ZX10 and ZX20. This assumption is supported by the observation of a similar number density and size of the Zn clusters and the similar increase in cathodic activity observed upon cathodic polarization in the two alloys following anodic dissolution (Figure 4.11b). The increasing cathodic reaction rates detected provide further evidence that the Zn redeposits indeed act as additional nano-cathodes in ZX-lean alloys. As such, they are expected to facilitate an accelerated Mg-matrix dissolution via nano-galvanic coupling.
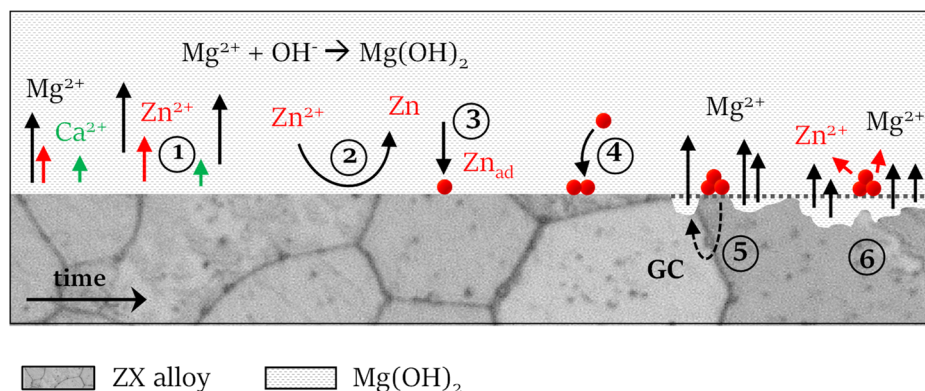
Figure 4.15: Schematic presentation of metallic Zn-cluster formation via interfacial dissolution–precipitation. 1: Mg-matrix dissolution, 2: Zn reduction on the Mg surface, 3: resulting Zn adatom serves as nucleus for a Zn cluster, 4: growth of metallic Zn cluster, 5: high nobility of Zn cluster promotes peripheral Mg-matrix dissolution, 6: separation from the matrix upon being undermined by the inward-growing corrosion front. The Zn cluster can dissolve under open-circuit conditions. Steps 1-4 are electrochemically driven, thus their kinetics are rapid. Steps 5-6, the formation of $Mg(OH)_2$ is chemically driven, and thus significantly slower. GC: galvanic coupling. The dotted grey line marks the original metal surface.

It merits comment that with Zn constituting an alloying element in ZX-lean alloys, its concentration is considerable larger than that of typical impurity values in Mg (on the order of a few tens to a few hundreds of ppm). Nevertheless, it is important to note that Zn never reaches the detrimental effect on the corrosion resistance known for common impurities in Mg. This can be explained by their difference in effective exchange-current densities for the hydrogen-reduction reaction $i_{0,H2/H+}$, which is much larger for Fe (1.0×10^{-6} A cm^{-2}) and Cu or Ag (both in the order of 10^{-8} A cm^{-2}) than for Zn (3.2×10^{-11} A cm^{-2}) [69]. In fact, the H_2-evolution analysis obtained *in vitro* (Figure 4.5) and the long-term *in vivo* analysis (Figure 4.13) illustrate that, despite the expected enhanced matrix dissolution facilitated by Zn redeposits, the effective corrosion rate stays at a sufficiently low level.

4.4.4 *Lean-alloying concept assures slow and homogeneous degradation*

Finally, we will revisit the lean-alloying concept followed in this study. Thus far, it was shown that reducing the Zn content from ZX50 (with 5 wt.% Zn) to ZX10 into the lean regime (i.e. Zn and Ca ≤ 1 at.%) leads to a vital reduction in the macroscopic corrosion rate [5]. The subsequently improved corrosion performance was attributed to the related change from IM1-type IMPs in ZX50 to the Mg_2Ca-type IMPs in ZX10. By comparing these two alloys, it was deduced that the rapid dissolution observed for ZX50 was due solely to Zn-rich IM1-type IMPs in this alloy, and that the IM1 phase should consequently be avoided in ZX alloys if a slow and homogeneous degradation is desired [55].

In this study, we demonstrated that a Zn reduction to 1.5 wt.% in ZX20, while still comprising the IM1-type IMPs, suffices to generate a degradation rate *in vitro* and *in vivo* in a small-animal model that is low enough to qualify the material for the use as temporary bone implants. The results further suggest that the IMP type in the limits of ZX-lean alloys can be used to alter their degradation rate, with the IM1 phase up- and the Mg_2Ca phase down-regulating the rate, while being low enough overall to avoid irritation of adjacent tissue and to facilitate early bone–implant contact. In terms of homogeneity of attack, the results show that the desired laterally homogeneous corrosion front can indeed be achieved irrespective of the IMP type – Mg_2Ca or IM1 phase – as long as the distribution of the IMPs is homogeneous and their size is at a nanometric scale.

With the identification of Zn redeposits we demonstrated the additional advantage of a low solute matrix content of noble elements: the lean-alloying concept keeps the inevitable noble-element redeposition low, thus minimizing the number of additional nano-cathodes on the corroding surface. By revealing the redeposition of Zn, it can now be rationalized that the relatively high Zn-solute matrix content for ZX50, amounting to about 3.6 wt.% (1.4 at.%) at 330 °C, represented an important contributor to the generally high corrosion rate observed for this alloy [8, 55, 70].

In summary, the lean composition of the ultrahigh-purity ZX alloys investigated in this study results in an unmatched biodegradation performance because of (i) their beneficial IMP characteristics, i.e. their low volume fraction ($\leq 1.5 \times 10^{-3}$) and small size ($d \leq 100$ nm) at a large number density ($N \geq 10^{18}$ m^{-3}); (ii) their low Zn-solute content (0.4 at.%) and thus low degree of redeposition, which may otherwise generate progressively accelerated degradation; and (iii) their impurity content in the low ppm range, which excludes impurity-derived noble-element redeposition.

Furthermore, the distinct difference in the biocorrosion behavior controlled by the IMP type suggests that a mixture of the two, i.e. Mg_2Ca and IM1 phase, can generate a variation of degradation rates that are between those of ZX10 and ZX20. This microstructural-design may thus be used for a tailoring of the degradation rate desired in a variety of biomedical applications.

4.5 Conclusions

In this study we designed two Mg–Zn–Ca-lean alloys, each with only one of the intermetallic phases relevant to the ZX-lean system, i.e. either the binary Mg_2Ca or the ternary IM1 phase. Using these model materials and using electrochemical methods in conjunction with transmission electron microscopy we investigated in detail the role of nanometric IMPs and that of Zn in the alloys' macroscopic biocorrosion behavior. The main conclusions drawn are as follows:

- An increase in the nominal Zn content from 1.0 wt.% (0.37 at.%) to 1.5 wt.% (0.56 at.%) changes the primary intermetallic phase from binary Mg_2Ca to ternary IM1 under the same processing conditions at 330 °C.

- IMPs composed of the Mg_2Ca phase dissolve with no observable remnants.

- IMPs composed of the IM1 phase act as cathodes, which shift the corrosion potential, E_{corr}, towards higher values. Following the separation of IMPs from the Mg matrix upon its disintegration, they remain embedded in the corrosion-product layer where they dissolve further under open circuit potential, E_{OCP}, conditions.

- Zn present as solute element in the Mg matrix in both Zn-containing alloys redeposits on the corroding surface, forming globular nanometric clusters.

- The noble-element redeposition of Zn is responsible for a time-dependent enhancement of cathodic activity.

- The cathodic activity of both types of nano-cathodes, i.e. noble IMPs and Zn redeposits, underlines the importance of the lean-alloying concept, which is expected to prevent progressively accelerated degradation.

- A higher degradation rate in both *in vitro* and *in vivo* conditions was established for ZX20, which contains ternary IM1-type IMPs, owing to IMP-induced matrix dissolution via nano-galvanic coupling.

- Histological analysis of explants reveals that both materials ZX10 and ZX20 are well tolerated by the surrounding bone tissue, and are well integrated with an early bone–implant contact already 4 weeks post-implantation. This indicates the suitability of these alloys as implant materials for the treatment of musculoskeletal conditions.

- The minor adjustment of nominal Zn content appears to be a suitable way for tailoring the degradation rate towards desired applications.

4.6 Acknowledgments

4.7 References

[1]   H. Du, Z. Wei, X. Liu, E. Zhang, Effects of Zn on the microstructure, mechanical property and bio-corrosion property of Mg–3Ca alloys for biomedical application, Materials Chemistry and Physics 125(3) (2011) 568-575.

[2]   A. Hänzi, A. Sologubenko, P. Gunde, M. Schinhammer, P.J. Uggowitzer, Design considerations for achieving simultaneously high-strength and highly ductile magnesium alloys, Philosophical Magazine Letters 92(9) (2012) 417-427.

[3]   P.-R. Cha, H.-S. Han, G.-F. Yang, Y.-C. Kim, K.-H. Hong, S.-C. Lee, J.-Y. Jung, J.-P. Ahn, Y.-Y. Kim, S.-Y. Cho, Biodegradability engineering of biodegradable Mg alloys: Tailoring the electrochemical properties and microstructure of constituent phases, Scientific Reports 3 (2013) 2367.

[4]   H. Bakhsheshi-Rad, E. Hamzah, A. Fereidouni-Lotfabadi, M. Daroonparvar, M. Yajid, M. Mezbahul-Islam, M. Kasiri-Asgarani, M. Medraj, Microstructure and bio-corrosion behavior of Mg–Zn and Mg–Zn–Ca alloys for biomedical applications, Materials and Corrosion 65(12) (2014) 1178-1187.

[5]   J. Hofstetter, M. Becker, E. Martinelli, A.M. Weinberg, B. Mingler, H. Kilian, S. Pogatscher, P.J. Uggowitzer, J.F. Löffler, High-strength low-alloy (HSLA) Mg–Zn–Ca alloys with excellent biodegradation performance, JOM 66(4) (2014) 566-572.

[6]   Y. Jang, Z. Tan, C. Jurey, Z. Xu, Z. Dong, B. Collins, Y. Yun, J. Sankar, Understanding corrosion behavior of Mg–Zn–Ca alloys from subcutaneous mouse model: Effect of Zn element concentration and plasma electrolytic oxidation, Materials Science and Engineering: C 48 (2015) 28-40.

[7]   D. Zander, N.A. Zumdick, Influence of Ca and Zn on the microstructure and corrosion of biodegradable Mg–Ca–Zn alloys, Corrosion Science 93 (2015) 222-233.

[8]   T. Kraus, S.F. Fischerauer, A.C. Hänzi, P.J. Uggowitzer, J.F. Löffler, A.M. Weinberg, Magnesium alloys for temporary implants in osteosynthesis: in vivo studies of their degradation and interaction with bone, Acta Biomaterialia 8(3) (2012) 1230-1238.

[9]   J. Zhang, H. Li, W. Wang, H. Huang, J. Pei, H. Qu, G. Yuan, Y. Li, The degradation and transport mechanism of a Mg-Nd-Zn-Zr stent in rabbit common carotid artery: A 20-month study, Acta Biomaterialia 69 (2018) 372-384.

[10]   A. Myrissa, S. Braeuer, E. Martinelli, R. Willumeit-Römer, W. Goessler, A.M. Weinberg, Gadolinium accumulation in organs of Sprague–Dawley® rats after implantation of a biodegradable magnesium-gadolinium alloy, Acta Biomaterialia 48 (2017) 521-529.

[11] A. Turyanskaya, M. Rauwolf, T. Grünewald, M. Meischel, S. Stanzl-Tschegg, J.F. Löffler, P. Wobrauschek, A.M. Weinberg, H. Lichtenegger, C. Streli, μXRF Elemental Mapping of Bioresorbable Magnesium-Based Implants in Bone, Materials 9(10) (2016) 811.

[12] F. Amerstorfer, S.F. Fischerauer, L. Fischer, J. Eichler, J. Draxler, A. Zitek, M. Meischel, E. Martinelli, T. Kraus, S. Hann, S.E. Stanzl-Tschegg, P.J. Uggowitzer, J.F. Löffler, A.M. Weinberg, T. Prohaska, Long-term in vivo degradation behavior and near-implant distribution of resorbed elements for magnesium alloys WZ21 and ZX50, Acta Biomaterialia 42 (2016) 440-450.

[13] D. Crapper, S. Krishnan, A. Dalton, Brain aluminum distribution in Alzheimer's disease and experimental neurofibrillary degeneration, Science 180(4085) (1973) 511-513.

[14] J. Hofstetter, S. Rüedi, I. Baumgartner, H. Kilian, B. Mingler, E. Povoden-Karadeniz, S. Pogatscher, P.J. Uggowitzer, J.F. Löffler, Processing and microstructure–property relations of high-strength low-alloy (HSLA) Mg–Zn–Ca alloys, Acta Materialia 98 (2015) 423-432.

[15] C. Zener, quoted by CS Smith, Trans. AIME 175 (1948) 15.

[16] Y.-N. Zhang, D. Kevorkov, J. Li, E. Essadiqi, M. Medraj, Determination of the solubility range and crystal structure of the Mg-rich ternary compound in the Ca–Mg–Zn system, Intermetallics 18(12) (2010) 2404-2411.

[17] H.-x. Li, S.-k. Qin, Y.-z. Ma, J. Wang, Y.-j. Liu, J.-s. Zhang, Effects of Zn content on the microstructure and the mechanical and corrosion properties of as-cast low-alloyed Mg–Zn–Ca alloys, International Journal of Minerals, Metallurgy, and Materials 25(7) (2018) 800-809.

[18] H. Bakhsheshi-Rad, M. Abdul-Kadir, M. Idris, S. Farahany, Relationship between the corrosion behavior and the thermal characteristics and microstructure of Mg–0.5 Ca–xZn alloys, Corrosion Science 64 (2012) 184-197.

[19] T. Cain, L. Bland, N. Birbilis, J. Scully, A compilation of corrosion potentials for magnesium alloys, Corrosion 70(10) (2014) 1043-1051.

[20] A. Südholz, N. Kirkland, R. Buchheit, N. Birbilis, Electrochemical properties of intermetallic phases and common impurity elements in magnesium alloys, Electrochemical and Solid-State Letters 14(2) (2011) C5-C7.

[21] M. Cihova, P. Schmutz, R. Schäublin, J.F. Löffler, Biocorrosion Zoomed In: Evidence for Dealloying of Nanometric Intermetallic Particles in Magnesium Alloys, Advanced Materials 31(42) (2019) 1903080.

[22] Y. Lu, A. Bradshaw, Y. Chiu, I. Jones, Effects of secondary phase and grain size on the corrosion of biodegradable Mg–Zn–Ca alloys, Materials Science and Engineering: C 48 (2015) 480-486.

[23] G.L. Song, A. Atrens, Corrosion mechanisms of magnesium alloys, Advanced Engineering Materials 1(1) (1999) 11-33.

[24] CompuTherm LLC, Pandat software package for calculating phase diagrams and thermodynamic properties of multi- component alloys, Madison, USA, www.computherm.com.).

[25] MatCalc software package for computer simulation of phase transformation and microstructure evolution in metallic systems, Vienna, Austria, www.matcalc-engineering.com.

[26] J.F. Löffler, P.J. Uggowitzer, C. Wegmann, M. Becker, H.K. Feichtinger, Process and apparatus for vacuum distillation of high-purity magnesium. European Patent Application PCT, EP 2013/000131–WO2013/1076442012, 2012.

[27] J. Hofstetter, E. Martinelli, A.M. Weinberg, M. Becker, B. Mingler, P.J. Uggowitzer, J.F. Löffler, Assessing the degradation performance of ultrahigh-purity magnesium in vitro and in vivo, Corrosion Science 91 (2015) 29-36.

[28]   A.C. Hänzi, P. Gunde, M. Schinhammer, P.J. Uggowitzer, On the biodegradation performance of an Mg–Y–RE alloy with various surface conditions in simulated body fluid, Acta Biomaterialia 5(1) (2009) 162-171.

[29]   G. Song, A. Atrens, D. St John, An hydrogen evolution method for the estimation of the corrosion rate of magnesium alloys, in: J.N. Hryn (Ed.) Magnesium Technology 2001, TMS, New Orleans, LA, USA, 2001, 254-262.

[30]   ASTM, Standard Practice for Laboratory Immersion Corrosion Testing of Metals, ASTM International, American Society for Testing and Materials G31-72, 2004.

[31]   M. Pourbaix, Atlas of electrochemical equilibria in aqueous solution, NACE 307 (1974).

[32]   F. Witte, V. Kaese, H. Haferkamp, E. Switzer, A. Meyer-Lindenberg, C. Wirth, H. Windhagen, In vivo corrosion of four magnesium alloys and the associated bone response, Biomaterials 26(17) (2005) 3557-3563.

[33]   L. Li, J. Gao, Y. Wang, Evaluation of cyto-toxicity and corrosion behavior of alkali-heat-treated magnesium in simulated body fluid, Surface and Coatings Technology 185(1) (2004) 92-98.

[34]   E. Willbold, F. Witte, Histology and research at the hard tissue–implant interface using Technovit 9100 New embedding technique, Acta Biomaterialia 6(11) (2010) 4447-4455.

[35]   A. Myrissa, E. Martinelli, G. Szakács, L. Berger, J. Eichler, S.F. Fischerauer, C. Kleinhans, N. Hort, U. Schäfer, A.M. Weinberg, In vivo degradation of binary magnesium alloys–a long-term study, BioNanoMaterials 17(3-4) (2016) 121-130.

[36]   J. Hofstetter, Development of high-strength low-alloy (HSLA) magnesium alloys for biomedical application, PhD thesis, ETH Zurich, Zurich, Switzerland, 2015.

[37]   M. Cihova, R. Schäublin, L.B. Hauser, S.S.A. Gerstl, C. Simson, P.J. Uggowitzer, J.F. Löffler, Rational design of a lean magnesium-based alloy with high age-hardening response, Acta Materialia 158 (2018) 214-229.

[38]   K. Oh-Ishi, R. Watanabe, C. Mendis, K. Hono, Age-hardening response of Mg–0.3 at.% Ca alloys with different Zn contents, Materials Science and Engineering: A 526(1) (2009) 177-184.

[39]   C. Davies, M. Barnett, Expanding the extrusion limits of wrought magnesium alloys, JOM Journal of the Minerals, Metals and Materials Society 56(5) (2004) 22-24.

[40]   M. Jiang, C. Xu, T. Nakata, H. Yan, R. Chen, S. Kamado, High-speed extrusion of dilute Mg-Zn-Ca-Mn alloys and its effect on microstructure, texture and mechanical properties, Materials Science and Engineering: A 678 (2016) 329-338.

[41]   N.T. Kirkland, N. Birbilis, M. Staiger, Assessing the corrosion of biodegradable magnesium implants: a critical review of current methodologies and their limitations, Acta Biomaterialia 8(3) (2012) 925-936.

[42]   K. Gusieva, C. Davies, J. Scully, N. Birbilis, Corrosion of magnesium alloys: the role of alloying, International Materials Reviews 60(3) (2015) 169-194.

[43]   E. Martinelli, M. Cihova, S. Bräuer, A. Myrissa, J. Eichler, W. Gössler, P.J. Uggowitzer, J.F. Löffler, A.M. Weinberg, Long-term in vivo response of biodegradable Mg–Zn–Ca alloys of varying Zn content, in preparation.

[44]   G.A. Parker, C.A. Picut, Atlas of histology of the juvenile rat, Academic Press 2016.

[45]   R. Schäublin, M. Becker, M. Cihova, S.S.A. Gerstl, D. Deiana, C. Hébert, S. Pogatscher, P.J. Uggowitzer, J.F. Löffler, Precipitation in the Mg–Zn–Ca alloy ZX20, in preparation.

[46] S.M. Baek, H.K. Park, J.I. Yoon, J. Jung, J.H. Moon, S.G. Lee, J.H. Kim, T.S. Kim, S. Lee, N.J. Kim, Effect of secondary phase particles on the tensile behavior of Mg-Zn-Ca alloy, Materials Science and Engineering: A 735 (2018) 288–294.

[47] B. Langelier, X. Wang, S. Esmaeili, Evolution of precipitation during non-isothermal ageing of an Mg–Ca–Zn alloy with high Ca content, Materials Science and Engineering: A 538 (2012) 246-251.

[48] A. Nayeb-Hashemi, J.B. Clark, Phase diagrams of binary magnesium alloys, ASM International, Metals Park, Ohio 44073, USA, 1988.

[49] Z. Zeng, Y. Zhu, S. Xu, M. Bian, C. Davies, N. Birbilis, J. Nie, Texture evolution during static recrystallization of cold-rolled magnesium alloys, Acta Materialia 105 (2016) 479-494.

[50] F. Mansfeld, Area relationships in galvanic corrosion, Corrosion 27(10) (1971) 436-442.

[51] N. Kirkland, J. Lespagnol, N. Birbilis, M. Staiger, A survey of bio-corrosion rates of magnesium alloys, Corrosion Science 52(2) (2010) 287-291.

[52] L. Bland, N. Birbilis, J. Scully, Exploring the effects of intermetallic particle size and spacing on the corrosion of Mg-Al alloys using model electrodes, Journal of The Electrochemical Society 163(14) (2016) C895-C906.

[53] L.G. Bland, J. Bhattacharyya, S. Agnew, J. Scully, Effect of Intermetallic Particle Size and Distribution on the Corrosion of an Mg-Al Alloy, Meeting Abstracts, The Electrochemical Society, 2016, 1327-1327.

[54] N.D. Nam, Role of zinc in enhancing the corrosion resistance of Mg-5Ca alloys, Journal of The Electrochemical Society 163(3) (2016) C76-C84.

[55] J. Hofstetter, E. Martinelli, S. Pogatscher, P. Schmutz, E. Povoden-Karadeniz, A.M. Weinberg, P.J. Uggowitzer, J.F. Löffler, Influence of trace impurities on the in vitro and in vivo degradation of biodegradable Mg–5Zn–0.3 Ca alloys, Acta Biomaterialia 23 (2015) 347-353.

[56] R. Buchheit, R. Grant, P. Hlava, B. McKenzie, G. Zender, Local dissolution phenomena associated with S phase (Al2CuMg) particles in aluminum alloy 2024-T3, Journal of the Electrochemical Society 144(8) (1997) 2621-2628.

[57] N. Dimitrov, J. Mann, K. Sieradzki, Copper redistribution during corrosion of aluminum alloys, Journal of the Electrochemical Society 146(1) (1999) 98-102.

[58] M. Taheri, J. Kish, N. Birbilis, M. Danaie, E. McNally, J. McDermid, Towards a physical description for the origin of enhanced catalytic activity of corroding magnesium surfaces, Electrochimica Acta 116 (2014) 396-403.

[59] D. Höche, C. Blawert, S.V. Lamaka, N. Scharnagl, C. Mendis, M.L. Zheludkevich, The effect of iron re-deposition on the corrosion of impurity-containing magnesium, Physical Chemistry Chemical Physics 18(2) (2016) 1279-1291.

[60] N. Birbilis, A. King, S. Thomas, G. Frankel, J. Scully, Evidence for enhanced catalytic activity of magnesium arising from anodic dissolution, Electrochimica Acta 132 (2014) 277-283.

[61] D. Lysne, S. Thomas, M. Hurley, N. Birbilis, On the Fe enrichment during anodic polarization of Mg and its impact on hydrogen evolution, Journal of The Electrochemical Society 162(8) (2015) C396-C402.

[62] E. Michailidou, H.N. McMurray, G. Williams, Quantifying the Role of Transition Metal Plating in the Cathodic Activation of Corroding Magnesium, ECS Transactions 75(27) (2017) 141-148.

[63] Y. Zhang, P. Gore, W. Rong, Y. Wu, Y. Yan, R. Zhang, L. Peng, J.-F. Nie, N. Birbilis, Quasi-in-situ STEM-EDS insight into the role of Ag in the corrosion behaviour of Mg-Gd-Zr alloys, Corrosion Science 136 (2018) 106-118.

[64]   M. Danaie, R.M. Asmussen, P. Jakupi, D.W. Shoesmith, G.A. Botton, The role of aluminum distribution on the local corrosion resistance of the microstructure in a sand-cast AM50 alloy, Corrosion Science 77 (2013) 151-163.

[65]   R.M. Asmussen, P. Jakupi, M. Danaie, G.A. Botton, D.W. Shoesmith, Tracking the corrosion of magnesium sand cast AM50 alloy in chloride environments, Corrosion Science 75 (2013) 114-122.

[66]   J. Li, W. Sun, B. Hurley, A.A. Luo, R.G. Buchheit, Cu redistribution study during the corrosion of AZ91 using a rotating ring-disk collection experiment, Corrosion Science 112 (2016) 760-764.

[67]   Z. Cano, M. Danaie, J. Kish, J. McDermid, G. Botton, G. Williams, Physical characterization of cathodically-activated corrosion filaments on magnesium alloy AZ31B, Corrosion 71(2) (2014) 146-159.

[68]   P.K. Bowen, J. Drelich, J. Goldman, Zinc exhibits ideal physiological corrosion behavior for bioabsorbable stents, Advanced Materials 25(18) (2013) 2577-2582.

[69]   E. McCafferty, Kinetics of Corrosion, in: E. McCafferty (Ed.), Introduction to Corrosion Science, Springer, New York, USA, 2010, 119-175.

[70]   T. Kraus, S. Fischerauer, S. Treichler, E. Martinelli, J. Eichler, A. Myrissa, S. Zötsch, P.J. Uggowitzer, J.F. Löffler, A.M. Weinberg, The influence of biodegradable magnesium implants on the growth plate, Acta Biomaterialia 66 (2018) 109-117.

5 Mechanical properties of ZX-lean alloys

Alloy development for deployment as biodegradable implant material generally aims at optimizing simultaneously the corrosion and mechanical properties. While the previous chapters focused on the corrosion properties, this chapter addresses the mechanical performance of ZX-lean alloys, aiming at identifying the main microstructural contributors to the alloys' strength and exploring their hardening potential upon artificial aging.

Identifying the microstructural contributors to the mechanical performance of Mg–Zn–Ca-lean alloys

5.1 Introduction

The mechanical performance of Mg alloys is governed by their microstructure, which in turn is controlled by the alloys' composition and thermomechanical history. Thermomechanical treatments are thus, besides alloying strategies [1, 2], very effective in controlling their mechanical properties [3-10].

This chapter focuses on the mechanical performance of ZX alloys, and specifically of ZX-lean alloys processed under the conditions described in section 1.1.5. '*Mg–Zn–Ca System*'. Note that in this chapter only aspects concerning the mechanical performance are considered while those concerning the material's corrosion resistance are covered in the previous chapters. However, it should be again emphasized that for the development of a successful (bio)material, both mechanical and corrosion performance need to be simultaneously optimized and carefully balanced. Here, the effect of Zn and Ca addition on Mg's mechanical properties is demonstrated first, followed by a presentation of thermomechanical treatment strategies to improve the mechanical performance further.

Zn is added to Mg for its reported effect to refine the grain size [11, 12] and improve the creep resistance [11]. Furthermore, Mg–Zn binary alloys possess some degree of age-hardening response [13, 14] and its intermetallic compounds provide precipitation hardening [15]. With its relatively high solubility in Mg (6.2 wt.% or 2.5 at.% at the eutectic temperature of 341 ºC [16]), it also plays a role in solid-solution strengthening [17], even if considered small [15]. Increasing strength was reported for a Zn addition of up to 5 wt.% and ascribed to a combined effect of solid-solution strengthening, precipitation hardening, and grain-boundary strengthening [12]. Further increase of the Zn content, however, was observed to result in reduced strength and lower ductility, owing to the coarser nature of the precipitates that turns them in initiators of premature fracture [12].

The addition of Ca to Mg is beneficial as it tends to weaken the texture developed by extrusion [3] and to generate grain refinement [18]. Owing to the low solubility of Ca (0.82 at.% at 516 ºC and practically no solubility at temperatures below 250 ºC [19]), precipitation occurs easily via formation of the Mg_2Ca phase. Its fine precipitation increases the material strength by precipitation hardening

and grain-growth retardation [18, 20], whereas its coarse precipitation is associated with declined age hardening [21] and deterioration of ductility [22, 23].

Upon co-alloying of Zn and Ca to Mg, Zn- and Ca-rich precipitates are formed, the precursors of which lead to hardening upon artificial aging [21, 24], which exceeds that of Mg–Zn or Mg–Ca binary systems [13, 14, 25]. In the mature state, Zn- and Ca-rich precipitates can retard grain growth by pinning grain boundaries [5, 26, 27] thereby assisting grain refinement, which is beneficial for both strength and ductility. However, care must be taken to prevent their overly coarse precipitation or excessive volume fraction. This is to be avoided because, on the one hand, it suppresses the formation of finely-dispersed precipitates that are important for age hardening [25], and, on the other hand, it may generate crack-initiation sites [28]. Already for precipitate sizes as small as a few micrometers, it was reported that they induce micro-crack formation that leads to detrimental macroscopic failure [28]. Finally, it was reported by Zeng et al. [29] that Zn and Ca segregate to the grain boundaries in Mg–Zn–Ca alloys, and that their segregation additionally assists grain refinement by retarding grain-boundary motion.

Much effort was devoted to further optimizing the mechanical properties of Mg–Zn–Ca alloys towards maximum grain refinement and age-hardening potential: from thermomechanical treatments such as extrusion [30], rolling [28, 31], powder-metallurgical routes, or severe plastic deformation [6, 7]; to the addition of additives, such as carbides, to control heterogeneous recrystallization and retard grain growth [32]; to a combination of these approaches [5, 8]. Indeed, plastic deformation via hot forming proved to be very effective in light of optimized strength and ductility by generating a small grain size and process-specific texture [3, 4, 6, 7]. In this context, extrusion in particular is an attractive process because it combines scalability, fast processing, and relatively low costs. It is well known that thermomechanical parameters, such as processing temperature [3, 4], processing speed [9], extrusion ratios [10], or processing modes such as direct opposed to indirect extrusion [4], severely influence the microstructure and thus the resulting mechanical properties.

Owing to this wealth of parameters impacting the microstructure and in turn the mechanical properties, the specific microstructure–mechanical properties correlations need to be separately characterized for each material, comprising its composition and processing conditions.

The aim of this chapter is to shed light on the microstructure–mechanical properties correlations of ZX-lean alloys processed under the conditions described in section 1.1.5. '*Mg–Zn–Ca System*'. On that account, the microstructural features characteristic of ZX-lean alloys, i.e. fine grain size and nanometric intermetallic particles, are carefully examined for their contribution to the strength of

ZX-lean alloys, aiming at demonstrating their individual importance to the mechanical performance. The contribution of solid-solution strengthening is disregarded here due to the rather low solute content in the Mg matrix (Zn at about 0.4 at.% and Ca at about 0.05 at.%) in the ZX-lean alloys of interest. Furthermore, the age-hardening potential of ZX-lean alloys is scrutinized as a potential approach to further enhance their mechanical performance.

5.2 Experimental details

5.2.1   Heat treatments

In order to evaluate the contribution of grain-boundary strengthening to the material strength of ZX-lean alloys, the grain size was varied by means of heat treatments. As-extruded ZX10 was heat treated at different temperatures between 250 to 375 °C at $\sqrt{D(T)\,t}$ = const., where D is the temperature-dependent diffusion coefficient taken here from the activation energy of Zn in Mg at 133 kJ mol^{-1}, and t is the time of heat treatment. The thermomechanical condition denominated 'as-extruded' refers here to an extrusion temperature of 300 °C (following the multi-step heat treatment presented in section 1.1.5. '*Mg–Zn–Ca System*', Figure 1.6), if not stated otherwise.

5.2.2   Microstructural analysis

Light microscopy. For grain-size analysis, samples were cut perpendicularly to the extrusion axis, and prepared by mechanical grinding and polishing followed by etching with picric acid to reveal the grain boundaries. The grain size was analyzed by applying the linear intercept method using the Lince® software (TU Darmstadt).

Transmission electron microscopy. Samples for TEM analysis were prepared first by mechanically grinding to a thickness of about 80 µm. They were then punched into standard 3 mm TEM disks. Electron transparency was achieved by Ar^{+}-ion milling using a precision-ion polishing system (PIPS™ II from Gatan, Inc.) at an incident angle of 3.5° and an acceleration voltage of 4 kV. At the end, the voltage was reduced to 0.5 kV for 20 min to achieve a good surface finish. Ion milling was performed at liquid-nitrogen temperature to prevent changes to the microstructure. The samples were stored in vacuum or under Ar atmosphere until further analysis.

TEM imaging was performed in an FEI Talos™ F200X operated at 80 kV. The TEM is equipped with a high-brightness field-emission gun. Imaging was either performed in scanning TEM (STEM) mode with a high-angle annular dark-field detector (HAADF-STEM mode) or in bright-field (BF) TEM mode.

Samples for TEM *in situ* heating were prepared by focused-ion beam milling (Zeiss NVision40) as FIB lamellae. Heating was provided by a MEMS chip (DENSsolutions) with a Pt-based heating coil embedded in a ~200 nm silicon-nitride membrane with ~10 µm holes. Each lamella was transferred over one of the holes, allowing to observe it unobstructed through the heating chip. For the *in situ* heating experiment, a dedicated double-tilt holder (Wildfire D6 model, DENSsolution) was deployed.

The experiment was conducted in the FEI Talos™ F200X operated at 80 kV and imaging was performed in STEM-HAADF mode.

5.2.3 Mechanical testing

Tensile tests. Tensile specimens were prepared according to DIN 50125 (either as M5, diameter = 3 mm, or M3, diameter = 2 mm). All specimens were prepared from extruded bars parallel to the extrusion direction. The specimens were machined from the ZX10 alloy either in their as-extruded or additionally heat-treated conditions (details in Table 5.1 below). Tests were conducted using an electromechanical universal testing machine (Schenck Trebel RSA100) with a 100 kN hydraulic load cell at room temperature and at a strain rate of 10^{-3} s^{-1}.

Artificial aging. The hardening potential of ZX-lean alloys was investigated for the ZX10 alloy by means of artificial-aging treatments. These were performed as an isothermal hold at 200 °C in an oil bath. The isothermal hold was interrupted at distinct times, namely 10 min and 30 min, and 1, 2, 5, 10, 24, 48, and 72 h, by quenching the sample in water. The sample surface was mechanically ground with SiC4000 to remove any impurities or oxide films that may contribute to hardness. The Vickers hardness was determined under a load of 5 kg and a hold time of 16 s on the cross-sectional plane of the extruded or aged rod. Ten individual indents were measured and averaged.

5.3 Results and discussion

5.3.1   Precipitation hardening

Figure 5.1 shows a TEM-BF image of ZX10 heat treated at 350 °C. It reveals grains delineated by grain boundaries and IMPs (in dark contrast) within the grains and at the grain boundaries. The inset to this image reveals dislocation lines that are pinned at the IMPs, causing their bowing (white arrows in Figure 5.1). When dislocations – as the vector of plasticity – are blocked, they increase the material's yield strength. Thus, clear evidence is provided in Figure 5.1 that the IMPs can strengthen the material. Some dislocations were observed to be pinned at additional sites at which no IMP is visible (white arrow heads in Figure 5.1). It is assumed that the pinning points are here either interactions with other dislocations on other glide planes (which are not visible in the image because of the selected diffraction conditions) or that significantly smaller precipitates (or clusters) are at the origin of the dislocation bowing, which are however not visible at the scale of investigation. Further analysis at larger magnification is required to elucidate this point.
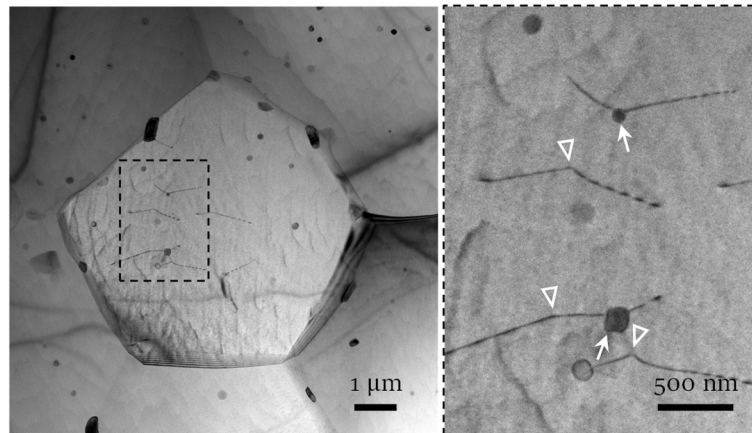
Figure 5.1: TEM bright-field image of ZX10 heat treated at 350 °C for 2.7 h, showing dislocation interactions with inner-grain precipitates. Arrows point at mature precipitates; arrow heads point at sites at which the dislocation interacts either with a dislocation on another glide plane or with a precipitate or cluster of a size non-visible at this scale.

In order to estimate the contribution of IMPs to the material strength, the line-tension model is considered [33]. It describes the particle-dislocation interaction for the case of dislocation bowing at the obstacle with the following equation:

$$\Delta TYS_{\text{IMPs}} = \frac{\alpha\,\mu\,b}{l} \qquad\qquad \text{(Eq. 5.1)}$$

where α is a dimensionless parameter describing the obstacle strength. Here α is set to 1, which corresponds to unshearable obstacles, in order to estimate the maximum possible contribution of the IMPs to hardening; μ is the matrix shear modulus, which is 17 GPa for Mg; b is the magnitude of the Burgers vector with 3.2 Å; and l is the interparticle spacing on the glide plane in m. The latter can be derived from the volume fraction, f_{IMPs}, and the size, d_{IMPs}, of IMPs according to the first member in Eq. 5.2 [34]. l can also be derived by accounting for the number density N_{IMPs} and the size d_{IMPs} determined experimentally by TEM, giving the second member in Eq. 5.2.

$$l = \frac{d_{\text{IMPs}}}{2\sqrt{f_{\text{IMPs}}}} \approx \frac{1}{\sqrt{2\,N_{\text{IMPs}}\,d_{\text{IMPs}}}} \qquad \text{(Eq. 5.2)}$$

In this approximation a spherical particle shape is assumed and only the IMPs' size and number density are taken into consideration. Their shape and orientation relative to the matrix, both known to affect the resulting strength [35], are summarized by the parameter α in Eq. 5.1.

The maximum value for $N_{\text{IMPs}}\,d_{\text{IMPs}}$ is achieved for the ZX10 alloy in its *as-extruded* condition, with 1.4×10^{18} m^{-3} for N_{IMPs} and 80 nm for d_{IMPs} derived from TEM analysis. With these values, the derived strength contribution is at maximum 3.1 MPa. For heat-treated conditions, concomitant with coarsened IMPs, i.e. larger d at a lower N, the maximum strength contribution is even lower. For instance, the heat treatment corresponding to Figure 5.1, at 350 °C for 2.7 h, gives at 1.0×10^{18} m^{-3} for N_{IMPs} and 150 nm for d_{IMPs} a maximum strength contribution of only 2.1 MPa (considering for the determination of N and d only those IMPs that were visible in the TEM analysis conducted). It should be noted that in this estimation in which α is set to 1, the type of IMP, which comprises a characteristic obstacle strength, is not taken into account. The role of IMP type on the material's strength is addressed below in section 5.3.3, '*Grain-boundary strengthening*' (Figure 5.5).

The simplified estimation based on the line-tension model shows clearly that the IMPs only play a subordinate role for the material's strength in terms of precipitation hardening. Nevertheless, the IMPs are essential for the material's performance because they present obstacles to grain-boundary movement, as elaborated upon below.

5.3.2   *Grain-boundary pinning observed by TEM in situ heating*

Figure 5.2 shows a sequence of STEM-HAADF images taken during a TEM *in situ* heating experiment. Figure 5.2a shows the ZX10 alloy in the *as-extruded* state at room temperature. Intermetallic particles are visible in brighter contrast. Complementary EDS analysis revealed that they are of type Mg$_2$Ca (see Figure 2.4 in section 2.3.2 '*Detailed phase analysis*'). A grain boundary runs vertically through the field of view in the middle of the image. Upon heating of the sample to

250 °C, the grain boundary moves – horizontally in the field of view from left to right (the direction of grain-boundary motion is marked with arrows in Figure 5.2b). The grain boundary is observed to interact with the IMPs (see arrow head in Figure 5.2c), causing its local pinning and its bowing-out in its migration direction in-between the IMPs. The bowing can advance as much as the obstacle strength of the IMP allows. The obstacle strength defines a critical pinning angle, past which the grain boundary detaches (Figure 5.2d). Thanks to a relatively high number density and quite homogeneous spatial distribution of the IMPs in the ZX-lean alloy, grain boundaries were, past their first detachments, observed to interact with new IMPs (see arrow heads in Figure 5.2d), thus constantly interacting with IMPs, which can therefore effectively slow down grain growth at elevated temperature. This dynamic *in situ* TEM analysis thus made possible to directly observe the effective grain-boundary pinning capability of the IMPs in the ZX10 alloy, and thus provides the experimental proof of what was previously suggested from stationary TEM analysis by Hofstetter et al. [4].

It should be noted that the grain-boundary motion observed here at the rather low heat-treatment temperature of 250 °C may not be representative for the material as bulk. In fact, *ex situ* heating of ZX10 at 250 °C for more than 15 days did not result in any grain growth (see below in Table 5.1). It is assumed that the minimal material thickness of the TEM foil may lead to a larger grain-boundary mobility due to the proximity of the free surfaces, and thus be responsible for a temperature shift in effective grain growth. A potential temperature shift, however, does not detract from the IMPs' role as grain-boundary obstacles in ZX-lean alloys.
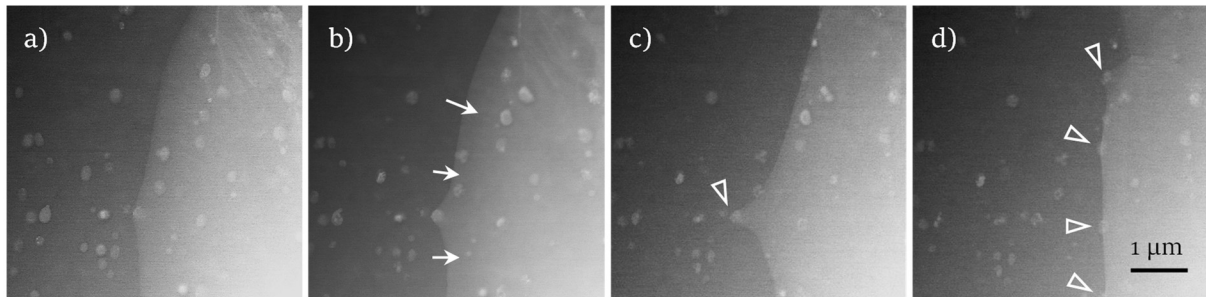
Figure 5.2: STEM imaging during *in situ* heating at 250 °C. (a) ZX10 in its *as-extruded* state at room temperature. Upon heating at 250 °C: (b) Grain-boundary motion after 10 min; the arrows indicate the direction of grain-boundary movement and bowing. (c) Grain-boundary pinning on an IMP (white arrow head) after 70 min. (d) The grain boundary had detached and is newly pinned by other IMPs (marked by arrow heads); the image was taken after 71 min, right after the grain boundary was detached from the IMP marked in (c).

5.3.3 Grain-boundary strengthening

The observation of grain-boundary–precipitate interaction presented in the previous section is well-described and referred to as *Zener pinning* (or *Zener drag*) [36]. It provides a maximum possible grain size D_{max} according to the *Zener–Smith* equation [36]:

$$D_{max} = \frac{2\, d_{IMP}}{3\, f_{IMP}}$$

(Eq. 5.3)

With the values for d_{IMP} and f_{IMP}, both experimentally obtained from TEM-image analysis taken for the *as-extruded* condition as stated above, this equation gives a maximum grain size D_{max} of about 50 μm. This value is substantially larger than the grain size experimentally determined for the *as-extruded* state at about 2 μm, thus suggesting that the latter does not present the equilibrium grain size. It must thus be expected that the IMPs in *as-extruded* ZX10 (with their characteristics for d_{IMPs} and f_{IMPs} as determined here by TEM) will not be able to resist grain growth when the material is subjected to sufficient thermal energy. The results thus underline the importance of relatively low temperatures during processing (here extrusion in the temperature regime of 300 – 330 °C) in order to maintain the fine-grained microstructure desired.

The relationship between the material's grain size and yield strength is described by the well-known *Hall–Petch* equation [37, 38]:

$$TYS = \sigma_0 + k_y\, D^{-\frac{1}{2}}$$

(Eq. 5.4)

where *TYS* is the tensile yield strength, σ_0 is the friction stress for dislocation movement, and k_y is the *Hall–Petch* constant (also stress-concentration factor), which describes the local stress needed at a grain boundary for the transmission of plastic flow.

In order to derive the values for k_y and σ_0 characteristic for the ZX10 alloy, the material is required in various grain sizes. To this end, various heat treatments were performed (Table 5.1) and tensile tests conducted to determine the dependency of *TYS* on grain size. Literature data available for ZX10 from a study by Hofstetter et al. [4] were additionally considered. In their study, a variation of the extrusion temperature led to different grain sizes. All thermomechanical conditions considered along with the resulting *TYS* are summarized in Table 5.1. The variation of extrusion temperatures between 300 and 400 °C resulted in a grain-size variation between 1.6 and 6.8 μm [4], with a progressive increase in grain size for higher extrusion temperatures. The variation of extrusion temperatures between 300 and 400 °C resulted in a grain-size variation between 1.6 and 6.8 μm, with the higher the temperature the larger the grains.

Table 5.1: Thermomechanical treatment parameters, average grain size, and tensile yield strength for samples investigated for the study of grain-boundary strengthening in ZX10. 'b' denotes the binary Mg_2Ca phase and 't' the ternary IM1 phase.

Sample condition	$T_{extrusion}$ (°C)	$T_{annealing}$ (°C)	$t_{annealing}$ (h)	D (µm)	IMP type*	TYS (MPa)	Reference
As extruded	300	-	-	1.6	b	238	[4]
	325	-	-	3.0	b	184	[4]
	375	-	-	4.52 ± 0.79	b	164.9 ± 2.5	This study
	400	-	-	6.8	b	140	[4]
Extruded + Heat treated	375	250	366	4.50 ± 0.33	t	165.9 ± 1.1	This study
	375	275	90	4.60 ± 0.44	t + b	165.3 ± 1.7	This study
	375	300	25	5.07 ± 0.51	t + b	148.2 ± 1.8	This study
	375	350	2.7	8.80 ± 1.17	b	120.4 ± 0.1	This study
	375	375	1	10.23 ± 1.24	b	115.1 ± 2.7	This study

Figure 5.3 shows light micrographs of ZX10 extruded at $T_{extrusion}$ = 375 °C followed by a heat treatment as indicated in Table 5.1. Minor grain growth occurred for heat treatments at 300 °C, and an increasingly pronounced grain growth was observed for increasing heat-treatment temperatures. Heat treatments at 250 and 275 °C, even though extensive in time, did not lead to a change in grain size and it remained at the same level as in the *as-extruded* state (with $T_{extrusion}$ = 375 °C) at about
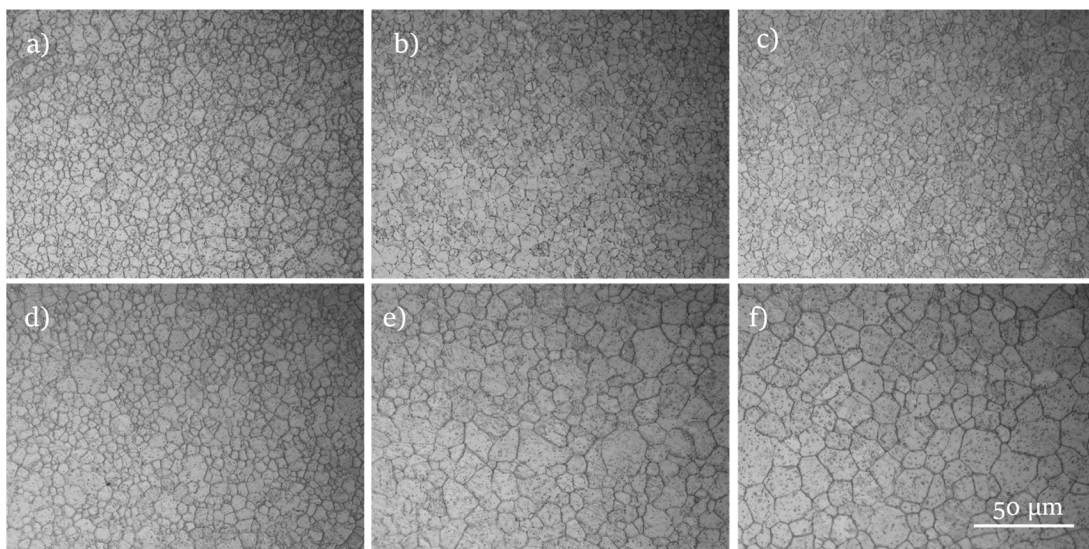

Figure 5.3: Etched light micrographs to reveal the grain boundaries of ZX10 in its (a) *as-extruded* state at an extrusion temperature of 375 °C, and following subsequent heat treatments at (b) 250 °C, (c) 275 °C, (d) 300 °C, (e) 350 °C and (f) 375 °C.

4.5 μm. Both sample conditions were nevertheless taken into consideration for analysis in addition to *the as-extruded* condition because thermodynamic calculations predict that all three differ in their IMP characteristics: while according to Figure 1.5 (simulated phase diagram of ZX10, see section 1.1.5, 'Mg–Zn–Ca System') the *as-extruded* condition is predicted to contain binary Mg_2Ca-type IMPs, a heat treatment at 250 °C is predicted to result in ternary IM1-phase-type IMPs and at 275 °C in a majority of ternary with some binary IMPs. This sample triplet thus allows to experimentally evaluate the role of IMPs on the material strength.

Figure 5.4 presents the tensile yield strength reported in Table 5.1 as a function of the reciprocal square root of the grain size for a grain-size regime from 1.6 μm to 10.2 μm. From the slope of the linear least-square-root fit, and at an infinite grain size, the value k_y is derived at 255 MPa $μm^{1/2}$ and $σ_0$ at 39 MPa, respectively. As a matter of comparison, the values for pure polycrystalline Mg are reported to be k_y = 150 – 200 MPa $μm^{1/2}$ [39, 40] and $σ_0$ = 8 – 36 MPa [39, 41, 42]. The variation of reported data may primarily origin from the various thermomechanical processing conditions applied throughout literature, which may cause a process-specific preferred crystallographic orientation [41-43]. The effect of texture and associated effect of the dominant deformation mechanism on the *Hall–Petch* relationship are not further addressed in this study and the interested reader is directed to literature such as Ref. [44].

Figure 5.4: Least-square fit of tensile yield strength over the reciprocal square root of the grain size D for ZX10 to determine the *Hall–Petch* parameter k_y and the friction stress for dislocation movement, $σ_0$. Using the parameters obtained from the linear fit of the measured data points (solid circles), additional data points are calculated (empty circles). It is seen that a grain size of 900 nm is required to obtain a *TYS* exceeding 300 MPa.

As for σ_o, the close fit for the grain-size dependent *TYS* in Figure 5.4 suggests σ_o to be largely constant throughout the different samples, i.e. the different thermomechanical conditions leading to different levels of solute content in α-Mg. It can thus be assumed that solid-solution strengthening, representing only one of the possible contributors to σ_o, is indeed negligible small in ZX10.

The slightly higher value of σ_o for ZX10 compared to pure Mg is ascribed to a combined contribution of (i) solute atoms in the Mg matrix resulting in solution-strengthening, (ii) intra-grain IMPs resulting in precipitation hardening, and (iii) residual stresses induced by the extrusion mainly resulting in dislocation hardening [42]. As mentioned above, texture effects were not considered for the determination of k_y and σ_o for ZX10. For that reason, the stated values are to be considered valid only for the alloy whose texture is typical of the extrusion process applied in the present study.

Irrespective of the variation for Mg and its alloys, a comparison of the *Hall–Petch* parameters k_y of ZX10 to other materials seems worth. For example, the values for polycrystalline aluminum at about k_y = 40 MPa $\mu m^{1/2}$ [45] or copper at about k_y = 140 MPa $\mu m^{1/2}$ are lower than those reported for Mg, which emphasizes the substantial role of grain refinement for Mg and its alloys.

Considering the thermal history of the samples used for the estimation of the grain-boundary contribution to the material's strength, it is to be mentioned that the individual data points in Figure 5.4 correspond to ZX10 with various IMP characteristics, i.e. type of IMP (binary or ternary phase), and their size, number density, and volume fraction. Regardless of these IMP variations, a close fit at R^2 = 0.98 is obtained solely by considering the related grain-size values. In this context, the samples are closely examined that belong to the sample triplet of constant grain size at about 4.50 µm, i.e. the samples (i) *as-extruded* at 375 °C, (ii) subsequently heat treated at 250 °C, and (iii) subsequently heat treated at 275 °C. Their thermomechanical history relates to different IMP types as previously mentioned. Nevertheless, irrespective of their IMP type the *TYS* was determined to a constant value of about 165 MPa for all three sample states (Table 5.1 and Figure 5.5).

These results thus underline the largely dominating contribution of grain-boundary strengthening over precipitation hardening, and provides experimental evidence for the minute role of IMPs in the strengthening of ZX10, as predicted above by the line-tension model in section 5.3.1, '*Precipitation hardening*'.

With the values determined for k_y and σ_o, the expected *TYS* of ZX10 for smaller grain sizes can be extrapolated by using Eq. 5.4. The predicted *TYS* values for grain sizes below 1 µm are included in Figure 5.4 (square-shaped data points). According to this approximation grain sizes of about 900 nm and 500 nm are required to reach *TYS* values of 300 MPa and 400 MPa, respectively. Possible
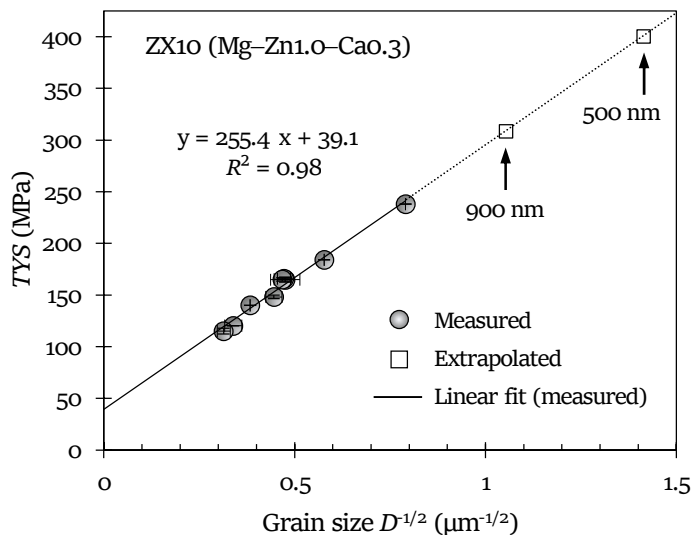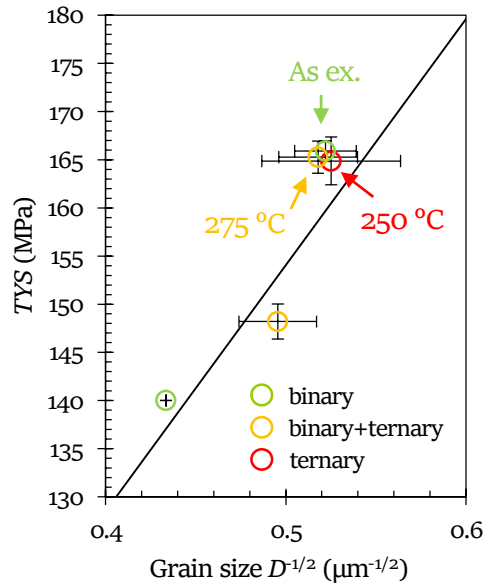
Figure 5.5: Least-square fit of tensile yield strength *TYS* over the reciprocal square root of the grain size *D* for ZX10 in a grain-size regime of 4.5 to 6.8 µm. For each data point, the attributed type of IMP – binary Mg_2Ca, ternary IM1 phase, or a mixture of both – is marked.

approaches to achieve these small grain sizes include severe plastic deformation, such as equal-channel angular pressing (ECAP, also known as ECAE stemming from equal-channel angular extrusion) [46], multipath extrusion [26], high-pressure torsion [47], or powder metallurgical routes [5, 48]. The relations presented here also suggest that an increase in the number density N_{IMP} of IMPs may control the grain size either by effectively preventing grain growth during hot forming, as demonstrated in section 5.3.2, '*Grain-boundary pinning observed by TEM in situ heating*', or by influencing the dynamic recrystallization by particle-induced nucleation processes, as presented in Ref. [49]. Tuning N_{IMP} (and d_{IMP}) may be possible by changing the nominal composition of the ZX-lean alloy while balancing the pre-extrusion thermomechanical treatments, or by introducing foreign particles made from e.g. oxides [50] or SiC [32]. Finally, a reduction in the processing temperature of hot forming to below 300 °C is expected to result in a smaller grain size [26, 51], and thus in improved mechanical performance, provided that a high degree of recrystallization is still attainable.

Another approach may be found in the alteration of the *Hall–Petch* 'strengthening parameter' k_y. In fact, studies have shown that the type of alloying elements in multicomponent Mg alloys influences k_y [42]. Interestingly, in the context of this thesis, Zn – presenting the main alloying element in the ZX system – was reported to effect k_y more strongly (difference to pure Mg: Δk_y = 18 GPa µm$^{1/2}$ per at.% of atomic-solute content) than other common alloying elements such as Al (Δk_y = 2 GPa µm$^{1/2}$ per at.%) or Y (Δk_y = 1 GPa µm$^{1/2}$ per at.%) [42]. Thus, an increase in Zn content

is expected to increase k_y [52], which would in turn generate a more effective yield-strength increase by grain-refinement strategies.

It should however be mentioned that a reduction of grain size below a critical value may generate deviations from the *Hall–Petch* relation valid for micro-crystalline materials and may even invert it [53, 54], owing to a predominating effect of grain-boundary activities at the nanometer scale. This effect, referred to as 'inverse *Hall–Petch* effect', is however generally observed for considerable smaller grain sizes on the order of tens of nanometers. The critical grain size below which the *Hall–Patch* effect reverses in ZX10, and thus sets the limit to which further grain refinement is advantageous, remains to be determined.

5.3.4   *Hardening potential*

In light of easy processability and fast processing while simultaneously achieving high final mechanical strength, hardenable alloys are of great interest. In order to evaluate the hardening potential of ZX-lean alloys, artificial-aging treatments were performed for two thermomechanical conditions: *T5* temper, i.e. *as extruded* + recrystallization-heat treated (*rht*, 325 °C/ 10 min) + artificially aged, and *T6* temper, i.e. *as extruded* + solution-heat treated (*sht*, 450 °C/ 10 min followed by water quenching) + artificially aged [55].

Figure 5.6 shows the hardening response of ZX10 *T5* and *T6* temper upon artificial aging at 200 °C. For *T5*, only a minor hardening increase is observed with a maximum $\Delta H_v \approx 3$ after 2 h artificial-aging time, reaching $H_v = 57.6 \pm 0.8$. Longer times lead to overaging of the material and consequently to a gradual loss of hardness. The miniscule hardening for *T5* temper can be explained by the presence of the Mg_2Ca phase in the *as-extruded* condition, which captures the Ca required for the formation of the Ca- and Zn-containing hardening phase (see [24, 56] and Figure 5.7).

For *T6*, the solution-heat treatment temperature chosen at 450 °C is above the solvus temperature of the Mg_2Ca phase, i.e. Ca is dissolved, forming a super-saturated solid solution (*SSSS*). Upon their dissolution, no obstacles exist for grain-boundary motion and the matrix-grain size grows rapidly from 2.0 ± 0.2 µm in the as-extruded state to 75 ± 17 µm in the *sht* state. The severe grain growth can explain the significant reduction of hardness by $\Delta H_v \approx -16$ observed, which results in a reduced hardness value at $H_v = 38.8 \pm 0.9$ for the *sht* condition. Upon artificial aging at 200 °C, a significant hardening response is observed with a hardness rapidly increasing and reaching a peak hardness of $H_v = 51.0 \pm 1.1$ already after 1 h.
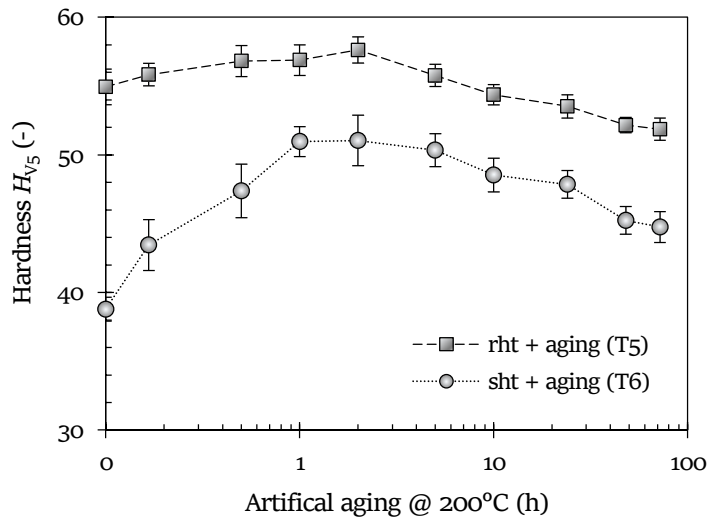
Figure 5.6: Artificial-aging response of the ZX10 alloy for *T5* and *T6* temper at 200 °C.

The age-hardening response in ZX alloys is, according to literature [24, 25] and our own observations on an Mg–Zn1.5–Ca0.25 alloy (in wt.%, ZX20) [56], associated with the formation of monolayered *Guinier–Preston* (G.P.) zones on the basal plane (Figure 5.7). These G.P. zones are assumed to be precursors to the IM1 phase [57]. Complementary high-resolution TEM and atom probe tomography analysis allowed us to reveal that these G.P. zones are rich in both Zn and Ca at an atomic ratio of 1 (Figure 5.7b-c, e-g, reported in [56]). Their detailed structure and precise atomic configuration, however, still remain to be characterized.

The greater kinetics and greater extent of hardening for *T6* compared to *T5* is explained by the larger pressure to precipitate in *T6* as a result of the *sht*, which creates a *SSSS*. Ca holds an important function in the precipitation of the hardening phase, rationalized by (i) its virtual insolubility in Mg at 200 °C [19] while Zn has still some solubility in Mg at about 1 at.% at this temperature [16], and (ii) its roughly 3-times greater diffusivity in Mg compared to the one of Zn [58]. All aspects considered, Ca has a greater driving force to precipitate from the *SSSS* state upon low-temperature artificial aging compared to Zn and is thus considered playing the key role in driving the early-stage precipitation and G.P.-zone formation in these type of alloys [56, 59]. Accordingly, when Ca is captured in the Mg_2Ca phase (which relates to the *as-extruded* condition), the driving force for Ca to precipitate is much diminished, explaining the small hardening response in the *T5* temper. Furthermore, a greater density of vacancies can be expected for the *sht* (and water-quenched) state (*T6*) compared to the *rht* state (*T5*), which would additionally support the diffusion required to form the hardening phase.
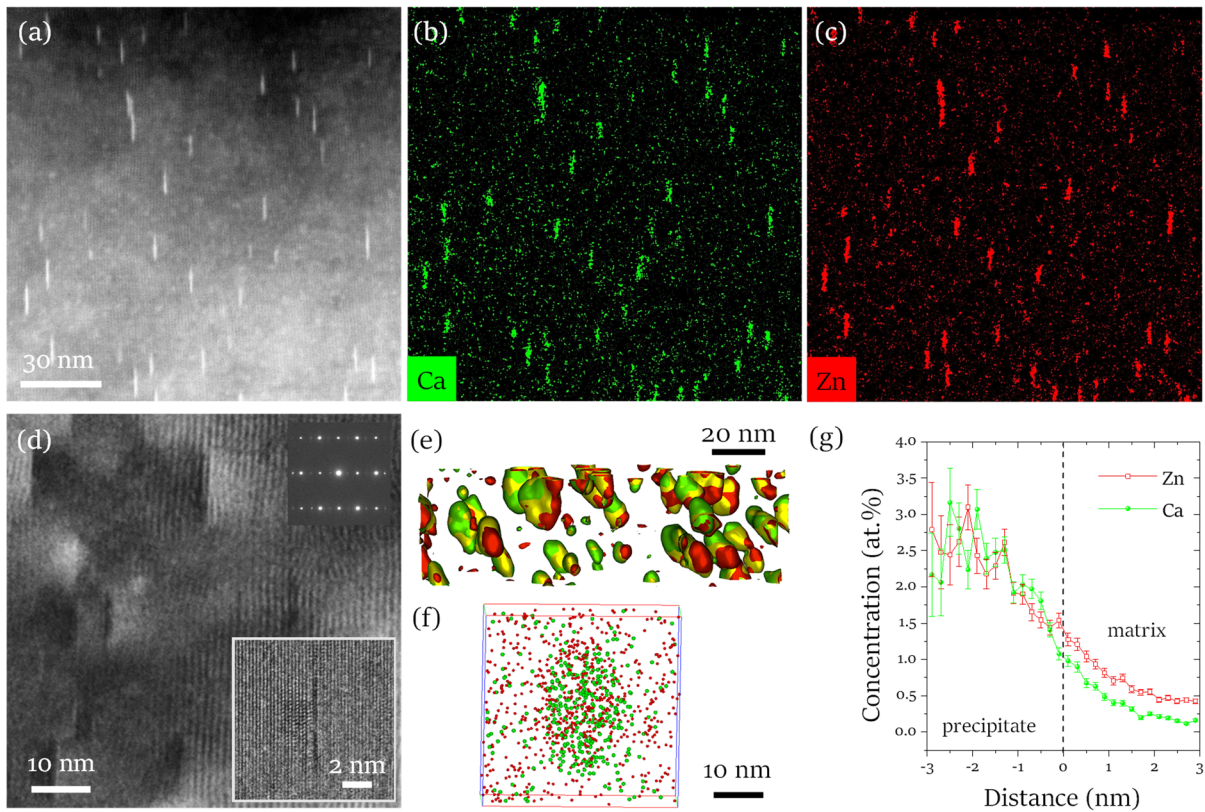
178

Figure 5.7: Analysis of *Guinier-Preston* (G.P.) zones formed upon artificial aging at 200 °C in a ZX-lean alloy with composition Mg–Zn1.5–Ca0.25 (ZX20). (a) The STEM-HAADF image reveals fine precipitates. (b, c) STEM-EDS corresponding to (a) shows that the precipitates are rich in Ca and Zn. (d) The bright-field TEM image shows that the precipitates are monolayered; the related selected-area diffraction pattern in the top-right inset to (d) reveals that the precipitates are present on the basal plane of the Mg matrix; and the bottom-right inset to (d) shows a single G.P. zone. (e-g) Atom probe tomography (APT) analysis to determine the chemical composition of the G.P. zones. (e) APT reconstruction showing isoconcentration surfaces set to 0.8 at.% for Zn, 0.4 at.% for Ca, and 1.06 at.% for Zn+Ca in red, green, and yellow, respectively. The positions of these three isoconcentration surfaces do not match but are slightly shifted owing to artefacts in the measurements. (f) Magnified view of a single precipitate showing individual atoms for Ca (green) and Zn (red). (g) A proximity histogram (proxigram) for an isoconcentration surface of Zn+Ca set to 1.5 at.% shows that the concentration of Zn and Ca increases towards the center of the precipitate and stabilizes at an equal concentration for Zn and Ca of about 2.5 at.%. The data contained in this figure will be reported in [56].

A prolonged aging time, exceeding 2 h at 200 °C, results in overaging due to coarsening of the precipitates and reduction of their number density [24], and consequently in a drastic reduction of the hardness, reaching H_v = 44.8 ± 1.2 after 72 h. Despite the considerable hardness increase for *T6* temper at about $\Delta H_{v,max} \approx 12$ cannot compensate the loss of hardness resulting from the required solution-heat treatment of $\Delta H_v \approx$ -16. Age-hardening as a measure to improve the material strength of ZX-lean alloys thus does not appear to be promising. Furthermore, the severe grain growth upon solution-heat treatment is expected to impede also the material's ductility besides its strength.

It is thus concluded that an effective combination of grain-boundary strengthening and precipitation hardening is at this stage of our understanding not feasible for the ZX-lean alloys. To overcome these limitations, thermally stable intermetallic phases are required that act as efficient obstacles for grain-boundary motion, thereby preserving the desired fine-grained microstructure. The optimum material comprises an additional intermetallic phase or precursor phase that efficiently hardens the material upon low-temperature artificial aging.

5.4 Conclusions

In this chapter the mechanical performance of ZX-lean alloys was investigated in light of their microstructure in order to determine the major microstructural contributors to the alloys' strength. The main conclusions drawn are as follows:

- The by far most important contributor to *TYS* is grain-boundary strengthening.

- The IMPs' contribution by precipitation-hardening to the *TYS* is with a maximum of 3 MPa negligible.

- Nevertheless, the precipitates, present as intermetallic particles (IMPs), have an important impact on the resulting mechanical performance.

- Artificial-aging response is negligible in *T5* temper.

- Artificial-aging efficiency is distinct for *T6* temper, but the loss in strength due to grain growth during *sht* overshadows the hardening response.

- Grain growth during *sht* must be prevented to realize the benefit of hardening for increasing the material's strength.

5.5 References

[1]   M.Ö. Pekgüleryüz, M.M. Avedesian, Magnesium alloying, some potentials for alloy development, Journal of Japan Institute of Light Metals 42(12) (1992) 679-686.

[2]   A. Hänzi, F. Dalla Torre, A. Sologubenko, P. Gunde, R. Schmid-Fetzer, M. Kuehlein, J.F. Löffler, P.J. Uggowitzer, Design strategy for microalloyed ultra-ductile magnesium alloys, Philosophical Magazine Letters 89(6) (2009) 377-390.

[3]   B. Zhang, L. Geng, L. Huang, X. Zhang, C. Dong, Enhanced mechanical properties in fine-grained Mg–1.0 Zn–0.5 Ca alloys prepared by extrusion at different temperatures, Scripta Materialia 63(10) (2010) 1024-1027.

[4]   J. Hofstetter, S. Rüedi, I. Baumgartner, H. Kilian, B. Mingler, E. Povoden-Karadeniz, S. Pogatscher, P.J. Uggowitzer, J.F. Löffler, Processing and microstructure–property relations of high-strength low-alloy (HSLA) Mg–Zn–Ca alloys, Acta Materialia 98 (2015) 423-432.

[5]   T. Zhou, M. Yang, Z. Zhou, J. Hu, Z. Chen, Microstructure and mechanical properties of rapidly solidified/powder metallurgy Mg–6Zn and Mg–6Zn–5Ca at room and elevated temperatures, Journal of Alloys and Compounds 560 (2013) 161-166.

[6]   L. Tong, M. Zheng, X. Hu, K. Wu, S. Xu, S. Kamado, Y. Kojima, Influence of ECAP routes on microstructure and mechanical properties of Mg–Zn–Ca alloy, Materials Science and Engineering: A 527(16-17) (2010) 4250-4256.

[7]   C. Zhang, S. Guan, L. Wang, S. Zhu, L. Chang, The microstructure and corrosion resistance of biological Mg–Zn–Ca alloy processed by high-pressure torsion and subsequently annealing, Journal of Materials Research 32(6) (2017) 1061-1072.

[8]   P. Dobroň, D. Drozdenko, J. Olejňák, M. Hegedüs, K. Horváth, J. Veselý, J. Bohlen, D. Letzig, Compressive yield stress improvement using thermomechanical treatment of extruded Mg-Zn-Ca alloy, Materials Science and Engineering: A 730 (2018) 401-409.

[9]   W.-j. Li, K.-k. Deng, X. Zhang, K.-b. Nie, F.-j. Xu, Effect of ultra-slow extrusion speed on the microstructure and mechanical properties of Mg-4Zn-0.5 Ca alloy, Materials Science and Engineering: A 677 (2016) 367-375.

[10]   L. Tong, M. Zheng, L. Cheng, S. Kamado, H. Zhang, Effect of extrusion ratio on microstructure, texture and mechanical properties of indirectly extruded Mg–Zn–Ca alloy, Materials Science and Engineering: A 569 (2013) 48-53.

[11]   C. Boehlert, K. Knittel, The microstructure, tensile properties, and creep behavior of Mg–Zn alloys containing 0–4.4 wt.% Zn, Materials Science and Engineering: A 417(1-2) (2006) 315-321.

[12]   S. Cai, T. Lei, N. Li, F. Feng, Effects of Zn on microstructure, mechanical properties and corrosion behavior of Mg–Zn alloys, Materials Science and Engineering: A 32(8) (2012) 2570–2577.

[13]   J.-F. Nie, Precipitation and hardening in magnesium alloys, Metallurgical and Materials Transactions A 43(11) (2012) 3891-3939.

[14] C. Mendis, K. Oh-Ishi, K. Hono, Enhanced age hardening in a Mg–2.4 at.% Zn alloy by trace additions of Ag and Ca, Scripta Materialia 57(6) (2007) 485-488.

[15] J. Jain, P. Cizek, W. Poole, M. Barnett, Precipitate characteristics and their effect on the prismatic-slip-dominated deformation behaviour of an Mg–6 Zn alloy, Acta Materialia 61(11) (2013) 4091-4102.

[16] H. Okamoto, Supplemental literature review of binary phase diagrams: Cs-In, Cs-K, Cs-Rb, Eu-In, Ho-Mn, K-Rb, Li-Mg, Mg-Nd, Mg-Zn, Mn-Sm, O-Sb, and Si-Sr, Journal of Phase Equilibria and Diffusion 34(3) (2013) 251-263.

[17] H. Somekawa, Y. Osawa, T. Mukai, Effect of solid-solution strengthening on fracture toughness in extruded Mg–Zn alloys, Scripta Materialia 55(7) (2006) 593-596.

[18] Y. Lee, A. Dahle, D. StJohn, The role of solute in grain refinement of magnesium, Metallurgical and Materials Transactions A 31(11) (2000) 2895-2906.

[19] A. Nayeb-Hashemi, J. Clark, The Ca– Mg (calcium-magnesium) system, Journal of Phase Equilibria 8(1) (1987) 58-65.

[20] J. Seong, W. Kim, Development of biodegradable Mg–Ca alloy sheets with enhanced strength and corrosion properties through the refinement and uniform dispersion of the Mg2Ca phase by high-ratio differential speed rolling, Acta Biomaterialia 11 (2015) 531-542.

[21] J. Nie, B. Muddle, Precipitation hardening of Mg-Ca (-Zn) alloys, Scripta Materialia 37(10) (1997) 1475-1481.

[22] Y. Chino, M. Kobata, H. Iwasaki, M. Mabuchi, Tensile properties from room temperature to 673 K of Mg-0.9 mass% Ca alloy containing lamella Mg2Ca, Materials Transactions 43(10) (2002) 2643-2646.

[23] E. Zhang, L. Yang, Microstructure, mechanical properties and bio-corrosion properties of Mg–Zn–Mn–Ca alloy for biomedical application, Materials Science and Engineering: A 497(1-2) (2008) 111-118.

[24] J. Oh, T. Ohkubo, T. Mukai, K. Hono, TEM and 3DAP characterization of an age-hardened Mg–Ca–Zn alloy, Scripta Materialia 53(6) (2005) 675-679.

[25] K. Oh-Ishi, R. Watanabe, C. Mendis, K. Hono, Age-hardening response of Mg–0.3 at.% Ca alloys with different Zn contents, Materials Science and Engineering: A 526(1) (2009) 177-184.

[26] Y. Du, M. Zheng, X. Qiao, K. Wu, X. Liu, G. Wang, X. Lv, M. Li, X. Liu, Z. Wang, The effect of double extrusion on the microstructure and mechanical properties of Mg–Zn–Ca alloy, Materials Science and Engineering: A 583 (2013) 69-77.

[27] T. Homma, J. Hinata, S. Kamado, Development of an extruded Mg–Zn–Ca-based alloy: new insight on the role of Mn addition in precipitation, Philosophical Magazine 92(12) (2012) 1569-1582.

[28] S.M. Baek, H.K. Park, J.I. Yoon, J. Jung, J.H. Moon, S.G. Lee, J.H. Kim, T.S. Kim, S. Lee, N.J. Kim, Effect of secondary phase particles on the tensile behavior of Mg-Zn-Ca alloy, Materials Science and Engineering: A 735 (2018) 288–294.

[29] Z. Zeng, Y. Zhu, S. Xu, M. Bian, C. Davies, N. Birbilis, J. Nie, Texture evolution during static recrystallization of cold-rolled magnesium alloys, Acta Materialia 105 (2016) 479-494.

[30] L. Geng, B. Zhang, A. Li, C. Dong, Microstructure and mechanical properties of Mg–4.0 Zn–0.5 Ca alloy, Materials Letters 63(5) (2009) 557-559.

[31] J.-Y. Lee, Y.-S. Yun, B.-C. Suh, N.-J. Kim, W.-T. Kim, D.-H. Kim, Comparison of static recrystallization behavior in hot rolled Mg–3Al–1Zn and Mg–3Zn–0.5 Ca sheets, Journal of Alloys and Compounds 589 (2014) 240-246.

[32] Z.-H. Wang, X.-D. Wang, Y.-X. Zhao, W.-B. Du, SiC nanoparticles reinforced magnesium matrix composites fabricated by ultrasonic method, Transactions of Nonferrous Metals Society of China 20 (2010) s1029-s1032.

[33] D. Hull, D.J. Bacon, Introduction to dislocations, Elsevier, Oxford, UK, 2011.

[34] J.W. Martin, Micromechanisms in particle-hardened alloys, Cambridge University Press, Cambridge, UK, 1980.

[35] J. Nie, Effects of precipitate shape and orientation on dispersion strengthening in magnesium alloys, Scripta Materialia 48(8) (2003) 1009-1015.

[36] C. Zener, quoted by CS Smith, Trans. AIME 175 (1948) 15.

[37] E. Hall, The deformation and ageing of mild steel: III discussion of results, Proceedings of the Physical Society. Section B 64(9) (1951) 747.

[38] N.J. Petch, The cleavage strengh of polycrystals, Journal of the Iron and Steel Institute 174 (1953) 25-28.

[39] P. Andersson, C.H. Cáceres, J. Koike, Hall-Petch parameters for tension and compression in cast Mg, Materials Science Forum, Trans Tech Publications, 2003, 123-128.

[40] D. Wilson, J. Chapman, Effects of preferred orientation on the grain size dependence of yield strength in metals, Philosophical Magazine 8(93) (1963) 1543-1551.

[41] D. Nagarajan, C. Cáceres, The Friction Stress of the Hall–Petch Relationship of Pure Mg and Solid Solutions of Al, Zn, and Gd, Metallurgical and Materials Transactions A 49(11) (2018) 5288-5297.

[42] I. Toda-Caraballo, E.I. Galindo-Nava, P.E. Rivera-Díaz-del-Castillo, Understanding the factors influencing yield strength on Mg alloys, Acta Materialia 75 (2014) 287-296.

[43] W. Yuan, S. Panigrahi, J.-Q. Su, R. Mishra, Influence of grain size and texture on Hall–Petch relationship for a magnesium alloy, Scripta Materialia 65(11) (2011) 994-997.

[44] Y. Wang, H. Choo, Influence of texture on Hall–Petch relationships in an Mg alloy, Acta Materialia 81 (2014) 83-97.

[45] N. Hansen, The effect of grain size and strain on the tensile flow stress of aluminium at room temperature, Acta Metallurgica 25(8) (1977) 863-869.

[46] A. Yamashita, Z. Horita, T.G. Langdon, Improving the mechanical properties of magnesium and a magnesium alloy through severe plastic deformation, Materials Science and Engineering: A 300(1-2) (2001) 142-147.

[47] M. Kai, Z. Horita, T.G. Langdon, Developing grain refinement and superplasticity in a magnesium alloy processed by high-pressure torsion, Materials Science and Engineering: A 488(1-2) (2008) 117-124.

[48] M. Pozuelo, C. Melnyk, W.H. Kao, J.-M. Yang, Cryomilling and spark plasma sintering of nanocrystalline magnesium-based alloy, Journal of Materials Research 26(7) (2011) 904-911.

[49] T. Al-Samman, Modification of texture and microstructure of magnesium alloy extrusions by particle-stimulated recrystallization, Materials Science and Engineering: A 560 (2013) 561-566.

[50] S. Hassan, M. Gupta, Effect of particulate size of Al2O3 reinforcement on microstructure and mechanical behavior of solidification processed elemental Mg, Journal of Alloys and Compounds 419(1-2) (2006) 84-90.

[51] H. Pan, G. Qin, M. Xu, H. Fu, Y. Ren, F. Pan, Z. Gao, C. Zhao, Q. Yang, J. She, Enhancing mechanical properties of Mg–Sn alloys by combining addition of Ca and Zn, Materials & Design 83 (2015) 736-744.

[52] C. Cáceres, G.E. Mann, J. Griffiths, Grain size hardening in Mg and Mg-Zn solid solutions, Metallurgical and Materials Transactions A 42(7) (2011) 1950-1959.

[53] H. Choi, Y. Kim, J. Shin, D. Bae, Deformation behavior of magnesium in the grain size spectrum from nano-to micrometer, Materials Science and Engineering: A 527(6) (2010) 1565-1570.

[54] T. Nieh, J. Wadsworth, Hall-Petch relation in nanocrystalline solids, Scripta Metallurgica et Materialia 25(4) (1991) 955-958.

[55] I.O.f.S. (ISO), Aluminium and Aluminium Alloys, Wrought Products - Temper Designations, 2007.

[56] R. Schäublin, M. Becker, M. Cihova, S.S.A. Gerstl, D. Deiana, C. Hébert, S. Pogatscher, P.J. Uggowitzer, J.F. Löffler, Precipitation in the Mg–Zn–Ca alloy ZX20, in preparation.

[57] M. Bamberger, G. Levi, J. Vander Sande, Precipitation hardening in Mg-Ca-Zn alloys, Metallurgical and Materials Transactions A 37(2) (2006) 481-487.

[58] B.-C. Zhou, S.-L. Shang, Y. Wang, Z.-K. Liu, Diffusion coefficients of alloying elements in dilute Mg alloys: A comprehensive first-principles study, Acta Materialia 103 (2016) 573-586.

[59] M. Cihova, R. Schäublin, L.B. Hauser, S.S.A. Gerstl, C. Simson, P.J. Uggowitzer, J.F. Löffler, Rational design of a lean magnesium-based alloy with high age-hardening response, Acta Materialia 158 (2018) 214-229.

6 Lean magnesium alloys with extended age-hardening response

The ZX-lean alloys proved to have an insufficient hardening potential and to lack the possibility of preserving the grain size during high-temperature processing. For this reason, this chapter aims at the design of a new alloy, likewise lean in its composition, but with an extended specific hardening potential, i.e. a large increase in tensile yield strength per at.% of alloying elements (ΔTYS per at.%). For lightweight structural applications, the design aspect of biosafety does not need to be taken into consideration in the choice of alloying elements. As a result, a whole new spectrum of alloying systems becomes available. In this study, we focus on the Mg–Al–Ca–Mn system.

Rational design of a lean magnesium-based alloy with high age-hardening response

Magnesium-based alloys that allow fast processing, easy formability and subsequent age hardening to their final strength are highly desirable for lightweight structural applications. In this study, a lean age-hardenable wrought Mg–Al–Ca–Mn alloy, which combines precipitation hardening and grain refinement by secondary-phase pinning, was designed via thermodynamic calculation. The resulting alloy, AXM100, with a nominal composition Mg–Al0.6–Ca0.28–Mn0.25 (in wt.%), shows a remarkable improvement in tensile yield strength of 70 and 100 MPa upon artificial aging from the *as-extruded* state (*T5*) and the *solution-heat-treated* state (*T6*), respectively, reaching 253 MPa for the latter. A multi-scale microstructural analysis, combining light microscopy, transmission electron microscopy and atom probe tomography, was performed. It revealed a fine dispersion of Al–Mn precipitates with a β-Mn structure and Al–Ca-rich *Guinier–Preston* (G.P.) zones, which have an Al-to-Ca ratio of about 2. The former are responsible for impeding grain growth and the latter for age hardening. In addition, a fine dispersion of nanometric Ca-rich clusters preceding the G.P.-zone formation were identified which may contribute to strength. While the microstructural analysis, in terms of volume fraction and composition of the phases, reveals the limitation of the calculations, the latter successfully predict the elements contained in the various phases that play a key role in the mechanical properties, thereby proving them to be an invaluable tool for alloy design. In fact, the alloy designed in this study shows, despite its leanness, an age-hardening potential of 87 MPa and 118 MPa per 1 at.% total alloying content for the *T5* and *T6* condition, respectively, which is the highest among the compositions known for this type of alloys.

6.1 Introduction

Simultaneous high formability and high strength are required for magnesium (Mg) alloys if they are to be more widely deployed as lightweight structural materials in automotive, high-speed rail or aircraft applications, and to be competitive to their aluminum counterparts. Reducing the alloying content can significantly improve their formability [1, 2] and thereby render their processability, e.g. by extrusion or rolling, economically more attractive. However, a lean-design concept appears counter-intuitive in terms of the desired high strength. Indeed, while an alloy's strength is generally governed by the combined contribution of solid-solution strengthening, precipitation hardening and grain-boundary strengthening, the former two become limited in case of a reduced alloying content. In terms of grain-boundary strengthening, the *Hall–Petch* relationship is mentioned, which describes the dependence of tensile yield strength (*TYS*) on grain size [3, 4]. The *Hall–Petch* constant amounts for Mg to 150 - 250 MPa $\mu m^{1/2}$ [5, 6], which is significantly larger than the one for polycrystalline aluminum (Al) at about 40 MPa $\mu m^{1/2}$ [7], showing the significance of grain refinement for Mg and its alloys. Strategies for achieving the fine-grained microstructure desired include severe plastic deformation (SPD), such as multi-pass equal-channel angular pressing [8] or high-pressure torsion [9], and powder metallurgical routes [10], but are limited by a low processing rate and cannot be easily scaled up.

Wrought alloys are attractive in terms of a high processing output. However, the high processing temperatures required significantly coarsen the grains and, thus, reduce the final strength [11, 12]. This may be compensated by dispersing secondary-phase particles that can pin grain boundaries, thereby suppressing grain growth [13]. Their presence, however, can result in an increased extrusion force required to shape the material. Lean age-hardenable wrought Mg-alloys have thus received considerable attention because of their potential to achieve the desired combination of easy formability with high strength of the final part; the latter obtained by means of precipitation hardening in an artificial-aging treatment following hot forming. A variety of Mg-based alloying systems are suitable for precipitation hardening [14]. Their effectiveness for age hardening is, however, often impaired by the overly coarse nature of precipitates [15, 16]. Indeed, dislocation motion is most effectively restricted by a high number of fine and uniformly dispersed precipitates [13]. Moreover, as in Mg-alloys it is the basal slip that dominates, precipitates located on the basal plane should most effectively increase the alloy's strength. This can be achieved by the precipitation of a metastable, fully coherent phase condensating as mono-layered, nanometric plates on its basal plane in large numbers, referred to as *Guinier–Preston* (G.P.) zones [14]. Many alloys containing rare-earth elements (REE) such as Y, Gd or Nd would satisfy this condition [14]. However, in light of the

growing environmental and economic awareness, new alloys are to be designed that get by without their use.

In this study we focus on the Mg–Al–Ca–Mn system, referred to as AXM, because it appears to fulfill the requirements of easy formability, high age-hardenability and low-cost REE-free composition [17-20]. Pioneering work on this system was done by Nakata *et al.* [17], who demonstrated a remarkable age-hardening potential for this system. In our study, we challenge the AXM system with the aim of optimizing its age-hardening potential while minimizing its alloying-element content.

6.2 Design concept

In the following, we present our design concept which builds on the simultaneous contribution of grain-boundary strengthening and precipitation hardening. This requires thermally stable precipitates for grain refinement and a post-extrusion artificial-aging treatment for a fine dispersion of G.P. zones. We performed thermodynamic calculations to identify a suitable alloy design which comprises both the alloy composition and the thermomechanical processing route (Figure 6.1 and Figure 6.2).

As a boundary condition for the calculations, the maximum total alloying content was set at 1 at.%. This lean-alloy concept, firstly, allows a *solution-heat-treatment (sht)* window for the relevant elements constituting the hardening phase, bringing them into solid solution for an effective hardening potential instead of the otherwise occurring coarse precipitation [15, 16]. Secondly, the leanness avoids a high solute content and a high volume fraction of secondary phases, thus minimizing the force required for hot forming [21]. In the following, we present first the design rules for bringing an effective precipitation hardening by G.P.-zone formation, and then the strategy for achieving grain refinement.

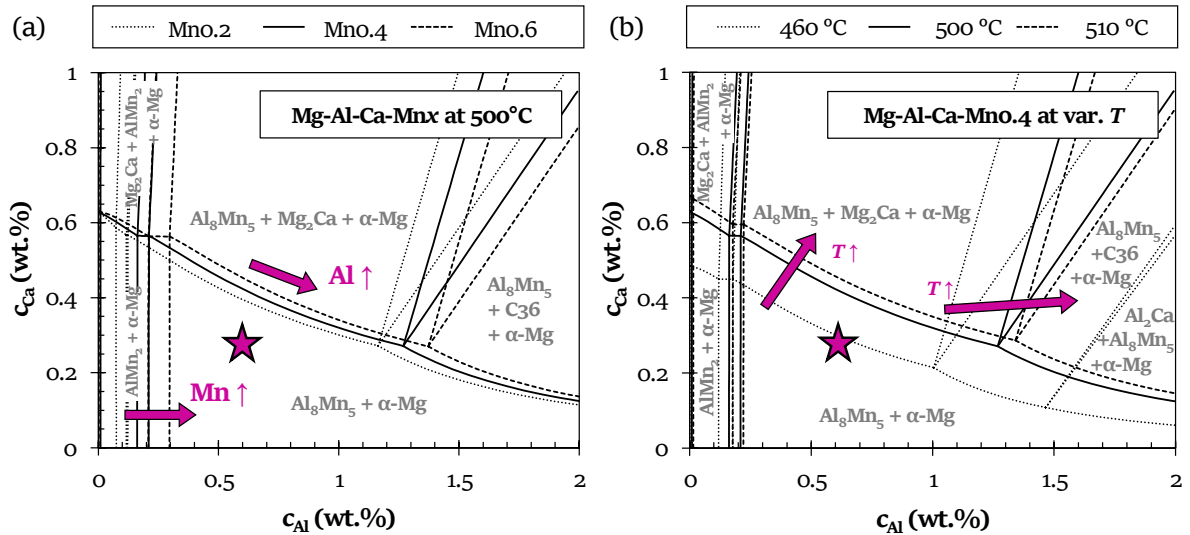**Figure 6.1**: Calculated phase diagrams of AXM as a function of Al and Ca with variations of (a) Mn content and (b) temperature.

6.2.1   Hardening phase: G.P. zones as precursors of the Al$_2$Ca phase

Both binary alloys Mg–Ca and Mg–Al show only a limited aging potential [14, 22, 23], but the simultaneous addition of Al and Ca to Mg can significantly increase the hardening response [22, 24].

Jayaraj *et al.* [22] demonstrated that the trace addition of 0.3 wt.% Al to binary Mg-Ca0.5 (wt.%) enhances the hardness increment significantly, from $\Delta H_V = 10$ without Al to $\Delta H_V = 32$ with Al. This was attributed to the formation of G.P. zones that form at low temperature upon disintegration of a super-saturated solid solution (*SSSS*). They are believed to have a C15 structure and to be the precursors of the fcc/ C36 Al_2Ca equilibrium phase [19, 22, 24]. These G.P. zones constitute the hardening phase considered in our alloying design. Because their precipitation is reported to originate from *SSSS* [14], the alloy composition is to be balanced accordingly to allow for an *sht* window which provides sufficient amounts of Ca and Al in solid solution to form those G.P. zones upon artificial aging. As the precise composition and structure of the G.P. zones are still unknown, the present alloy design relies on thermodynamic calculations which predict the Al_2Ca phase, i.e. assume an Al-to-Ca atomic ratio of 2.

The alloy's total amount of Al and Ca, as well as their ratio, appear to sensitively govern the level of the aging response [18, 22]. The lower concentration limit of both elements is set by their solubility in Mg, which restricts their driving force to precipitate. This is more pronounced for Al, which has a significantly higher solubility in Mg than Ca. The upper concentration limit, in contrast, is mainly defined by Ca: on the one hand, ease of formability is known to decline severely with increased Ca content [20, 21]; on the other hand, the low solubility of Ca in Mg [25] stabilizes the Mg_2Ca phase even at low Ca amounts (Figure 6.1a). The solubility of Ca and the Mg_2Ca phase is further decreased by the presence of Al (Figure 6.1a). An excess of the Al and Ca content is reached when it impedes the possibility of the *sht* window required to obtain an *SSSS* for Ca. This would promote the coarse formation of equilibrium phases Mg_2Ca (C14), Al_2Ca (C15), $(Mg,Al)_2Ca$ or $(Al,Mg)_2Ca$ (both C36). This is detrimental in two ways: first, the amount of Al and Ca in solid solution is depleted, which in turn impedes the formation of the desired G.P. zones; second, the coarse precipitation of equilibrium phases is impairing the mechanical performance because they may act as crack-initiation sites [18]. With regard to their ratio, the assumed composition for the desired G.P. zones of Al_2Ca is recalled, which suggests that the minimum required concentration of Al should amount to twice that of Ca. The sensitivity with which the Al-to-Ca ratio determines the hardening potential is evident from the aforementioned work by Jarayaj *et al.* [22], who studied the aging potential of dilute Mg–Al–Ca alloys with varying Al-to-Ca ratios by adjusting the Al content at a constant Ca content of 0.5 wt.%. In fact, they observed an enhanced hardness increment with the successive increase in the Al content from 0 to 0.1 to 0.3 wt.% Al. However, the expected increase with further Al addition could not be achieved. This is probably due to surpassing the upper limit for Al and Ca, thereby promoting the formation of coarse Mg_2Ca phase (Figure 6.1a) and thus limiting the hardness potential.

6.2.2 *Grain refinement via thermally stable Al$_8$Mn$_5$ dispersoids*

Before considering the simultaneous presence of Al, Ca and Mn in Mg, we will examine the isolated impact of Mn in Mg. Mn addition was shown to refine the grain size in several wrought Mg alloys [26-29]. In Al-containing wrought Mg alloys, this grain refinement is explained by the formation of Al–Mn dispersoids that retard grain growth by pinning the grain boundaries [20, 28]. Due to their high thermal stability, with a predicted solvus temperature at 600°C for the optimized alloy composition of this study (Figure 6.3), this effect should persist at elevated processing temperatures. According to *Zener* [13], the pressure with which grain-boundary motion is restricted by such secondary-phase precipitates increases with a reduction of their size, given a constant volume fraction. The processing-related measures taken to obtain the characteristics required of such dispersoids are presented below in the section 6.2.3, '*Thermomechanical conditions*'.

Finally, when concurrently adding Al, Mn and Ca to combine the effects of grain-boundary pinning by thermally stable Al–Mn dispersoids and age hardening via G.P. zones with an assumed Al$_2$Ca composition, the consumption of Al by Mn for the formation Al–Mn phase needs to be taken into account. Note that the Al–Mn phase is stable in the *sht* temperature regime (Figure 6.3). With this in mind, only the remaining Al content in solid solution that was not consumed by Mn is available to form the hardening Al–Ca phase during artificial aging. Assuming the Al–Mn phase to be of the type Al$_8$Mn$_5$, as reported in literature [30] and predicted by the calculations (Figure 6.1) [31], an excess of Al over Mn is essential. The required extent of Al excess is, in turn, set by the Ca content available in solid solution at the *sht* temperature chosen, and should correspond to the Al-to-Ca atomic ratio of 2. This set of rules is confirmed by a study conducted on Mg–Al0.27–Ca0.13–Mn0.21 (in at.%) with a corresponding Al-to-Mn atomic ratio of about 5 to 4 [32]. Besides a generally satisfying mechanical performance, this alloy showed only a marginal age-hardening response of about ΔH_V = 7, corresponding to an increase of roughly 16% [32]. Another study, conducted on Mg-Al0.3-Ca0.2Mnx (in at.%), showed that an increase in Mn content from 0.1 to 0.2 at.% caused the alloy's aging response to deteriorate significantly [33]. On this basis, maximizing the Ca content in solid solution with subsequent appropriate balancing of Al and Mn appears reasonable. The Ca content, however, needs to be kept within the limits to still allow the required *sht* window for Ca. Figure 6.1b shows, using the example of a constant Mn content of 0.4 wt.%, that Ca can be fully solubilized at temperatures above 460 °C. While the solubility can be increased further with temperature (Figure 6.1b), it is limited by the solidus temperature, which is predicted to be 517 °C for the optimized composition (Figure 6.3). It is also evident that a high Ca content in solid solution can only be obtained when both Ca and Al are kept low (Figure 6.1b), thereby underlining the essence

of the lean-alloying design. Figure 6.3 shows the calculated phase diagram for the optimized composition

6.2.3   *Thermomechanical conditions*

Figure 6.2 depicts the sequence of thermomechanical conditions applied to explore the potential of the alloy design presented. It comprises fast cooling from the melt to avoid precipitation during cooling, followed by a homogenization heat treatment. The latter features slow heating to an intermediate temperature: this is envisioned to generate the desired fine precipitation of the Al–Mn dispersoids in a high number density. Their formation before extrusion is crucial if they are to act as obstacles to grain-boundary motion during dynamic recrystallization and during heat treatments after extrusion. A high extrusion temperature of 400 to 480 °C was chosen with the aim of achieving easy formability, and to bring a high fraction of Ca into solid solution in the *as-extruded* state (Figure 6.1b and Figure 6.3). In fact, an extrusion temperature exceeding the solvus temperature of the Mg_2Ca phase is desired because the resulting high solute content in the *as-extruded* condition may render a subsequent *sht* unnecessary, i.e. a *T5* condition would correspond to a pseudo-*T6* condition, and would therewith result in economically more attractive processing routes. This temperature is predicted to be 460 °C. In a final step, an artificial-aging treatment was performed in the temperature range of 175 and 225ºC, which seems to be a compromise between sufficiently fast aging and a low risk for rapid overaging.
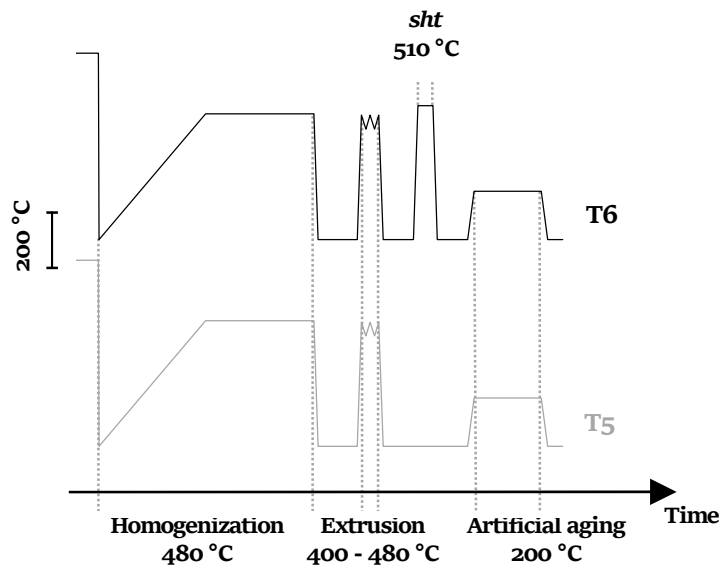
Figure 6.2: Thermomechanical processing sequence defining the *T5* and *T6* tempers.

Taking these design aspects into account, a lean AXM alloy was designed with composition Mg–Al0.6(0.54)–Ca0.28(0.17)–Mn0.25(0.11) in wt.% (in at.%). The corresponding phase diagram is presented in Figure 6.3. In the following, we validate the design concept by thoroughly investigating the microstructure-mechanical properties relationships by means of multiscale microstructural investigations using light microscopy, transmission electron microscopy and atom probe tomography. The microstructural insights gained are used to assess the validity of the predicted phases via thermodynamic calculation.
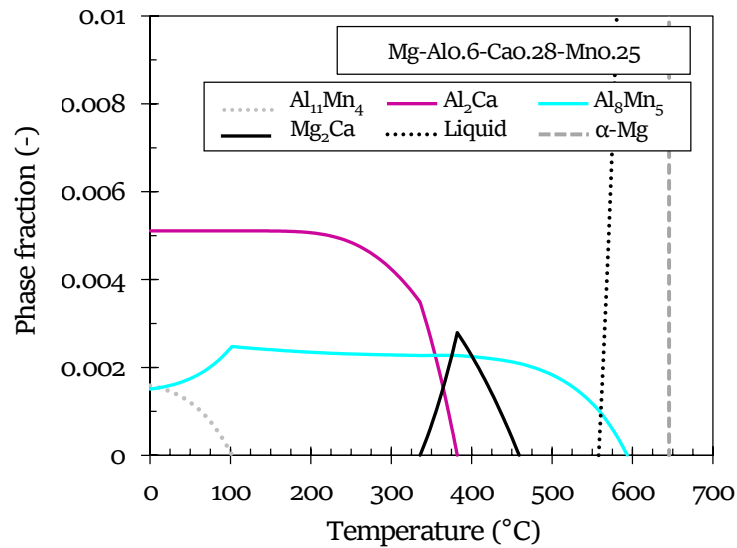
Figure 6.3: Phase fraction as a function of temperature for the resulting alloy Mg–Al0.6(0.54)–Ca0.28(0.17)–Mn0.25(0.11) in wt.% (in at.%) (AXM100).

6.3 Experimental details

6.3.1 Thermodynamic calculations

Thermodynamic calculations of possible phases in AXM were performed using the Pandat™ software package for multi-component systems, taking input from the PanMg2018_TH [31] database. All the calculations presented in this study assume thermodynamic equilibrium.

6.3.2 Processing

The alloy with nominal composition Mg–Al0.6(0.54)–Ca0.28(0.17)–Mn0.25(0.11) in wt.% (in at.%), hereafter referred to as AXM100, was prepared by melting of Mg (99.95% purity), Al (99.7%), Ca (98.5%) and Mn (as $MnCl_2$ compound, 98.5%) in a graphite crucible in a resistance oven under an Ar/SF_6 atmosphere at 700 °C. The crucible was cooled quickly to room temperature on a water-cooled cupper block to avoid precipitation during cooling. The ingots were homogenized by heating to 480 °C at a rate of 4 K min^{-1} and kept at that temperature for 6 h in order to form the Al–Mn dispersoids. Ingots were extruded into bars of 10 mm diameter using a direct extrusion process at 400, 450 and 480 °C with a ram speed of 0.5 mm s^{-1} to 2.5 mm s^{-1} and an extrusion ratio of 25, corresponding to exit speeds of 750 to 3750 mm min^{-1}, respectively. Cooling with pressurized air was applied on the bars close to the exit position of the extrusion machine. Both alloy production and the extrusion process took place at *Leichtmetallkompetenzzentrum Ranshofen GmbH,* Austria. Note that the extrusion machine employed in this study has an upper force limit of 1.5 MN, requiring a minimum temperature of 400 °C to achieve the desired extrusion rates.

6.3.3 Artificial aging

In order to study the hardening potential of AXM100, artificial-aging treatments were performed for two thermomechanical conditions: *T5* temper, i.e. a*s extruded* + artificially aged, and *T6* temper, i.e. solution-heat-treated (*sht*) + artificially aged (Figure 6.2) [34]. The artificial-aging treatment was performed in an oil bath at 200 °C for various durations ranging from 10 minutes to 72 hours, followed by a water quench. The *sht* parameters of 510 °C and 10 min were chosen according to the predicted solvus temperature of the Mg_2Ca phase of 460 °C (Figure 6.3) and the alloy's onset of melting at 518 °C experimentally obtained using differential scanning calorimetry (data not shown). Note that this *sht* condition, which is a central part of our strategy, corresponds to a state in which Al_2Ca and Mg_2Ca phases should be completely dissolved, while the Al–Mn-rich phase is expected to persist (see Figure 6.3). This *pseudo-sht* state, while admittedly not strictly complying with a

solution-heat treatment, is intentional because the presence of such thermally stable Al–Mn dispersoids are meant to prevent grain growth at elevated temperatures.

The age-hardening response of AXM100 upon isothermal holding at 200 °C for the *T5* and *T6* condition was characterized by Vickers hardness under a load of 5 kg. Vickers hardness on the cross-sectional plane of the extrusion direction was determined at each time point with 10 averaged individual indents.

For a detailed analysis of the material's mechanical behavior and corresponding microstructure, four thermomechanical-treatment conditions were considered: (1) *as extruded*, (2) *peak-aged T5*, (3) *sht*, and (4) *peak-aged T6*. The *peak-aged* conditions present the duration of the artificial-aging treatments for which maximum hardness was obtained.

6.3.4 Tensile tests

Tensile specimens, with two specimens per condition, were prepared according to DIN 50125 (M5, diameter = 3 mm). All specimens were prepared from extruded bars parallel to the extrusion direction. Tests were conducted using a Schenck Trebel electromechanical universal testing machine with a 100 kN hydraulic load cell at room temperature and at a strain rate of 10^{-3} s^{-1}.

6.3.5 Light microscopy

For grain-size analysis, samples of each condition were prepared by mechanical grinding and polishing followed by etching with picric acid to reveal the grain boundaries. Three individual micrographs per condition were analyzed by applying the linear intercept method (Lince®, TU Darmstadt).

6.3.6 Electron microscopy

Transmission electron microscopy (TEM) was performed to determine the chemical distribution of the alloying elements and the number density, size and spatial distribution of the precipitates present at the four different conditions. TEM specimens were prepared as standard 3 mm diameter disks by mechanically grinding the material to about 100 µm thickness and punching it into a 3 mm disk, followed by Ar-ion milling to achieve electron transparency using a precision ion polishing system (PIPS™ II) from Gatan, Inc.. Ion milling was performed at liquid-nitrogen temperature to prevent changes in the microstructure.

TEM imaging was performed in an FEI Talos™ F200X operated at 200 kV and equipped with a field-emission gun. Imaging was mainly performed in scanning TEM mode with a high-angle annular dark-field detector (HAADF-STEM mode) at a camera length of 98 mm to reveal the secondary

phases. In HAADF-STEM imaging mode, the resulting image gives a contrast that is proportional to about $Z^{3/2}$, with Z being the atomic number. To reveal the G.P. zones, the camera length was adjusted to 145 mm. At least three different areas per thermomechanical condition were assessed to determine the precipitate's number density and size. The number density N was evaluated by manual counting of the precipitates in a given area and their size was determined by manually measuring the diameter in ImageJ software. The relative error on N is associated to the statistical error $\frac{1}{\sqrt{n}}$ with n being the number of precipitates counted in the micrographs. In this study n was between 400 and 1600, resulting in a relative error on N between 2.5 and 5%. The TEM foil thickness, necessary to estimate the number density of precipitates and G.P. zones, was determined using stereographic pairs of images taken at +15 ° and -15 °.

Elemental distribution maps were recorded by energy dispersive X-ray spectroscopy (EDS) performed with an FEI Super-X detector. The acquisition time for each map was 15 min, providing a good compromise between adequate noise reduction in the data and minimization of beam damage, with a dwell time of 10 µsec to further minimize beam damage during mapping.

Electron diffraction patterns were obtained for the Al–Mn-rich precipitates in nanodiffraction mode at 80 kV to avoid beam damage. Spot patterns were acquired for two zone axes and analyzed using CrysTBox diffractGUI software [35], and were compared with simulated patterns obtained using jEMS software [36].

6.3.7   Atom Probe Tomography

Specimens from the *peak-aged T6* condition were prepared for atom probe tomography (APT) by mechanically tripod-polishing a wedge-shaped 3 mm disk, followed by Ar-ion milling in a PIPS™-II (Gatan, Inc.) and finally shaping it into APT tips using an FEI Helios 600i dual-beam focused ion beam (FIB-SEM) instrument. Annular milling of the tips resulted in APT tip apex radii of about 50 nm. The tips were vacuum-transferred from the FIB directly into the Cameca local electrode atom probe (LEAP™ 4000X-HR™) tomograph to avoid oxidation, with a vacuum environment remaining below 10^{-5} mbar at all times. The acquisition was performed at 65 K in laser-pulsed mode, applying a 200 kHz frequency of 150 pJ energy, resulting in an Mg^{++}/Mg^{+} Charge-State-Ratio (CSR) of 0.3. 3D-reconstruction and analysis were performed using IVAS 3.6.14 software from Cameca. The default reconstruction parameters were deemed satisfactory after correlating the resulting reconstruction with the observed nanostructures in TEM.

6.4 Experimental results

In the following sections, we first present the impact of processing conditions on the quality of the extruded AXM100 material before focusing on the aging response of AXM100. We then take the conditions that lead to the greatest hardening, referred to as the *peak-aged* condition, to elucidate the mechanical properties and their microstructure; with the aim of establishing a detailed understanding of the microstructure-property relationships in AXM100.

6.4.1   Processability

Figure 6.4 depicts the processing outcome at varying extrusion exit speeds and temperatures, evaluated by visual inspection of the resulting surface quality. It was rated as defect-free, as containing micro-cracks, or as containing severe surface cracks (Figure 6.4b). The latter occurred when either a too high extrusion temperature, a too high speed, or a combination of both were deployed (Figure 6.4b, red crosses). This characteristic repetitive circumferential cracking, referred to as *fir-tree cracking* or *speed cracking,* is a common phenomenon occurring in hot extrusion, and is attributed to local melting caused by friction-induced heating during the deformation process [37]. At lower temperatures or lower speeds the resulting surface quality is adequate. The processing window identified for the applied 'direct extrusion' is marked by a grey triangle in Figure 6.4. Note that extrusion was limited to a minimum extrusion temperature of 400 °C by the extrusion force of the system used.
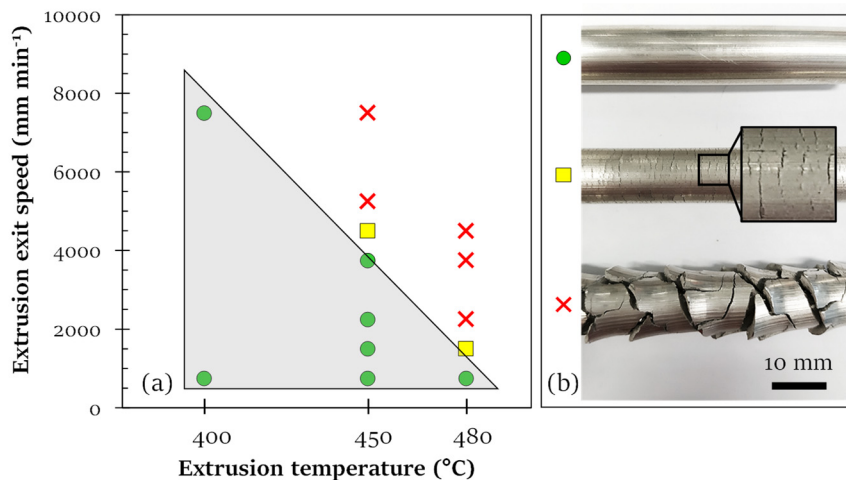
Figure 6.4: (a) Qualitative assessment of the extrusion outcome for various extrusion speeds and temperatures as evaluated by the surface quality. Each data point represents an individual extrusion process. The surface quality was rated as either defect-free (green circles), as containing micro-cracks (yellow squares) or as containing severe surface cracks (red crosses). (b) Representative photographs of these three conditions. Only extruded bars with defect-free surfaces were selected for this study.

To select the best extrusion condition in this processing window, the hardening potential following extrusion was additionally considered. From an economic point of view, a *T5* treatment is preferable to a *T6* treatment, because it requires no additional *sht*. A sufficient age-hardening response under such conditions requires sufficient availability of dissolved Ca and Al in the extruded material for the desired formation of the hardening Al_2Ca phase upon artificial aging. For Ca, this requirement implies the need to dissolve the Mg_2Ca phase, which would otherwise consume most of the Ca. To satisfy this condition, the extrusion temperature chosen must be above or close to the solvus temperature of the Mg_2Ca phase, which, according to the phase diagram in Figure 6.3, is 460 °C. For Al, sufficient amounts in solution for the formation of the Al_2Ca phase is ensured for the full temperature range from room temperature to above the melting temperature, according to the design concept of this study. This takes the consumption of Al by Mn to form Al_8Mn_5 into account, yet leaves a sufficient quantity dissolved in the Mg matrix for the formation of the Al_2Ca hardening phase.

With this in mind, and considering the processing window, indicated by the grey triangle in Figure 6.4, rods extruded at the intermediate temperature of 450 °C were chosen for the detailed analysis of AXM100. This ensures a good surface quality and potentially good hardening capability upon artificial aging.

6.4.2   Age-hardening response

The following section presents the hardening response of AXM100 upon isothermal aging at 200 °C, comparing two initial conditions, the *as-extruded* (*T5* temper) and *sht* condition (*T6* temper), and two different extrusion exit speeds.

Figure 6.5 shows the Vickers hardness as a function of artificial-aging time at 200 °C and at two extrusion speeds (slow at 750 and fast at 3750 mm min^{-1}) for AXM100 in *T5* and *T6* temper. Considering first the slow extrusion speed, the material in its *as-extruded* condition exhibits an average H_V = 47.3 ± 0.6. Upon isothermal aging at 200 °C, the hardness increases steadily with ΔH_V = 3.8 to H_V = 51.09 ± 1.2 within the first 60 min; from this point onwards the hardening rate slows down significantly, increasing only marginally with prolonged aging time and reaching its maximum of H_V = 54.03 ± 1.0 after 48 h. In the *sht* condition the hardness is slightly reduced to H_V = 44.5 ± 1.6. However, upon isothermal holding at 200 °C it increases rapidly and reaches a peak hardness after only 2 h with an increase of ΔH_V = 17 to H_V = 61.8 ± 1.2, followed by a slight decrease for prolonged aging times, to H_V of 58.4 ± 1.7 at 72 h.

With respect to the processing speed, it appears that for *T5* condition the hardness potential is greater when the extrusion is faster (Figure 6.5), amounting to an enhancement from ΔH_V = 3.8

when extruded slowly to ΔH_V = 5.3 after 60 min, and to ΔH_V = 6.3 after 2 h, when extruded faster. In contrast, the hardening response of the *T6* condition seems to be independent of the processing speed, reaching ΔH_V = 17.3 and ΔH_V = 16.7 for slow and fast extrusion, respectively, both achieved after 2 hours. Nevertheless, the overall hardening response of the *T5* condition upon aging stays always considerably below that of the *T6* condition, regardless of the extrusion speed.
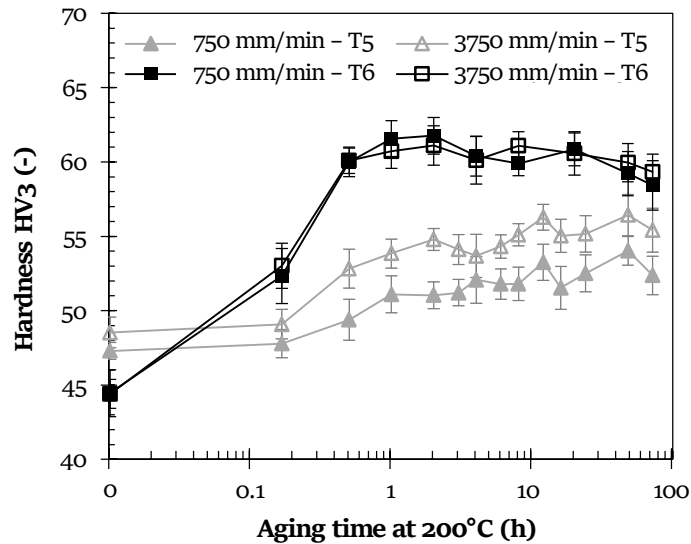
Figure 6.5: Vickers hardness of AXM100 as a function of artificial aging time at 200 °C starting from the as-extruded state (*T5* temper) and from the *sht* state (*T6* temper) and processed at two different extrusion exit-speeds, 750 and 3750 mm min-1.

For all further analyses, the aging time to achieve peak aging was set to 90 min for both *T5* and *T6*. This duration represents a compromise between the time required to achieve peak-hardness for *T5*, i.e. 1 h, and *T6*, i.e. 2 Furthermore, the material extruded at 750 mm min^{-1} was chosen for the detailed analysis due to the material's lower risk at slower processing rates to show impairment by microstructural changes, induced by speed cracking, which may visually be non-detectable.

6.4.3   *Tensile behavior*

Figure 6.6 presents the engineering stress–strain response in tension for AXM100 in its *as-extruded* and *sht* condition, plus in the corresponding *peak-aged T5* and *T6* conditions, respectively.

For the *peak-aged T5* temper, a significant increase in the tensile yield strength (*TYS*) of about 70 MPa relative to the *as-extruded* condition was observed, corresponding to an increase of ~43%, reaching 236 MPa. This contrasts with the small increment of the hardening response of 8.5%, evaluated by Vickers hardness, corresponding to ΔH_V = 4. Note that this increase was achieved after only 90 min of artificial aging at 200 °C. For the *peak-aged T6* temper, a remarkable increase in the

TYS of close to 100 MPa relative to the *sht* condition was achieved, corresponding to an increase of ~62%, reaching 253 MPa (Figure 6.6).

A satisfying elongation to fracture (A_f) of 14% is observed for the *as-extruded* condition. The material suffers, however, from a drastic reduction thereof in the different heat-treated conditions, with an average of 9% in the *sht* condition and 7 and 8% in the *peak-aged T5* and *peak-aged T6* condition, respectively. The shapes of the stress-strain curves presented in Figure 6.6 indicate that specimens in the heat-treated conditions suffer from premature failure which occurred before the ultimate tensile strength (*UTS*) was reached.
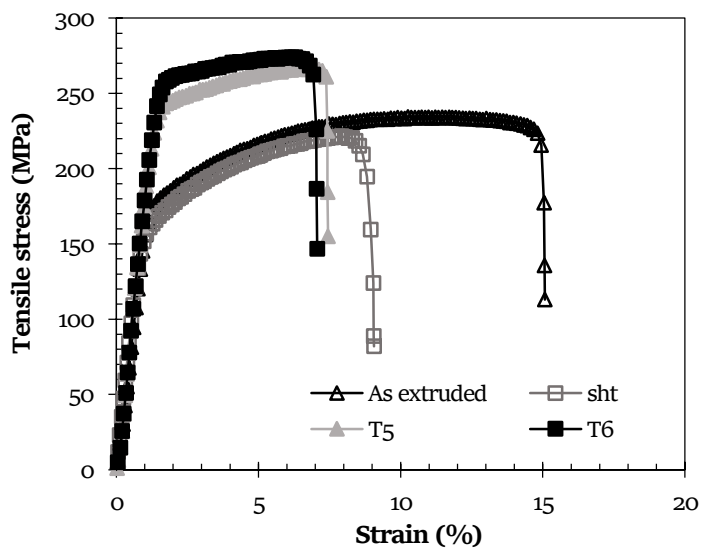
Figure 6.6: Stress–strain response to tensile-loading condition of AXM100 for the four different thermomechanical treatment conditions.

Table 6.1 summarizes the values of *TYS*, *UTS* and A_f determined in the tensile tests.

Table 6.1: Mechanical properties of AXM100 evaluated upon tensile testing at room temperature. *TYS*: tensile yield strength; *UTS*: ultimate tensile strength; Af: elongation to fracture.

Condition	TYS (MPa)	UTS (MPa)	A_f (%)
As extruded	165 ± 7.8	232 ± 2.7	14 ± 0.3
Peak-aged T5	236 ± 2.1	265* ± 1.9	7 ± 1.1
sht	156 ± 0.1	225* ± 5.3	9 ± 2.5
Peak-aged T6	253 ± 0.2	277* ± 4.2	8 ± 2.9

* Failure before *UTS* was reached.

To understand the microstructural relationships to the mechanical properties, a detailed microstructure analysis of samples of all four thermomechanical conditions, i.e. *as extruded*, *sht*, *peak-aged T5* and *peak-aged T6*, was performed.

6.4.4 Microstructural investigations

Light microscopy

Figure 6.7 depicts optical micrographs of the *as-extruded* and *sht* conditions along with the corresponding grain-size histograms. The optical micrograph of the *as-extruded* condition reveals an almost fully recrystallized microstructure with an average grain size of about $27 \pm 18\,\mu m$ (Figure 6.7a). The corresponding grain-size histogram clearly shows a substantial proportion of considerably smaller grains below 12 µm (Figure 6.7c). The optical micrograph of the *sht* condition shows that the high temperature during *sht* at 510 °C for 10 min induced on the one hand static recrystallization, resulting in a fully recrystallized microstructure, but on the other hand a slight grain growth, increasing the average grain size to $34 \pm 18\,\mu m$ (Figure 6.7b). The ratio of small grains below 12 µm significantly declined upon *sht*, as visible from this micrograph (Figure 6.7b) and supported by the corresponding grain-size histogram (Figure 6.7d).
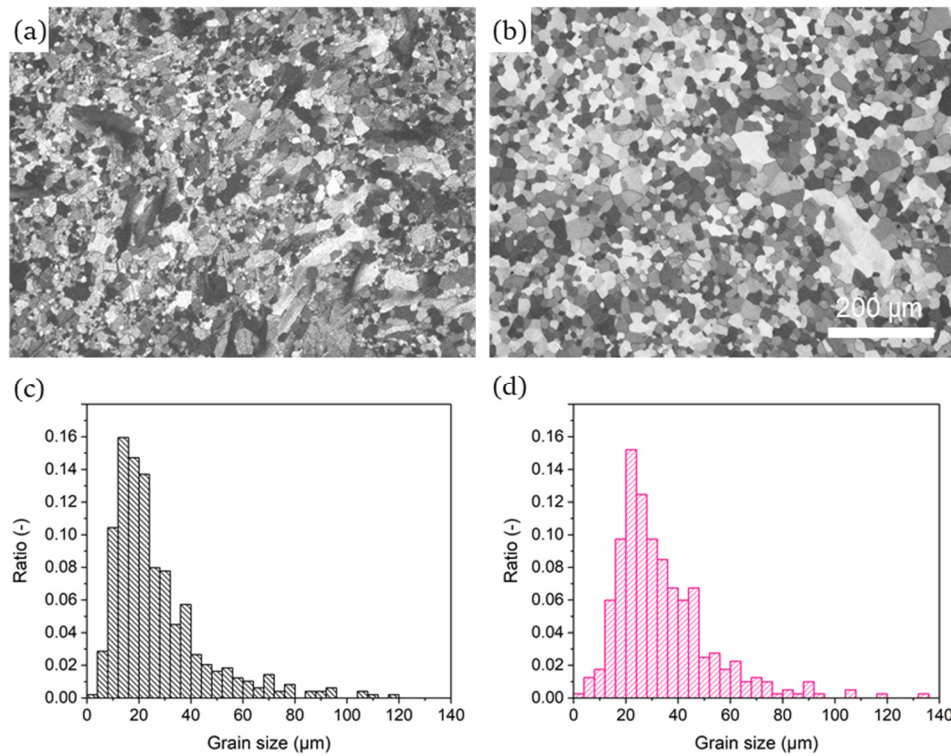

Figure 6.7: Light micrographs and grain-size histograms derived for the (a, c) *as-extruded* and (b, d) *sht* conditions. The micrographs show cross-sections taken perpendicularly to the extrusion axis. The scale bar is indicated in (b).

The low-temperature exposure during artificial-aging treatment at 200 °C for 90 min did not result in further grain growth and the average grain size was determined to be 29 ± 9 and 32 ± 12 µm for *peak-aged T5* and *T6*, respectively (not shown).

While the average grain size was approximately the same for all conditions, areas with significantly larger grains ($d > 60$ µm) are present, predominantly in the *sht* condition.

Electron microscopy

Figure 6.8 presents representative STEM HAADF images at moderate magnification and the corresponding STEM EDS maps of the four thermomechanical conditions, revealing the characteristics of secondary-phase precipitates in terms of their spatial distribution, number density and size, as well as their chemical composition.

In the HAADF micrographs in Figure 6.8a-d, the secondary-phase precipitates appear brighter than the Mg matrix, corresponding to the presence of elements heavier than Mg, thereby indicating Ca, Al and/or Mn in the precipitates. Those nanometer-scaled precipitates appear homogeneously distributed across the grains.

The corresponding EDS maps in Figure 6.8a-d reveal that these finely distributed secondary-phase precipitates are of two types: either single-precipitated Al–Mn-rich dispersoids, or two adjacent precipitates with one being an Al–Mn-rich dispersoid and the other being an Mg–Ca-rich phase. Such two-sided precipitates are referred to as Janus particles to account for the co-presence of two phases (Figure 6.9).

While the Al–Mn dispersoids are present in all four thermomechanical conditions and are homogeneously distributed across the grains, the Janus particles are only observed in the *as-extruded* (Figure 6.8a) and *peak-aged T5* (Figure 6.8c) condition. Note that matrix regions close to grain boundaries lack them. It appears that the number density of the Janus particles is reduced in the *peak-aged T5* condition compared to the *as-extruded* condition. Some of them are marked with white arrows in Figure 6.8c. The characteristics of these two types of precipitates are described in detail further below. In addition, a third phase is present that is more scattered, coarser and usually in the form of elongated precipitates located at the grain boundaries (clearly visible in Figure 6.8a and c, but also observed in the other conditions). EDS maps reveal that they consist of about 62 at.% Mg, 27 at.% Ca and 7 at.% Al. The elemental ratios suggest that they are of type $Mg_2(Ca,Al)$. Note that no grain-boundary bowing around such precipitates is observed, which would indicate a role as obstacles to grain-boundary motion. Lastly, Ca segregation at the grain boundaries is evident for all conditions, which is accompanied by its depletion in their vicinity.
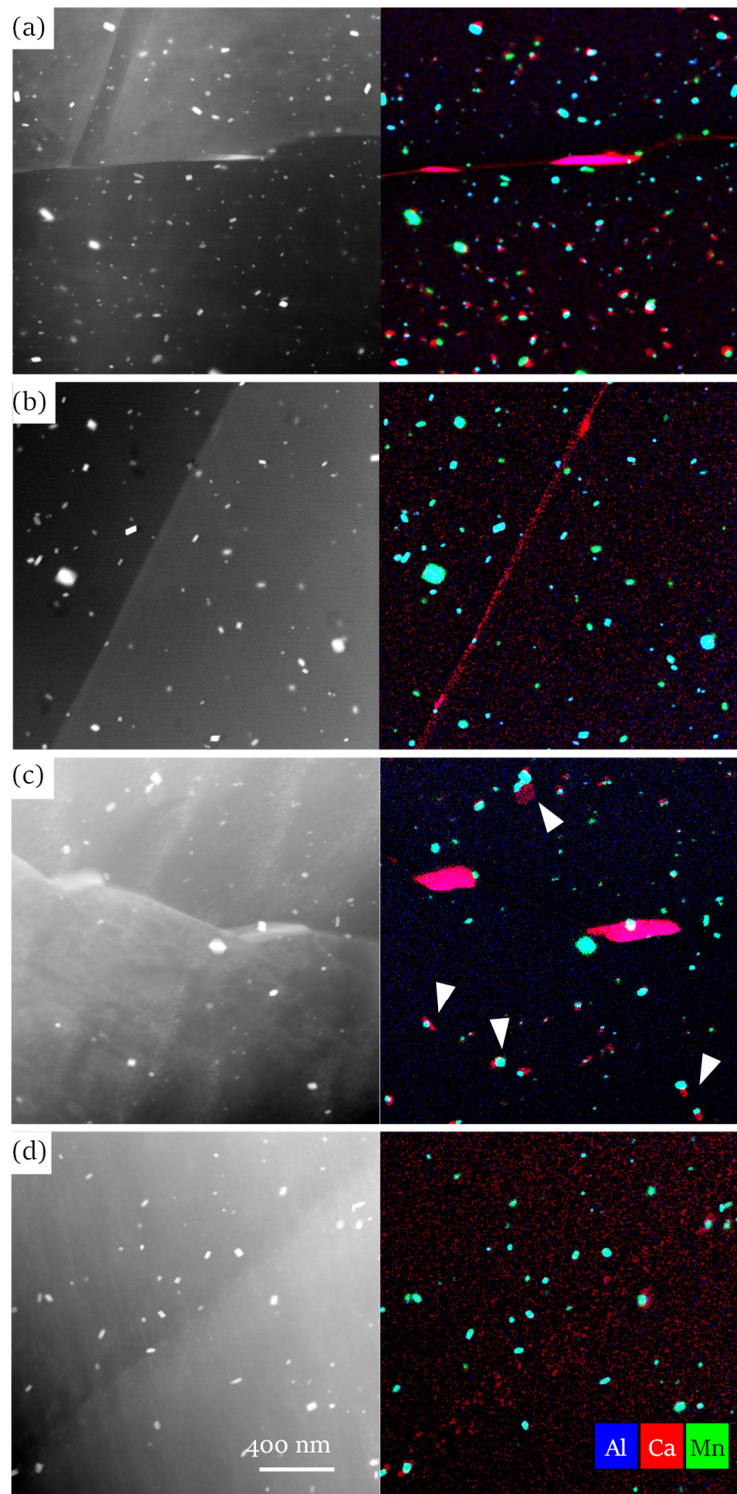
Figure 6.8: STEM HAADF images and corresponding STEM EDS chemical maps of the four thermomechanical conditions: (a) *as extruded*; (b) *sht*; (c) peak-aged *T5*; and (d) peak-aged *T6*. The elemental color code for EDS maps and the scale bar are indicated in (d).

Al–Mn dispersoids

The number density of Al–Mn dispersoids was estimated from STEM stereo images and determined to be on the order of 5×10^{19} m^{-3} for all conditions. Likewise, the dispersoids' size is comparable across the conditions and determined to be about 20 nm. Precise number densities and sizes of the four conditions are given in Table 6.2.

The EDS spectrum displayed in Figure 6.9d is typical of the Al–Mn dispersoids. It reveals that Mn is present in larger quantities than Al, with an Mn-to-Al ratio of about 2. Note that the EDS spectrum was acquired in very thin areas of the TEM foil, where the precipitate occupies the whole sample thickness and thus avoids the contribution of the matrix, increasing the accuracy of this analysis. The additional peaks at 0 keV and at 0.525 keV relate to the electronic noise of the EDS system and to oxygen contamination of the sample surface, respectively. APT analysis confirmed the higher Mn content compared to that of Al with a composition of the dispersoids determined as 57.6 at.% Mn, 40.4 at.% Al and 1.4 at.% Mg. This finding contradicts the thermodynamic simulation, which predicts an occurrence of the Al_8Mn_5 phase, and will be discussed later.

Janus particles

Figure 6.9 depicts typical Janus particles, with the Mg–Ca phase co-precipitated at the site of the Al–Mn dispersoids. As mentioned above, they are referred to as Janus particles due to their co-appearance. Both sides are each about 10 to 30 nm in size. EDS analysis shows that Mg and Ca are present in a ratio of about 2 to 1 (Figure 6.9c), which is typical of the Laves-type Mg_2Ca phase, as predicted by the thermodynamic calculation (Figure 6.3). The EDS spectrum further reveals some solubility of Al in Mg_2Ca.

The Janus particles appear in a high number density in the *as-extruded* state. Note, however, that in this condition, Al–Mn dispersoids are present without the simultaneous appearance of the Mg_2Ca phase in areas adjacent to the grain boundaries, where the matrix is generally depleted in Ca (Figure 6.8a). In the *peak-aged T5* condition (Figure 6.8c) Janus particles are also present, although in lower number densities than in the *as-extruded* condition. Upon exposure to 510 °C for 10 min, the Mg_2Ca phase dissolves and is thus observed neither in the *sht* (Figure 6.8b) nor in the *peak-aged T6* condition (Figure 6.8d).
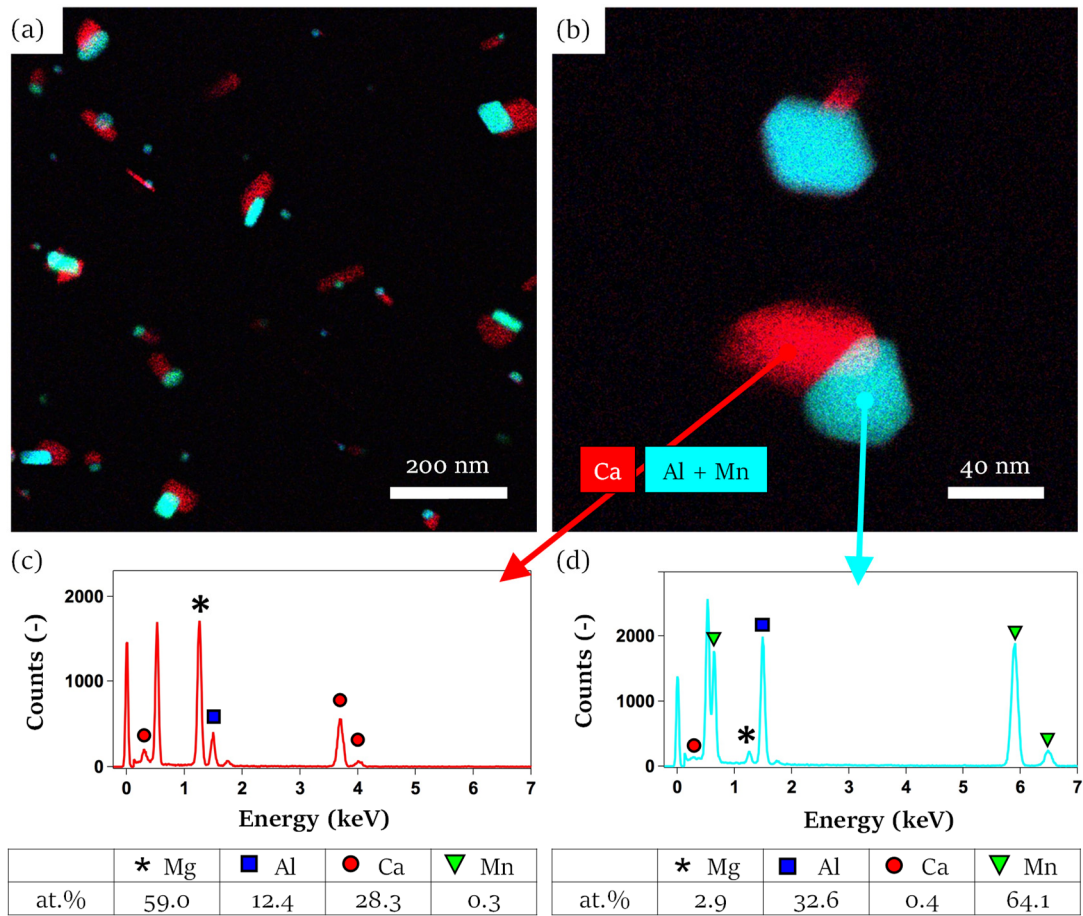
Figure 6.9: Chemical map of the Janus particles. (a, b) STEM EDS chemical maps of the two phases composing a Janus particle. Quantified EDS spectra of (c) an Mg–Ca-rich precipitate and (d) an Al–Mn-rich precipitate.

High resolution electron microscopy

Figure 6.10 presents high-resolution (HR)-STEM images taken with the incident beam along the $< 2\bar{1}\bar{1}0]$ (Figure 6.10a) or $< 10\bar{1}0]$ (Figure 6.10b) zone axis of the Mg matrix. They reveal a dense dispersion of G.P. zones for *peak-aged T5* and *peak-aged T6* specimens. No G.P. zones were observed in the *as-extruded* and the *sht* condition. The G.P. zones are located on the basal plane of the Mg matrix, as revealed by the diffraction pattern in Figure 6.10a. Note that the spot pattern corresponds to the Mg matrix only and does not reveal possible additional spots due to the presence of the G.P. zones. The inset to Figure 6.10b shows a single, mono-layered G.P. zone.
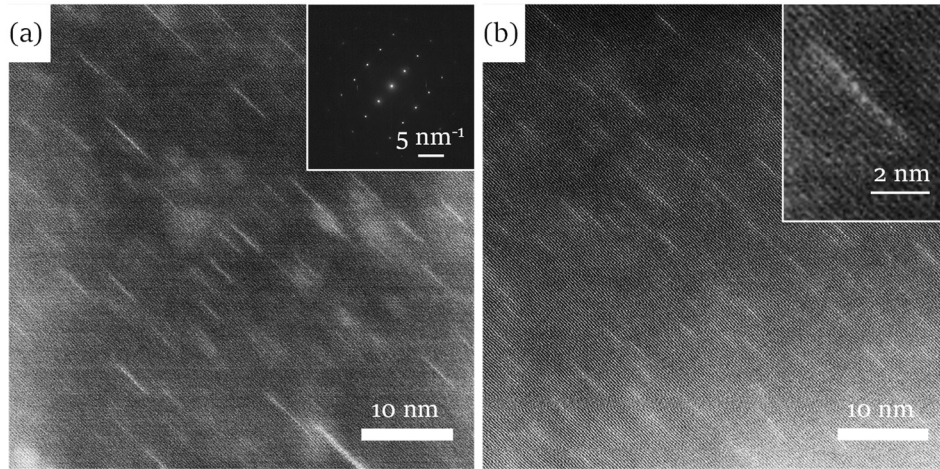
Figure 6.10: HAADF images for (a) peak-aged *T5* (taken along the $< 2\overline{1}10]$ direction) and (b) peak-aged *T6* (taken along the $< 10\overline{1}0]$ direction). The inset to (a) shows the diffraction pattern of the matrix. The inset to (b) shows the magnification of a single monolayered G.P. zone.

The number density of G.P. zones was determined as 0.57×10^{23} m^{-3} and 2.63×10^{23} m^{-3} for *peak-aged T5* and *peak-aged T6,* respectively. No depletion of G.P. zones around the Al–Mn-rich dispersoids was observed for either temper. Their size was determined as 3.6 ± 0.8 nm and 2.8 ± 0.7 nm for the *peak-aged T5* and *peak-aged T6* condition, respectively. The number densities and sizes are given in Table 6.2.

Table 6.2: Number density N, diameter d and volume fraction f of Al–Mn dispersoids and *Guinier–Preston* zones for the four thermomechanical conditions considered. Spherical geometry was assumed for the Al–Mn dispersoids and plate geometry for the G.P. zones. The G.P.-zone volume was calculated with $d_{G.P.}$ as the plate diameter and the interplanar distance of the Mg crystal at about 0.26 nm as the plate thickness.

	Al–Mn dispersoids			**Guinier–Preston zones**		
Condition	N_{Al-Mn} (% Error)	d_{Al-Mn}	f_{Al-Mn}	$N_{G.P.}$ (% Error)	$d_{G.P.}$	$f_{G.P.}$
	(m^{-3})	(nm)	(-)	(m^{-3})	(nm)	(-)
As extruded	5.85×10^{19} (2.6)	20 ± 8	2.45×10^{-4}	/	/	/
Peak-aged T5	5.93×10^{19} (2.6)	18 ± 8	1.81×10^{-4}	0.57×10^{23} (4.9)	3.6 ± 0.8	1.51×10^{-4}
sht	5.6×10^{19} (2.8)	21 ± 9	2.72×10^{-4}	/	/	/
Peak-aged T6	4.91×10^{19} (4.6)	24 ± 9	3.55×10^{-4}	2.63×10^{23} (4.4)	2.8 ± 0.7	4.22×10^{-4}

Atom probe tomography

Figure 6.11a depicts the atom map obtained by APT from the *peak-aged T6* temper. The sample volume of roughly 120 nm × 80 nm × 25 nm (viewed in the x-z projection) presents the matrix region between the Al–Mn dispersoids with a high number of G.P. zones. The sample comprises the

208

edge of an Al–Mn dispersoid emphasizing its relative size difference with respect to the G.P. zones. In this reconstruction, purple-colored isoconcentration surfaces display gradient concentrations of 2.1 at.% (Al+Ca), marking the G.P. zones. Magnification of one such G.P. zone (inset to Figure 6.11a) shows that Al alone is present in an ordered, mono-layered plane, whereas Ca atoms are situated diffusely around it. Because HR-STEM imaging has shown clearly that the G.P. zones appear as ordered monolayers (inset to Figure 6.10b), the apparent delocalization of Ca observed in the APT atom map is ascribed to the combined impact of preferential evaporation and local magnification APT artefacts [38, 39]. For this reason, isoconcentration-surface analysis was chosen, which includes a volume rather than a mono-layered precipitate, thereby considering both Al and Ca. Proximity histograms extracted from these precipitates reveal an Al-to-Ca ratio of about 2 - 2.5 within the G.P.-zone volume (Figure 6.11b). Preferential presence of Mn at the side of G.P. zones was detected, although their contribution to G.P.-zone formation is minor at about 0.2 at.% within the G.P. zones compared to 0.03 at.% in the matrix. Due to the fine-scale dimensions of the G.P. zones, the local magnification and preferential evaporation artefacts limit a clear statement on the amount of Mg atoms in the G.P. zones.

In addition, Ca-solute clusters are occasionally observed which are locally separated from the G.P. zones. These Ca clusters are depicted in Figure 6.11a (arrows) as red-colored isoconcentration surfaces and display a gradient concentration of 0.65 at.% Ca. It was found that they contain only a small amount of Al (Figure 6.11c) and are, at about 0.7 - 1.5 nm in radius, considerably smaller in size than the ordered G.P. zones. Finally, the matrix composition was retrieved from the APT data, and the alloying elements amount to 0.20 at.% Al, 0.09 at.% Ca and 0.03 at.% Mn.
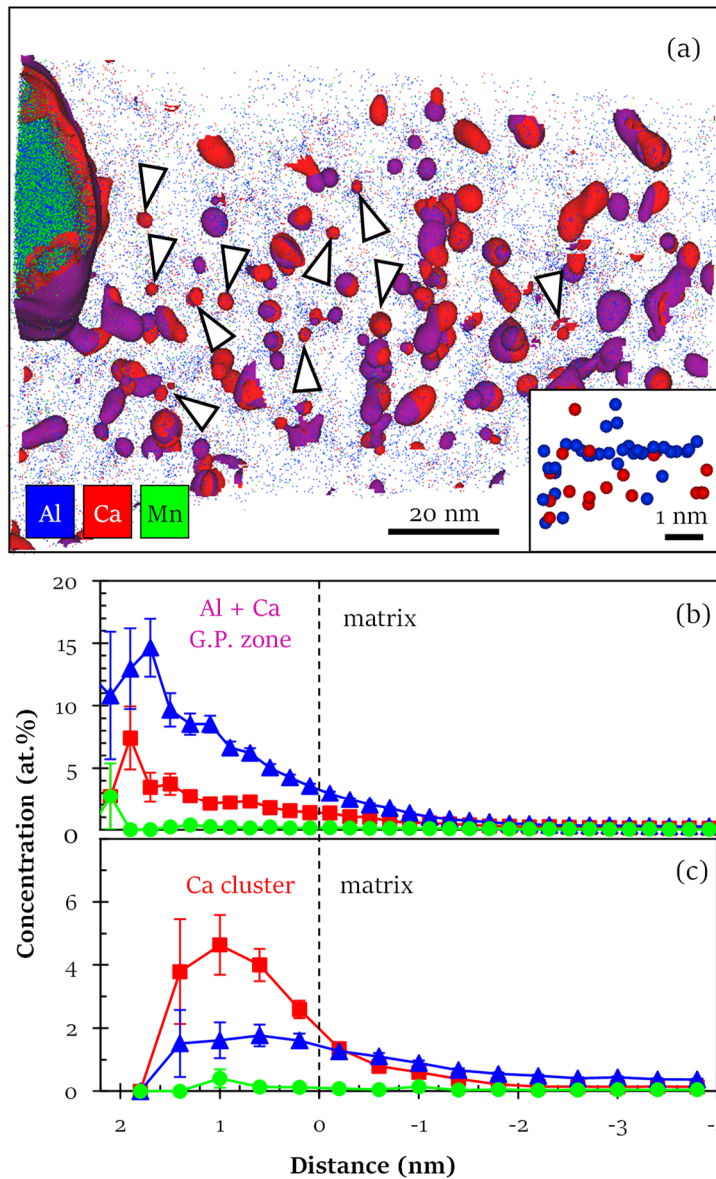
Figure 6.11: (a) 3D-reconstruction of peak-aged *T6* temper obtained by APT. The reconstruction includes isoconcentration surfaces for the conditions c_{Al+Ca} = 2.1 at.% and c_{Ca} = 0.65 at.%. Inset: Magnified view of a single G.P. zone. (b-c) Proximity histograms showing the elemental concentrations of Al, Ca and Mn as a function of distance from the precipitate-matrix or cluster-matrix boundary for the isoconcentration surfaces of (b) G.P. zones and (c) Ca clusters. Ca clusters are marked with white arrows in (a).

6.5 Discussion

Here we consider the microstructural contributors to the mechanical properties of AXM100 and distinguish between the material's strength in its *as-extruded* condition, referred to as *base strength*, and that after age hardening. The composition, structure and volume fraction of the two main phases, Al–Mn dispersoids and G.P. zones, are evaluated and compared to the predictions by thermodynamic calculations. In the following estimations, basal slip is assumed to be the only active slip system. This assumption is based on the grain-size regime determined for the alloy studied in which basal slip largely dominates over other slip systems.

6.5.1 G.P. zones

This study shows that AXM100 in both conditions, *T5* and *T6*, experiences a considerable hardness increase upon artificial aging. The hardening response manifests itself in a significant improvement in *TYS* for both conditions (Figure 6.6). The aging response is attributed to ordered mono-layered G.P. zones that form on the basal plane of the hexagonal Mg lattice (Figure 6.10). Their roughly 5 times larger number density and 20% smaller size in the *peak-aged T6* compared to the *peak-aged T5* condition (Table 6.2) account for the larger hardness increment (Figure 6.5) and the increase in *TYS* (Figure 6.6).

The contribution of precipitation hardening is estimated using equation 6.1 [40], which allows describing the particle-dislocation interaction for the case of shearable obstacles:

$$\Delta TYS_{\text{G.P.}} = \sqrt{\frac{3}{4\pi\beta}} \frac{k^{\frac{3}{2}}M\mu}{\sqrt{b}} \sqrt{f_{\text{G.P.}} \frac{d_{\text{G.P.}}}{2}} \qquad \text{(Eq. 6.1)}$$

In this equation, β is a parameter equal to 0.5 according to [40], k is a measure for the obstacle strength, M is the Taylor factor with 3 for polycrystalline Mg alloys, μ is the matrix shear modulus with 17 GPa, b is the magnitude of the Burgers vector with 3.2 Å, and $f_{\text{G.P.}}$ is the volume fraction of the G.P. zones derived from their number density $N_{\text{G.P.}}$ and volume. The latter is calculated for mono-layered plates with the thickness taken as the Mg interplanar distance of 0.26 nm and the average diameter $d_{\text{G.P.}}$, as given in Table 6.2. With these values and by adjustment of k to about 0.161, ΔTYS can be fairly well matched with $\Delta TYS_{\text{calc.}}^{\text{T5}}$ = 66 MPa and $\Delta TYS_{\text{calc.}}^{\text{T6}}$ = 98 MPa to the experimental values of $\Delta TYS_{\text{exp.}}^{\text{T5}}$ = 71 MPa and $\Delta TYS_{\text{exp.}}^{\text{T6}}$ = 97 MPa, respectively. The close to equal value of k for *T5* and *T6* required to match the experimental values suggests that indeed the same type of hardening mechanism operates in both conditions.

The chemical composition of the G.P. zones was investigated using a correlative approach combining TEM and APT. HR-STEM images reveal an ordered, mono-layered arrangement of heavier atoms in the G.P. zone (inset to Figure 6.10b), indicating Ca, which has a significantly higher atomic number than Mg and Al, thus exhibiting a brighter contrast. Conversely, Al has an atomic number close to that of Mg, making its appearance non-distinguishable in an Mg matrix. The limited visibility of Al atoms in STEM imaging can be compensated by APT analysis, which reveals that Al is present as mono-layered precipitates. For Ca, however, APT suffers from an artefact due to a potential preferential field-evaporation rate of Ca compared to Al [38]. Based on the combination of these two methods it can be concluded that G.P. zones are composed of both Al and Ca atoms as previously reported [22, 41] and suggested by the thermodynamic calculations (Figure 6.3). Isoconcentration-surface analysis using APT reveals that the Al-to-Ca ratio is about 2 to 2.5. This ratio differs from the previously reported composition of Mg-Ca6-Al7 (in at.%) [22], obtained for G.P. zones of about 3 nm in size in the Mg–Al–Ca system. The significant contribution of Mg, however, which is reported in [22] and also observed in the present study, cannot be definitely ascribed to the G.P. zones but may stem from local magnification effects, a known artefact in APT when field-evaporating different phases [39].

The minor contribution of Mn to the G.P. zones detected was previously observed by Homma *et al.* [41] and explained by the high affinity of Mn to Al, which causes a replacement of Ca by Mn. APT also revealed a size dependence of the G.P.-zone composition. While the majority of G.P. zones (in *T6 peak-aged* condition) appear to have the composition mentioned, with an Al-to-Ca ratio of 2 to 2.5, smaller precipitates appear to be mainly composed of Ca and present as solute clusters rather than ordered precipitates (Figure 6.11).

The size-dependent composition observed is expected to provide an insight into the precipitation sequence of G.P. zones and equilibrium Al_2Ca-phase formation in AXM100: Ca atoms would cluster first, followed by the formation of ordered Al–Ca-rich G.P. zones as metastable precipitates with an Al-to-Ca ratio of about 2 to 1 (Figure 6.10 and Figure 6.11**Figure 6.11**). These are then gradually replaced by the equilibrium Al_2Ca phase [22, 24, 42], with a predicted C15 structure according to the thermodynamic calculations for AXM100. *sht* not only brings Ca atoms into solid solution, generating an *SSSS* condition, but also leads to a significant fraction of vacancies when the material is water-quenched. These quenched-in vacancies, in combination with the roughly 10-fold greater diffusivity of Ca in Mg compared to Al [43], can explain the initial Ca clustering. This is further supported by the significantly larger solubility of Al in Mg, at about 3.3 at.%, while Ca, which is approximately insoluble at the artificial-aging temperature of 200 °C [25], has a strong tendency to decompose.

Based on these observations, the following precipitation sequence for the Al–Ca phase from *SSSS* for the lean composition AXM100 is proposed:

$$\text{SSSS} \rightarrow \begin{matrix} \text{Ca / solute} \\ \text{atom} \\ \text{clusters} \end{matrix} \rightarrow \begin{matrix} \text{ordered G.P. zones} \\ \text{with Al:Ca} \sim 2, \\ \text{monolayer } (0001)_\alpha \end{matrix} \rightarrow \begin{matrix} \text{Al}_2\text{Ca, fcc, C15,} \\ a = 0.802 \text{ nm;} \\ \{111\}_{C15} = (0001)_\alpha \end{matrix}$$
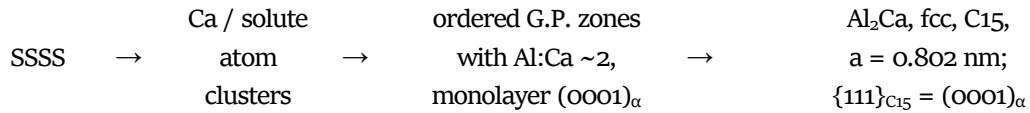
However, in the *as-extruded* state, the Ca atoms required for G.P.-zone formation are not available in solid solution but mainly present in the Mg_2Ca phase, forming Janus particles with the Al–Mn dispersoids (Figure 6.9). Note that the co-precipitation of Mg_2Ca at the sites of Al–Mn dispersoids may occur because Ca segregation is facilitated by the strained lattice around the dispersoids. The Mg_2Ca phase is dissolved upon *sht* (Figure 6.8b), bringing all Ca in solid solution for an effective hardening response in *T6* condition. In contrast, remnants of Janus particles in the *peak-aged T5* condition (Figure 6.8c) show that the Ca reservoir, the Mg_2Ca phase, was not exhausted for the chosen aging parameters of 90 min and 200 °C. Yet the microstructural analysis of the phases reveals a depletion of the Janus particles in *peak-aged T5* compared to the *as-extruded* condition (Figure 6.8), providing evidence that the Ca solutes that form the G.P. zones originate from the Mg_2Ca phase. Age hardening can thus still occur despite the capture of Ca in the Mg_2Ca phase in the Janus particles, if one accounts for the high diffusivity of Ca atoms in Mg and the pre-existence of Al atoms in solid solution. Ca is therefore considered to be the main carrier of transformation from the Mg_2Ca equilibrium phase to the metastable Al–Ca phase, present as G.P. zones, at the origin of considerable hardening.

It is to be noted that the solute clusters may present an important contributor to the material strength by impeding dislocation motion, and may account for the difference between the experimentally obtained and expected values. Their role, however, in terms of dislocation interaction, and specifically their obstacle strength, requires a more detailed investigation.

Considering the continuous hardness increase for *T5* condition (Figure 6.5), which appears to persist even after 72 h of artificial aging, prolonged aging times may yield a higher hardness increment by achieving complete exhaustion of the Ca reservoir. However, it is not expected that the hardness of *T5* can reach that of *T6* independently of the aging time. This is because the G.P. zones in the *T5* condition precipitate in larger sizes (Table 6.2), which limits their number density, and is thus detrimental to hardening.

The observation of an incompletely exhausted Ca reservoir in *T5* may also explain the fact that the age-hardening response shows a dependence on extrusion speed only for *T5* but not for *T6* temper, with a faster extrusion resulting in a higher hardness increment for the former (Figure 6.5).

The friction-induced temperature rise during extrusion, which is higher the faster the extrusion [11], brings the material temperature closer to the solvus temperature of the Mg_2Ca phase, thereby bringing more Ca atoms into solid solution (Figure 6.3). This is further supported if the quenching rate after extrusion is considered. This is enhanced when the extrusion speed is faster, because less time passes between the exit of the hot bar and its introduction into the air-quenching system. A fast quenching rate, in turn, prevents the precipitation of Janus particles upon cooling and leaves Ca in solid solution. G.P. zones, which form from *SSSS*, then precipitate in smaller sizes and concurrently in greater number density. This was confirmed by the detailed microstructural analysis of the *peak-aged T6* and its comparison with the *T5* condition. The hardness increment is therefore larger, the more Ca is present in solid solution at the beginning of the artificial-aging treatment. Because for the *T6* condition an *sht* treatment precedes the aging treatment, effectively bringing all Ca atoms into solid solution, no difference in aging response between the two extrusion rates was observed for *T6*.

6.5.2 *Al–Mn dispersoids*

Al–Mn dispersoids are prominent microstructural features of the AXM100 material. Because their number density and size are about the same for all four thermomechanical conditions studied, their contribution to age hardening can be excluded. This is, instead, ascribed entirely to the precipitation of the G.P. zones and potentially to the Ca-rich clusters described above. The Al–Mn dispersoid may, however, play a role in defining the base strength of the material, i.e. that in the non-aged state. In fact, solid-solution strengthening and work hardening can both be disregarded, the former due to the leanness of the alloy and the latter due to a dislocation density which is low enough to be neglected. Only the difference of *TYS* and H_V measured between the *as-extruded* and *sht* condition of about ΔTYS = 9 MPa (Table 6.1) and ΔH_V = 4 (Figure 6.5), respectively, can be ascribed to the dislocation density, which is presumably higher after extrusion but reduced by the high-temperature *sht*. The increment, however, is relatively small. Thus, we can conclude that the base strength of AXM100 is governed by the material's grain size and by precipitation hardening via the Al–Mn dispersoids, present in all conditions (Figure 6.8).

The precipitation-hardening contribution of the Al–Mn dispersoids is estimated using the line-tension model [44], which allows to describe the particle-dislocation interaction for the case of dislocation bowing at the obstacle as:

$$\Delta TYS_{Al-Mn} = \frac{\alpha \, \mu \, b}{l} \qquad\qquad \text{(Eq. 6.2)}$$

where α is the obstacle strength. Here it is taken as 1, corresponding to unshearable obstacles, to estimate the greatest possible hardening contribution of the dispersoids. Further, μ is the matrix

shear modulus with 17 GPa for Mg, b is the magnitude of the burgers vector with 3.2 Å and l is the interparticle spacing on the glide plane. The latter is derived from the number density N_{Al-Mn} and size d_{Al-Mn} of the dispersoids (Table 6.2) according to the following equation (6.3) [45], which is expressed as the volume fraction f_{Al-Mn} and assuming spherical particles:

$$l = \frac{d_{Al-Mn}}{2 \sqrt{f_{Al-Mn}}} \approx \frac{1}{\sqrt{2 \, N_{Al-Mn} \, d_{Al-Mn}}} \qquad \text{(Eq. 6.3)}$$

In this approximation only the dispersoids' size and number density are taken into consideration, whereas the dispersoid shape and orientation relative to the matrix, both known to affect the resulting strength [46], are summarized by the parameter α in Eq. 6.2. With the values N_{Al-Mn} and d_{Al-Mn} from Table 6.2, the derived strength contribution is at a maximum of about 8 MPa. This simplified estimation shows clearly that the Al–Mn dispersoids only play a subordinate role for the material's strength in terms of precipitation hardening. Nevertheless, these thermally stable Al–Mn dispersoids are essential for the material's performance because they present obstacles to grain-boundary movement, as discussed below.

A closer look at the dispersoid's composition, obtained by STEM-EDS measurements (Figure 6.9) and confirmed by APT (Figure 6.11), indicate that their Mn content exceeds that of Al, as previously observed [29]. This finding is surprising considering the Al_8Mn_5 phase predicted by thermodynamic calculations using the Pandat database and by literature [20, 30].

In order to identify the structure of the Al–Mn dispersoids, a detailed analysis was conducted using nanodiffraction. Figure 6.12 presents experimental diffraction patterns obtained along two different zone axes in an Al–Mn dispersoid of about 50 nm in size. The periodic spot patterns indicate single-crystallinity, in contrast to a nano-structured precipitate that would yield diffraction with a ring pattern or an aperiodic spot pattern. Each diffraction pattern was tentatively matched with simulated patterns of different candidate structures. The experimentally obtained diffraction patterns (Figure 6.12) were carefully analyzed by matching them with simulated ones of different structures from literature, using diffractGUI software. The candidate structures considered were the Al_8Mn_5 phase, as predicted by the thermodynamic simulation (Figure 6.3), in a rhombohedral form [47] and cubic form [48], but also tetragonal $Al_{0.89}Mn_{1.11}$ [49], hexagonal $Al_{0.9}Mn_{1.1}$ [50], cubic AlMn (45:55) [51], cubic β-Mn [52], and α-Mn [53]. The latter two accommodate up to 40 at.% Al, satisfying the condition of Mn being the dominant element. It appears that the best matches between the experimental and simulated patterns were obtained for three structures, namely β-Mn, rhombohedral Al_8Mn_5, and α-Mn. Figure 6.12 presents, in addition to two experimental diffraction patterns named 'zone axis 1' and 'zone axis 2', the best matches found for those structures and the

corresponding zone axes. Note that they include double diffraction and the first-order Laue zone (FOLZ), in addition to the zero-order Laue zone [54]. It appears that all three structures provide a reasonable fit for zone axis 1, while β-Mn provides the best match for zone axis 2, followed by Al_8Mn_5. In the latter orientation, α-Mn lacks the FOLZ information observed in the outskirts of the experimental pattern and can therefore be excluded. In contrast, in zone axis 1 there are two small FOLZ diffraction spots at the top left of the picture which match with β-Mn only. Further evidence is taken from the angle between the two zone axes. The theoretical angle between the two matching zone axes of β-Mn ([101] and [313]) was 13.26°, and matches rather well with the experimentally applied tilt of 11.5°. In comparison, the theoretical angle between the zone axes of Al_8Mn_5 ([212] and [313]) amounts to 9.4°. From the correlatively analyzed diffraction patterns, the tilt angle and chemical information obtained from EDS and APT, we can conclude that the Al–Mn dispersoids are of β-Mn type. This finding is associated with the recently reported co-existence of Al_8Mn_5 and β-Mn phase in an AXM10203 alloy [20]; however, no Al_8Mn_5 precipitates were identified in this study.
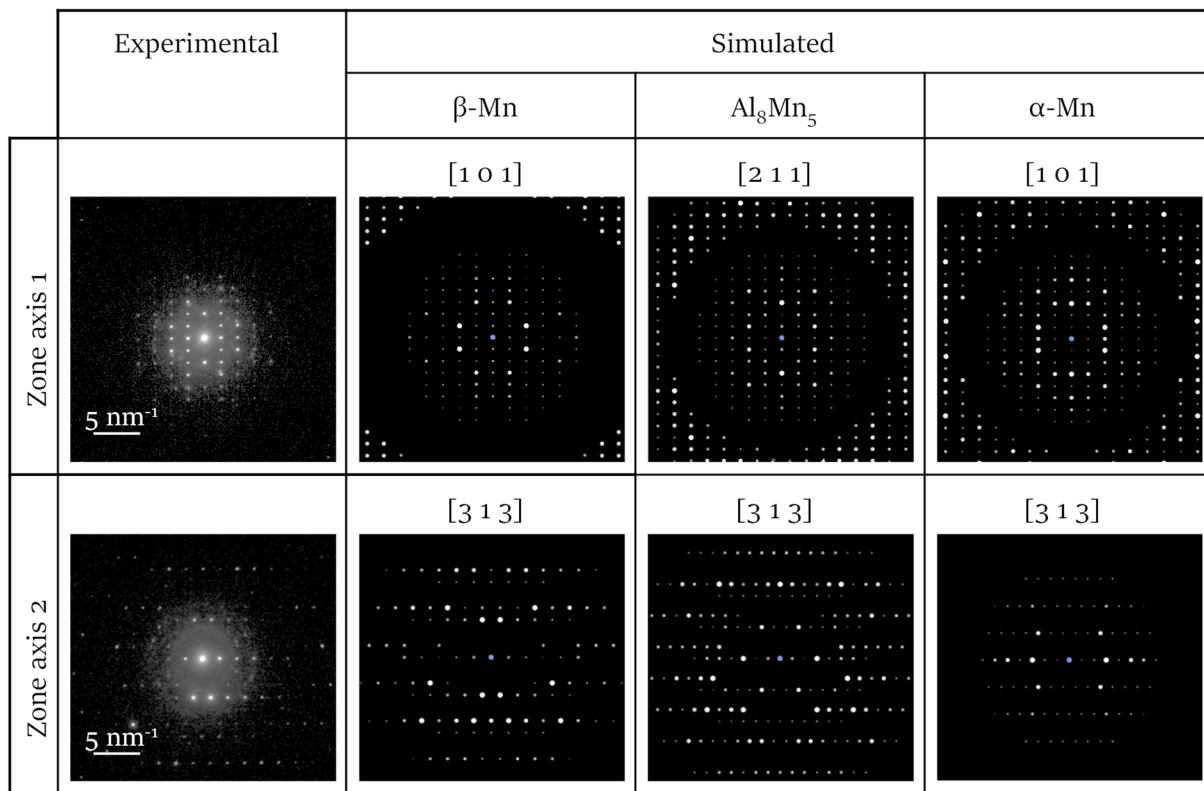

Figure 6.12: Left: Spot patterns experimentally obtained by nanodiffraction in two different zone axes of the Al–Mn dispersoids. Right: Simulated patterns for three reported possible structures, β-Mn, Al_8Mn_5 and α-Mn.

6.5.3 Mg₂Ca phase

Evaluating the contribution of the phases present to precipitation hardening, the role of the Mg₂Ca phase as part of the Janus particles is, likewise, a minor one. We come to this conclusion by considering their size which is similar to that of the Al–Mn dispersoids and, more importantly, their co-presence with the Al–Mn dispersoids (Figure 6.9). The nature of Janus particles approximately doubles the overall obstacle size, which, however, only negligibly reduces the significantly larger interparticle spacing on the slip plane. Because the latter is by far the stronger determining factor in precipitation hardening according to Eq. 6.2, the Mg₂Ca phase cannot strengthen the material considerably. In sum, the strength contribution of both Al–Mn dispersoids and Mg₂Ca phase are minor in comparison with the experimentally obtained base hardness and base strength in the *as-extruded* state.

6.5.4 Grain size

Finally, the grain size as a contributor to the material's base strength is assessed. Its contribution is estimated by the well-known *Hall–Petch* equation [3, 4]:

$$\Delta TYS_{\text{grain size}} = \ k_{\text{y}}\, D^{-\frac{1}{2}} \qquad\qquad (\text{Eq. 6.4})$$

where k_{y} is the *Hall–Petch* coefficient at 150 to 250 MPa μm$^{1/2}$ [5, 6] and D is the average grain size. With D at about 30 μm, the contribution of grain-boundary strengthening to *TYS* amounts to a maximum of about 45 MPa. Note that with these values there is a discrepancy between the estimated and experimental base-strength value (TYS^{sht} = 156 MPa). The former is at most at about 70 MPa as derived from summing the friction stress for dislocation movement, reported to be 12 to 18 MPa for Mg [5, 55], the dispersoid's maximum strength contribution about 8 MPa, and the grain-boundary strengthening of 45 MPa. In this estimation, however, we have not considered the contribution of solid-solution hardening of Al and Ca and texture effects. Nevertheless, from these simple calculations at the given boundary conditions, it can be concluded that the grain size significantly dominates the *TYS* over the Al–Mn dispersoids.

The essence of the Al–Mn dispersoids, however, comes into play as obstacles for grain-boundary motion, thereby impeding grain growth at elevated temperatures. Indeed, the material resists excessive grain coarsening; this is experimentally evident from the approximately constant average grain size in all four thermomechanical conditions studied, with only a minor increase upon *sht*, and was previously observed in the AXM system [20, 29]. The obstacle-mediated grain-growth limitation, referred to as *Zener* drag, provides a maximum grain size D_{max}, which can be estimated by the *Zener–Smith* equation [13]:

$$D_{\max} = \frac{2\,d_{\text{Al-Mn}}}{3\,f_{\text{Al-Mn}}} \qquad\qquad\qquad \text{(Eq. 6.5)}$$

where d and f are the dispersoid diameter and volume fraction, respectively. From this equation the maximum grain size amounts to about 60 μm. This agrees fairly well with the experimentally determined average grain size of about 30 μm, noting the presence of a few coarse and significantly larger grains, especially in the center of the extruded bar (Figure 6.7).

In light of the essential contribution of grain-boundary strengthening, the resistance to grain coarsening upon *sht* is crucial to maintaining the benefits of a substantial age-hardening response in the *T6* temper. It is therefore an essential aspect of the performance of AXM100 as a hardenable lean wrought-alloy.

The grain size is not only crucial for the material's strength, but can also explain the low ductility observed (Table 6.1). In Mg alloys different grain-size levels result in different deformation modes to be active [56, 57]. This is, *inter alia*, expressed in a raised probability of twin deformation over slip deformation at increased grain size [57, 58]. The presence of twins may be the cause of the low elongation to fracture observed (Figure 6.6), because in Mg alloys twin boundaries can act as crack nucleation sites [11, 59]. In fact, twin formation was frequently observed in this AXM100 alloy and in related representatives of this alloy system, independently of the thermomechanical condition (data not shown). In this light, the occasionally observed significantly larger grains (> 60 μm) (Figure 6.7) are detrimental and a reduction of the grain size to below the critical value at which slip deformation dominates over twinning deformation would thus improve ductility [57, 60]. This appears feasible by modification of the extrusion-process parameters towards a reduced extrusion temperature [61]. A lower extrusion temperature would simultaneously allow an increase of the extrusion speed (Figure 6.4), provided that an extrusion device without the present force limitation is used.

The critical grain size, at which non-basal slip occurs over twin deformation, was observed by Kobayashi *et al.* as 7 μm [62] for AZ31. This was later supported by Wang *et al.* [60] to be 4 μm. The reduction in grain size would thus lead, apart from an expected improvement in ductility, to an enhanced *TYS*. An estimate of *TYS* based on Eq. 6.4, with a grain size of 4 μm and with the same *Hall–Petch* constant as above (k_y= 250 MPa μm$^{1/2}$), yields 125 MPa, which is about 175% higher than the *TYS* obtained for a grain size of 30 μm.

It should, however, be mentioned that with a reduction in grain size to a range where non-basal slip systems are activated, the hardening effectiveness of the G.P. zones is expected to decline. This is because G.P. zones precipitating on the basal plane (Figure 6.10) would become less effective as obstacles to slip, when increasing the likelihood of non-basal slip with a reduction in grain size. The

reported threshold value below which non-basal slip systems are activated and enable dislocations to bypass the G.P. zones, is about 4 to 7 µm. The optimal grain size is thus to be balanced in order to benefit from both mechanisms, namely grain refinement and precipitation strengthening.

6.5.5   *Comparison of experimental data and calculations*

The insights gained into the various precipitation phases, in terms of their phase composition and volume fraction, are now compared with the values predicted by the thermodynamic calculations. The calculations had predicted Al_8Mn_5 and Al_2Ca as the phases presenting the dispersoids blocking the grain boundaries and the precipitates composing the hardening phase, respectively. Figure 6.3 presents their calculated volume fractions. The content of alloying elements and their ratios were balanced accordingly. Microstructural analysis of the resulting alloy revealed, however, that the predicted Al_8Mn_5 phase is indeed a β-Mn phase, which accommodates up to 40 at.% Al (Figure 6.9d and Figure 6.11). The calculations therefore overestimated the Al content required to form the Al–Mn phase. In contrast, they supported the suggested Al-to-Ca ratio of 2 for the formation of G.P. zones. While due to local magnification effects in APT analysis no conclusive statement can be made as to the contribution of Mg to the G.P. zones, its contribution would likewise lead to an overestimation of the Al content. Recalculation, taking into account the lower demand in Al, may therefore produce an improved alloy composition.

The phase volume fractions were estimated for the *peak-aged T6* condition using the experimentally obtained sizes and number densities (Table 6.2). This estimation shows a significantly lower volume fraction for both phases, with 3.6×10^{-4} and 4.2×10^{-4} for the Al–Mn and the Al–Ca phase, respectively, than that predicted by thermodynamic simulations, with 2.3×10^{-3} and 5.0×10^{-3}, respectively. Keeping in mind that the calculation assumes thermodynamic equilibrium, this result is not surprising and suggests that equilibrium is not reached in *peak-aged T6* condition. This is supported by the matrix composition derived from APT analysis, which with 0.2 at.% Al, 0.09 at.% Ca and 0.03 at.% Mn accommodates a significantly larger solute content than that predicted by the calculations: 0.09 at.% Al, 0.001 at.% Ca and 1.5×10^{-6} at.% Mn. Taking this higher remaining matrix's solute content and the overestimated Al need for the Al–Mn-dispersoid formation into account, it is suggested that the Al content could be reduced further without negatively affecting the hardening potential. This would benefit an even leaner alloy composition.

The design concept envisages an *sht* window for obtaining complete solution of Ca. Indeed, the microstructural analysis shows that the Mg_2Ca phase, present in the Janus particles in the *as-extruded* condition (Figure 6.8a), is completely dissolved upon exposure to 510 °C for 10 min (Figure 6.8b). The solvus temperature of the Mg_2Ca phase is predicted to be at about 460 °C (Figure 6.3). On this

basis an extrusion temperature of 450 °C was chosen, which, considering the friction-induced temperature raise, gains a high Ca content in solution in the *as-extruded* condition. The presence of a significant volume fraction of Mg_2Ca phase in the *as-extruded* state (Figure 6.8a) suggests, however, that either the real solvus temperature of the Mg_2Ca phase is higher than the predicted value, or that this phase precipitates during cooling from the extrusion temperature.

Table 6.3: Comparison of AXM-alloys as to their age-hardening potential in light of the lean-alloying concept.

Alloy	Composition	Condition	*TYS* in peak-aged condition	∆TYS	∆*TYS*/ (Al+Ca+Mn)	Reference
	wt.% (at.%)	(-)	(MPa)	(MPa)	(MPa/at.%)	
AXM100	Al0.6(0.54)-Ca0.28(0.17)-Mn0.25(0.11)	T5	236	71	87	This study
AXM0301502	Al0.30(0.27)-Ca0.21(0.13)-Mn0.47(0.21)	T5	207	37	61	[32]
AXM030204	Al0.27(0.30)-Ca0.31(0.19)-Mn0.84(0.37)	T5	210	20	23	[33]
AXM030304	Al0.34(0.32)-Ca0.32(0.19)-Mn0.43(0.19)	T5	220	54	77	[29]
AXM030302	Al0.33(0.30)-Ca0.34(0.20)-Mn0.24(0.11)	T5	188	52	85	[29]
AXM100	Al0.6(0.54)-Ca0.28(0.17)-Mn0.25(0.11)	T6	253	97	118	This study
AXM1021	Al1.08(0.98)-Ca0.24(0.15)-Mn1.03(0.46)	T6	263	68	43	[63, 64]
AXM10304	Al1.31(1.19)-Ca0.33(0.20)-Mn0.46(0.21)	T6	287	100	63	[17]

Table 6.3 compares the alloy developed in this study with other AXM alloys reported in literature. The alloys' *TYS* in the peak-aged condition for both *T5* and *T6* are compared as well as their hardening increment upon artificial aging (∆*TYS*). In addition, the latter is normalized by the total alloying-element content, giving a value ∆*TYS* per at.% total alloying-element content. This normalized value is used to evaluate the alloy's age-hardening potential in light of the envisaged lean-alloy concept. In fact, for both *T5* and *T6* the normalized hardening increment is at 87 MPa/ at.% for *T5* condition and 118 MPa/ at.% for *T6* condition the largest among those of the alloys reported. The alloy which shows the most attractive mechanical properties thus far is AXM10304, developed by Nakata *et al.* [17]. This alloy shows a remarkable combination of high *TYS* and ∆*TYS*: 287 MPa and 100 MPa, respectively. Due to the low processing temperature of 275 °C, however, a *T6* treatment is

implied in order to bring enough Ca in solution. This excludes the economically more attractive *T5* processing route. The AXM100, in contrast, processed here at 450 °C, has the drawback of a coarsened grain size. However, it shows significant hardening also in *T5*, making it an attractive candidate for industrial applications.

Assuming that the attainable extrusion speed depends on the amount of solute atoms and secondary-phase particles in the matrix, our alloy, with less than 1 at.% alloying elements, may be an ideal candidate for high-speed extrusion, provided that a suitable extrusion machine with a greater possible extrusion force is deployed. If extrapolated to 275 °C from the grey triangle in Figure 6.4, an extrusion speed of roughly 20 m min^{-1} could be achieved. This value accords with the regime reported in [17].

6.6 Conclusions

In this study we have rationally designed a lean AXM alloy using thermodynamic calculations comprising its composition and the thermomechanical treatment conditions for its production. The strength of the developed alloy, Mg–Al0.6–Ca0.28–Mn0.25, in wt.%, was evaluated by tensile testing, with a particular focus on its potential for hardening upon artificial aging. The mechanical properties were studied in conjunction with an assessment of the microstructure using TEM and APT to understand the origin of the material's strength at the nanometric scale. The main conclusions drawn are as follows:

- Despite the very low alloying content of less than 1 at.%, our AXM100 alloy exhibits substantial hardening upon artificial aging at 200°C for 90 min: $\Delta TYS \approx 70$ MPa for *T5* condition and 100 MPa for *T6* condition, reaching a *TYS* of 253 MPa for the latter.

- Scattered Al–Mn dispersoids of about 20 nm in size are present in all conditions, indicating their thermal stability. They successfully retard grain growth during *sht*.

- Nanodiffraction combined with STEM-EDS and APT analysis reveals that the Al–Mn dispersoids are composed of β-Mn phase, with a composition close to $Mn_{60}Al_{40}$ (in at.%).

- Further grain refinement would increase the alloy's strength, and help increase the material's ductility by activating non-basal dislocation slip.

- Ordered G.P. zones precipitating densely on the basal plane of the Mg matrix are responsible for the significant hardening response upon artificial aging. Their nanometric size is smaller and their number density larger in the *T6* condition than in the *T5* condition, explaining the larger hardening increment in *T6*.

- Correlative analysis combining high-resolution STEM and APT allows us to infer that the G.P. zones are thin plates composed of Al and Ca with a ratio of about 2, which is close to the equilibrium phase composition Al_2Ca.

- Ca plays a key role in the precipitation of the Al–Ca G.P. zones from solid solution (*T6* condition) and originates from the dissolution of the Mg_2Ca phase (*T5* condition). This is facilitated by its insolubility at low temperature and its high diffusivity in Mg.

- The Mg_2Ca phase co-precipitates at the sites of the Al–Mn dispersoids, forming Janus particles in the *as-extruded* state. The Mg_2Ca phase serves as a Ca reservoir for the formation of Al–Ca-rich G.P. zones.

- Nanometric Ca-rich clusters were identified by APT that may not only act as precursors to G.P. zones, but also contribute to the alloy's strength.

- Thermodynamic calculations, provided the limitations assessed in this work are taken into account, prove to be an invaluable tool for the rational design of hardenable Mg-based lean alloys.

6.7 Acknowledgements

6.8 References

[1]   C. Davies, M. Barnett, Expanding the extrusion limits of wrought magnesium alloys, JOM Journal of the Minerals, Metals and Materials Society 56(5) (2004) 22-24.

[2]   D.L. Atwell, M.R. Barnett, Extrusion limits of magnesium alloys, Metallurgical and Materials Transactions A 38(12) (2007) 3032-3041.

[3]   E. Hall, The deformation and ageing of mild steel: III discussion of results, Proceedings of the Physical Society. Section B 64(9) (1951) 747.

[4]   N.J. Petch, The cleavage strength of polycrystals, Journal of the Iron and Steel Institute 174 (1953) 25-28.

[5]   P. Andersson, C.H. Cáceres, J. Koike, Hall-Petch parameters for tension and compression in cast Mg, Materials Science Forum, Trans Tech Publications, 2003, 123-128.

[6]   D. Wilson, J. Chapman, Effects of preferred orientation on the grain size dependence of yield strength in metals, Philosophical Magazine 8(93) (1963) 1543-1551.

[7]   N. Hansen, The effect of grain size and strain on the tensile flow stress of aluminium at room temperature, Acta Metallurgica 25(8) (1977) 863-869.

[8]   A. Yamashita, Z. Horita, T.G. Langdon, Improving the mechanical properties of magnesium and a magnesium alloy through severe plastic deformation, Materials Science and Engineering: A 300(1-2) (2001) 142-147.

[9]   M. Kai, Z. Horita, T.G. Langdon, Developing grain refinement and superplasticity in a magnesium alloy processed by high-pressure torsion, Materials Science and Engineering: A 488(1-2) (2008) 117-124.

[10]   M. Mabuchi, T. Asahina, H. Iwasaki, K. Higashi, Experimental investigation of superplastic behaviour in magnesium alloys, Materials Science and Technology 13(10) (1997) 825-831.

[11]   M. Jiang, C. Xu, T. Nakata, H. Yan, R. Chen, S. Kamado, High-speed extrusion of dilute Mg-Zn-Ca-Mn alloys and its effect on microstructure, texture and mechanical properties, Materials Science and Engineering: A 678 (2016) 329-338.

[12]   J. Hofstetter, S. Rüedi, I. Baumgartner, H. Kilian, B. Mingler, E. Povoden-Karadeniz, S. Pogatscher, P.J. Uggowitzer, J.F. Löffler, Processing and microstructure–property relations of high-strength low-alloy (HSLA) Mg–Zn–Ca alloys, Acta Materialia 98 (2015) 423-432.

[13]   C. Zener, quoted by CS Smith, Trans. AIME 175 (1948) 15.

[14]   J.-F. Nie, Precipitation and hardening in magnesium alloys, Metallurgical and Materials Transactions A 43(11) (2012) 3891-3939.

[15]   K. Oh-Ishi, R. Watanabe, C. Mendis, K. Hono, Age-hardening response of Mg–0.3 at.% Ca alloys with different Zn contents, Materials Science and Engineering: A 526(1) (2009) 177-184.

[16]   S. Celotto, TEM study of continuous precipitation in Mg–9 wt% Al–1 wt% Zn alloy, Acta Materialia 48(8) (2000) 1775-1787.

[17]   T. Nakata, C. Xu, R. Ajima, K. Shimizu, S. Hanaki, T. Sasaki, L. Ma, K. Hono, S. Kamado, Strong and ductile age-hardening Mg-Al-Ca-Mn alloy that can be extruded as fast as aluminum alloys, Acta Materialia 130 (2017) 261-270.

[18]   Z. Li, X. Zhang, M. Zheng, X. Qiao, K. Wu, C. Xu, S. Kamado, Effect of Ca/Al ratio on microstructure and mechanical properties of Mg-Al-Ca-Mn alloys, Materials Science and Engineering: A 682 (2017) 423-432.

[19]   S. Xu, K. Oh-Ishi, S. Kamado, F. Uchida, T. Homma, K. Hono, High-strength extruded Mg–Al–Ca–Mn alloy, Scripta Materialia 65(3) (2011) 269-272.

[20]   T. Nakata, C. Xu, R. Ajima, Y. Matsumoto, K. Shimizu, T. Sasaki, K. Hono, S. Kamado, Improving mechanical properties and yield asymmetry in high-speed extrudable Mg-1.1 Al-0.24 Ca (wt.%) alloy by high Mn addition, Materials Science and Engineering: A 712 (2018) 12-19.

[21]   N. Stanford, The effect of calcium on the texture, microstructure and mechanical properties of extruded Mg–Mn–Ca alloys, Materials Science and Engineering: A 528(1) (2010) 314-322.

[22]   J. Jayaraj, C. Mendis, T. Ohkubo, K. Oh-Ishi, K. Hono, Enhanced precipitation hardening of Mg–Ca alloy by Al addition, Scripta Materialia 63(8) (2010) 831-834.

[23]   J.B. Clark, Age hardening in a Mg-9 wt.% Al alloy, Acta Metallurgica 16(2) (1968) 141-152.

[24]   A. Suzuki, N. Saddock, J. TerBush, B. Powell, J. Jones, T. Pollock, Precipitation strengthening of a Mg-Al-Ca–based AXJ530 die-cast alloy, Metallurgical and Materials Transactions A 39(3) (2008) 696-702.

[25]   A. Nayeb-Hashemi, J.B. Clark, Phase diagrams of binary magnesium alloys, ASM International, Metals Park, Ohio 44073, USA, 1988.

[26]   J. She, F. Pan, W. Guo, A. Tang, Z. Gao, S. Luo, K. Song, Z. Yu, M. Rashad, Effect of high Mn content on development of ultra-fine grain extruded magnesium alloy, Materials & Design 90 (2016) 7-12.

[27]   L. Tong, M. Zheng, S. Xu, S. Kamado, Y. Du, X. Hu, K. Wu, W. Gan, H. Brokmeier, G. Wang, Effect of Mn addition on microstructure, texture and mechanical properties of Mg–Zn–Ca alloy, Materials Science and Engineering: A 528(10) (2011) 3741-3747.

[28]   S.A. Khan, Y. Miyashita, Y. Mutoh, Z.B. Sajuri, Influence of Mn content on mechanical properties and fatigue behavior of extruded Mg alloys, Materials Science and Engineering: A 420(1) (2006) 315-321.

[29]   T. Nakata, C. Xu, Y. Matsumoto, K. Shimizu, T. Sasaki, K. Hono, S. Kamado, Optimization of Mn content for high strengths in high-speed extruded Mg-0.3 Al-0.3 Ca (wt%) dilute alloy, Materials Science and Engineering: A 673 (2016) 443-449.

[30]   L. Han, H. Hu, D.O. Northwood, N. Li, Microstructure and nano-scale mechanical behavior of Mg–Al and Mg–Al–Ca alloys, Materials Science and Engineering: A 473(1-2) (2008) 16-27.

[31]   CompuTherm LLC, Pandat software package for calculating phase diagrams and thermodynamic properties of multi- component alloys, Madison, USA, www.computherm.com.).

[32]   T. Nakata, T. Mezaki, R. Ajima, C. Xu, K. Oh-Ishi, K. Shimizu, S. Hanaki, T. Sasaki, K. Hono, S. Kamado, High-speed extrusion of heat-treatable Mg–Al–Ca–Mn dilute alloy, Scripta Materialia 101 (2015) 28-31.

[33]   T. Nakata, K. Shimizu, Y. Matsumoto, S. Hanaki, S. Kamado, Effect of Mn Content on Microstructures and Mechanical Properties of Mg-Al-Ca-Mn Alloys Fabricated by High-Speed Extrusion, Magnesium Technology 2015, Springer, Cham, Switzerland, 2015, 241-246.

[34]   I.O.f.S. (ISO), Aluminium and Aluminium Alloys, Wrought Products - Temper Designations, 2007.

[35] M. Klinger, A. Jäger, Crystallographic Tool Box (CrysTBox): automated tools for transmission electron microscopists and crystallographers, Journal of Applied Crystallography 48(6) (2015) 2012-2018.

[36] P. Stadelmann, EMS-a software package for electron diffraction analysis and HREM image simulation in materials science, Ultramicroscopy 21(2) (1987) 131-145.

[37] P.K. Saha, Aluminum extrusion technology, ASM International, 2000.

[38] M. Miller, G. Smith, An atom probe study of the anomalous field evaporation of alloys containing silicon, Journal of Vacuum Science and Technology 19(1) (1981) 57-62.

[39] M. Miller, M. Hetherington, Local magnification effects in the atom probe, Surface Science Letters 246(1-3) (1990) A181.

[40] A. Deschamps, Y. Brechet, Influence of predeformation and ageing of an Al–Zn–Mg alloy—II. Modeling of precipitation kinetics and yield stress, Acta Materialia 47(1) (1998) 293-305.

[41] T. Homma, S. Nakawaki, K. Oh-Ishi, K. Hono, S. Kamado, Unexpected influence of Mn addition on the creep properties of a cast Mg–2Al–2Ca (mass%) alloy, Acta Materialia 59(20) (2011) 7662-7672.

[42] T. Homma, S. Hirawatari, H. Sunohara, S. Kamado, Room and elevated temperature mechanical properties in the as-extruded Mg–Al–Ca–Mn alloys, Materials Science and Engineering: A 539 (2012) 163-169.

[43] B.-C. Zhou, S.-L. Shang, Y. Wang, Z.-K. Liu, Diffusion coefficients of alloying elements in dilute Mg alloys: A comprehensive first-principles study, Acta Materialia 103 (2016) 573-586.

[44] D. Hull, D.J. Bacon, Introduction to dislocations, Elsevier, Oxford, UK, 2011.

[45] J.W. Martin, Micromechanisms in particle-hardened alloys, Cambridge University Press, Cambridge, UK, 1980.

[46] J. Nie, Effects of precipitate shape and orientation on dispersion strengthening in magnesium alloys, Scripta Materialia 48(8) (2003) 1009-1015.

[47] J. Visser, On the structure of (Cr5Al8) 26R. A correction, Acta Crystallographica Section B: Structural Crystallography and Crystal Chemistry 33(1) (1977) 316-316.

[48] J. Braun, M. Ellner, B. Predel, Structure of the High-Temperature Phase Cr5al8(H), Journal of Alloys and Compounds 183 (1992) 444-448.

[49] P.B. Braun, J.A. Goedkoop, An X-ray and neutron diffraction investigation of the magnetic phase Al0. 89Mn1. 11, Acta Crystallographica 16(8) (1963) 737-740.

[50] W. Koster, E. Wachtel, Aufbau Und Magnetische Eigenschaften Der Aluminium-Mangan-Legierungen Mit Mehr Als 25-at-Percent Mn, Zeitschrift Fur Metallkunde 51(5) (1960) 271-280.

[51] M. Ellner, The structure of the high-temperature phase MnAl (h) and the displacive transformation from MnAl (h) into Mn5Al8, Metallurgical Transactions A 21(6) (1990) 1669-1672.

[52] C.B. Shoemaker, D.P. Shoemaker, T. Hopkins, S. Yindepit, Refinement of the structure of β-manganese and of a related phase in the Mn–Ni–Si system, Acta Crystallographica Section B: Structural Crystallography and Crystal Chemistry 34(12) (1978) 3573-3576.

[53] A. Bradley, J. Thewlis, The crystal structure of α-manganese, Proceedings of the Royal Society of London. Series A, Containing Papers of a Mathematical and Physical Character 115(771) (1927) 456-471.

[54] D.B. Williams, C.B. Carter, Transmission Electron Microscopy - A Textbook for Materials Science, Plenum Press, New York, NY, U.S.A., 1996.

[55] C. Cáceres, G.E. Mann, J. Griffiths, Grain size hardening in Mg and Mg-Zn solid solutions, Metallurgical and Materials Transactions A 42(7) (2011) 1950-1959.

[56] J. Koike, T. Kobayashi, T. Mukai, H. Watanabe, M. Suzuki, K. Maruyama, K. Higashi, The activity of non-basal slip systems and dynamic recovery at room temperature in fine-grained AZ31B magnesium alloys, Acta Materialia 51(7) (2003) 2055-2065.

[57] M. Barnett, Z. Keshavarz, A. Beer, D. Atwell, Influence of grain size on the compressive deformation of wrought Mg–3Al–1Zn, Acta Materialia 52(17) (2004) 5093-5103.

[58] S. Xu, K. Oh-ishi, H. Sunohara, S. Kamado, Extruded Mg–Zn–Ca–Mn alloys with low yield anisotropy, Materials Science and Engineering: A 558 (2012) 356-365.

[59] F. Yang, S. Yin, S. Li, Z. Zhang, Crack initiation mechanism of extruded AZ31 magnesium alloy in the very high cycle fatigue regime, Materials Science and Engineering: A 491(1-2) (2008) 131-136.

[60] J.T. Wang, J.Q. Liu, J. Tao, Y.L. Su, X. Zhao, Effect of grain size on mechanical property of Mg–3Al–1Zn alloy, Scripta Materialia 59(1) (2008) 63-66.

[61] T. Nakata, T. Mezaki, C. Xu, K. Oh-ishi, K. Shimizu, S. Hanaki, S. Kamado, Improving tensile properties of dilute Mg-0.27 Al-0.13 Ca-0.21 Mn (at.%) alloy by low temperature high speed extrusion, Journal of Alloys and Compounds 648 (2015) 428-437.

[62] T. Kobayashi, J. Koike, Y. Yoshida, S. Kamado, M. Suzuki, K. Maruyama, Y. Kojima, Grain size dependence of active slip systems in an AZ 31 magnesium alloy, Journal of the Japan Institute of Metals 67(4) (2003) 149-152.

[63] T. Nakata, C. Xu, R. Ajima, Y. Matsumoto, K. Shimizu, T. Sasaki, K. Hono, S. Kamado, Improving mechanical properties and yield asymmetry in high-speed extrudable Mg-1.1 Al-0.24 Ca (wt%) alloy by high Mn addition, Materials Science and Engineering: A 712 (2018) 12-19.

[64] T. Nakata, C. Xu, T. Sasaki, Y. Matsumoto, K. Shimizu, K. Hono, S. Kamado, Development of High-Strength High-Speed-Extrudable Mg–Al–Ca–Mn Alloy, Magnesium Technology 2017, Springer, Cham, Switzerland, 2017, 17-21.

7 Conclusions and Outlook

7.1 Conclusions

Wrought Mg–Zn–Ca-lean alloys have previously been demonstrated to combine the properties that are essential for their deployment as a biomedical implant, namely a biologically safe composition, high strength ($TYS \approx 240$ MPa, $UTS \approx 265$ MPa), extended ductility ($A_f \approx 30\%$), and a slow and homogeneous degradation. However, the characterization of material properties focused thus far on a macroscopic length scale, with limited insights into the role of the metal's micro- and nanostructure. An in-depth understanding of the microstructure–property correlations, however, is not only interesting from a fundamental research point of view, but also crucial to ensure a safe and controllable degradation behavior in the human body. A solid understanding of the microstructural key players that govern the materials' overall behavior also sets the premises to potentially tune their degradation rate and improve their mechanical properties.

7.1.1 Correlation between microstructure and corrosion properties

A thorough analysis of the microstructure provides the basis for its correlation with the properties observed. For the microstructure's relation to the corrosion susceptibility, the phases' composition, volume fraction and distribution rather than their structure were in focus. Analytical TEM using EDS showed, on the one hand, that Zn is dissolved in the Mg_2Ca phase at a temperature-dependent concentration. On the other hand, ultra-high resolution imaging with corresponding EDS analysis at the atomic scale revealed the ternary IM1 phase to be composed of $Ca_3Mg_{11}Zn_4$, which is at the upper end of Mg content for the composition range reported in literature with $Ca_3Mg_xZn_{15-x}$ ($4.6 \leq x \leq 12$). The $Ca_3Mg_{11}Zn_4$ phase experimentally identified contradicts the one predicted by thermodynamic calculations, i.e. $Ca_2Mg_6Zn_3$, and thus urges to refine the corresponding database.

IMPs of both phases were analyzed first for their local corrosion behavior and then for their role in the macroscopic alloy degradation. For the local analysis, protocols for *ex situ* cross-sectional TEM and quasi-*in situ* planar-view TEM analyses were developed and deployed in conjunction. This methodology allowed, on the hand one, for the observation of rapid preferential dissolution of nanometric Mg_2Ca-type IMPs, identifying them as the local anode and as nucleation sites for Ca/P/O-rich corrosion products. On the other hand, a greater corrosion resistance of the IM1-phase-type IMPs and of the grain boundaries was observed, identifying them as local cathodes.

The methodological advances provided with the TEM-based protocols allowed for the *in statu nascendi* observation of intermetallic-particle dealloying acting on the IM1 phase, with Ca and Mg preferentially dissolving and Zn retaining via cathodic protection. This generates a progressive

accumulation of Zn and thus a gradual ennoblement of the IMPs. These observations present the first documented evidence of dealloying of cathodically active intermetallic phases in Mg alloys. Placed in the context of electrochemical theory, the observations are explained by a cathodically polarized dealloying mechanism, which is suggested to be broadly applicable to other intermetallic phases and other alloying systems.

From a methodological perspective, the successful establishment of quasi-*in situ* TEM analysis for Mg-corrosion studies in this thesis not only allowed to obtain insights into the acting corrosion mechanisms on the nanoscale but also to assist in defining the experimental window for emerging real *in situ* TEM studies.

To address the role of IMP-type in the macroscopic degradation behavior two approaches were followed, both assisted by thermodynamic calculations: In the first approach, specific heat treatments were applied to modify the IMP type while keeping the nominal composition constant. An extended low-temperature heat treatment at 250 °C led indeed to the desired transition from the binary Mg_2Ca to the ternary IM1 phase, and could thus support the predictions made by the calculated phase diagram. However, the macroscopic degradation rate was not affected by the IMP type, which suggested that their size or volume fraction may be sub-critical as to have an up-scale impact on the degradation rate. A definite conclusion, however, could not be drawn, because the heat treatments applied had induced considerable coarsening of the IMPs, under simultaneous reduction of their number density, and their segregation to the grain boundaries, which both may have affected the IMPs' behavior in a micro-galvanic cell.

In the second approach, a slight adjustment of the nominal Zn content was utilized to modify the IMP type while keeping other microstructural characteristics constant that may influence the corrosion susceptibility. Two model materials were successfully designed for this purpose, ZX10 and ZX20, which differ in their Zn content as little as 0.5 wt.% (0.19 at.%). Their microstructures were found to indeed differ only in the phase-type composing the IMPs, with ZX10 and ZX20 hosting the Mg_2Ca and the IM1 phase, respectively. A greater hydrogen volume and larger current and charge transient for ZX20 compared to ZX10 revealed the faster *in vitro* degradation of ZX20. Electrochemical analysis revealed a larger cathodic activity of ZX20 at the origin of the faster degradation, expressed as a shift in E_{corr} towards higher values and higher cathodic reaction rates. Thanks to detailed insights obtained by complementary TEM analysis, ZX20's greater cathodic activity could be ascribed to the IM1-type IMPs contained. These results thus clarify that the IMPs – despite their nanometric size and low volume fraction – can indeed control the macroscopic degradation rate.

For both alloys, HR-TEM analysis unveiled the presence of nanometric Zn clusters, 2 – 10 nm in size, which were found embedded in the spongy corrosion products. High-resolution EDS analysis could rule out the clusters to be IMP remnants or oxides, but instead suggested that they are composed entirely of Zn. Redeposition via discharge of Zn ions on the Mg substrate was discussed to be at the cluster's origin – a mechanism that is reported in literature for other noble elements. While there seems little doubt in literature about the mechanism itself, direct experimental evidence of the redeposits and understanding of their characteristics, such as their composition, structure and morphology, is scarce, mainly due to the limited resolution of conventional analytical methods. While the HR-TEM analysis in this thesis could add to the morphological description, further analysis is needed to reveal the clusters' detailed properties. In fact, a detailed understanding of the cluster properties would assist in validating the mechanisms that underlie their formation.

Overall, the Zn redeposits are accounted responsible for a dynamic increase of the alloy's cathodic activity with progressing material dissolution. This behavior was observed for both alloys when a suitable polarization strategy was applied, but was not detected for XHP Mg. Zn redeposition leading to the formation of additional nano-galvanic cells on the Mg surface is, thus, considered to play a crucial role in the long-term corrosion susceptibility of ZX alloys, even for only minor alloying of Zn as for the ZX-lean alloys investigated in this thesis.

7.1.2 *In vivo degradation and biological response to Mg–Zn–Ca-lean alloys*

It is a generally recognized challenge that *in vitro* experiments may not allow for an accurate prediction of the complex *in vivo* situation. To test whether the degradation characteristics identified *in vitro* are indeed relevant and representative for the real *in vivo* situation, ZX-lean alloys ZX10 and ZX20 were implanted in the femurs of rats and the degradation behavior and biological response evaluated over a course of 52 weeks. Micro-CT analysis of the remaining implant volume over time indeed confirmed the faster degradation of ZX20 compared to ZX10. Importantly, the degradation of *both* materials was homogeneous and slow with no accumulation of hydrogen gas in the adjacent tissue. This result disproves the hypothesis earlier communicated in literature that the IM1 phase (here contained in ZX20) must generally be avoided to achieve a sufficient reduction of the degradation rate as to avoid tissue irritation and rapid and inhomogeneous implant disintegration. By contrast, the results obtained here show that when the IM1 phase is present as nanometric IMPs ($d \leq 100$ nm) at a low volume fraction ($\leq 1.5 \times 10^{-3}$) and at a large number density ($N \geq 10^{18}$ m^{-3}), a corrosion attack manifests that is homogeneous at the scale relevant for the implant application and remains sufficiently slow. The results show further that a small adjustment of the nominal Zn content, from 1.0 wt.% (0.37 at.%) in ZX10 to 1.5 wt.% (0.56 at.%) in ZX20, with the concomitant

change of the IMP type from Mg_2Ca to the IM1 phase, respectively, can be utilized to finely tailor the degradation rate *in vivo*.

Histological analysis showed for both materials an early bone–implant contact 4 weeks *post operationem* and only a minor layer of fibrous cells surrounding the implant at 4 weeks *post operationem*, which however vanished completely with further implantation time. Based on the early osseointegration and virtual absence of adverse tissue reactions observed, both materials are from a biomedical point-of-view evaluated suitable for their use as implants in contact with bone.

7.1.3   *Correlation between microstructure and mechanical properties*

A material suitable for structural applications, be it for load-bearing biomedical implants or for lightweight structural application in the context of transportation or building industry, needs to fulfill requirements regarding mechanical strength.

Determination of the size and number density of IMPs contained in the ZX10 alloy by TEM analysis allowed to quantify their individual contributions to the material's strength. The contribution by precipitation hardening was found to be independent from the IMP-phase type and overall neglectable at a maximum of about 3 MPa. TEM-based *in situ* heating experiments revealed that the IMPs efficiently pin the grain boundaries at elevated temperature, thus playing a critical role in the mechanical properties by ensuring a small grain size. In fact, grain-boundary strengthening was identified as the major contributor to the alloy's mechanical strength, with a *Hall-Petch* constant k_y determined at 255 MPa $\mu m^{1/2}$.

With the attempt to further improve the mechanical strength of ZX-lean alloys, their age-hardening potential was evaluated. It was found though that the hardening response was scarce upon *T5* aging ($\Delta H_V = 3$), and while *T6* peak-aging could achieve an appreciable increase of about $\Delta H_V = 12$ (corresponding to ~30% increase compared to the *sht* condition), the strength benefit was too small as to compensate for the loss of strength ($\Delta H_V = -16$) due to severe grain growth (from 2 μm to 70 μm) during *sht*.

The observation of a limited hardening potential of the ZX-lean alloys had motivated the development of a new hardenable wrought Mg-based lean alloy. The Mg–Al–Ca–Mn (AXM) system was chosen for its potential to combine grain-boundary strengthening and age-hardenability. A rational design concept was followed assisted by thermodynamic calculations and directed towards a microstructure with an Al–Mn and an Al–Ca phase, anticipated to function as a pinning phase and hardening phase, respectively. The alloying elements were balanced accordingly, resulting in an optimized alloy with a composition Mg–Al0.6(0.54)–Ca0.28(0.17)–Mn0.25(0.11) (AXM100, in wt.% (at.%)).

The design concept proved successful, with the alloy developed exhibiting a large age-hardening response of ΔTYS = 70 MPa and 100 MPa following $T5$ and $T6$ peak-aging, respectively. Considering the total alloying-element content at only 0.82 at.%, AXM100 exhibits the largest specific age-hardening response of the reported AXM alloys to date, at 87 MPa at.%$^{-1}$. Insights obtained from multiscale microstructural analysis, comprising light microscopy, TEM and APT, were able to explain the microstructural origins of the mechanical performance: precipitation of Al–Ca-rich G.P. zones are responsible for the hardening, and they are smaller in size and greater in number density in $T6$- compared to $T5$-peak-aged condition. Ca was found to be the driving force in the nucleation of the G.P. zones, forming Ca clusters as precursors to the ordered G.P. zones. Additionally, thermally stable dispersoids were identified, which successfully retard grain growth during sht, thus preserving the grain-boundary strengthening effect. Their composition and structure was experimentally determined to match the β-Mn phase with a $Mn_{60}Al_{40}$ stoichiometry, which opposes the Al_8Mn_5 phase predicted by the simulations. However, despite the efficient suppression of grain growth upon heat treatments, the overall grain size resulting from extrusion was relatively coarse at ~30 µm, concomitant with an overall satisfactory but not superior strength of TYS = 253 MPa and UTS = 277 MPa at maximum. Further grain refinement is thus necessary to make AXM100 a competitive alternative to commercially available alloys.

7.2 Outlook

The results and observations obtained in this thesis project motivate further research. Some potential future research directions are presented as follows.

Effect of IMP spacing. It was observed that the IM1 phase contained in the ZX20 alloy generates a significantly increased macroscopic corrosion rate compared to the ZX10 alloy, while the same phase contained in heat-treated ZX10 had accelerated the matrix dissolution only locally without an impact on the macroscopic scale. It was hypothesized that the difference in the IMPs' size and distribution in ZX20 and HT-ZX10, concomitant with different spacing between them, is responsible for this discrepancy. To test this hypothesis, model materials are to be designed, which contain the IMPs in a constant volume fraction but with varying size and spacing and at a constant nominal composition, and their macroscopic degradation rate is to be quantified.

Details of dealloying. The identification of dealloying of the cathodically active IM1 phase presents one of the key findings of this thesis. The preferential dissolution of Ca and Mg led to a porous attacked IMP periphery and a Zn-enriched remnant. Owing to the IMPs' increasing cathodic activity, the dealloying process entails their increasingly effective galvanic activity to accelerate preferential

matrix dissolution. It is thus important to understand in detail the IMPs' modified composition and structure following dealloying. In this context, it should be addressed how far into the IMP the dealloying process can proceed before diffusion limitation dominates. Ultra-high resolution TEM imaging and chemical analysis of the IMPs as a function of dissolution stages have the potential to reveal such details. Furthermore, it is expected that a threshold exists for the IMP's Zn content, above which the Zn-rich IMP suffers dealloying, and below which complete dissolution occurs. To test this hypothesis and potentially determine this threshold, future research should aim at synthesizing the IM1 phase with varying Zn content and studying their dissolution behavior.

Details of Zn redeposits. A critical role is ascribed to the Zn redeposition in the corrosion susceptibility of ZX-lean alloys, and other Zn-rich Mg alloys, as it gradually increases the cathodic reaction rates. However, apart from the observation of Zn- or Zn-rich clusters in the corrosion-product layer and anti-correlation with Ca and O, no further characterization is yet available on their detailed morphology, structure or composition to allow answering the question (among others) of whether they are indeed composed entirely of Zn and whether they are indeed metallic. Furthermore, the Zn redeposits were found exclusively as distinct nanometric clusters whereas a continuous Zn-rich layer at the metal–corrosion-product-layer interface was absent. Such a noble-element layer at the interface was previously reported for alloying elements in Mg, such as Al and Zn. The absence of a layer for the ZX-lean alloys studied here suggests that either their Zn content is sufficiently low as to prevent coalescence of the redeposited Zn or that the time of investigation was too short as to reach coalescence. Further investigations at an even higher magnification and at more advanced material-dissolution stages are necessarily to shed light on the details of Zn redeposition.

In situ TEM analysis. Emerging TEM-based *in situ* exposure to a corrosive environment has the potential to unveil the dynamic changes and sequential events of local corrosion attack, and to allow accessing the phenomena that occur very rapidly, i.e. at a shorter time scale than what can reasonably be achieved in quasi-*in situ* experiments. The quasi-*in situ* protocols elaborated in this thesis set the premises for identifying experimental conditions suitable for real *in situ* experiments of Mg alloys.

In vivo validation. The corrosion phenomena of IMP dealloying and Zn-cluster formation were identified in simulated body experimental conditions. It is yet to be confirmed that these observations are representative for the degradation behavior of ZX alloys in a more complex *in vivo* environment. Such investigations require access to explants that are specifically prepared for TEM analysis, i.e. embedded in a suitable resin to withstand the ultra-high vacuum and high-energy beam present in TEM.

Improvement of mechanical properties by grain-size reduction. The crucial role of grain refinement in the mechanical performance of Mg is well-known and was shown to be critical also for the lean wrought alloys of both alloying systems investigated in this thesis: ZX and AXM. Further grain refinement is thus the strategy of choice to improve the mechanical strength of both alloys.

One incentive is the reduction of the extrusion temperature, which is well-known to have a direct impact on the grain size. A temperature reduction was thus far limited by the simultaneously increasing extrusion force, which exceeded the feasible force of the extrusion device available to the project. This limitation can now be overcome with a newly acquired extrusion device at ETH Zurich. A temperature reduction will, however, lower the possible extrusion speed and, for temperatures < 300 °C, restrict dynamic recrystallization. The latter may make static post-extrusion heat treatments necessary to counteract a severe loss in ductility. Alternatively, a pre-study on a related alloy, Mg–Zn0.45–Ca0.45 (ZX00, in wt.%), had revealed the potential of multi-paths extrusion for an effective grain refinement. In fact, extrusion of only two paths was already sufficient to achieve a significant grain-size reduction. A reduced extrusion speed as well as the necessity for an additional extrusion path or post-extrusion processing step contradict the economic aspiration for process optimization. A reasonable balance of improved mechanical properties and reasonable costs is thus to be found.

An alternative approach to achieve the reduced grain size desired relies on the role of precipitates in influencing dynamic recrystallization and retarding grain growth. According to the *Zener* principle, the maximum grain size manifesting is a function of both number density and size of precipitates. Both can be influenced by heat treatments. Pre-extrusion heat treatments are thus to be varied and their impact evaluated first on the precipitate characteristics, and then in turn on the resulting grain size. While low-temperature heat treatments (< 250 °C) may result in a larger number density of nucleation sites, medium temperatures and time present levers for ripening of the precipitates to their desired size. On the one hand, static TEM analysis should closely accompany these efforts to understand the impact of the thermomechanical processing steps on the precipitate characteristics. On the other hand, *in situ* TEM analyses at elevated temperature and/or mechanical strain allow for the quantification of the precipitates' obstacle strength generated to impede grain-boundary motion.

Increased hardening potential following two-step artificial aging. The observation that AXM100 exhibits a relatively fast hardening response upon artificial aging at 200 °C (black curve in Figure 7.1) had motivated an investigation of the material's hardening behavior upon storage at room temperature, i.e. natural aging. Indeed a slight hardening increase by $\Delta H_V \approx 5$ was observed after 12 weeks at room temperature. Interestingly, a subsequent artificial aging at 200 °C resulted in a superior peak hardness (gray curve in Figure 7.1) compared to the peak-aged *T6* condition. Even

more interesting from an application point of view is the observation that the same superior peak hardness can be achieved by replacing the natural-aging step by a pre-aging step at low temperature, i.e. 100 ºC, for only 2 h (green curve in Figure 7.1). It is hypothesized that the preceding natural aging or pre-aging results in a greater number of nucleation sites for the precipitation of the hardening phase compared to the single-step artificial aging at 200 ºC performed in this thesis. The Ca clusters, which were found to form prior to the G.P. zones, may also contribute to the hardening. A detailed microstructural analysis employing correlative TEM and APT is required to identify the microstructural origins of the hardening behavior observed.
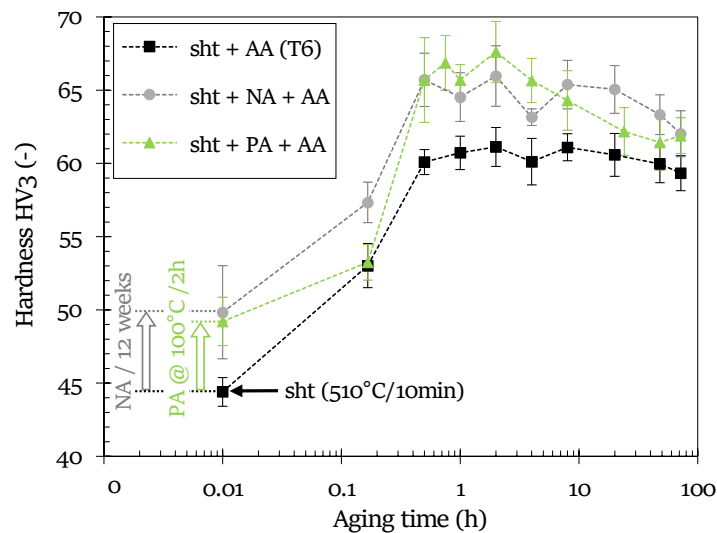

Figure 7.1: Superior peak-aging performance for an AXM100 alloy upon artificial aging (AA; at 200 C) following pre-conditioning by either natural aging (NA; at room temperature for 12 weeks) or by pre-aging (PA; at 100 ºC for 2 h).

Appendix

Curriculum Vitae

Date of birth:	July 9th, 1987
Place of birth:	59821 Arnsberg, Germany
Nationality:	German

Academic Education

2014 – 2019	**Swiss Federal Institute of Technology (ETH), Zurich, Switzerland** Ph.D. in Materials Science · Department of Materials; Laboratory of Metal Physics and Technology
2007 – 2013	**Karlsruhe Institute of Technology (KIT), Karlsruhe, Germany** Bioengineering; Degree: *Diplom Ingenieur* (Equal to *B.Eng.*+*M.Eng.*), Grade 1.4*
2011	**Kungliga Tekniska Högskolan (KTH), Stockholm, Sweden** Exchange semester; lectures in Materials Science and Medicine

Research experiences

2014 – 2019	**Laboratory of Metal Physics and Technology at ETHZ** Doctoral student and research assistant · Research field: biodegradable implant material development and characterization, biocorrosion, microstructural analysis, electron microscopy
2013 – 2014	**Natural and Medical Science Institute (NMI), University of Tübingen, Laboratory for BioMEMS and Sensors, Reutlingen, Germany** *Researcher* · Research field: active implantology and sensor-based biomaterial testing, thin film technology, *in vitro + in vivo* evaluation
Nov. 2012 – Mai 2013	**Institute for Biological Interfaces 1 (IBG1) at KIT** *Diplomarbeit (degree project/ equal to Master thesis), Grade: 1.0* · Thesis topic: Development and characterization of a new film-based three-dimensional microfluidic system
Apr. 2012 – Sep. 2012	**Institute for Biological Interfaces 1 (IBG1) at KIT** *Student research assistant* · Fabrication of film-based micro-systems for biomedical research
Jun. 2010 – Aug. 2010	**Center for Advanced Microstructures and Devices (CAMD), Louisiana State University, Baton Rouge, USA** *Visiting research scholar* · Topic: Tailoring the adhesion of HeLa Cells on Parylene-C biocompatible films by surface modification

* scale: 1-6, with 1.0 being the highest score.

Teaching and industry experience

Mar. 2015 – Mar. 2019	**Laboratory of Metal Physics and Technology at ETHZ** · Laboratory class "corrosion" for BSc. students in Materials Science
Oct. 2010 – Mar. 2011	**Solae LLC, Part of DuPont Company, St. Louis, USA** *Internship* · Projects in Process Engineering; main project: Development of a membrane system with automation
Oct. 2008 – Oct. 2009	**Institute for Applied Mechanics at KIT** Tutor for class "technical mechanics" for BSc. students in Bioengineering and Process Engineering.

Student supervision

Anna Nelson (Bachelor Thesis, 2018):

Effect of the addition of Zinc on the hardening responds of magnesium-based AXM-lean alloys

Victor Chausse (Master Thesis, 2017):

Mg-based 3D scaffolds as a biodegradable drug delivery system

Kai von Petersdorff-Campen (Master Thesis, 2017):

Analysis of corrosion products of a biodegradable Mg–Zn–Ca-lean alloy as a function of its microstructure

Lukas Hauser (Bachelor Thesis, 2016):

Age-hardening response of low-alloyed Mg–Al–Ca–Mn-alloys

Nicole Schai (Master Thesis, 2016):

A new design strategy for porous ordered Mg scaffolds: development and characterization

Kay Sanvito (Bachelor Thesis, 2016):

A novel antimicrobial coating for magnesium ribbons as biodegradable drug carriers

Giulia Biffi (Bachelor Thesis, 2016):

Correlation of corrosion behavior and surface free energy of biodegradable Mg–Zn–Ca alloys

Nadine Peneder (Master Project, 2015):

Melt Spinner – Planar Flow Casting Process Parameter Optimization for MgCa0.3 ribbons

Carmen Lauener (Bachelor Thesis, 2015):

Impact of aging temperature on the electrochemical behavior of biodegradable Mg–Zn–Ca alloys

Scholarships

Nov. 2012 – Apr. 2013	Stiftung Industrieforschung (Foundation for Industrial Research) Scholarship for Diplomarbeit (Degree project, eq. to Master thesis)
Aug. 2011 – Dec. 2011	DAAD Erasmus from the German Academic Exchange Service Scholarship for an exchange program at Royal Institute of Technology (Kungliga Tekniska Högskolan (KTH)), Stockholm, Sweden
Jun. 2010 – Aug. 2010	DAAD RISE (Research Internships in Science and Engineering) from the German Academic Exchange Service *Full ride for a summer research project in the USA*

Award

Aug. 2017	Young Scientist Best Presentation Award Microscopy Conference Lausanne, Switzerland

Voluntary work

Since Jul. 2018	Representative of the Scientific Staff of the Department of Materials in the *Materials Alumni ETH* board
Since Dec. 2014	Board member of Scientific Staff Association at the Department of Materials at ETHZ · Involvement in university politics on the department level · Organization of Department Colloquium Series
Jul. 2014 – Jul. 2017	Vice president of the Scientific Staff Association at the Department of Materials at ETHZ and representative in the department conference and teaching commission
Jan. 2010 – Apr. 2012	Active member of the student association at the Department of Mechanical Engineering and Process Engineering at KIT

Publications and Conference contributions

Journal publications

Cihova, M., Schmutz, P., Schäublin, R., Löffler, J.F., *Biocorrosion zoomed in: evidence for dealloying of intermetallic nanoparticles in magnesium alloys*, Adv. Mat. 31(42) (2019) 1903080.

Cihova, M., Martinelli, E., Schmutz, P., Myrissa, A., Schäublin, R., Weinberg, A.M., Uggowitzer, P.J., Löffler, J.F., T*he role of zinc in the biocorrosion behavior of resorbable Mg–Zn–Ca alloys*, Acta Biomat. 100 (2019) 398-414.

Kleger, N., **Cihova, M.**, Masania, K., Studart, A. R., Löffler, J. F., *3D printing of Salt as a Template for Magnesium with structured porosity*, Adv. Mat. 31(37) (2019), 1903783.

Soderlind, J., **Cihova, M.**, Schäublin, R., Risbud, S., Löffler, J.F., *Towards refining microstructures of biodegradable magnesium alloy WE43 by spark plasma sintering*, Acta Biomat. 98 (2019) 67–80.

Cihova, M., Schäublin, R., Hauser, L., Gerstl, S., Simson, C., Uggowitzer, P.J., Löffler, J.F., *Rational design of a lean magnesium-based alloy with high age-hardening response*, Acta Mat. 158 (2018), 214-229.

Johnston, S., Shi, Z., Hoe, C., Uggowitzer, P.J., **Cihova, M.**, Löffler, J.F., Dargusch, M.S. and Atrens, A., *The influence of two common sterilization techniques on the corrosion of Mg and its alloys for biomedical applications*, J. of Biomed. Mat. Res. B: Appl. Biomat. 106(5) (2018), 1907-1917.

Koenig, G., Ozcelika, H., Haesler, L., **Cihova, M.**, Ciftci, S., Dupret-Bories, A., Debrya, C., Stelzle, M., Lavalle, P., Vranaf, E. N., *Cell-laden hydrogel/titanium microhybrids: Site-specific cell delivery to metallic implants for improved integration*, Acta Biomat. 33 (2016), 301–310.

Schäublin, R., Becker, M., **Cihova, M.**, Pogatscher, S., Gerstl, S. S. A., Uggowitzer, P.J., Löffler, J.F., *Precipitation in the Mg–Zn–Ca alloy ZX20,* submitted to Acta Mat.

Holweg, P., **Cihova M.**, Donohue, N., Clement, B., Schwarze, U., Sommer, N.G., van den Beucken, J.J.J.P., Berger, L., Löffler J.F., Hohenberger, G., Weinberg, A.-M., *Fracture stabilization with resorbable magnesium implants in a large growing-animal model*, submitted to Acta Biomat.

Cihova, M., von Petersdorff-Campen, K., Schmutz, P., Schäublin, R., Uggowitzer, P.J., Löffler, J.F., *Early-stage biocorrosion of ZX-lean alloy with tailored intermetallic phases*, in preparation.

E. Martinelli, **M. Cihova**, S. Bräuer, A. Myrissa, J. Eichler, W. Gössler, P.J. Uggowitzer, J.F. Löffler, A.M. Weinberg, *Long-term in vivo response to biodegradable Mg–Zn–Ca alloys of varying Zn content,* in preparation.

Conference proceedings

Cihova, M., Schäublin, R., Gerstl, S.S.A., Hauser, L.B., Simson, C., Papenberg, N., Gneiger, S., Schlögl, C.M., Uggowitzer, P.J., Löffler, J.F., *Mikrostruktur-Eigenschafts-Korrelationen in aushärtbaren mageren Mg-Legierungen*, 10. Ranshofener Leichtmetalltage (2018), Linz, Austria.

Uggowitzer, P.J., **Cihova, M.**, Horwatitsch, D., Hametner, T., Pogatscher, S., Klaumünzer, D., Löffler, J. F., *Designkonzepte für niedriglegierte hochfeste Magnesiumlegierungen*, 9. Ranshofener Leichtmetalltage (2016), Bad Ischl, Austria.

Berger, L., Eichler, J., **Cihova, M.**, Martinelli, E., Kleinhans, C., Löffler, J., Weinberg, A.-M., *In-vivo comparison of chemically polished vs. unpolished magnesium-based screws in ovine tibiae*, Front. Bioeng. Biotechnol. Conference Abstract: 10th World Biomaterials Congress (2016), Montreal, Canada, doi:10.3389/conf.FBIOE.2016.01.00010.

Johnston, S., Shi, Z., **Cihova, M.**, Hofstetter, J., Dargusch, M., Atrens, A., *Optimising the surface treatment of ultra-high purity mg alloy wire*, Front. Bioeng. Biotechnol. Conference Abstract: 10th World Biomaterials Congress (2016), Montreal, Canada, doi: 10.3389/conf.FBIOE.2016.01.02451.

Cihova, M., Biffi, G., Uggowitzer, P. J., Löffler, J. F., *Grain-boundary strengthening of MgZnCa lean alloys*, European Cells and Materials, Vol. 32 Suppl. 6 (2016), p. 3., 7th Symposium on Biodegradable Metals for Biomedical Applications, Esterel, Québec, Canada.

Cao, J., Hofstetter, J., **Cihova, M.**, Trinh, W., Mingler, B., Uggowitzer, P. J., Löffler, J. F., *Variations in degradation of ultrahigh-purity MgZnCa alloys by thermal treatment*, European Cells and Materials, Vol. 30. Suppl. 3, p. 21, 7th Symposium on Biodegradable Metals for Biomedical Applications (2015), Carovigno, Italy.

Conference presentations

Cihova, M., Schmutz, P., Martinelli, E., Schäublin, R., Myrissa, Anastasia, Weinberg, A. M., Uggowitzer, P. J., Löffler, J. F., *Biocorrosion zoomed in: Nanoscale insights into the biodegradation behavior of Mg–Zn–Ca-lean alloys,* 4th European Symposium on Intelligent Materials (2019) Kiel, Germany. (Invited Lecture)

Cihova, M., Martinelli, E., Schäublin, R., Weinberg, A. M., Schmutz, P., Uggowitzer, P. J., Löffler, J. F., *Microstructure–biocorrosion correlation of Mg–Zn–Ca-lean alloys with varying Zn content,* 10th Symposium on Biodegradable Metals for Biomedical Applications (2018) Oxford, England. (Keynote Lecture)

Cihova, M., *Impact of Heat-Treatment Induced Microstructural Changes on the Properties of Biodegradable Mg–Zn–Ca-Lean Alloys*, 12th Annual Materials and Processes Graduate Symposium (2017) Zurich, Switzerland. (Poster Presentation)

Cihova, M., Hauser, L., Schäublin, R., Horwatitsch, D., Hametner, T., Pogatscher, S., Uggowitzer, P. J., Löffler, J.F., *Design concept of hardenable magnesium-lean alloys processed by high-speed extrusion,* 2nd Conference on Light Materials (2017) Bremen, Germany. (Oral Presentation)

Cihova, M., von Petersdorff-Campen, K., Schäublin, R., Schmutz, P., Löffler, J.F., *Transmission electron microscopy study of the early-stage biocorrosion events in magnesium-based lean alloys*, 9th Symposium on Biodegradable Metals for Biomedical Applications (2017) Bertinoro, Italy. (Keynote Lecture)

Cihova, M., von Petersdorff-Campen, K., Schäublin, R., Deiana, D., Uggowitzer, P. J., Schmutz, P., Löffler, J.F., *Early stage biocorrosion of magnesium-based alloys studied by TEM*, Microscopy Conference (2017) Lausanne, Switzerland. (Oral Presentation)

Cihova, M., Schäublin, R., Schmutz, P., Uggowitzer, P.J., Löffler, J.F., *Microstructure-corrosion relation of biodegradable Mg-Zn-Ca-lean alloys*, Swiss Corrosion Science Day (2017) Dübendorf, Switzerland. (Oral Presentation)

Cihova, M., Eichler, J., Martinelli, E., Berger, L., Uggowitzer, P. J., Weinberg, A. M., Löffler, J. F., *MgZnCa-lean alloys as temporary implant material for osteosynthesis*, Material Science and Engineering, Darmstadt, Germany (2016). (Oral Presentation)

Cihova, M., Biffi, G., Uggowitzer, P. J., Löffler, J. F., *Grain-boundary strengthening of MgZnCa lean alloys*, 8th Symposium on Biodegradable Metals for Biomedical Applications (2016), Esterel, Québec, Canada. (Oral Presentation)

Cihova, M., Cao, J.D., Lauener, C. and Löffler, J.F., *Corrosion behavior of biodegradable Mg-Zn-Ca alloys after thermal treatment*, 10th World Biomaterials Congress (2016) Montreal, Canada. (Oral Presentation)

Cao, J., Hofstetter, J., **Cihova, M.**, Trinh, W., Mingler, B., Uggowitzer, P. J., Löffler, J. F., *Variations in degradation of ultrahigh-purity MgZnCa alloys by thermal treatment*, 7th Symposium on Biodegradable Metals for Biomedical Applications (2015), Carovigno, Italy. (Poster Presentation)